

**POLITECNICO DI TORINO**



**Doctor of Philosophy in Chemical Engineering**

*Department of Applied Science and Technology  
PhD Coordinator: Prof. Marco Vanni*

*XXVII Cycle (2012-2014)*

PhD Thesis

**Development of innovative materials used in  
electrochemical devices for the renewable  
production of hydrogen and electricity**

*Academic Tutors:*

Prof. Bernardo Ruggeri – Politecnico di Torino

Prof. Guido Saracco – Politecnico di Torino

*Co-Tutors:*

Ph.D. Simelys Hernández – Istituto Italiano di Tecnologia

Ph.D. Tonia Tommasi – Istituto Italiano di Tecnologia

*PhD Student:*

Diana C. Hidalgo D.

(No. 189140)

2014

## ***Acknowledgements***

*Over the last three years as PhD student, I have learned great things not only about science and academics, but also about the life, the truth and the faith.*

*I would like to express my special appreciation and thanks to my tutors, Prof. Bernardo Ruggeri and Prof. Guido Saracco, you have been wonderful mentors for me. Your advice on both research as well as on my career have been priceless.*

*I would like to thank my co-supervisors, Dr. Simelys Hernández and Dr. Tonia Tommasi. I am grateful for their patience, fruitful discussions and explanations, as well as personal support and motivation. Simelys, thank for encouraging me to apply for the PhD Program and for joining me on each of my achievements.*

*Special thanks to past and present members of the CSHR@PoliTO (Istituto Italiano di Tecnologia) and of the Politecnico di Torino, for their great help and guidance: Diego Manfredi, Marco Armandi, Angelica Chiodoni, Marco Fontana, Sergio Bocchini, Valentina Cauda, Adriano Sacco, Andrea Lamberti, Flaviana Calignano, Samuele Porro, Edvige Celasco, Camilo Fernandez, Fabrizio Pirri, Sara Perrucci and Lidia Calleri.*

*I would like to thank people who made the time of my stay in Istituto Italiano di Tecnologia such an unique experience: Marco Di Donato, Valeria Agostino, Karthikeyan DV, Marco Fontana and Riccardo Canali. Specially, Carminna Ottone and Vivian Farias, for our friendship and thank you for all the pleasant lunches together and the nice breaks.*

*I am exceptionally lucky to meet such incredible friends during the time of my Ph.D. studies: Sorani Montenegro, Katherine González, Elena Iannaccone, Alfredo Scarpa, Teresa Bonelli, Valeria Foddai, Laura Gaita, Camillo Fernandez, Simone Ansaloni and Simone Scelfo. Specially, I thank to Thalluri Mouli and Andrea Luongo who always supported and cheered me so that I could focus on my way.*

*A special thanks for the people that more than everyone else have contributed to the success of my PhD: my family. Words cannot express how grateful I am to my Mama, Papa, sister, brother and nephew, your prayer for me was what sustained me thus far. Specially, I thank my husband Sergio who is my biggest supporter, greatest friend and closest spiritual partner in all ways, who spent sleepless nights and was always my support in the moments when there was no one to answer my queries.*

*I dedicate this work who for many years has been my spiritual and professional guide  
To you, that with humanity and human simplicity have stolen my heart  
This thesis is for the man I love - my husband Sergio Castillo.*

## Abstract

One of the most important challenges for our society is providing powerful devices for renewable energy production. Many technologies based on renewable energy sources have been developed, which represent a clean energy sources that have a much lower environmental impact than conventional energy technologies. Nowadays, many researches focus their attention on the development of renewable energy from solar, water, organic matter and biomass, which represent abundant and renewable energy sources. This research is mainly focused on the development of promising electrode materials and their potential application on emerging technologies such as artificial photosynthesis and microbial fuel cell (MFC). According to desired proprieties of functional materials, this research was focused on two main materials: (1)  $\text{TiO}_2$  for the development of electrodes for the water splitting reaction due to its demonstrated application potential as photocatalyst material and (2) carbon-based materials for the development of electrodes for MFC.

In the first part of the investigation, different  $\text{TiO}_2$  nanostructures have been studied including: synthesis, characterization and test of  $\text{TiO}_2$ -based materials with the aim of improving the limiting factors of the photocatalytic reaction: charge recombination and separation/migration processes. The photo-catalytic properties of different  $\text{TiO}_2$  nanostructures were evaluated including:  $\text{TiO}_2$  nanoparticles (NPs) film,  $\text{TiO}_2$  nanotubes (NTs) and  $\text{ZnO@TiO}_2$  core-shell structures. Photo-electrochemical activity measurements and electrochemical impedance spectroscopy analysis showed an improvement in charge collection efficiency of 1D-nanostructures, related to a more efficient electron transport in the materials. The efficient application of both the  $\text{TiO}_2$  NTs and the  $\text{ZnO@TiO}_2$  core-shell photoanodes opens important perspectives, not only in the water splitting application field, but also for other photo-catalytic applications (e.g. photovoltaic cells, degradation of organic substances), due to their chemical stability, easiness of preparation and improved transport properties. Additionally, in order to improve the photo-catalytic activity of  $\text{TiO}_2$  NPs, PANI/ $\text{TiO}_2$  composite film was synthesized. PANI/ $\text{TiO}_2$  composite film was successfully applied as anode material for the PEC water splitting reaction showing a significant increase in the photocatalytic activity of  $\text{TiO}_2$  NPs composite film essentially attributed to the efficient separation of the generated electron and hole pairs. To date, no cost-effective materials system satisfies all of the technical requirements for practical hydrogen production under zero-bias conditions. For this propose, to promote the sustainability of the process, the bias

require to conduct PEC water splitting reaction could be powered by MFC systems in which many efforts have been done to improve power and electricity generation as is explained below.

In this work, different strategies were also applied in order to improve the performance of anode materials for MFCs. The investigation of commercial carbon-based materials demonstrated that these materials, normally used for other ends are suitable electrodes for MFC and their use could reduce MFC costs and improve the energy sustainability of the process. In addition, to enhance power generation in MFC by using low-cost and commercial carbon-based materials, nitric acid activation (C-HNO<sub>3</sub>) and PANI deposition (C-PANI) were performed on commercial carbon felt (C-FELT) in order to increase the performance of MFC. Electrochemical determinations performed in batch-mode MFC revealed a strong reduction of the activation losses contribution and an important decrease of the internal resistance of the cell using C-HNO<sub>3</sub> and C-PANI of about 2.3 and 4.4 times, respectively, with respect to C-FELT. Additionally, with the aim of solving different MFC operational problems such as: biofouling, low surface area and large-scale MFC, an innovative three-dimensional material effectively developed and used as anode electrode. The conductive carbon-coated Berl saddles (C-SADDLES) were successfully used as anode electrode in batch-mode MFC. Electrochemical results suggested that C-SADDLES offer a low-cost solution to satisfy either electrical or bioreactor requirements, increasing the reliability of the MFC processes, and seems to be a valid candidate for scaled-up systems and for continuous mode application of MFC technology. In addition, the electrochemical performance and continuous energy production of the most promising materials obtained during this work were evaluated under continuous operation MFC in a long-term evaluation test. Remarkable results were obtained for continuous MFCs systems operated with three different anode materials: C-FELT, C-PANI and C-SADDLES. From polarization curves, the maximum power generation was obtained using C-SADDLES (102 mW·m<sup>-2</sup>) with respect to C-FELT (93 mW·m<sup>-2</sup>) and C-PANI (65 mW·m<sup>-2</sup>) after three months of operation. The highest amount of electrical energy was produced by C-PANI (1803 J) with respect to C-FELT (1664 J) and C-SADDLES (1674 J). However, it is worth to note that PANI activity was reduced during time by the operating conditions inside the anode chamber.

In order to demonstrate the wide application potential MFC, this work reports on merging heterogeneous contributions and combining the advantages from three separate fields in a system which enables the ultra-low-power monitoring of a microbial fuel cell voltage status and enables pressure monitoring features of the internal conditions of a cell. The solution is

conceived to provide an efficient energy source, harvesting wastewater, integrating energy management and health monitoring capabilities to sensor nodes which are not connected to the energy grid. Finally, this work presented a general concept of the integration of both devices into a hybrid device by interfacing PEC and MFC devices (denoted as PEC-MFC), which is proposed to generate electricity and hydrogen using as external bias the potential produce by microbial fuel cell.

# Content

<b>Introduction</b>	<b>Pag.</b>
I.1. Worldwide energy demand	1
I.2. Technologies for renewable energy production	2
I.3. Energy production using proton exchange membrane devices	3
I.4. Materials for renewable energy generation	5
I.5. Objectives and structure of the thesis	6
I.6. References	8

## Chapter 1

### **Literature review - The use of semiconductors for photoelectrochemical water splitting applications**

1.1. Introduction	11
1.2. Research background	11
1.3. Photocatalysts	12
1.3.1. Mechanisms of semiconductor photocatalytic water splitting	12
1.3.2. Photocatalytic activity under visible light	14
1.3.2.1. Doping with transition-metal ions having a $d^n$ ( $0 < n < 10$ ) electronic configuration	16
1.3.2.2. Valence band control using an anion's p orbitals or the s orbitals of p-block metal ions	16
1.3.2.3. Spectral sensitization	17
1.4. Photoelectrode requirements and cell configurations	17
1.4.1. Requirements and trade-offs	18
1.4.2. Nanostructured electrodes	19
1.4.3. PEC devices configuration	20
1.5. References	23

## Chapter 2

### **Thick mesoporous $\text{TiO}_2$ films through a sol-gel method involving a non-ionic surfactant: characterization and enhanced performance for water photo-electrolysis**

2.1. Introduction	27
2.2. Experimental	28
2.2.1. Materials and sol-gel synthesis of TiO <sub>2</sub> nanoparticles	28
2.2.2. Deposition of TiO <sub>2</sub> films	29
2.2.3. Characterizations	29
2.2.4. Photoelectrochemical tests	29
2.3. Results and discussion	30
2.3.1. Thermal properties of TiO <sub>2</sub> solution	30
2.3.2. Characterization of TiO <sub>2</sub> nanoparticles in powder form	31
2.3.3. Characterization of TiO <sub>2</sub> films	34
2.3.4. Photo-electrochemical performances	37
2.3.4.1. Photoactivity of one-layer films	37
2.3.4.2. Modeling of EIS data	39
2.3.4.3. Stability and photoactivity of multi-layer films	42
2.4. Conclusions	44
2.5. References	44

## **Chapter 3**

### **Comparison of photocatalytic and transport properties of TiO<sub>2</sub> and ZnO nanostructures for solar-driven water**

Introduction	47
3.1. Experimental	50
3.1.1. Synthesis of the nanostructures	50
3.1.1.1. TiO <sub>2</sub> nanoparticles film fabrication by sol-gel synthesis	50
3.1.1.2. TiO <sub>2</sub> nanotube arrays fabrication by anodic oxidation	50
3.1.1.3. ZnO nanowires grown by hydrothermal synthesis	51
3.1.1.4. ZnO@TiO <sub>2</sub> core-shell heterostructures prepared by sol-gel impregnation	51
3.1.2. Morphological and optical characterization	51
3.1.3. Photo-electrochemical characterization	52
3.2. Results and discussion	53
3.2.1. Morphology and structure	53
3.2.2. Optical properties	55

3.2.3. Photo-electrochemical activity for the water splitting reaction	57
3.2.4. Electrochemical impedance spectroscopy analysis	61
3.2.5. Electronic properties vs. PEC behavior of TiO <sub>2</sub> NTs and ZnO@TiO <sub>2</sub> core-shells	64
3.3. Conclusions	69
3.4. References	70

## Chapter 4

### Enhanced performance of PANI-TiO<sub>2</sub> nanocomposite mesoporous films for sun-driven water splitting

4.1. Introduction	74
4.2. Experimental	78
4.2.1. Sol-gel synthesis and deposition of TiO <sub>2</sub> nanoparticles	78
4.2.2. Polyaniline synthesis	79
4.2.3. Deposition of polyaniline on TiO <sub>2</sub> films	79
4.2.4. Materials and characterization	79
4.2.5. Photoelectrochemical tests of TiO <sub>2</sub> and PANI-TiO <sub>2</sub> composites films	80
4.3. Results and discussion	81
4.3.1. Physico-chemical characterization of TiO <sub>2</sub> and PANI-TiO <sub>2</sub> films	81
4.3.2. Photoelectrochemical characterization of TiO <sub>2</sub> and PANI-TiO <sub>2</sub> films	83
4.4. Conclusions	89
4.5. References	90

## Chapter 5

### Literature review - Microbial fuel cell for electricity generation

5.1. Introduction	94
5.2. History of microbial fuel cell development	94
5.3. Bioelectricity generation using microbial fuel cell	95
5.4. Electron transfer in microbial fuel cell	98
5.5. Microbes used in microbial fuel cells	100
5.6. MFC reactor components	101
5.6.1. Electrodes	101
5.6.1.1. Surface properties	102

5.6.1.2. Structure	102
5.6.1.3. Base material	103
5.6.2. Electrolyte	103
5.6.3. Membrane	104
5.7. MFC design	104
5.8. Effect of operating conditions	106
5.8.1. Substrate	106
5.8.2. pH buffer and electrolyte	107
5.8.3. Proton exchange system	108
5.8.4. Operating conditions in the anodic chamber	108
5.8.5. Operating conditions in the cathodic chamber	109
5.9. Electrochemical characterization techniques	110
5.9.1. Choice of electrode configuration	110
5.9.2. Open Circuit voltage	110
5.9.3. MFC polarization techniques	111
5.9.4. Current interruption (CI)	112
5.9.5. Electrochemical impedance spectroscopy	112
5.9.6. Cyclic voltammetry	114
5.10. Factors limiting the electrical energy generation	115
5.10.1. Electrical parameters	115
5.10.2. Activation losses	116
5.10.3. Ohmic losses	116
5.10.4. Mass transfer	117
5.10.5. Electron quenching reactions and energy efficiency	117
5.11. References	117

## **Chapter 6**

### **New approach for low-cost microbial fuel cells for energy sustainable waste-streams treatment**

6.1. Introduction	123
6.2. Experimental	124
6.2.1. Electrodes materials and preparation	124
6.2.2. MFC configuration and operation	124

6.2.3. Characterization and electrochemical measurements	125
6.3. Results and discussion	126
6.3.1. Properties of commercial carbon-based materials as electrode in MFC	126
6.3.2. Power generation	128
6.4. Conclusions	131
6.5. References	132

## **Chapter 7**

### **Surface modification of commercial carbon felt used as anode for Microbial Fuel Cells (MFCs)**

7.1. Introduction	134
7.2. Experimental	136
7.2.1. Materials	136
7.2.2. Anode material preparation	136
7.2.2.1. Activation of commercial carbon felt by nitric acid	136
7.2.2.2. Synthesis and deposition of PANI on carbon felt	136
7.2.3. Characterizations of anode materials	137
7.2.4. MFCs configuration and operation	137
7.2.5. Electrochemical characterizations	138
7.3. Results and discussion	139
7.3.1. Characterizations of anode materials	139
7.3.2. Power generation	144
7.4. Conclusions	148
7.5. References	149

## **Chapter 8**

### **Streamlining of commercial berl saddles: a new material to improve the performance of microbial fuel cells**

8.1. Introduction	151
8.2. Experimental	153
8.2.1. Materials	153
8.2.2. Deposition of conductive carbon layer on Berl saddles	153
8.2.3. Characterization of Berl saddles	154

8.2.4. MFC configuration and operation	154
8.2.5. Electrochemical measurements and analyses	155
8.3. Result and discussion	156
8.3.1. Characterization of Berl saddles	156
8.3.2. Electrochemical characterization of carbon-coated Berl saddles	160
8.3.3. Cost analysis of carbon-coated Berl saddles	164
8.4. Conclusions	166
8.5. References	166

## **Chapter 9**

### **Continuous electricity generation using microorganisms from seawater in microbial fuel cells (MFCs): long-term evaluation of promising anode materials**

9.1. Introduction	169
9.2. Experimental	172
9.2.1. Materials	172
9.2.2. Bacterial growth conditions	173
9.2.3. Determination of bacterial communities	173
9.2.4. MFC configuration and operation	173
9.2.5. Physical-chemical characterization of MFC parameters	175
9.2.6. Electrochemical measurements and energy production using MFC	175
9.3. Results and discussion	176
9.3.1. Physicochemical characterization of MFC parameters	176
9.3.2. Microorganisms identification	179
9.3.3. Power generation	181
9.3.4. Energy production using MFC	186
9.3.5. Variation of the applied external resistance	187
9.4. Conclusions	189
9.5. References	190

## **Chapter 10**

### **A low complexity wireless microbial fuel cell monitor using piezoresistive sensors and impulse-radio ultra-wide-band**

10.1. Introduction	194
--------------------	-----

10.2. Experimental	196
10.2.1. System Concept	196
10.2.2. Microbial fuel cells	197
10.2.3. Piezoresistive pressure sensor	198
10.2.4. IR-UWB transmitter	199
10.3. Results and discussion	200
10.3.1. MFC operation	200
10.3.2. Complete system	201
10.5. Conclusion	203
10.6. References	203

## **Prospective**

### **A hybrid solar-microbial device for sustainable hydrogen and electricity generation**

P.1. Introduction	206
P.2. Experimental	207
P.2.1. PEC and MFC configuration and operation	207
P.2.2. Electrochemical and photo-electrochemical characterization	209
P.3. Results and discussion	210
P.4. Future works	213
P.5. References	214

<b>Summary</b>	<b>216</b>
----------------	------------

# Introduction

In this introductory Chapter the worldwide energy demand is described, focused on devices for renewable energy production. A description of the commonly used proton exchange membrane (PEM) devices for energy production is provided with specific applications on water splitting and microbial fuel cell technologies. Finally, to clarify the scenario in which this work is contextualized an overview of the objectives and structure of the thesis is reported.

## I.1. Worldwide energy demand

The era in which human kind could only rely on plain solar power and its main derivatives (biomass, fuel wood, wind, hydropower) to empower its energy needs, vanished 100 years ago. Coal ended the long dominance of fuel wood in the United States around 1885. The latter was surpassed in 1951 by petroleum and a few years later by natural gas. Since then, the intensified use of fossil fuels has massively increased our energy consumption and our dependency on it [1]. The need for power is nowadays mainly satisfied by the use of conventional energy sources based on oil, coal, natural gas and nuclear power that have proven to be highly effective drivers of economic progress. Unfortunately, the environmental impact of most of these energy sources is tremendous, mainly because of the emission of greenhouse gases, which causes the increase in the global averaged temperature affecting the equilibrium in all the ecosystems. Moreover, from 2010 to 2040, the world's population is projected to rise from 7 billion to nearly 9 billion, and the global economy will increase in more than double [2]. Over that same period, global energy demand is likely to rise by about 35 percent, related with an important rising on the demand of energy in the developing countries, leading to an expected planetary emergency of gigantic dimensions (see Figure I.1) [2]. In this panorama, the potential impact of renewable energy sources is enormous as they can in principle meet many times the world's energy demand providing sustainable energy services based on the use of routinely available indigenous resources. A global transition to renewable energy is already underway, and the developments of more efficient systems continue to increase, while the price of oil and gas continues to fluctuate. Renewable energy offers an alternative to conventional sources and grants us greater control over future energy prices and supply [3]. Clearly, during this new era an answer must be found to a most

intriguing quest: the generation of sustainable energy and in particular energy production from renewable energy sources.

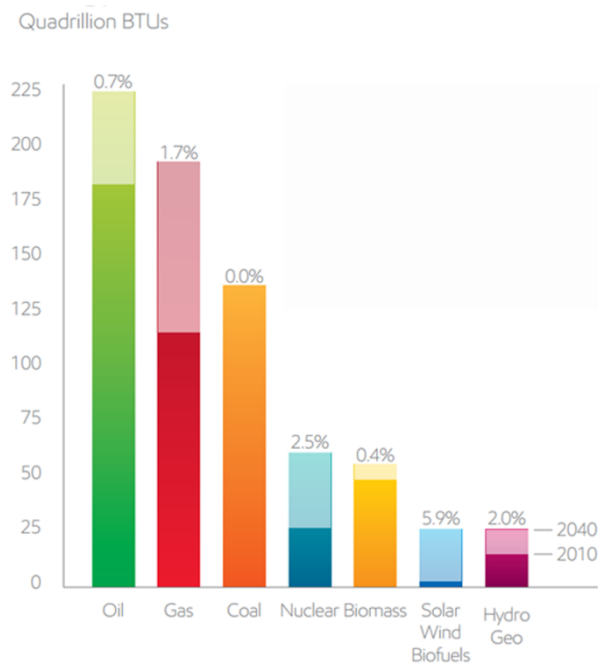


**Figure I.1.** Global energy demand [2]

### I.2. Technologies for renewable energy production

Prior to the development of coal in the mid 19th century, nearly all energy used was renewable. Almost without a doubt the oldest known use of renewable energy, in the form of traditional biomass to fuel fires [4]. Moving into the time of recorded history, the primary sources of traditional renewable energy were human labor, animal power, water power, wind, in grain crushing windmills, and firewood, a traditional biomass. In the 1970s environmentalists promoted the development of renewable energy both as a replacement for the eventual depletion of oil, as well as for an escape from dependence on oil [5]. From 1992 onwards, renewable energy has become a top priority for the governments in all the European countries due to the increasing global concerns about climate change and scarcity of fossil fuels [6, 7]. Such targets require that low carbon technologies for generating energy, become usual, rather than ‘alternative’, as is currently often the case. Nowadays, renewable energy technologies for energy generation vary in a wide technology-choices: solar photovoltaic panels, wind turbines of different scale, energy from waste plants, biomass fuelled plant at scales from small combined heat and power plant to large scale power stations, hydro schemes and ocean technologies (e.g. tidal and wave devices) [8]. Other renewable energy technologies are still under development and include: cellulosic ethanol, hot-dry-rock

geothermal power, ocean energy, artificial photosynthesis and microbial fuel cells (MFCs) [8-10]. These technologies are not yet widely demonstrated or have limited commercialization. To this purpose, many efforts have been done to develop cost-effective and high efficient energy production systems, however up-to-day above technologies are under development and are not commercially available [11, 12]. In order to encourage the development of renewable energies, this research is mainly focused on the study of promising materials and their potential application on emerging technologies such as artificial photosynthesis and microbial fuel cell to produce clean and renewable energy by using the appropriate PEM devices.

### **I.3. Energy production using proton exchange membrane devices**

A fuel cell (FC) is a device that converts the chemical energy contained in a fuel into electricity through a chemical reaction with oxygen or another oxidizing agent [13]. Fuel cells are classified primarily by the kind of electrolyte they employ. This classification determines the kind of chemical reactions that take place in the cell, the kind of catalysts required, the temperature range in which the cell operates, the fuel required, and other factors [14]. These characteristics, in turn, affect the applications for which these cells are most suitable. There are several types of fuel cells currently under development, each with its own advantages, limitations, and potential applications. Some types of fuel cells are: proton exchange membrane (PEM) fuel cells, direct methanol fuel cells, alkaline fuel cells, phosphoric acid fuel cells, molten carbonate fuel cells, solid oxide fuel cells and regenerative fuel cells [14]. In particular, PEM-FC is an electrochemical FC fed with hydrogen, which is oxidized at the anode, and oxygen that is reduced at the cathode. The protons released during the oxidation of hydrogen are conducted through the PEM at the cathode. Since the PEM membrane is not electrically conductive the electrons released from the hydrogen travel along the electrical detour provided and an electrical current is generated, as shown in Figure I.2.

Based on the configuration of PEM-FC that is: anode, cathode and PEM, also simplify the separation and storage of the products obtained, several devices for renewable energy generation have emerged in the last year and many of these are not already commercially available such as: (a) photoelectrochemical cell (PEC) for hydrogen production through water splitting reaction and (b) microbial fuel cells (MFC) for direct electricity generation by microorganisms activity (see Figure I.3), systems on which this work is focused. Both hydrogen and electricity generated by using renewable energy process are of great interest in order to resolve the two main problems related with the current energy demand: (1) the use of

fossil fuels which cause serious environmental problems, such as global warming, climate changes, melting of ice caps, rising sea levels, acid rain, pollution, ozone layer depletion, oil spills, forest and agricultural land damage caused by mining of coal, and so on [14], and (2) the important rising on the demand of energy as a result of population growth and economic development, thus expected a global energy emergency for the future generations.

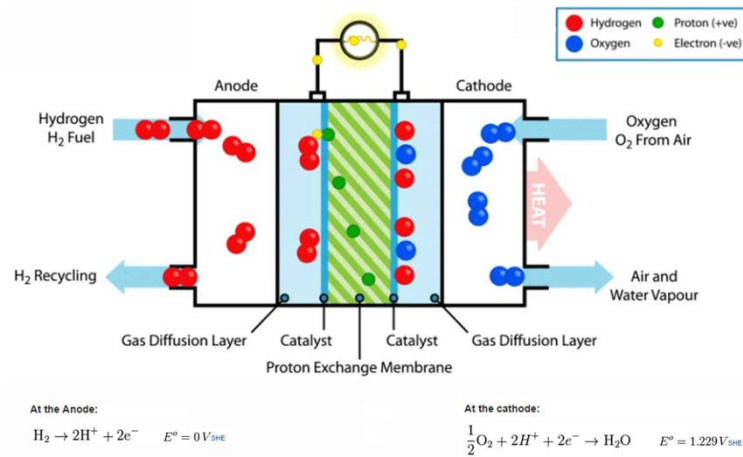


**Figure I.2.** Diagram of fuel cell operation

Hydrogen is an excellent energy carrier with many unique properties. It is the lightest, most efficient, and cleanest fuel. In this sense, photoelectrochemical water splitting emerged as a promising technology for the production of hydrogen, because uses two renewable energy sources such as water and solar light. Thus, also the combination of water, solar light and electricity produced by renewable energy devices (i.e. photovoltaic or MFC systems), potentially offers the cleanest and sustainable way to produce hydrogen. However, the search for suitable materials to be employed for the water dissociation into molecular hydrogen and oxygen is still an open challenge. Similarly to photoelectrochemical cell for hydrogen production explained above, MFCs configuration typically consist of anode, cathode and proton exchange membrane [15]. MFCs are bioelectrochemical systems that directly convert chemical energy of organic compounds into electricity via microbial metabolism. Even with the remarkable improvements in power density obtained up-to date, the large-scale applications of MFCs have yet to be implemented due to low energy generation and high costs [16, 17]. Therefore, in order to make MFCs a sustainable energy process, the power density should be significantly increased; in this respect, the electron transfer from bacteria to the anode seems to be one of the limiting steps in the energy generation in MFCs [18]. Research has been and is currently being conducted into several research groups, but until

today hydrogen and electricity production by using renewable energy process represent an important challenge due to the low efficiencies and high costs involved, in such regard new active materials must be developed.

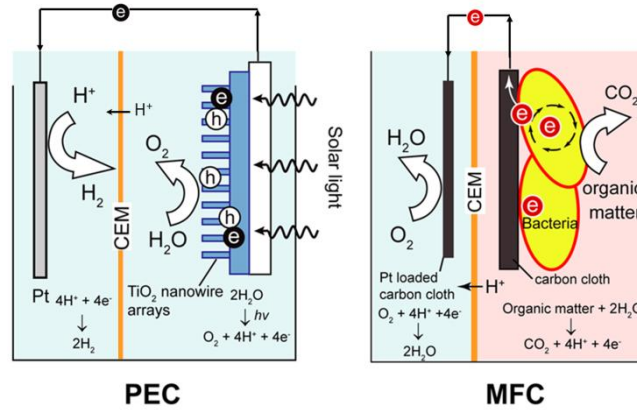


**Figure I.3.** Schematic configuration of a PEC and MFC with PEM configuration

#### I.4. Materials for renewable energy generation

Driven by recent discoveries and innovation in the science and technology of materials, applications based on functional materials are becoming increasingly important. The development of functional materials for sustainable energy involve research, development, manufacture and application of materials for energy production. A wide variety of materials for sustainable energy applications have been developed and many other are currently under development [15, 19-21]. In particular, in systems based on proton exchange membrane configurations, the research of functional materials have been focused on the developments of membranes, catalysts, electrolytes, novel cathodes and anodes, in order to improve the global performances of the cells. Many researchers have been devoted to this end and the research of innovative and more efficient materials continues to be an important challenge. Focusing the attention on anode materials for renewable energy generation, a wide variety of possibilities could be studied. However, in order to restrict the range of possibility, preferred properties have to be identified and evaluated for each particular system. In this respect, a brief description of the main desired properties of the anode materials used in photoelectrochemical water splitting and microbial fuel cell are explained below.

In the research for functional materials for photoelectrochemical water splitting has been found that a suitable anode material should exhibits high photocatalytic efficiency, optimal environmental compatibility and good chemical and optical stability [22]. Thus, it has been found that the photochemical water-splitting reaction can be catalyzed by over 140 metal

oxides, perovskites and oxynitrides [23]. Since 1972, after the pioneering work of Fujishima and Honda [24], titanium dioxide ( $\text{TiO}_2$ ) is the most commonly studied material for photocatalysts. It up to now  $\text{TiO}_2$  is close to be ideal photocatalyst. Different routes have been adopted for enhancing its photocatalyst performances. However, charge recombination and separation/migration processes are the two most important competitive processes that largely affect the efficiency of the photocatalytic reaction. Because of this, unfortunately, solar-to-hydrogen efficiency is limited and currently continues to be an open challenge [25]. To render  $\text{TiO}_2$  a suitable material to be used for the water splitting reaction, in this work are studied and compared the performance of different  $\text{TiO}_2$  nanostructures used as anode electrode in order to improve the photoelectrochemical properties of  $\text{TiO}_2$ .

Comparable with photoelectrochemical water splitting, a wide range of functional materials have been evaluated in order to select the most promising anode material for MFCs application. However, even with the remarkable improvements in power density obtained up-to date, the electron transfer from bacteria to the anode seems to be one of the limiting steps in the energy generation in MFCs [18]. An ideal anode material should promote bacterial attachment and facilitate electron transfer. For this reason, in order to promote high biocatalytic activity, some specific features of electrode materials are required, such as high surface roughness, good biocompatibility and efficient electron transfer between bacteria and electrode surface [16]. Conventional carbon materials (i.e. carbon brush, carbon felt, carbon paper) have been widely used as anode materials because of their good conductivity, stability, biocompatibility and low cost [21]. However, the limited surface area of these materials seems to restrict both biofilm formation and power generation [26, 27]. In order to improve bacterial adhesion and electron transfer, electrode surface modification and/or activation have become a new topic of interest in the research field of MFCs [28-32]. To address these issues, in this work different strategies have been developed to improve the performances on commercial carbon-based materials including: physico-chemical modifications and development of promising materials with a high potential of application for the scaling up of the MFCs process.

### **I.5. Objectives and structures of the thesis**

This work presents the results of the investigation carried out in two devices for renewable energy generation: (1) PEC for hydrogen generation through water splitting reaction and (2) MFC for direct electricity generation by microorganisms activity. They main parameters and operational conditions of these systems are discussed. The investigation was focused on the

development of anodic materials with the aim of improve the performance of the mentioned devices. The properties of a wide range of functional materials were analyzed in depth in order to select the most promising materials able to offer the best performance under each particular operation. To reach this purpose the investigation was focused on two main materials:

1. Due to its demonstrated application potential as photocatalysts materials,  $\text{TiO}_2$  was selected as based materials for the development of anodic electrodes for the water splitting reaction carried out in the PEC. Thus, different  $\text{TiO}_2$  nanostructures have been synthesized, characterized and tested with the aim of improve the limiting factors of the photocatalytic reaction: charge recombination and separation/migration processes.

2. Because of its unique properties, carbon based materials were selected as the most promising materials for the development anodic electrodes for MFC. The evaluation of different commercial, modified and synthesized carbon-based materials were studied, in order to improve the electron transfer from bacteria to the anode in MFCs and thus, increase the energy production of the system.

This work is composed of ten chapters, basically divided on literature review, experimental part, applications of the materials in the devices and conclusions, many of which are a compilation of the papers published and submitted for publication as a result of this PhD thesis as is described below. Chapters from I to IV include the research related to the investigation of PEC for hydrogen production by water splitting reaction. In Chapter I a brief literature review focused on  $\text{TiO}_2$ : synthesis, photoelectrochemical properties and application is described. Chapter II includes development of  $\text{TiO}_2$  nanoparticles by an optimized sol-gel synthesis procedure to obtain  $\text{TiO}_2$  films as anode electrode for photoelectrochemical water splitting. Chapter III reports the investigation of different  $\text{TiO}_2$  nanostructures and their performance for the photoelectrochemical water splitting reaction. Chapter IV includes the deposition of polyaniline in  $\text{TiO}_2$  mesoporous films and its use as sensitizer for photocatalytic water splitting system.

Chapters from V to X include the research related to the investigation on MFC for direct electricity generation by microorganisms activity. Chapter V gives a literature review based on: components, operation and electrochemical characterization of MFCs. In Chapter VI an experimental investigation of several low-cost commercial carbon-based materials used as electrodes for MFC was performed. Chapter VII reports the surface modifications of carbon felt, in order to increase the electrochemical performance of this commercial material used as anode electrode in MFCs. In Chapter VIII an innovative tridimensional anode electrode is

proposed as a suitable packing material for bacteria growth and proliferation in MFCs. Chapter IX provides a long-term evaluation of the performance of three different anode materials: (a) commercial carbon felt, (b) polyaniline-coated carbon felt and (b) the innovative carbon-coated Berl saddles developed in our labs used as anode electrodes in MFC. In Chapter X, applications of the energy produced in the MFC systems are presented. Furthermore, innovative prospective of the combination of both systems PEC and MFC are presented, and preliminary results are reported through a hybrid solar-microbial device for sustainable hydrogen and electricity generation. Finally, a summary and final remarks are included at the end of the thesis.

## **I.6. References**

- [1] Aelterman P. Microbial fuel cells for the treatment of waste streams with energy recovery: Ghent University; 2009.
- [2] [exxonmobil.com/energyoutlook](http://exxonmobil.com/energyoutlook). The Outlook for Energy: A View to 2040 (2014).
- [3] Sørensen B. Chapter 1 - Perspectives on Energy Resources. In: Sørensen B, editor. Renewable Energy (Fourth Edition). Boston: Academic Press; 2011. p. 3-34.
- [4] Roebroeks W, Villa P. On the earliest evidence for habitual use of fire in Europe. *Proceedings of the National Academy of Sciences* 2011;108:5209-14.
- [5] Hubbert MK. Nuclear energy and the fossil fuels: Shell Development Company, Exploration and Production Research Division Houston, TX; 1956.
- [6] Smith WJ. Projecting EU demand for natural gas to 2030: A meta-analysis. *Energy Policy* 2013;58:163-76.
- [7] Krupp C. Electrifying rural areas: extending electricity infrastructure and services in developing countries. *Physical Infrastructure Development: Balancing the Growth, Equity, and Environmental Imperatives* 2010:203.
- [8] E. Moula MM, Maula J, Hamdy M, Fang T, Jung N, Lahdelma R. Researching social acceptability of renewable energy technologies in Finland. *International Journal of Sustainable Built Environment* 2013;2:89-98.
- [9] Collings AF, Critchley C. Artificial photosynthesis: from basic biology to industrial application: John Wiley & Sons; 2007.
- [10] Shah V. Emerging environmental technologies: Springer; 2008.
- [11] Nocera DG. The Artificial Leaf. *Accounts of Chemical Research* 2012;45:767-76.

- [12] Pant D, Van Bogaert G, Diels L, Vanbroekhoven K. A review of the substrates used in microbial fuel cells (MFCs) for sustainable energy production. *Bioresource Technology* 2010;101:1533-43.
- [13] Campanari S, Casalegno A. *Fuel cells: state of the art*. 2007.
- [14] Barbir F. *PEM fuel cells: theory and practice*: Academic Press; 2013.
- [15] Logan BE, Hamelers B, Rozendal R, Schröder U, Keller J, Freguia S, et al. Microbial fuel cells: methodology and technology. *Environmental science & technology* 2006;40:5181-92.
- [16] Wei J, Liang P, Huang X. Recent progress in electrodes for microbial fuel cells. *Bioresource Technology* 2011;102:9335-44.
- [17] Hidalgo D, Tommasi T, Cauda V, Porro S, Chiodoni A, Bejtka K, et al. Streamlining of commercial Berl saddles: A new material to improve the performance of microbial fuel cells. *Energy* 2014;71:615-23.
- [18] Tang X, Guo K, Li H, Du Z, Tian J. Electrochemical treatment of graphite to enhance electron transfer from bacteria to electrodes. *Bioresource Technology* 2011;102:3558-60.
- [19] Steele BCH, Heinzl A. Materials for fuel-cell technologies. *Nature* 2001;414:345-52.
- [20] Hisatomi T, Kubota J, Domen K. Recent advances in semiconductors for photocatalytic and photoelectrochemical water splitting. *Chemical Society Reviews* 2014.
- [21] Zhou M, Chi M, Luo J, He H, Jin T. An overview of electrode materials in microbial fuel cells. *Journal of Power Sources* 2011;196:4427-35.
- [22] Linsebigler AL, Lu G, Yates JT. Photocatalysis on TiO<sub>2</sub> Surfaces: Principles, Mechanisms, and Selected Results. *Chemical Reviews* 1995;95:735-58.
- [23] Ismail AA, Bahnemann DW. Photochemical splitting of water for hydrogen production by photocatalysis: A review. *Solar Energy Materials and Solar Cells* 2014;128:85-101.
- [24] Fujishima A, Honda K. Electrochemical Photolysis of Water at a Semiconductor Electrode. *Nature* 1972;238:37-8.
- [25] Xiaobo C, Samuel SM. Titanium dioxide nanomaterials: synthesis, properties, modifications, and applications. *Chem Rev* 2007;107:2891-959.
- [26] Logan B, Cheng S, Watson V, Estadt G. Graphite fiber brush anodes for increased power production in air-cathode microbial fuel cells. *Environmental science & technology* 2007;41:3341-6.
- [27] Chaudhuri SK, Lovley DR. Electricity generation by direct oxidation of glucose in mediatorless microbial fuel cells. *Nat Biotech* 2003;21:1229-32.

- [28] Rosenbaum M, Zhao F, Quaas M, Wulff H, Schröder U, Scholz F. Evaluation of catalytic properties of tungsten carbide for the anode of microbial fuel cells. *Applied Catalysis B: Environmental* 2007;74:261-9.
- [29] Li C, Zhang L, Ding L, Ren H, Cui H. Effect of conductive polymers coated anode on the performance of microbial fuel cells (MFCs) and its biodiversity analysis. *Biosensors and Bioelectronics* 2011;26:4169-76.
- [30] Liang P, Wang H, Xia X, Huang X, Mo Y, Cao X, et al. Carbon nanotube powders as electrode modifier to enhance the activity of anodic biofilm in microbial fuel cells. *Biosensors and Bioelectronics* 2011;26:3000-4.
- [31] Park DH, Zeikus JG. Improved fuel cell and electrode designs for producing electricity from microbial degradation. *Biotechnology and Bioengineering* 2003;81:348-55.
- [32] Cheng S, Logan BE. Ammonia treatment of carbon cloth anodes to enhance power generation of microbial fuel cells. *Electrochemistry Communications* 2007;9:492-6.

# Chapter 1

## Literature review - The use of semiconductors for photoelectrochemical water splitting applications

### 1.1. Introduction

In this Chapter, a brief review of the historical development of water splitting photocatalysts is described. The special emphasis is put on the study of the photocatalysts properties of semiconductors materials with potential applications as photocatalysts. A description of the mechanisms of photocatalytic water splitting for hydrogen production using semiconductors is included. Photocatalyst modification techniques to enhance the performance of  $\text{TiO}_2$  for hydrogen production are discussed. Finally, photoelectrode requirements and cell configurations are explained.

### 1.2. Research background

Recently, hydrogen has received considerable attention as an ideal fuel for the future. Hydrogen fuel can be produced from clean and renewable energy sources and, thus, its life cycle is clean and renewable. However, presently, renewable energy contributes only about 5% of the commercial hydrogen production primarily via water electrolysis, while other 95% hydrogen is mainly derived from fossil fuels. Thus, renewable hydrogen production is not popular yet because the cost is still high and has a low efficiency [1]. Research in this field was initiated by the demonstration of photoelectrochemical (PEC) water splitting using a single-crystal  $\text{TiO}_2$  (rutile) photoanode and a Pt cathode with an external bias [2], well-known as the Honda-Fujishima effect. When a  $\text{TiO}_2$  anode, an n-type semiconductor, is illuminated by light with energy greater than the band gap of  $\text{TiO}_2$ , electrons and holes are generated in the conduction band and valence band, respectively. When an anodic potential is applied through an external circuit, the electrons migrate through the bulk to reach the Pt counter electrode, thereby reducing  $\text{H}^+$  into  $\text{H}_2$ . Meanwhile, the holes that were left behind on the surface of the  $\text{TiO}_2$  oxidize water, forming  $\text{O}_2$ . The overall reaction process is illustrated in Figure 1.1. Recently, numerous PEC cells have been developed, many of which were designed specifically for the efficient utilization of solar energy. However, due to a lack of suitable photoelectrode materials with appropriate band-gap structures and stability, the systems proposed to date have been rather complicated [3-5]. To address this issue,

photocatalytic water-splitting using TiO<sub>2</sub> for hydrogen production offers a promising way for clean, low-cost and environmentally friendly production of hydrogen by solar energy.

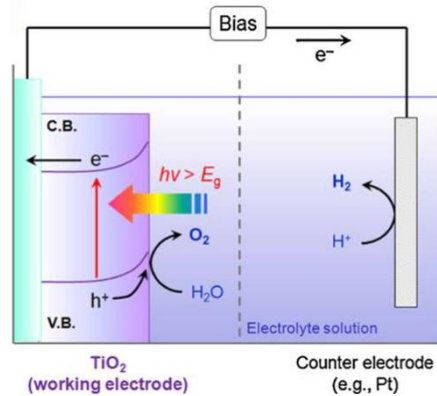


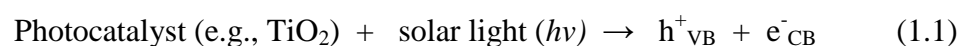
**Figure 1.1.** PEC water splitting using a TiO<sub>2</sub> photoanode

### 1.3. Photocatalysts

Semiconductor photocatalysis has received much attention during last three decades as a promising solution for both energy generation and environmental problems [2, 4, 6-8]. In recent years, scientific and engineering interest in heterogeneous photocatalysis has been also focused on environmental applications such as wastewater treatment and air purification [9, 10]. Both photocatalytic water/air purification and photocatalytic hydrogen production require essential photogeneration of hole/electron pairs. However, the utilization of holes/electrons pairs as well as the systems process are different as is explained in more detail below.

#### 1.3.1. Mechanisms of semiconductor photocatalytic water splitting

The electronic structure of a semiconductor plays a key role in semiconductor photocatalysis. Unlike a conductor, a semiconductor consists of valence band (VB) and conduction band (CB). Energy difference between these two levels is said to be the bandgap ( $E_g$ ). Without excitation, both the electrons and holes are in valence band. When semiconductors are excited by photons with energy equal to or higher than their bandgap energy level, electrons receive energy from the photons and are thus promoted from VB to CB if the energy gain is higher than the bandgap energy level [1]. For the TiO<sub>2</sub> semiconductor, the reaction is expressed as:



The photo-generated electrons ( $e^-_{CB}$ ) and holes ( $h^+_{VB}$ ) can recombine in bulk or on surface of the semiconductor within a very short time, releasing energy in the form of heat or photons. Electrons and holes that migrate to the surface of the semiconductor without recombination can, respectively, reduce and oxidize the reactants adsorbed by the semiconductor. The reduction and oxidation reactions are the basic mechanisms of photocatalytic hydrogen production and photocatalytic water/air purification, respectively. Both surface adsorption as well as photocatalytic reactions can be enhanced by nanosized semiconductors as more reactive surface area is available.

TiO<sub>2</sub> is the most popular photocatalyst because of its relatively high activity, chemical stability, availability with low production costs, and non-toxicity, it has been widely studied and proven to have a potential to completely oxidize a variety of organic compounds, including persistent organic pollutants. For photocatalytic water/air remediation as an environmental application, VB holes are the important elements that induce the oxidative decomposition of the organic pollutants. The positive hole can oxidize pollutants directly, but mostly they react with water (i.e., hydroxide ion, OH<sup>-</sup>) to produce the hydroxyl radical (•OH), which is a very powerful oxidant having an oxidation potential of 2.8 V vs. NHE. •OH rapidly attacks organic molecules at the surface and in solution, and can mineralize them into CO<sub>2</sub>, H<sub>2</sub>O, etc. The reducing CB electrons are more important when photocatalytic reaction is applied for hydrogen production from water splitting as shown in Figure 1.2. In order to initiate the hydrogen production, the conduction band level must be more negative than the hydrogen production level. The redox potential for the overall water splitting reaction (eq. 1.2) at pH 7 is  $E_H = -1.23$  V vs. NHE, with the corresponding half-reactions of -0.41 V (eq 1.4) and 0.82 V (eq 1.5), which gives a  $\Delta G^0 = +237$  kJ/mole) [11] are shown below:



Presently, the energy conversion efficiency from solar to hydrogen by TiO<sub>2</sub> photocatalytic water-splitting is still low, mainly due to the following reasons [1, 12]:

(1) Recombination of photo-generated electron/hole pairs: CB electrons can recombine with VB holes very quickly and release energy in the form of unproductive heat or photons;

(2) Fast backward reaction: decomposition of water into hydrogen and oxygen is an energy increasing process, thus backward reaction (recombination of hydrogen and oxygen into water) easily proceeds;

(3) Inability to utilize visible light: the band gap of  $\text{TiO}_2$  is about 3.2 eV and only UV light can be utilized for hydrogen production. Since the UV light only accounts for about 4% of the solar radiation energy while the visible light contributes about 50%, the inability to utilize visible light limits the efficiency of solar photocatalytic hydrogen production.

In order to resolve the above listed problems and make solar photocatalytic hydrogen production feasible, continuous efforts have been made to promote the photocatalytic activity and enhance the visible light response. Addition of electron donors (hole scavengers), addition of carbonate salts, noble metal loading, metal ion doping, anion doping, dye sensitization, composite semiconductors, metal ion-implantation etc., were investigated and some of them have been proved to be useful to enhance hydrogen production. The above listed techniques influencing  $\text{H}_2$  production have been grouped under two broad classifications, such as ‘chemical additives’ and ‘photocatalyst modification techniques’ [1]. Different strategies based on  $\text{TiO}_2$  photocatalyst modifications techniques can be adopted which are discussed in the following sections.

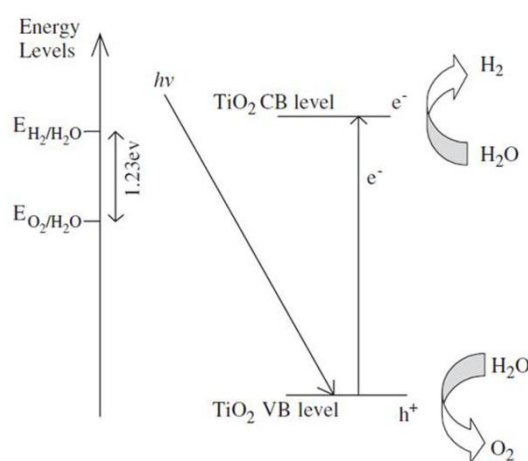


**Figure 1.2.** Mechanism of  $\text{TiO}_2$  photocatalytic water-splitting for hydrogen production

### 1.3.2. Photocatalytic activity under visible light

A large number of metal oxides and sulfides have been examined as photocatalysts for hydrogen production and environmental applications. The majority of the simple metal oxide photocatalysts, however, are primarily active under UV irradiation ( $\lambda < 385 \text{ nm}$  or  $E_g \geq 3.0 \text{ eV}$ ), present in only a small portion of solar light (Table 1.1). For example,  $\text{TiO}_2$  has a wide

band-gap energy of 3.0 ~ 3.2 eV which prevents the utilization of visible-light that accounts for most of solar energy. More recently, significant efforts have also been made to develop new or modified semiconductor photocatalysts that are capable of using visible-light ( $\lambda = 400\text{--}700\text{ nm}$ ). The difficulty in developing a suitable photocatalyst can thus be attributed to the lack of known materials that meet these three requirements: (1) band edge potentials suitable for overall water splitting, (2) bandgap energy lower than 3 eV, and (3) stability in the photocatalytic reaction. To date, numerous attempts have been made to prepare a photocatalytic material that efficiently functions under visible light. In UV-active metal oxide photocatalysts, as mentioned, the bottoms of the conduction bands are slightly below 0 V (vs. NHE) at pH 0, and the tops of the valence bands are above 3 V. This makes the band gap of the material too large to harvest visible light, but suggests that metal oxide photocatalysts have sufficient potential to oxidize water because of the difference between the oxidation potential of  $\text{H}_2\text{O}$  into  $\text{O}_2$  (1.23 V vs. NHE) and the valence band-edge potential (ca. 3 V vs. NHE). It is therefore very important to design the band structure of a metal oxide while keeping the conduction band potential. The primary approaches to making a wide-gap metal oxide sensitive to visible light are schematically illustrated in Figure 1.3 and can be classified as follows.

**Table 1.1.** Band-gap energies for several common semiconductor materials [13, 14]

Semiconductor	Band-gap energy (eV)
Diamond	5.4
$\text{TiO}_2$	3.0~3.2
$\text{WO}_3$	2.7
$\text{ZnO}$	3.2
$\text{SnO}_2$	3.5
$\text{SrTiO}_3$	3.4
$\text{Fe}_2\text{O}_3$	2.2
$\text{CdS}$	2.4
$\text{ZnS}$	3.7
$\text{CdSe}$	1.7
$\text{GaP}$	2.3
$\text{GaAs}$	1.4
$\text{SiC}$	3

### **1.3.2.1. Doping with transition-metal ions having a $d^n$ ( $0 < n < 10$ ) electronic configuration.**

Doping a wide-gap metal oxide with foreign elements is one of the most well-known approaches for modification of the metal oxide crystal, and in most cases a crystal lattice point of the host material is replaced with the dopant. When the dopant is a transition-metal cation that has a partially filled d orbital (i.e.,  $d^n$  ( $0 < n < 10$ ) configuration) or is an anion such as  $C^{4-}$ ,  $N^{3-}$ , or  $S^{2-}$ , a donor or acceptor level is formed in the forbidden band of the material as a center for absorption at visible wavelengths [15]. However, doping also hinders the rapid migration of photogenerated electrons or holes in the material, since the dopant frequently provides a discrete energy level rather than an energy band [16]. Moreover, in most cases, it is difficult to maintain charge balance when a dopant is introduced into the host metal oxide, generating vacancies that act as recombination centers for photogenerated electrons and holes. The doping method is therefore somewhat disadvantageous in the development of an efficient visible-light-responsive oxide-based photocatalyst [15, 17].

### **1.3.2.2. Valence band control using an anion's p orbitals or the s orbitals of p-block metal ions.**

Semiconductors having a continuous valence band formed by atomic orbitals of the constituent elements would be more desirable. Such “valence band-controlled photocatalysts” have been reported by many groups [18-20]. Undoped metal oxides that exhibit activity for the  $H_2$  and/or  $O_2$  evolution half-reactions were reported by Kudo et al. who demonstrated that certain metal oxides containing  $Bi^{3+}$  [21],  $Ag^+$  [22], and  $Sn^{2+}$  [23] cations are capable of harvesting visible photons to cause photocatalytic reactions. Both  $AgNbO_3$  and  $SnNb_2O_6$  are rare oxide photocatalysts that have the ability to reduce and oxidize water in the presence of sacrificial reagents under visible light. Lee et al. reported the photocatalytic properties of  $PbBi_2Nb_2O_9$ , an Aurivillius phase perovskite that has a band gap of 2.88 eV [24]. Under visible light ( $> 420$  nm), the oxide material exhibits a relatively high activity for both water reduction and oxidation in the presence of methanol and silver nitrate, respectively. According to band structure calculations using the Wien97 program, they concluded that the bottom of the conduction band of  $PbBi_2Nb_2O_9$  consists mostly of empty Nb4d orbitals, while the top of the valence band is formed by hybridized Bi6s and Pb6s orbitals. The hybridized orbitals are likely to raise the position of the valence band, giving a smaller band gap than that of compounds that do not contain Pb and Bi in their structure. In addition to  $WO_3$ , many other metal oxides with a visible-light response have been reported to use the s electrons of

the constituent elements ( $\text{Pb}^{2+}$ ,  $\text{Bi}^{3+}$ ,  $\text{Ag}^+$ , and  $\text{Sn}^{2+}$ ). Some have achieved both  $\text{H}_2$  and  $\text{O}_2$  evolution individually in the presence of suitable sacrificial reagents. Although overall water splitting using these metal oxides has yet to be achieved, some have been successfully applied to Z-scheme water-splitting systems mimicking natural photosynthesis in green plants, which involves two-step photoexcitation [17].

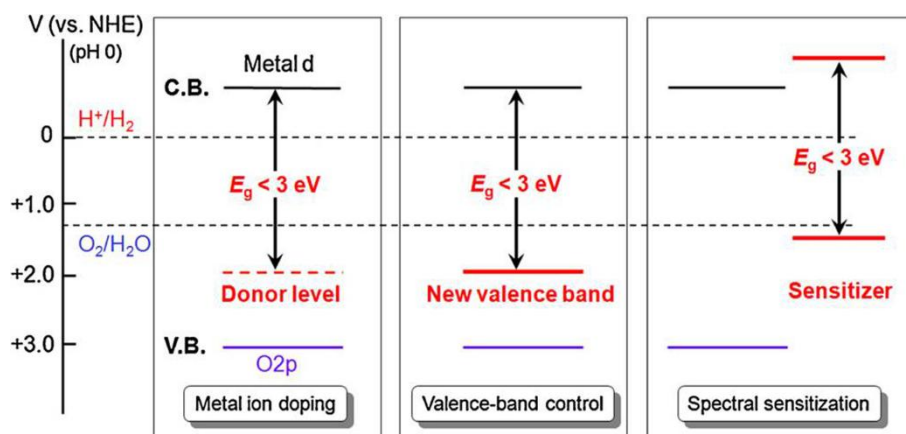


**Figure 1.3.** Conceptual drawing of strategies to develop a visible-light-driven photocatalyst through modification of a metal oxide [12]

### 1.3.2.3. Spectral sensitization

Sensitization methods are widely used to utilize visible-light for energy conversion. In case of sensitization with organic dyes, dye molecule electrons excited by visible light can be injected to the CB of semiconductor to initiate the catalytic reactions. Similarly, sensitization with a small band-gap semiconductor is made by coupling a large band-gap semiconductor with a small band-gap semiconductor with a more negative conduction level (i.e., hybrid or composite photocatalyst). In composite photocatalyst, the CB electrons photo-generated from a small band-gap semiconductor by the absorption of visible-light can be injected to the CB of a large band gap semiconductor, while the photo-generated holes are trapped in a small band-gap semiconductor. Thus, an effective electron-hole separation can be achieved [12, 25].

## 1.4. Photoelectrode requirements and cell configurations

The most critical aspect of the design of a photoelectrochemical device for water splitting is the choice of suitable photoanode and/or photocathode materials. Several of the requirements imposed on these materials appear to be in conflict, and certain trade-offs have to be made. In some cases, these trade-offs can be avoided by adopting smart architectures and materials

combinations. The remainder of this chapter gives a few general considerations and approaches.

#### **1.4.1. Requirements and trade-offs**

Most of the requirements for suitable water-splitting photoanode and/or photocathode materials have already been alluded to in the previous sections of this chapter. They can be summarized as follows [26, 27]:

- Good (visible) light absorption

The spectral region in which the semiconductor absorbs light is determined by the bandgap of the material. The minimum bandgap is determined by the energy required to split water (1.23 eV) plus the thermodynamic losses (0.3–0.4 eV [28]) and the overpotentials that are required at various points in the system to ensure sufficiently fast reaction kinetics (0.4–0.6 eV) [29, 30]. As a result, the bandgap should be at least 1.9 eV, which corresponds to an absorption onset at 650 nm. Below 400 nm the intensity of sunlight drops rapidly, imposing an upper limit of 3.1 eV on the bandgap. Hence, the optimum value of the bandgap should be somewhere between 1.9 and 3.1 eV, which is within the visible range of the solar spectrum. In a thorough analysis, Murphy et al. [29] suggested an optimum bandgap of 2.03 eV, which would lead to a solar-to-hydrogen efficiency of 16.8%.

- High chemical stability in the dark and under illumination

The chemical stability requirement is a severe one that limits the usefulness of many photoactive materials. Most non-oxide semiconductors either dissolve or form a thin oxide layer that prevents charge transfer across the semiconductor/electrolyte interface. Oxide semiconductors are more stable, but may be prone to anodic or cathodic decomposition. The general trend is that the stability against (photo)corrosion increases with increasing bandgap [26]. Although this conflicts with the requirement of visible light absorption, a small bandgap and good chemical stability are not necessarily mutually exclusive (although one could argue that a small bandgap is often accompanied by a high valence band energy, which would indeed result in a less stable material).

- Band edge positions that straddle the water reduction and oxidation potentials

Few semiconductors fulfill the third requirement, which states that the band edges should straddle the water reduction and oxidation potentials. It suggests that the band edges of non-

oxide semiconductors tend to be better suited toward the reduction of water (high  $E_{CB}$ ), whereas those of oxide semiconductors favor water oxidation (low  $E_{VB}$ ). As pointed out originally by Gerischer [31], and reiterated later by Weber [32], it is the quasi-Fermi levels that should straddle the water redox potentials. Although the interpretation of the quasi-Fermi level as a thermodynamic driving force may not be entirely appropriate under all conditions, using it within the context of the third requirement seems reasonable [26].

- Efficient charge transport in the semiconductor

The fourth requirement is easily fulfilled in some materials ( $TiO_2$ ,  $WO_3$ ); while in others it is one of the main causes of poor overall conversion efficiencies. One can distinguish intrinsic and extrinsic charge transport factors. The electronic band structure of the material gives important clues with regard to the intrinsic charge carrier mobilities. Extensive overlap of metal 3d orbitals usually leads to high electron mobilities, whereas the overlap of O-2p orbitals determines the hole mobility in most metal oxides. Extrinsic factors, in particular shallow donors/acceptors and recombination centers, are perhaps even more important [26, 33].

- Low overpotentials for reduction/oxidation of water

For n-type semiconductors, the fifth requirement implies that hole transfer across the semiconductor/electrolyte interface should be sufficiently fast in order to compete with the anodic decomposition reaction. More generally, interfacial charge transfer should be fast enough to avoid the accumulation carriers at the surface, as this would lead to a decrease of the electric field and a concomitant increase in electron–hole recombination. To improve the kinetics of charge transfer, catalytically active surface species can be added. Examples of effective oxygen evolution catalysts are  $RuO_2$  [5],  $IrOx$  [34], and Co-based compounds [35], whereas Pt, Rh [36], Cr–Rh,  $RuO_2$ , or  $NiOx$  [37, 38] are usually employed as a catalysts for hydrogen evolution [26].

#### **1.4.2. Nanostructured electrodes**

Nanostructured electrode morphologies can be used to address some of the intrinsic material's limitations and trade-offs mentioned above. The most obvious advantage of a nanostructured morphology is the increase in specific surface area. The concomitant increase in the number of surface sites greatly enhances the overall charge transfer kinetics at the semiconductor/electrolyte interface. A second advantage is the shorter diffusion path lengths

for the photogenerated charge carriers. This is illustrated by the nanowire array photoelectrode shown in Figure 1.4a, where the minority carriers only have to travel half the diameter of the nanowire in order to reach the semiconductor/electrolyte interface [39]. If transport of majority carriers is also an issue, one could employ an array of a conducting wires, which are coated with a thin film of the photoactive semiconductor (Figure 1.4b). Here, both minority and majority carriers benefit from the short distance ( $\leq d$ ) that they have to travel before reaching the electrolyte and conducting core, respectively. This is sometimes referred to as a “guest–host” structure, in which the light absorbing nanosized guest material is attached to a nanostructured host scaffold [26, 40]. The advantages are not limited to the highly regular nanowire array architecture shown in Figure 1.4; nanostructures based on dendritic or cauliflower-type morphologies or randomly packed spheres offer similar advantages [40-42].

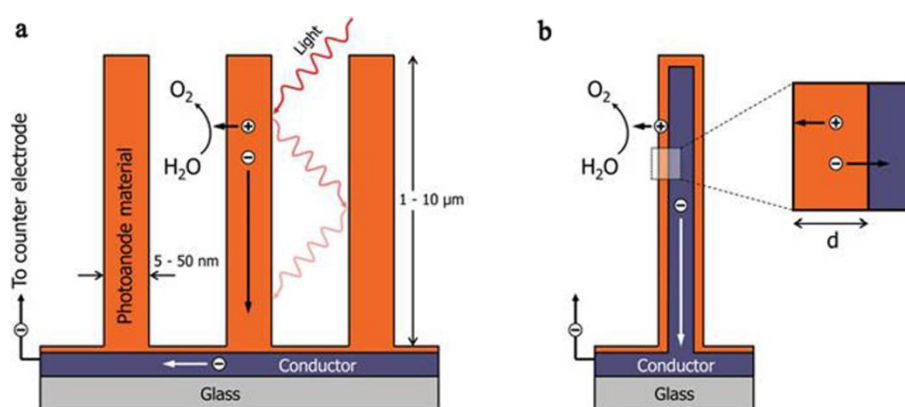


**Figure 1.4.** (a) Nanowire array photoanode, and (b) an array based on highly conducting nanowires coated with a thin photoanode film [26]

### 1.4.3. PEC devices configuration

The generally proposed architecture for water splitting devices is based on the presence of separate compartments for the water oxidation and the reduction reactions. The reaction chambers are separated by a proton exchange membrane (PEM), similar to the ones already in use for hydrogen fuel cells (FC) [43, 44] and for water-electrolyzers [45, 46]. A PEM-PEC is constituted by three principal components as shown in Figure 1.5 [47]: the membrane electrode assembly (MEA) with the anode, the cathode and the polymeric electrolyte membrane (usually made in Nafion [48]); two reaction chambers (respectively anodic and cathodic) where water/electrolyte flows, and the housing system, that has to contain transparent windows for solar light illumination. In PEM-PEC, the electrodes have also to

support the light harvester material, able to capture the solar photons and to further reduce the bias potential, and for this purpose carbon cloth cannot be employed. As shown in Figure 1.5, the MEA of PEC should be transparent to the light on both the anodic and cathodic side, so that also the cathodic electrode can absorb and take advantage of the part of the solar spectrum not exploited by the anodic material. The PEM-PEC electrode support has to be electrically conductive (at least on the photocatalyst side), transparent to the visible light, porous, mechanically robust and permit an easy attachment of catalysts and/or bio-molecules, q-dots, or other photo-active nanoparticles. To this purpose, the design of new transparent, conductive and porous electrodes to be employed in PEC as support for photo-active materials is an open challenge.

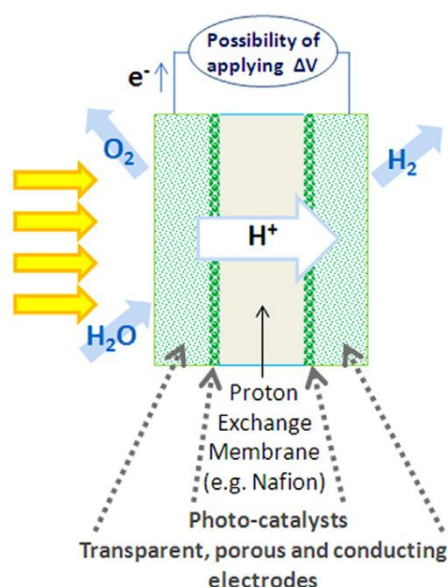


**Figure 1.5.** MEA assemblies for a PEM photoelectrochemical cell configuration

When the conduction and valence bands do not straddle the water reduction and oxidation potentials, or if the available overpotentials for water splitting are insufficient, a combination of two or more semiconductors may offer a solution. In such a device, one semiconductor acts as a regular photoanode or photocathode. The other semiconductor(s) function(s) as either a complementary photoelectrode, or as an integrated photovoltaic device that provides a bias voltage. Figure 1.6 shows some examples of possible configurations.

Configuration Figure 1.6a is the one we have used throughout this chapter to illustrate the main principles of photoelectrochemical water splitting.  $\text{SrTiO}_3$ , is one of very few materials that have been observed to split water in this configuration [49]. However, the efficiency is less than 1% due to its large bandgap (3.2 eV). Cuprous oxide,  $\text{Cu}_2\text{O}$ , and p-type SiC are

candidates for configuration Figure 1.6b. While  $\text{Cu}_2\text{O}$  has been found to suffer from photoreduction to metallic Cu [50, 51], other reports indicate that it may be stable under the right conditions [52, 53]. The 4H polytype of silicon carbide is one of the few chemically stable photocathode materials able to split water, but its efficiency is also low ( $E_g = 3.26 \text{ eV}$ ) [54].

In configurations Figure 1.6c and Figure 1.6d, a bias voltage is applied to the photoanode and photocathode, respectively, through an integrated p–n junction. Turner et al. [4] have demonstrated such a monolithic tandem device based on a photocathode of p-type  $\text{GaInP}_2$  in combination with a GaAs p–n junction. They achieved an impressive solar-to-hydrogen efficiency of 12.4%, but the rapid degradation and high cost of the device limit its practical use. Gratzel and Augustynski used a dye-sensitized solar cell (DSSC) to bias a  $\text{WO}_3$  or  $\text{Fe}_2\text{O}_3$  photoanodes [14, 55]. The photoanode absorbs the blue part of the solar spectrum ( $E_g = 2.6 \text{ eV}$  for  $\text{WO}_3$ ), whereas the DSSC absorbs red light. This approach is somewhat similar to configuration Figure 1.6c, except for the fact that the p–n junction is replaced by a separate DSSC device. The advantage is that the entire system can be made from low-cost and stable metal oxides. A remaining challenge is to address the significant light scattering of the individual (nanostructured) components, which severely limits the efficiency of the total system [56].

In configurations Figure 1.6e and Figure 1.6f an additional bias potential is generated by a single additional absorber instead of a p–n junction. An example of configuration Figure 1.6e is a device based on n-type  $\text{TiO}_2$  ( $E_g = 3.2 \text{ eV}$ ) and p-type GaP ( $E_g = 2.25 \text{ eV}$ ) [57]. The difference in band gaps ensures that a large part of the solar spectrum is used. This is not the case for p–n homojunctions, and devices such as n- $\text{Fe}_2\text{O}_3$ /p- $\text{Fe}_2\text{O}_3$  [58] will not be very efficient because of this. The n–n heterojunction of configuration Figure 1.6f was first studied many years ago, and was not considered to be very useful since the photogenerated holes in the buried n-type semiconductor could not reach the photoanode/electrolyte interface [59]. More recently, however, Yang et al. [60] showed that n-type Si underneath n-type  $\text{TiO}_2$  “boosts” the energy of  $\text{TiO}_2$  conduction band electrons. This increases the available overpotential for the reduction of water and improves the kinetics [26].

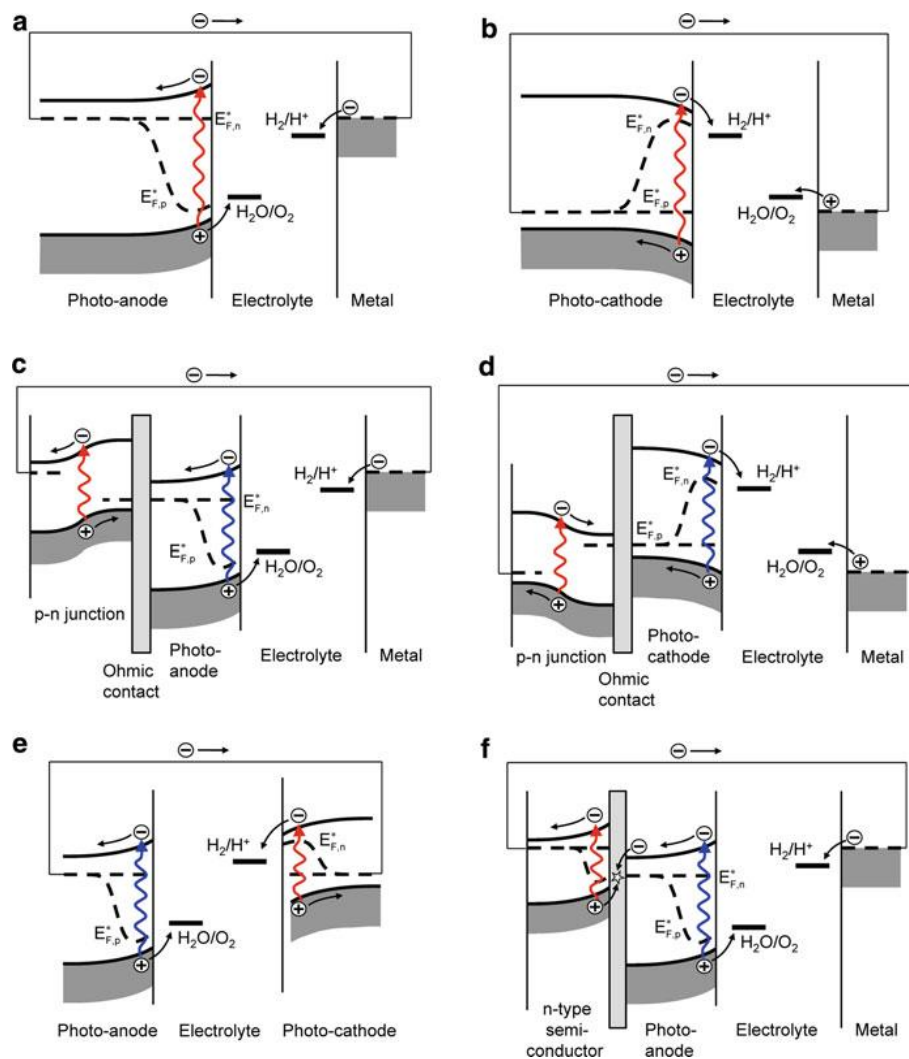


**Figure 1.6.** Examples of possible PEC configurations under illumination [26]. Standard single semiconductor devices based on a photoanode (a) or photocathode (b) with a metal counter electrode. Monolithic devices based on a photoanode (c) or photocathode (d) biased with an integrated p–n junction. p–n junction photoelectrochemical device (e), and an n–n heterojunction PEC device based on a photoanode deposited on top of a second n-type semiconductor that “boosts” the energy of the electrons (f)

### 1.5. References

- [1] M. Ni, M.K. Leung, D.Y. Leung, K. Sumathy, *Renewable and Sustainable Energy Reviews*, 11 (2007) 401-425.
- [2] A. Fujishima, K. Honda, *Nature*, 238 (1972) 37-38.
- [3] Y. Sakai, S. Sugahara, M. Matsumura, Y. Nakato, H. Tsubomura, *Canadian journal of chemistry*, 66 (1988) 1853-1856.

- [4] O. Khaselev, J.A. Turner, *Science*, 280 (1998) 425-427.
- [5] S. Licht, B. Wang, S. Mukerji, T. Soga, M. Umeno, H. Tributsch, *The Journal of Physical Chemistry B*, 104 (2000) 8920-8924.
- [6] R. Asahi, T. Morikawa, T. Ohwaki, K. Aoki, Y. Taga, *Science*, 293 (2001) 269-271.
- [7] Z. Zou, J. Ye, K. Sayama, H. Arakawa, *Nature*, 414 (2001) 625-627.
- [8] S.U. Khan, M. Al-Shahry, W.B. Ingler, *Science*, 297 (2002) 2243-2245.
- [9] J.-M. Herrmann, *Catalysis today*, 53 (1999) 115-129.
- [10] D. Bahnemann, *Solar energy*, 77 (2004) 445-459.
- [11] A. Kudo, H. Kato, I. Tsuji, *Chemistry Letters*, 33 (2004) 1534-1539.
- [12] K. Maeda, *Journal of Photochemistry and Photobiology C: Photochemistry Reviews*, 12 (2011) 237-268.
- [13] D.S. Bhatkhande, S.B. Sawant, J.C. Schouten, V.G. Pangarkar, *Journal of Chemical Technology and Biotechnology*, 79 (2004) 354-360.
- [14] M. Grätzel, *Nature*, 414 (2001) 338-344.
- [15] H. Kato, A. Kudo, *The Journal of Physical Chemistry B*, 106 (2002) 5029-5034.
- [16] J.-M. Herrmann, J. Disdier, P. Pichat, *Chemical physics letters*, 108 (1984) 618-622.
- [17] R. Niishiro, R. Konta, H. Kato, W.-J. Chun, K. Asakura, A. Kudo, *The Journal of Physical Chemistry C*, 111 (2007) 17420-17426.
- [18] J. Yoshimura, Y. Ebina, J. Kondo, K. Domen, A. Tanaka, *The Journal of Physical Chemistry*, 97 (1993) 1970-1973.
- [19] A.R. Lim, S.H. Choh, M.S. Jang, *Journal of Physics: Condensed Matter*, 7 (1995) 7309.
- [20] K. Sayama, A. Nomura, Z. Zou, R. Abe, Y. Abe, H. Arakawa, *Chem. Commun.*, (2003) 2908-2909.
- [21] Y.H. Ng, A. Iwase, A. Kudo, R. Amal, *The Journal of Physical Chemistry Letters*, 1 (2010) 2607-2612.
- [22] Y. Hosogi, H. Kato, A. Kudo, *Journal of Materials Chemistry*, 18 (2008) 647-653.
- [23] Y. Hosogi, H. Kato, A. Kudo, *The Journal of Physical Chemistry C*, 112 (2008) 17678-17682.
- [24] H.G. Kim, D.W. Hwang, J.S. Lee, *Journal of the American Chemical Society*, 126 (2004) 8912-8913.
- [25] M. Radoičić, Z. Šaponjić, I. Janković, G. Ćirić-Marjanović, S. Ahrenkiel, M. Čomor, *Applied Catalysis B: Environmental*, 136 (2013) 133-139.
- [26] R. van de Krol, M. Grätzel, *Photoelectrochemical hydrogen production*, Springer, 2011.

- [27] R. van de Krol, Y. Liang, J. Schoonman, *Journal of Materials Chemistry*, 18 (2008) 2311-2320.
- [28] M.F. Weber, M. Dignam, *International Journal of Hydrogen Energy*, 11 (1986) 225-232.
- [29] A. Murphy, P. Barnes, L. Randeniya, I. Plumb, I. Grey, M. Horne, J. Glasscock, *International Journal of Hydrogen Energy*, 31 (2006) 1999-2017.
- [30] J.R. Bolton, S.J. Strickler, J.S. Connolly, *Nature*, 316 (1985) 495-500.
- [31] H. Gerischer, *Journal of The Electrochemical Society*, 113 (1966) 1174-1182.
- [32] M.F. Weber, M.J. Dignam, *Journal of The Electrochemical Society*, 131 (1984) 1258-1265.
- [33] Y. Liang, C.S. Enache, R. van de Krol, *International Journal of Photoenergy*, 2008 (2008).
- [34] W.J. Youngblood, S.-H.A. Lee, Y. Kobayashi, E.A. Hernandez-Pagan, P.G. Hoertz, T.A. Moore, A.L. Moore, D. Gust, T.E. Mallouk, *Journal of the American Chemical Society*, 131 (2009) 926-927.
- [35] M.W. Kanan, D.G. Nocera, *Science*, 321 (2008) 1072-1075.
- [36] K. Maeda, K. Teramura, D. Lu, T. Takata, N. Saito, Y. Inoue, K. Domen, *Nature*, 440 (2006) 295-295.
- [37] A. Kudo, Y. Miseki, *Chemical Society Reviews*, 38 (2009) 253-278.
- [38] H. Kato, K. Asakura, A. Kudo, *Journal of the American Chemical Society*, 125 (2003) 3082-3089.
- [39] G.K. Mor, H.E. Prakasam, O.K. Varghese, K. Shankar, C.A. Grimes, *Nano letters*, 7 (2007) 2356-2364.
- [40] K. Sivula, F.L. Formal, M. Grätzel, *Chemistry of Materials*, 21 (2009) 2862-2867.
- [41] C. Santato, M. Ulmann, J. Augustynski, *Advanced Materials*, 13 (2001) 511-514.
- [42] I. Cesar, A. Kay, J.A. Gonzalez Martinez, M. Grätzel, *Journal of the American Chemical Society*, 128 (2006) 4582-4583.
- [43] J. Bockris, S. Srinivasan, (1969).
- [44] T. Thampan, S. Malhotra, J. Zhang, R. Datta, *Catalysis today*, 67 (2001) 15-32.
- [45] F. Barbir, *Solar energy*, 78 (2005) 661-669.
- [46] S.A. Grigoriev, V.I. Poremsky, V.N. Fateev, *International Journal of Hydrogen Energy*, 31 (2006) 171-175.
- [47] S. Hernández, M. Tortello, A. Sacco, M. Quaglio, T. Meyer, S. Bianco, G. Saracco, C.F. Pirri, E. Tresso, *Electrochimica Acta*, 131 (2014) 184-194.

- [48] S.J. Peighambaroust, S. Rowshanzamir, M. Amjadi, *International Journal of Hydrogen Energy*, 35 (2010) 9349-9384.
- [49] J. Mavroides, J. Kafalas, D. Kolesar, *Applied Physics Letters*, 28 (1976) 241-243.
- [50] H. Schoppel, *GERISCHE. H, Ber. Bunsenges. Phys. Chem.*, 75 (1971) 1237.
- [51] G. Nagasubramanian, A.S. Gioda, A.J. Bard, *Journal of The Electrochemical Society*, 128 (1981) 2158-2164.
- [52] P. De Jongh, D. Vanmaekelbergh, J.J.d. Kelly, *Journal of The Electrochemical Society*, 147 (2000) 486-489.
- [53] M. Hara, T. Kondo, M. Komada, S. Ikeda, K. Shinohara, A. Tanaka, J. Kondo, K. Domen, *JCS, Chem. Commun.*, 3 (1998) 357-358.
- [54] D.H. van Dorp, N. Hijnen, M. Di Vece, J.J. Kelly, *Angewandte Chemie International Edition*, 48 (2009) 6085-6088.
- [55] M. Grätzel, *Chemistry Letters*, 34 (2005) 8-13.
- [56] J. Brillet, M. Cornuz, F.L. Formai, J.-H. Yum, M. Grätzel, K. Sivula, *Journal of Materials Research*, 25 (2010) 17-24.
- [57] A. Nozik, *Applied Physics Letters*, 29 (1976) 150-153.
- [58] J. Turner, M. Hendewerk, G. Somorjai, *Chemical physics letters*, 105 (1984) 581-585.
- [59] P.A. Kohl, S.N. Frank, A.J. Bard, *Journal of The Electrochemical Society*, 124 (1977) 225-229.
- [60] Y.J. Hwang, A. Boukai, P. Yang, *Nano letters*, 9 (2008) 410-415.

## Chapter 2

### Thick mesoporous TiO<sub>2</sub> films through a sol-gel method involving a non-ionic surfactant: characterization and enhanced performance for water photo-electrolysis

#### 2.1. Introduction

Crystalline TiO<sub>2</sub> phases are attractive materials for devices like photocatalysts [1], photoelectrodes [2], gas sensors [3] and electrochromics [4]. When in film form, the activity strongly depends on the crystal structure, thickness and porosity. Anatase nanocrystallites are the most active [5]: for many applications, a highly porous structure with large surface area featuring a large number of catalytic sites is desired [6]. To prepare mesoporous films, sol-gel method [7], supercritical method [8], direct deposition from aqueous solutions [9], hydrothermal crystallization [10], ultrasonic spray pyrolysis [11] and sputtering technique [12] have been used. Most mesoporous TiO<sub>2</sub> materials prepared by sol-gel process are in the form of powders or thin films. As highly reactive solutions of titanium alkoxide precursors are used in aqueous media to form the Ti–O–Ti network [13], this route can lead to the precipitation of amorphous particles with uncontrolled structure. The control of TiO<sub>2</sub> formation rate, its crystal size and morphology is attempted [14] basically through the use of structured templates, i.e. surfactant micelles, polymer nanospheres, etc. [15-17]. The presence of surfactant molecules hampers hydrolysis and condensation reaction by capping the titania precursor [18, 19], which may induce porosity in the titania inorganic network [1, 6, 13, 20]. Another route to homogeneous titania nanoparticles operates in the absence of added water molecules, which are only formed in the esterification reaction of Acetic acid (AcOH) in alcohol solvent (i.e. Isopropanol (iPrOH)) [18]. By coupling such synthesis route with the use of nonionic surfactants (Tween 20, Tween 80 and Triton X-100) [6, 13], TiO<sub>2</sub> thin films with good homogeneity and reproducibility have been prepared by a multiple layers dip-coating technique, obtaining thicknesses of about 100 nm per layer. Also, recent results show that carrying out the sol-gel synthesis with a high water content in the presence of AcOH as catalyst favors the nucleophilic attack of water on TTIP and suppresses its fast condensation, yielding nanocrystalline TiO<sub>2</sub> materials with notably higher activity than the standard Degussa P-25 TiO<sub>2</sub> [21-23]. However, little work has been devoted to investigate the use of surfactants in the AcOH assisted sol-gel method in aqueous media, for the formation of mesoporous TiO<sub>2</sub> films and the analysis of their structural and photocatalytic properties.

Moreover, the use of surfactant has not been studied to obtain TiO<sub>2</sub> transparent thick films (thickness > 1 μm) with mesoporous structure and large surface area, obtained after few coatings, that might increase the number of active sites and promote the activity of TiO<sub>2</sub> films.

In this Chapter is reported a novel sol-gel spin coating method for preparing transparent TiO<sub>2</sub> thick films made of nanocrystalline particles with mesoporous structure, developed through the modification of a sol gel synthesis procedure starting from TTIP, glacial AcOH and excess water with the incorporation of the nonionic surfactant Tween 20. The latter has been used as pore-directing agent because it is environmentally friendly and highly viscous, which is beneficial to increase the film thickness (per coating layer) and to obtain TiO<sub>2</sub> films without cracks. A thermal treatment in a rotary evaporator has been optimized to raise the concentration of TiO<sub>2</sub> nanoparticles in the final sol, so yielding an increase in the thickness of the film per coated layer. Such procedure allows the preparation of mesoporous and homogeneous thick films in few deposition steps. The effect of the surfactant and titania concentration on the optical structural and morphological properties of TiO<sub>2</sub> films has been studied. Finally, the photo-catalytic activity and carrier dynamics of these mesoporous TiO<sub>2</sub> films have been evaluated in the water photo-electrolysis reaction (WPER). The results of this research are part of the publication entitled: “Thick mesoporous TiO<sub>2</sub> films through a sol-gel method involving a non-ionic surfactant: characterization and enhanced performance for water photo-electrolysis”. D. Hidalgo, R. Messina, A. Sacco, D. Manfredi, S. Vankova, E. Garrone, G. Saracco, S. Hernández. (2014) International Journal of Hydrogen Energy.

## **2.2. Experimental**

### **2.2.1. Materials and sol-gel synthesis of TiO<sub>2</sub> nanoparticles**

TTIP (97%), glacial AcOH (99.7%), Tween 20, all from Sigma Aldrich, were used as purchased. TTIP, glacial AcOH and water were at fixed molar ratios 1:10:300 [21], whereas the molar ratio (R) between Tween 20/TTIP was varied between range from 0.25 to 1. Firstly, TTIP was hydrolyzed in glacial AcOH, then Tween 20 was added under vigorous stirring. The mixture was added drop wise to the De-Ionized water and the final solution was aged under continuous stirring for 48 h at ambient temperature. The sol obtained was treated in a rotary evaporator at 40 °C for 2 h under vacuum conditions. The final TiO<sub>2</sub> sol, homogeneous and stable for weeks, was then used for the preparation of TiO<sub>2</sub> nanoparticles in both forms of powder and film. All TiO<sub>2</sub> powders have been obtained by drying the TiO<sub>2</sub> sol at 100 °C for

24 h, with subsequent calcination at 500 °C for 1 h in air (using a heating rate of 1 °C/min) and a final natural cooling to room temperature.

### **2.2.2. Deposition of TiO<sub>2</sub> films**

TiO<sub>2</sub> films were supported onto fluorine-doped tin oxide glass substrates (FTO, 7Ω/cm<sup>2</sup>) over an area of 2 x 2 cm<sup>2</sup>. First, the support was cleaned in acetone using an ultrasonic bath and then rinsed with ethanol. A “piranha” solution 3:1 (Sulfuric Acid: Hydrogen Peroxide) was then employed to remove organic residues on the surface. The concentrated TiO<sub>2</sub> solution, obtained after the rotary evaporator treatment, was spin-coated with a spinner model Spin 150 by using a two steps program: 500 rpm for 10 s followed by 3000 rpm for 10 s. The films were dried at 50 °C for 15 min and then maintained 45 min at room temperature before spin-coating the successive layer. A maximum of 3 layers per each molar ratio were deposited. Finally, the films were annealed at 500 °C for 15 min in air, using a heating rate of 1 °C/min, and let cool down.

### **2.2.3. Characterizations**

Thermal analysis of the final TiO<sub>2</sub> sols for all R values was carried out from room temperature to 800 °C at a heating rate of 1 °C/min in air, using a thermogravimetric analyzer (TGA) model Pyris Diamond with “*Extar V6.2*” software by Perkin Elmer. TiO<sub>2</sub> powders and films have been characterized through different techniques. X-ray diffraction (XRD) analysis were performed by using a X-ray diffractometer Cu-Kα x-ray tube ( $\lambda = 1.54 \text{ \AA}$ ) with an accelerating voltage of 40 KV. A porosimetry analyzer (Tristar II 3020) was used to investigate the structural characteristics of TiO<sub>2</sub> materials including Brunauer Emmett Teller (BET) surface area, porosity and pore size distribution. UV-Vis spectra were measured in the diffuse reflectance mode using a spectrophotometer model Cary 500 by Varian, and the optical band gap was estimated using the Tauc’s method [22]. Particles size, morphology and thickness of TiO<sub>2</sub> films were analyzed using a ZEISS Supra 40 Field Emission Scanning Electron Microscope (FESEM). A profilometer model KLA-Tencor P-10 Surface Profiler has also been used to measure the film thicknesses.

### **2.2.4. Photoelectrochemical tests**

Photo-activity and carrier dynamics of films were studied using the spin-coated electrodes for the WPER in 0.1M NaOH electrolyte (pH = 12.7). The titania films were used as anodes

(working electrodes), a Pt wire was employed as cathode (counter electrode), and Ag/AgCl (NaCl 3 M) was used as reference electrode in a typical three electrodes configuration, using a Potentiostat model CHI760 by CH Instruments for the photo-electrochemical (PEC) tests. Current-voltage ( $I$ - $V$ ) curves were recorded through Linear Sweep Voltammetry (LSV) performed in the range -0.7 V to 0.6 V vs. Ag/AgCl at a scan rate of 10 mV/s. The behavior of the photocatalyst under AC response was investigated with Electrochemical Impedance Spectroscopy (EIS) in the frequency range of 100 mHz to 1MHz, with an amplitude of 25 mV, under different applied DC potentials in the range -0.5 V to 0.5 V with 0.2 V steps. LSV and EIS tests were performed in the dark and under illumination (using a 450W Xe lamp by Newport). EIS data was modeled using the ZSimpWin (EChemSoftware) software. Current-time ( $I$ - $t$ ) curves have been obtained by Chronoamperometry measurements at -0.1 V vs. Ag/AgCl under continuous dark-light cycles during 40 min. The distance between the film and the light source has been regulated to have an intensity of the incident light of 68 W/m<sup>2</sup> in the UV region (280 - 400 nm) and of 1000 W/m<sup>2</sup> in the Vis-NIR range (400 - 1050 nm). The irradiance has been measured with a Delta Ohm Photo-radiometer model HD2102.1, using three different probes: one model LP471UVA and LP471UVB for the UV range (280-315 nm and 315 – 400 nm, respectively) and another model LP471RAD for the Vis-NIR range.

## **2.3. Results and discussion**

### **2.3.1. Thermal properties of TiO<sub>2</sub> solution**

Before use, the surfactant used as template has to be removed [24], a procedure which has been followed by TGA. Figure 2.1 shows the thermogravimetric curve for the TiO<sub>2</sub> sol with R = 0.50.

A first fast weight loss observed below 100 °C corresponds to the water removal. The second mass decrease between 100 and 300 °C is due to the decomposition of organic compounds [25], while the third region with a lower slope ranging from 300 to 450 °C is most probably due to the oxidation of carbonaceous residues [26]. No further weight loss was observed up to 500 °C. Therefore, all powders and films were calcined at 500 °C. Since the amount of TiO<sub>2</sub> sol used to form the films is considerably lower respect to what needed to obtain the powders, the temperature was maintained for 15 min in the former case and for 1 h in the latter.

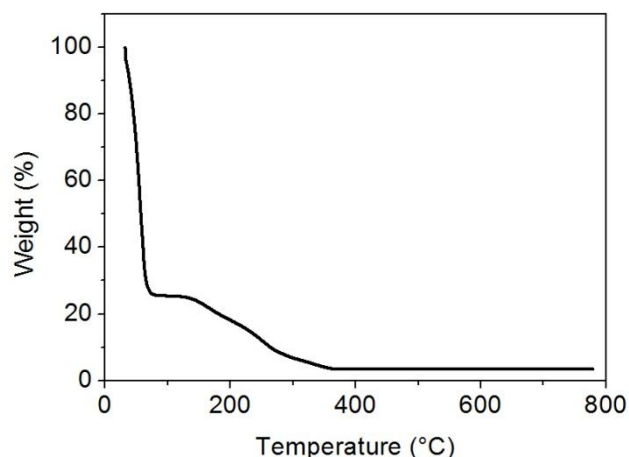


**Figure 2.1.** TGA curve of TiO<sub>2</sub> sol prepared using a Tween 20/TTIP molar ratio (R) of 0.50

### 2.3.2. Characterization of TiO<sub>2</sub> nanoparticles in powder form

Direct characterization of TiO<sub>2</sub> films is difficult due to the tiny amount of TiO<sub>2</sub> material involved. Characterization so concerned the TiO<sub>2</sub> powder after a similar thermal treatment used for the TiO<sub>2</sub> films [6, 27, 28]. Morphologic, crystallographic and optical results, reported below, concern TiO<sub>2</sub> nanoparticles with different R values, including the template free sample. XRD patterns in Figure 2.2 show the diffraction peaks at  $2\theta = 25.4^\circ, 37.9^\circ, 48.2^\circ, 54.0^\circ, 55.2^\circ$ , corresponding to the (101), (004), (200), (105), and (211) planes of the anatase phase, respectively.

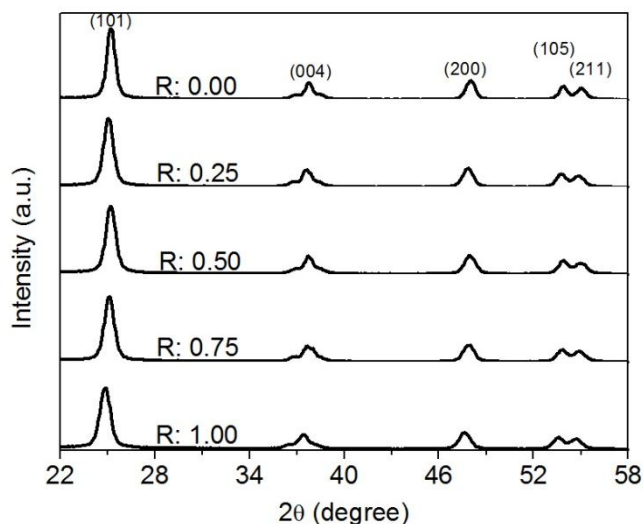


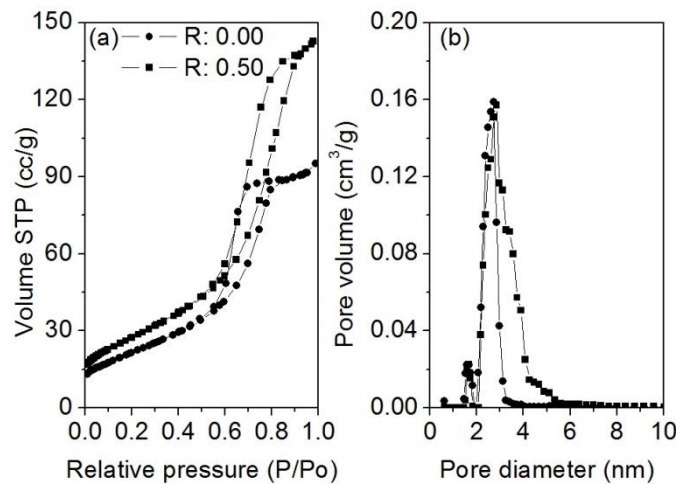
**Figure 2.2.** XRD spectra of TiO<sub>2</sub> powder made with different Tween 20/TTIP molar ratios, calcined at 500 °C for 1 h

The average particle size was calculated by applying the Scherrer equation on the anatase (101) diffraction peak (the highest intensity peak for pure anatase):

$$D = \frac{k\lambda}{\beta \cos\theta} \quad (2.1)$$

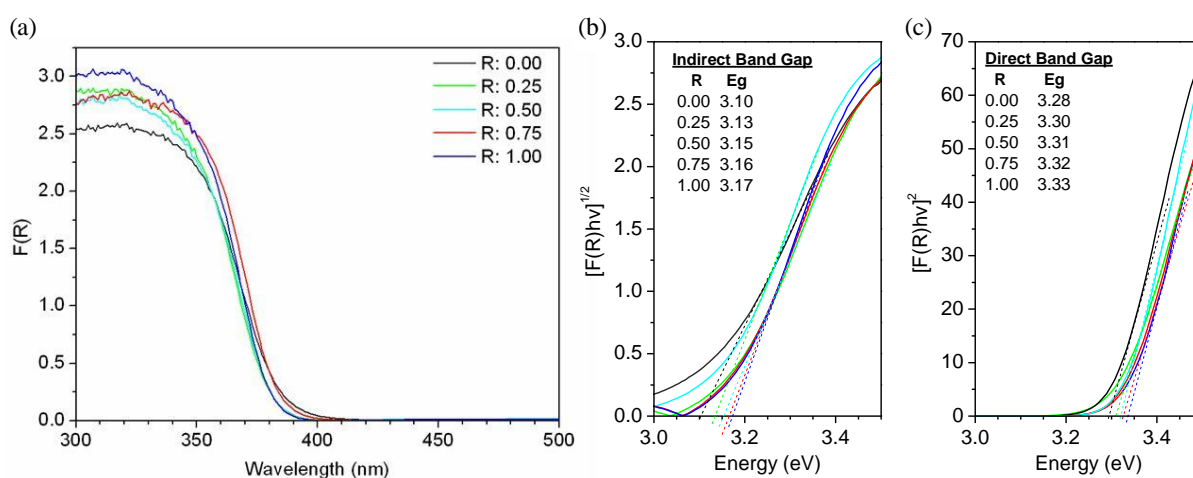
where  $D$  is the crystal size of the  $\text{TiO}_2$ ,  $k$  a constant (0.89),  $\lambda$  the X-ray wavelength (1.54 Å),  $\beta$  the full width at half maximum (FWHM) of the  $\text{TiO}_2$  peak and  $\theta$  is the diffraction angle. Results are summarized in Table 2.1. The average crystal size of  $\text{TiO}_2$  powder without Tween 20 was approximately 25 nm. Addition of surfactant decreases the crystal size for all the samples to 17-20 nm, in agreement with the literature [6, 18, 20], indicating that surfactants as Tween 20 inhibit crystallite growth in a sol gel system.

Figure 2.3 shows the nitrogen adsorption-desorption isotherms and the pore size distribution obtained for the powders with  $R = 0$  and  $R = 0.5$ , the latter representing the behavior of all the powders with a non-zero  $R$  values. Related data are summarized in Table 2.1. Isotherms in Figure 2.3a are typical type IV curves, characteristic of well-developed mesoporous materials [29].  $\text{TiO}_2$  powders exhibited a narrow mono-modal pore size distribution, ranging from 2 to 5 nm, which implies good homogeneity of the pores (as also seen in Figure 2.3b). The presence of Tween 20 did not change the hysteresis loop and the type of pore size distribution of the  $\text{TiO}_2$  particles. In contrast, surfactant incorporation forms new pores from 3 to 5 nm (Table 2.1 and Figure 2.3b), that increase the pore volume of about 1.5 to 1.6 times with respect to the un-modified titania; as a consequence the BET surface area increased of the same order of magnitude. Addition of Tween 20 leads to a remarkable enhancement of the BET surface area and the porosity of  $\text{TiO}_2$  particles, in agreement with the literature [6, 18, 30].



**Figure 2.3.** (a) Nitrogen adsorption at 77 K concerning  $\text{TiO}_2$  powders synthesized with and without surfactant, and (b) corresponding pore size distribution

The diffuse reflectance spectra (DRS) of TiO<sub>2</sub> powders with different R are shown in Figure 2.4. Increase in R values results in a moderate increase of the intensity (ca. 15%). A decrease in particle size was noted for increasing R values (Table 2.1): this suggests that the increase of the Kubelka-Munk function F(R) probably does not correspond to a true increase in absorption (indeed difficult to account for) but to a less marked scattering by the smaller nanoparticles. Indeed, the Kubelka-Munk model predicts that the F(R) function is equal to the ratio  $k/\sigma$ , where  $k$  is the absorption coefficient and  $\sigma$  is the scattering coefficient. Similar results for titania mesoporous structures have been reported [14, 31].



**Figure 2.4.** (a) Diffuse reflectance spectra of TiO<sub>2</sub> powders at different Tween 20/TTIP molar ratios, (b) Tauc plots and band gaps calculated from UV-Vis Diffuse reflectance measurements on TiO<sub>2</sub> powders made with different Tween 20 loadings, using  $n = 1/2$  for indirect transition and (c)  $n = 2$  for direct transition.

The DRS spectra of all powders in Figure 2.4a were analyzed using Tauc's method [22], which allows to determine simultaneously both the nature of the band-to-band transition (either direct or indirect) and the actual values of the optical band gap ( $E_g$ ). Application of Tauc's method [22] consisted in plotting the data from the DRS spectra in Fig. 2.4a as  $[F(R)hv]^n$  against  $hv$ , where F(R) is the Kubelka-Munk function and  $hv$  the photon energy (eV), equal to  $1239/\lambda$  (nm). A linear region just above the optical absorption edge is expected, with  $n = 2$  for direct transition, or  $n = 1/2$  for indirect transition [22]. Both types of plots have been evaluated (Figs. 2.4b and 2.4c). Linearity is much more satisfactory with  $n = 2$  than with  $n = 1/2$ . Extrapolation of the linear portions yielded the  $E_g$  values reported in Table 2.1. Only the case  $n = 2$  yielded values close to the universally accepted  $E_g$  value for anatase, 3.23 eV [22]. Both findings point to the fact that direct

indirect band-to-band transitions take place. All samples proved to behave as direct semiconductors, in contrast with bulk anatase, as observed in few studies, both experimental and theoretical [32, 33]. For direct bandgap semiconductors, electronic transition from the valence band to the conduction band is electrical dipole allowed and the electronic absorption, as well as emission, is usually strong. Hence, a direct bandgap transition may result in a more efficient absorption of solar energy with consequent better performances of materials for the solar devices [22]. The  $E_g$  values resulted to be close to the expected value of 3.23 eV, and to be little dependent on the R value [34].

**Table 2.1.** Effect of Tween 20 loading on crystal size, thickness, BET surface area, pore volume and porosity of TiO<sub>2</sub> nanoparticles

<b>R</b>	<b>Crystal size (nm)</b>	<b>BET (m<sup>2</sup>/g)</b>	<b>Pore volume (cm<sup>3</sup>/g)</b>	<b>Direct Band Gap (eV)</b>
0.00	25	78.2	0.135	3.28
0.25	19.8	94.2	0.202	3.30
0.50	18.5	94.8	0.208	3.31
0.75	17.7	104.5	0.209	3.32
1.00	16.8	117.4	0.216	3.33

### 2.3.3. Characterization of TiO<sub>2</sub> films

Figure 2.5 reports a small portion of the X-ray diffraction spectra of TiO<sub>2</sub> films with 1, 2 and 3 spin-coated layers, respectively, using the titania sol with R = 0.50, featuring the peak at 25.4°, the (101) reflection. The increase in intensity suggests a larger amount of matter supported on the FTO-glass with different number of layers [20]. Generally, several layers of TiO<sub>2</sub> are required to observe the XRD pattern [28]: the fact that in the present case one layer suffices is evidence of the efficiency of the preparation method.

FESEM pictures are reported in Figure 2.6. The film with R = 0 (Figure 2.6a) was not homogeneous and featured many cracks. When Tween 20 was used, films were transparent, reproducible, homogeneous and crack-free, with a highly interconnected network of titania nanoparticles organized in a mesoporous structure (Figures 2.6b to 2.6f). Moreover (Figures 2.6c and 2.6d), the films surface shows, in addition to mesopores, particular star-like

macropores, the deeper the larger R value, probably generated by the outburst of gaseous products of decomposition or combustion (inset of Figure 2.6d). The crystallites in all films exhibited a nearly round shape and have not been significantly altered by incorporating the surfactant into the sol. The average crystal size in FESEM images of the film with R = 0 is ca. 30 nm, whereas in the presence of surfactant it is lower than 20 nm, which is in agreement with the XRD results. EDX analysis (not reported) shows the presence of mainly Ti and O without any significant impurities, in particular those related to carbonaceous residues, removed during the heat treatment at 500 °C.

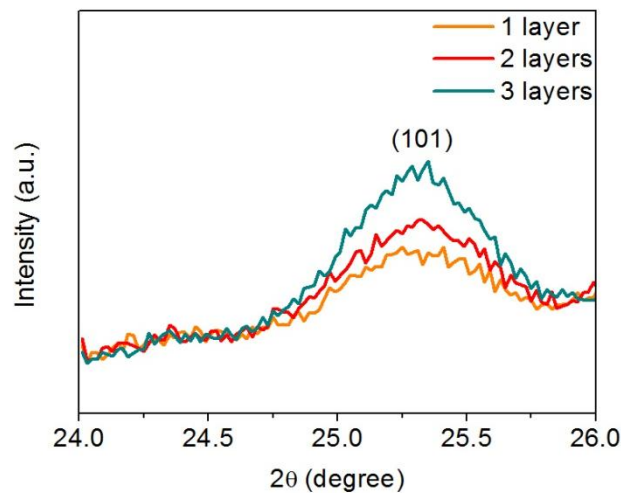


**Figure 2.5.** XRD spectra of TiO<sub>2</sub> films made with 1, 2, and 3 spin-coated layers, prepared by using the titania sol with R=0.50

Film thickness was measured by both FESEM analysis in cross section (Figures 2.6e and 2.6f) and using a profilometer. As shown in Figure 2.7, the average film thickness rises by increasing the R value. However, the increase of thickness slows down for increasing R. This could be related, on the one hand, to an increase in the viscosity of the sol by the surfactant causing a higher thickness per coated layer [6, 20], and, on the other hand, to a more slippery surface with a higher R value that reduces the friction during the spinning process, and thus the thickness among successive layers.

For R = 1 films ca. 1.2 μm thick are obtained by only one spin coating run (Figure 2.6e). It is worth of note that for common synthesis using acetic-acid assisted sol-gel method modified with same type of non-ionic surfactant, the maximum thickness for one layer was below 400 nm with R values up to 3 [6], and a larger thickness has been reached with more than 6 layers [20]. The main result of the present work is thus that a larger amount of material can be

deposited in a single run, with a larger number of active sites, still keeping the mesoporous network of TiO<sub>2</sub> nanoparticles. All these characteristics are desirable in order to enhance the TiO<sub>2</sub> film performance for photo-catalytic applications.

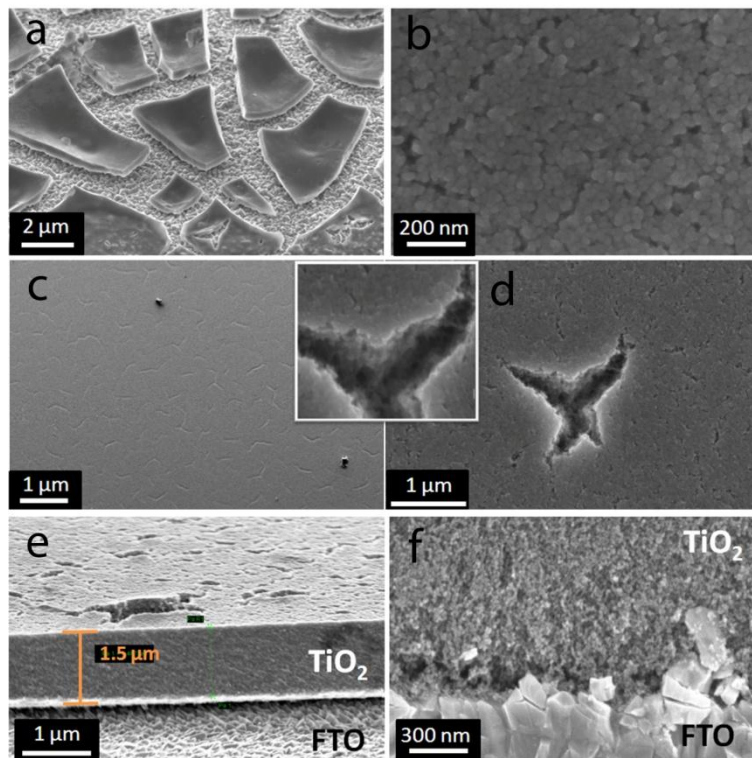


**Figure 2.6.** (a) FESEM images of the TiO<sub>2</sub> film made without addition of surfactant. (b) - (d) top views and (e) - (f) cross sections of TiO<sub>2</sub> films prepared with a Tween 20/TTIP molar ratio of R= 1

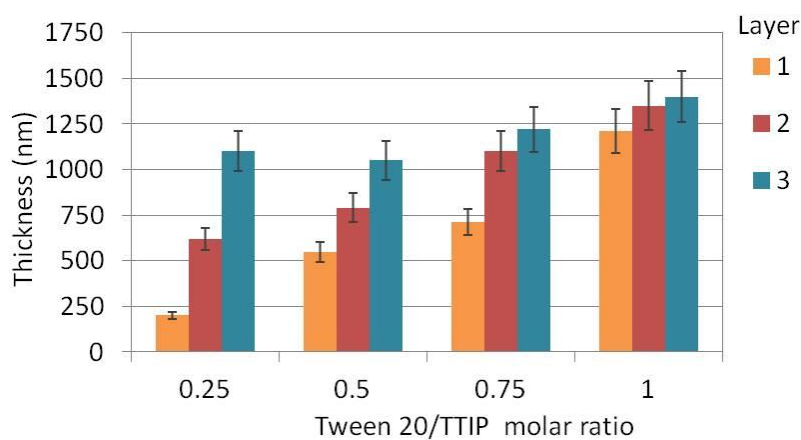


**Figure 2.7.** Thickness of TiO<sub>2</sub> films as a function of both Tween 20/TTIP molar ratio in the titania sol and number of layers

## 2.3.4. Photo-electrochemical performances

### 2.3.4.1. Photoactivity of one-layer films

Figure 2.8 shows the  $I$ - $V$  curves of the one-layer  $\text{TiO}_2$  films made with different  $R$ . As expected, in the dark the current is negligible up to a potential of ca. 1.4 V vs. RHE, where water electrolysis occurs at a value definitely higher than the theoretical one ( $E^\circ = 1.23$  V vs. RHE), because of overpotential effects of the  $\text{TiO}_2$  semiconductor. Upon UV-Vis irradiation, a sudden increase in the current is observed at potentials lower of than  $E^\circ$ , the WS reaction being photo-assisted. The common explanation is that, as expected for a n-type semiconductor [35, 36], under UV illumination electrons move from the valence band to the conduction band leaving behind holes able to perform the water oxidation step [35].

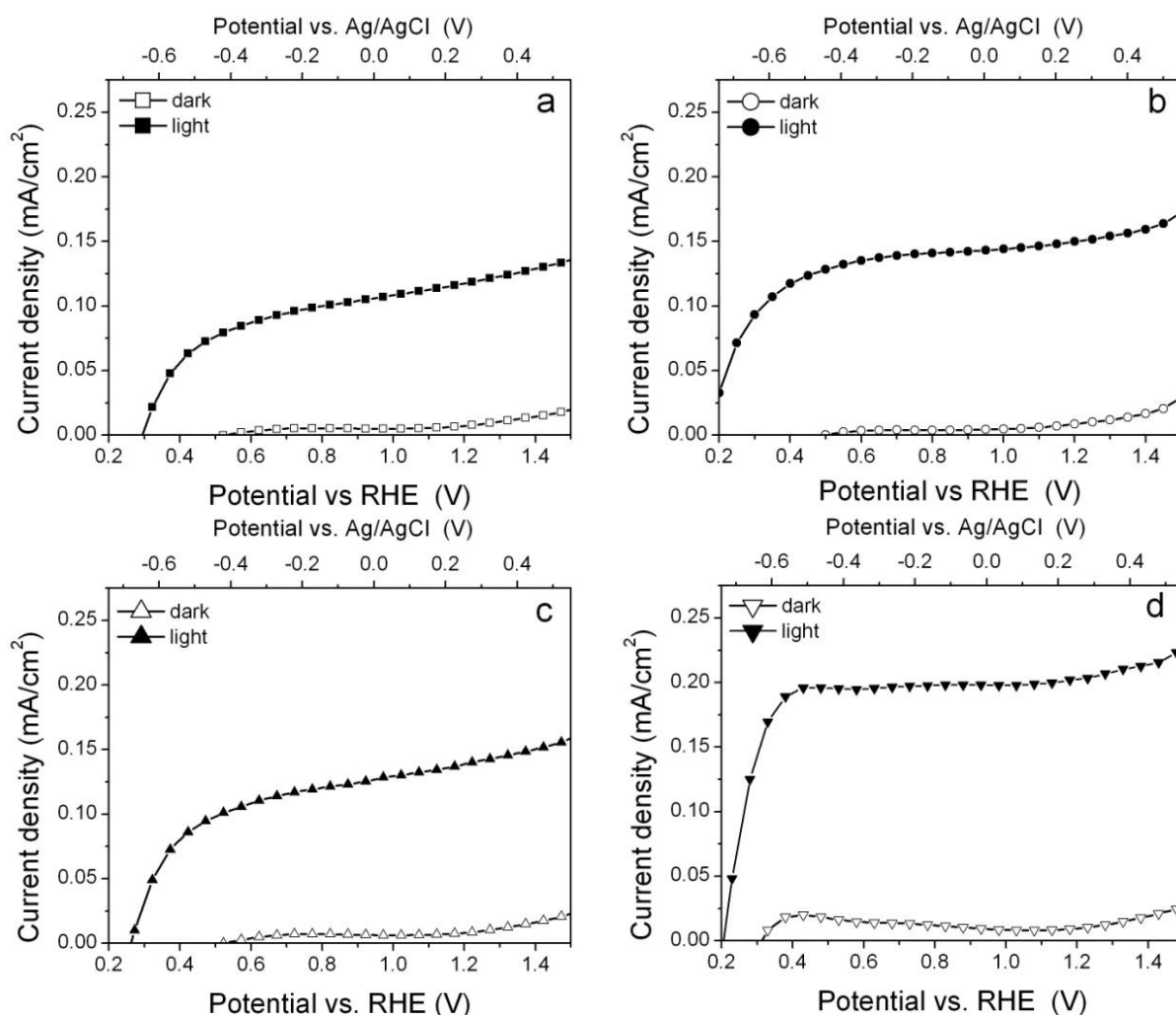


**Figure 2.8.**  $I$ - $V$  curves of one layer  $\text{TiO}_2$  films made with different Tween 20 loadings: (a)  $R=0.25$ , (b)  $R=0.50$ , (c)  $R=0.75$  and (d)  $R=1:00$ , in the dark and under UV-Vis illumination

With increasing  $R$ , the photo-catalytic activity of  $\text{TiO}_2$  films rises, though with a lower difference between the samples with  $R = 0.50$  and  $0.75$ . Such increase has to be attributed to the two factors, as previously discussed: on the one hand, a larger active surface area and pore volume (Table 2.1); on the other hand, a higher amount of anatase nanocrystalline material in the substrate, due to the higher thickness of the film (as already shown in Figure 2.7). In addition, the faradaic efficiency of the films was evaluated through  $\text{H}_2$  evolution measurements, giving for all the samples values higher than 95%.

Coming to EIS measurements, Figure 2.9a reports as an example the Nyquist plot obtained with the sample  $R = 0.50$  at different applied potentials, both in the dark and under illumination. As for all the titania films under study, the total impedance is reduced by the increasing of the applied potential in both conditions. The only differences are the smaller impedance values obtained in the light, as a result of electron-hole pair generation. Moreover, upon UV-Vis irradiation but at a fixed potential, the impedance of the films is additionally lowered when increasing the  $R$  ratio, as can be seen in the Nyquist diagram on Figure 2.9b. Such results are consistent with the enhancement in the photocurrent with the increase of the potential and the surfactant loading observed in the  $I$ - $V$  curves (Figure 2.8).

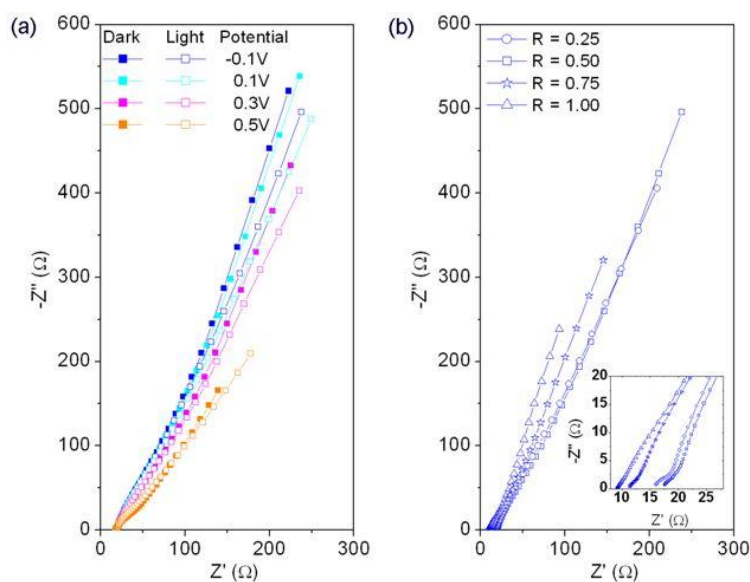


**Figure 2.9.** Nyquist plots of EIS measurements on: (a) one layer film made with  $R=0.5$ , in function of the applied potential (vs. Ag/AgCl) under dark (filled symbols) and upon UV-Vis illumination (open symbols); (b) one layer films made with different Tween 20 loadings, at -0.1 V vs. Ag/AgCl under UV-Vis illumination. The lines represent the data obtained from the fitting of experimental values using the equivalent circuit shown in Figure 2.10a

### 2.3.4.2. Modeling of EIS data

The EIS data was modeled with the equivalent circuit (EC) shown in Figure 2.10a, which has been previously used to evaluate the different charge transport phenomena occurring at n-type TiO<sub>2</sub> semiconductors and other porous materials [37-39]. In Figure 2.10a, **R** indicates a resistance and **Q** is a constant phase elements (CPE), representing a non-ideal capacitance associated with a non-uniform current distribution in the heterogeneous materials. The impedance of a CPE is defined as:

$$Z_{\text{CPE}} = \frac{1}{(j\omega)^n Q} \quad (2.2)$$

where  $n$  ( $0 < n < 1$ ) is the CPE index [37], while the capacitance associated with the CPE is given by:

$$C = Q^{\frac{1}{n}} R^{\frac{1}{n}-1} \quad (2.3)$$

In the proposed circuit, **R<sub>s</sub>** is the series resistance, which include the resistances of: the FTO film, the external electrical contacts and the liquid electrolyte. The two parallels **R//Q** regards the two distinct charged regions induced in the semiconducting electrodes during the electrochemical processes. By one side, **R<sub>H</sub>** and **C<sub>H</sub>** are the resistance and the capacitance at the Helmholtz double layer, respectively, formed at the titania/electrolyte interface and consisting of charged ions from the electrolyte adsorbed on the solid electrode surface. On the other side, **R<sub>dl</sub>** and **C<sub>dl</sub>** are the resistance and the capacitance on the depletion layer in the semiconductor, respectively. This is the space charge layer (depleted of majority charge carriers) formed in the semiconductor side, adjacent to the interface with the electrolyte, across which a potential gradient exists [38, 39].

In general, a good agreement between experimental and fitted data has been obtained, as can be seen through the perfect correlation between the markers and the straight lines in Figures 2.9a and 2.9b. Table 2.2 reports a summary of the parameters calculated through the fitting procedure; there, the process time constants were calculated through the following expression:

$$\tau = R \cdot C \quad (2.4)$$

From Table 2.2 it can be seen that the series resistance is similar in all the experiments, as expected, since it is mostly influenced by both the solution conductivity and the distance between the electrodes, which were maintained constant among all the tests. Moreover, in both dark and light conditions, as the Tween 20/TTIP ratio is increased, it is observed a

gradual increase in the oxide layer capacitance,  $C_{dl}$ , and a reduction on the transport resistance,  $R_{dl}$ . Thus, the time constant for the charge transfer inside the semiconductor ( $\tau_{dl}$ ) remains quite stable till  $R = 0.75$ . After that value, the  $C_{dl}$  increases by more than 3 times and consequently the  $\tau_{dl}$  follows the same trend, as shown in Figures 2.10b. The slower charge transport in the titania film with  $R = 1$  could be caused by: *a*) its higher thickness, that induces a longer and tortuous pathway, with a consequent higher probability of electron-hole recombination, *b*) a worse interconnection between the smaller particles due to the higher porosity in the structure. Nevertheless, the difference on  $\tau_{dl}$  values between  $R = 0.25$  and  $R = 1$  is less than one order of magnitude. Thus, the slower transport in the films with higher  $R$  has a lower influence on the photo-catalytic activity with respect to the higher quantity of  $TiO_2$  material available for the reaction. Concerning the CPE index  $n_{dl}$ , all the values reported in Table 2.2 are almost equal to unity, so they are independent on the Tween 20/TTIP ratio. This result has to be expected, since the CPE index can be regarded as an ideality factor of the capacitance, and in the case of the depletion layer inside the  $TiO_2$  a quasi-ideal behavior can be associated to the  $C_{dl}$ .

Conversely, the higher is  $R$  the lower are the capacitance and the resistance values in the Helmholtz layer ( $C_H$ ,  $R_H$ ), under both dark and illumination. Thus, the charge transfer at the interface between the electrolyte and the titania nanoparticles is twice faster, i.e.  $\tau_H$  is reduced by about a half, for every rise in  $R$  of 0.25. This result is in good agreement with the higher surface area and pore volume of the titania films prepared with a higher surfactant quantity. In fact the enhancement of the surface area permits a more intimate contact between the titania nanoparticles and the electrolytic solution, responsible for the reduction of the charge transfer resistance  $R_H$ . In this case, the CPE index values  $n_H$  show a dependency on the Tween 20/TTIP ratio, as a consequence of the increasing of the porosity for high  $R$  values, which leads to the formation of a semiconductor/electrolyte interface that cannot be considered as “flat”.

Moreover, upon illumination, even if the  $C_H$  values slightly increase due to the accumulation of the photo-generated charges at the electrolyte/semiconductor interface, a further decrease of the  $\tau_H$  values is observed in Figure 2.10b. This has to be ascribed to the considerable reduction of the  $R_H$  values, as a consequence to the faster kinetics of the water oxidation reaction in the light. Thus, the lower  $\tau_H$  values of the film with higher  $R$  ratio, leads to a comprehensive faster charge transfer in the oxide-solution interface and, therefore, to an increased reaction rate at the surface of the photocatalyst [39, 40].

In addition, the  $\tau_{dl}$  values are also lower under illumination, and this reflects the reduction of the impedance values already noticed in the Figure 2.9a, which are a consequence of both the faster electron conduction in the porous material and the reduction of carriers recombination [39]. On the other hand, it is worth of notice that the increase in the photo-current (reported in Figure 2.8) with the increase of R follows the trend of the charge transfer in the double layer (see Figure 2.10c), thus indicating that this is the limiting step in the water oxidation process. Therefore,  $\tau_H$  is one of the most important parameters that must be tuned for the improvement of water splitting photocatalyst materials.

From the analysis of the photo-electrochemical and EIS results, it is evident that the photocatalytic performance of the films is not only a function of the thickness of the electrodes, but it also depends on the good quality of the material and the nature of the structure: crystallinity, surface area, good interconnection among the particles, porosity, optical properties, etc [39]. Thus, the higher performances exhibited by the  $R = 1$  film is a combination of the higher thickness reached after only one deposited layer, together with the high quality of the obtained material.

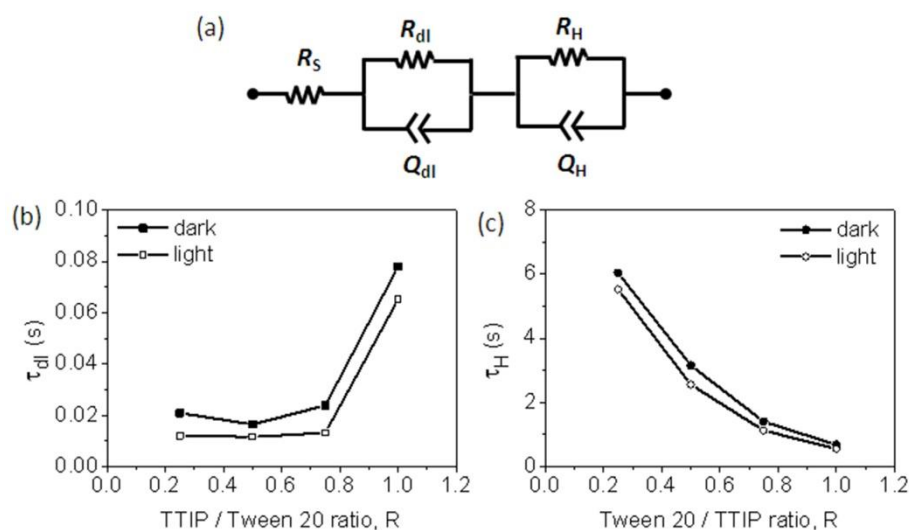


**Figure 2.10.** (a) Equivalent circuit used for the modeling of EIS results. (b) and (c): time constants calculated from EIS measurements on one layer films made with different Tween 20 loadings, at -0.1 V vs. Ag/AgCl, in the dark and under UV-Vis illumination

**Table 2.2.** Parameters calculated from the fitting of EIS results on titania films made with different Tween 20 loadings at -0.1V vs. Ag/AgCl, in dark and under UV-Vis light

	$R$	$R_s (\Omega)$	$\tau_{dl} (s)$	$C_{dl} (F)$	$R_{dl} (\Omega)$	$n_{dl}$	$\tau_H (s)$	$C_H (F)$	$R_H (\Omega)$	$n_H$
<b>dark</b>	0.25	18.39	2.10E-02	2.14E-03	9.812	1.00	6.04	1.22E-03	4957	0.89
	0.5	17.13	1.65E-02	2.06E-03	8.005	1.00	3.16	8.51E-04	3709	0.81
	0.75	11.54	2.39E-02	3.41E-03	7.01	1.00	1.41	5.53E-04	2544	0.75
	1	9.622	7.80E-02	1.27E-02	6.146	0.96	0.684	3.71E-04	1843	0.69
<b>light</b>	0.25	17.34	1.21E-02	1.36E-03	8.89	0.96	5.53	2.74E-03	2018	0.92
	0.5	15.69	1.16E-02	1.60E-03	7.28	0.98	2.56	1.33E-03	1926	0.89
	0.75	11.44	1.32E-02	2.03E-03	6.49	0.99	1.13	8.08E-04	1401	0.81
	1	8.942	6.52E-02	1.10E-02	5.951	0.96	0.561	4.42E-04	1270	0.65

#### 2.3.4.3. Stability and photoactivity of multi-layer films

Figure 2.11 shows the anodic currents for different cycles of darkness and UV-Vis illumination. The anodic photocurrent appeared immediately after the light was turned on, due to instantaneous photo-induced electron transition to the conduction band, and then slightly increases until steady state photocurrent is reached. When the light was turned off, the photocurrent decreased quickly down to zero. No decay in the photocurrent of any of the films have been observed after the multiples light ON-OFF cycles, so confirming the good stability and adhesion of the material in the substrate.

Regarding the performance of the multiple layer films, Figure 2.11a shows an increase of about 67% in the photocurrent density of the one layer TiO<sub>2</sub> film per every additional layer with R = 0.25. Figure 2.11b and 2.11c show that for films made with R = 0.5 and 0.75, the photoactivity increases by 25% only when passing from one to two layers, while no changes (with R = 0.5) or even a few reduction (with R = 0.75) is observed by the coating of a third layer. Finally, a decrease in the photocurrent density is noticed in Figure 2.11d with the increase in the number of layers using R = 1. This result is related to the few increase in the thickness already seen in Figure 2.7, that has been explained by the decrease in the adhesion between successive deposited layers, when the higher amounts of surfactant (R = 0.75 and 1) have been used.

However, it should be emphasized that increasing film thickness with the addition of the Tween 20 surfactant can improve the photocatalytic activity of these TiO<sub>2</sub> films from the first deposited layer, through the contribution in the porous structure. Results in Figure 2.11 show that the optimum number of layers is three for TiO<sub>2</sub> films made with R = 0.25, while the optimum number of layers is only one for TiO<sub>2</sub> films with R = 1. Considering that they have similar pore size, it is believed that a much higher porosity of TiO<sub>2</sub> film (with the higher surfactant loading) could cause more number of water molecules to pass through the upper surface of the film, that will moreover found a higher number of reactive sites due to the higher thickness.

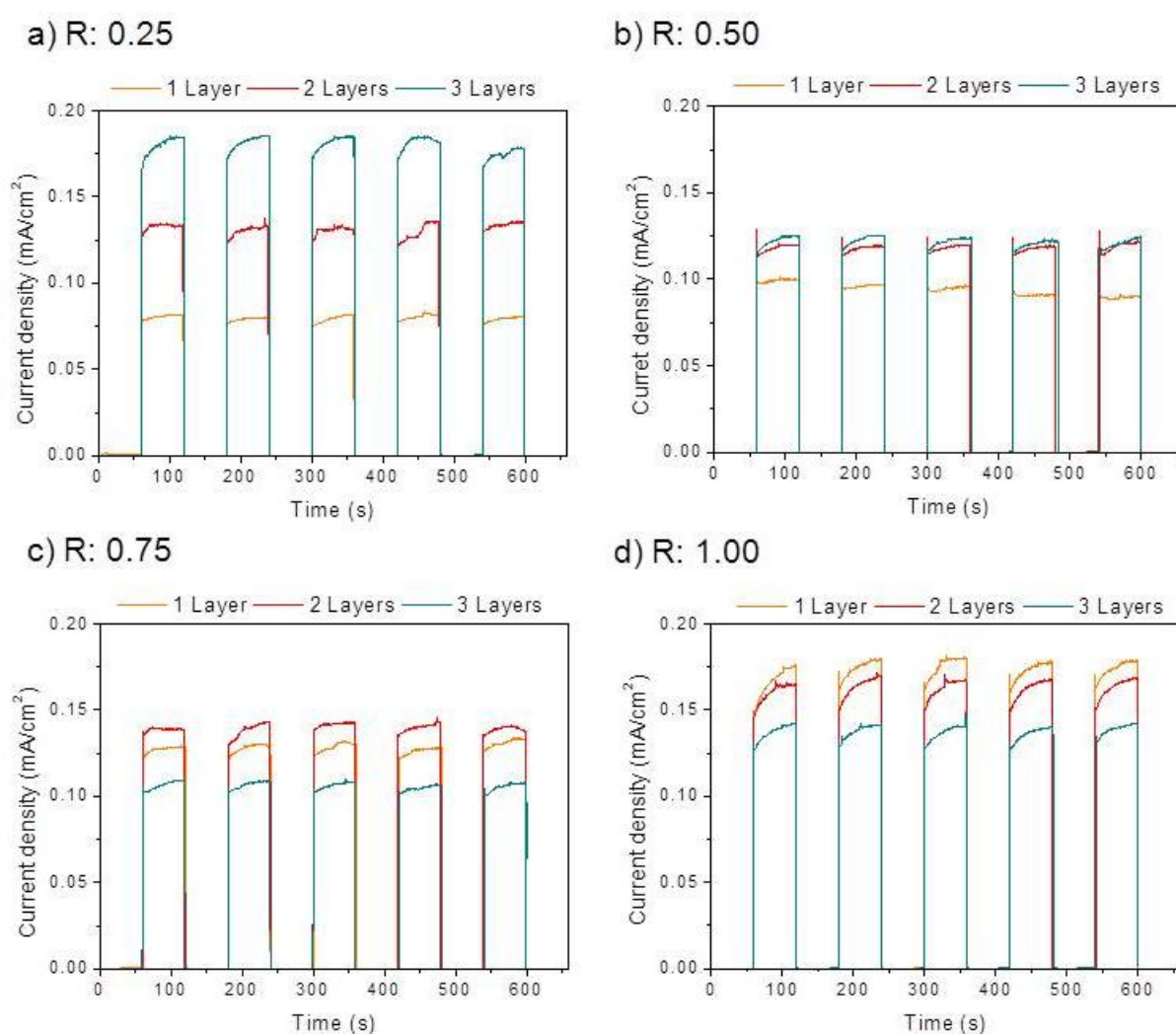


**Figure 2.11.** Current density vs. time of TiO<sub>2</sub> films with different number of layers and different Tween 20/TTIP molar ratios, at -0.1 V vs. Ag/AgCl under multiple dark-light cycles

## 2.4. Conclusions

A new and low-cost synthesis procedure has been implemented for the fabrication of thick, mesoporous, transparent and crackless TiO<sub>2</sub> films, using an Acetic acid catalyzed sol gel synthesis with a high water ratio modified by the addition of a non-ionic surfactant. The high porosity, surface area, homogeneity and amount of material deposited on the substrate surface, together with the good electronic transport and stability over time, result in an improved photo-catalytic performance of the titania films. Such enhanced features, demonstrated for the photo-electrochemical water splitting reaction, are promising for other applications, in particular, if such highly mesoporous films could be used as supports for both visible-light harvester or catalysts materials, able to increase the efficiency of the titania films by improving light absorption, in the former case, or by reducing the activation overpotential, in the latter. Finally, the titania films prepared with this procedure could also be used in technological processes as interconnection layer between different nanostructured metal oxides, which has been made for instance to bond free-standing TiO<sub>2</sub> nanotubes membranes into a transparent conductive oxide to be used in a solar energy production system (i.e. dye sensitized solar cell) [41].

## 2.5. References

- [1] J. Yu, X. Zhao, Q. Zhao, *Thin solid films*, 379 (2000) 7-14.
- [2] B. O'regan, M. Grfitzeli, *Nature*, 353 (1991) 737-740.
- [3] S. Hazra, S. Basu, *Sensors and Actuators B: Chemical*, 115 (2006) 403-411.
- [4] C.-S. Hsu, C.-K. Lin, C.-C. Chan, C.-C. Chang, C.-Y. Tsay, *Thin solid films*, 494 (2006) 228-233.
- [5] M.M. Yusuf, H. Imai, H. Hirashima, *Journal of sol-gel science and technology*, 25 (2002) 65-74.
- [6] H. Choi, E. Stathatos, D.D. Dionysiou, *Thin solid films*, 510 (2006) 107-114.
- [7] J. Yu, X. Zhao, J. Du, W. Chen, *Journal of sol-gel science and technology*, 17 (2000) 163-171.
- [8] J. Jiao, Q. Xu, L. Li, T. Tsubasa, T. Kobayashi, *Colloid and Polymer Science*, 286 (2008) 1485-1491.
- [9] K. Shimizu, H. Imai, H. Hirashima, K. Tsukuma, *Thin solid films*, 351 (1999) 220-224.
- [10] D. Zhang, T. Yoshida, H. Minoura, *Advanced Materials*, 15 (2003) 814-817.
- [11] M.D. Blešić, Z. Šaponjić, J. Nedeljković, D. Uskoković, *Materials letters*, 54 (2002) 298-302.

- [12] T. Viseu, M. Ferreira, *Vacuum*, 52 (1999) 115-120.
- [13] H. Choi, E. Stathatos, D.D. Dionysiou, *Applied Catalysis B-Environmental*, 63 (2006) 60-67.
- [14] C.-C. Chan, C.-C. Chang, W.-C. Hsu, S.-K. Wang, J. Lin, *Chemical Engineering Journal*, 152 (2009) 492-497.
- [15] C. Yu, B. Tian, D. Zhao, *Current Opinion in Solid State and Materials Science*, 7 (2003) 191-197.
- [16] G.J.d.A. Soler-Illia, C. Sanchez, B. Lebeau, J. Patarin, *Chemical Reviews*, 102 (2002) 4093-4138.
- [17] Z. Liu, Z. Jin, X. Liu, Y. Fu, G. Liu, *Journal of sol-gel science and technology*, 38 (2006) 73-78.
- [18] E. Stathatos, P. Lianos, C. Tsakiroglou, *Microporous and Mesoporous Materials*, 75 (2004) 255-260.
- [19] Ö. Dag, I. Soten, Ö. Çelik, S. Polarz, N. Coombs, G.A. Ozin, *Advanced Functional Materials*, 13 (2003) 30-36.
- [20] Y. Chen, E. Stathatos, D.D. Dionysiou, *Surface & Coatings Technology*, 202 (2008) 1944-1950.
- [21] N. Venkatachalam, M. Palanichamy, V. Murugesan, *Materials Chemistry and Physics*, 104 (2007) 454-459.
- [22] K. Madhusudan Reddy, S.V. Manorama, A. Ramachandra Reddy, *Materials Chemistry and Physics*, 78 (2003) 239-245.
- [23] B.R. Li, X.H. Wang, M. Yan, L.T. Li, *Key Engineering Materials*, 224 (2002) 577-580.
- [24] M. García-Benjume, M. Espitia-Cabrera, M. Contreras-Garcia, *International Journal of Photoenergy*, 2012 (2012).
- [25] O. Galkina, V. Vinogradov, A. Agafonov, A. Vinogradov, *International Journal of Inorganic Chemistry*, 2011 (2012).
- [26] M.L. García-Benjume, M.I. Espitia-Cabrera, M.E. Contreras-García, *Materials Characterization*, 60 (2009) 1482-1488.
- [27] C.-Y. Tsai, S.-Y. Tam, Y. Lu, C.J. Brinker, *Journal of membrane science*, 169 (2000) 255-268.
- [28] L.R. Paez, *Ceramics Silikaty*, 48 (2004) 66-71.
- [29] S. Agarwala, M. Kevin, A. Wong, C. Peh, V. Thavasi, G. Ho, *ACS applied materials & interfaces*, 2 (2010) 1844-1850.

- [30] F. Bosc, A. Ayrat, P.-A. Albouy, C. Guizard, *Chemistry of Materials*, 15 (2003) 2463-2468.
- [31] J. Yu, J. Yu, J. Zhao, *Applied Catalysis B: Environmental*, 36 (2002) 31-43.
- [32] R. Asahi, Y. Taga, W. Mannstadt, A. Freeman, *Physical Review B*, 61 (2000) 7459.
- [33] N. Serpone, D. Lawless, R. Khairutdinov, *Journal of Physical Chemistry*, 99 (1995) 16646-16654.
- [34] M.I. Litter, *Applied Catalysis B: Environmental*, 23 (1999) 89-114.
- [35] J.J. Kelly, Z. Hens, D. Vanmaekelbergh, Z. Hensalso, *Encyclopedia of Electrochemistry*, (2007).
- [36] L. Balan, R. Schneider, J. Ghanbaja, P. Willmann, D. Billaud, (2006).
- [37] E. Barsoukov, J.R. Macdonald, *Impedance spectroscopy: theory, experiment, and applications*, John Wiley & Sons, 2005.
- [38] T. Lopes, L. Andrade, H.A. Ribeiro, A. Mendes, *International Journal of Hydrogen Energy*, 35 (2010) 11601-11608.
- [39] A. Zaban, A. Meier, B.A. Gregg, *The Journal of Physical Chemistry B*, 101 (1997) 7985-7990.
- [40] N. Baram, Y. Ein-Eli, *The Journal of Physical Chemistry C*, 114 (2010) 9781-9790.
- [41] A. Lamberti, A. Sacco, S. Bianco, D. Manfredi, F. Cappelluti, S. Hernandez, M. Quaglio, C.F. Pirri, *Physical Chemistry Chemical Physics*, 15 (2013) 2596-2602.

## Chapter 3

### Comparison of photocatalytic and transport properties of TiO<sub>2</sub> and ZnO nanostructures for solar-driven water splitting

#### 3.1. Introduction

With increasing concern over the fossil fuel depletion and the environment degradation, energy is one of the greatest issues facing humanity in the coming years. Hydrogen, present in the water molecules, is an efficient energy carrier and is also environment friendly: so using solar energy to split water into oxygen and hydrogen (also called “artificial photosynthesis”) is a key point towards the development of sustainable and renewable energy devices.

More than 40 years after the pioneering work of Fujishima and Honda [1], the search for suitable semiconductors to be employed for the water dissociation into molecular hydrogen and oxygen is still an open challenge. It has been found [2] that the photochemical water-splitting reaction can be catalyzed by over 140 metal oxides, perovskites and oxynitrides, and the principal controlling factors of the photocatalysis activity have been identified. Nevertheless many questions concerning the molecular mechanisms of water reduction and oxidation and the charge transfer dependence on the electronic and structural properties have not been completely solved, and the ideal semiconducting photocatalyst has still to be identified. At the same time, research efforts focused on proposing artificial photosynthesis devices have recently greatly increased in number and importance, but functional prototypes with convenient efficiencies are yet to be fabricated [3].

The H<sub>2</sub> photocatalytic generation involves three principal steps: (i) absorption of photons (with energy higher than the semiconductor band gap ( $E_g$ ) and consequent generation of electron/hole ( $e^-/h^+$ ) pairs in the semiconductor, (ii) excited charge carriers separation and migration within the semiconductor, and (iii) surface reaction of the carriers with water molecules. To provide the water splitting, the bottom of the semiconductor conduction band must be in a more negative energy position with respect to the reduction potential of water to produce H<sub>2</sub>; and the top of the valence band must be more positive than the oxidation potential of water to produce O<sub>2</sub>. Furthermore, the photo-catalyst must be stable in aqueous solutions under photo-irradiation. The total amount of generated H<sub>2</sub> molecules is determined by the amount of excited electrons at the water/photo-catalyst interface capable of reducing

water. Charge recombination and separation/ migration processes are the two most important competitive processes that largely affect the efficiency of the photocatalytic reaction. Charge recombination reduces the number of  $e^-/h^+$  pairs by emitting light or generating phonons. Efficient charge separation, fast charge carrier transport and limited bulk/surface charge recombination, are thus fundamental characteristics for an optimal semiconductor photocatalyst material.

Since 1972 [1], titanium dioxide ( $\text{TiO}_2$ ) has been the most commonly studied material for photocatalysis. It exhibits an appropriate band gap of about 3.2 eV, together with high photocatalytic efficiency, good chemical and optical stability, optimal environmental and biological compatibility [4]. Zinc oxide ( $\text{ZnO}$ ) has also been largely considered because of its band gap energy, that is comparable to  $\text{TiO}_2$  [5], with the energy levels located almost at the same positions, its higher electron mobility and lifetime [6], relatively lower production costs and easy fabrication under a variety of nanostructures such as nanowires, nanoribbons, nanobelts, nanocombs, nanospheres, nanofibers, nanotetrapods [7]. Up to now  $\text{TiO}_2$  and  $\text{ZnO}$  are close to be ideal photocatalysts. They are relatively inexpensive and they provide photo-generated holes with high oxidizing power due to their wide band gap energy. Unfortunately their solar-to-hydrogen efficiency is limited by the high band gap and the many electron-hole recombination centers [8]; moreover,  $\text{ZnO}$  has the disadvantage of a facile dissolution under UV light irradiation in aqueous solution [9].

Different routes have been adopted for enhancing the photocatalyst performances. Based on the fact that size, shape and also defects significantly affect the final performances, the optimization of the morphology and the crystalline structure has been studied, and a large variety of micro and nanostructures has been suggested [10]. In particular, one-dimensional nanostructures such as nanorods, nanotubes and nanowires have emerged as very promising alternative to nanoparticle-based architectures: the cylindrical and/or tubular configuration is very convenient to increase the surface area without affecting the total geometric surface and the unidirectional electric channel should allow a better charge transport [11]. Moreover, many strategies to change the chemical composition and surface properties of the semiconductor have been tried, for instance by ion implantation, doping, dye sensitization [12] or hydrogenation [13], and also hybrid nanostructures have been proposed, such as core-shell nanocomposites, which consist of an inner nanostructure encapsulated inside an outer shell of a different material. In particular, for water splitting reactions, the  $\text{ZnO}@TiO_2$  core-shell heterostructures offer fine advantages: the  $\text{TiO}_2$  shell functions as a protective layer to reduce the  $\text{ZnO}$  degradation and the multi-dimensional contact permits to fully utilize the

heterojunction between the two semiconductors, which exhibits very favorable electron-transfer properties that are beneficial to an effective separation of the photo-generated  $e^-/h^+$  pairs [14].

In this chapter, the aim is to compare the photo-electrochemical (PEC) properties of four different photo-electrodes based on  $TiO_2$  and ZnO nanostructures having the same active area and similar thicknesses, for the light-activated water splitting under simulated sunlight (AM1.5G) conditions. The examined nanostructured electrodes are composed of: (i)  $TiO_2$  nanoparticles ( $TiO_2$  NPs) in a mesoporous film prepared by sol-gel and spin-coating technique on Fluorinated Tin Oxide (FTO)-covered glasses, (ii)  $TiO_2$  nanotubes ( $TiO_2$  NTs) grown on Ti foils [16], (iii) ZnO nanowires (ZnO NWs) and (iv) ZnO@ $TiO_2$  core-shell structures grown on FTO-covered glass substrates.  $TiO_2$  NPs film was deposited following the experimental procedure described in Chapter 2 and published by Hidalgo et al., [15]. Both  $TiO_2$  NTs and ZnO NWs [17] materials were synthesized by different research group at Istituto Italiano di Tecnologia initially for application in Solar Cells and Electronic Devices and, in this chapter is presented the electrochemical characterization of the mentioned materials with application in water splitting. Finally, ZnO@ $TiO_2$  core-shell structures fabricated by covering the ZnO nanowires with sol-gel synthesized  $TiO_2$  nanoparticles [18, 19].

All the four nanostructures were synthesized ad hoc and the thicknesses of the four photocatalytic nanostructures have been fixed at about 1.5  $\mu m$ . The morphological and optical properties obtained for the four nanostructures are presented and discussed. The PEC properties have been obtained through linear sweep voltammetries in the dark and under simulated sunlight (100  $mW/cm^2$ ). The different charge transport mechanisms and interfacial kinetics for the solar activated water splitting reaction have been studied by means of electrochemical impedance spectroscopy (EIS) analysis. The role of key parameters such as electronic properties, specific surface area and photo-catalytic activity on the performance of these materials are analyzed in view of the practical application of these nanostructures in a solar water splitting device.

The results of this research are part of the publication entitled: "Comparison of photocatalytic and transport properties of  $TiO_2$  and ZnO nanostructures for solar-driven water splitting". S. Hernández, D. Hidalgo, A. Sacco, A. Chiodoni, A. Lamberti, V. Cauda, E. Tresso, G. Saracco. (2015) Physical Chemistry Chemical Physics. Submitted.

## **3.2. Experimental**

### **3.2.1. Synthesis of the nanostructures**

#### **3.2.1.1. TiO<sub>2</sub> nanoparticles film fabrication by sol-gel synthesis**

Titanium (IV) isopropoxide (TTIP, 97%), glacial acetic acid (AcOH, 99.7%) and the surfactant Tween 20, all from Sigma Aldrich were used as purchased. Firstly, TTIP was hydrolyzed in glacial AcOH and then the Tween 20 was added under vigorous stirring. The mixture was added dropwise to the deionized water and the final solution was aged under continuous stirring for 48 h at ambient temperature. TTIP, glacial AcOH, Tween 20 and water were at fixed molar ratios 1:10:1:300. The obtained solution was treated in a rotary evaporator at 40 °C for 2 h under vacuum conditions. The final sol containing the TiO<sub>2</sub> nanoparticles, homogeneous and stable for weeks, has then been used for the preparation of the TiO<sub>2</sub> NPs film. The sol was deposited onto FTO-coated glass (7 Ω/sq from Solaronix) in an exposed area of 2 cm x 2 cm by spin-coating technique using a two-step deposition program: (1) 500 rpm for 10 s followed by (2) 3000 rpm for 10 s. The deposited film was dried at 360 °C for 30 min before spin-coating every successive layer. A total of three deposited layers was reached. Finally, the film was annealed at 500 °C in air using a heating rate of 1 °C/min, followed by natural cooling to room temperature. Further details of the synthesis and characterization of this films are described in Chapter 2.

#### **3.2.1.2. TiO<sub>2</sub> nanotube arrays fabrication by anodic oxidation**

TiO<sub>2</sub> nanotube arrays were grown by a quick anodic oxidation of Ti foil (250 μm thick, 99.6%-purity, Goodfellow) in an electrolytic solution made of 0.5 wt% NH<sub>4</sub>F (98%, Sigma Aldrich) and 2.5 wt% deionized water in ethylene glycol (99.5%, Sigma Aldrich). The Ti foils were manually cut in 2 cm x 4 cm pieces and carefully cleaned by ultra-sonication in acetone and subsequently in ethanol. A rapid etching in a HF (1 wt%) aqueous solution was performed in order to remove the native oxide on the commercial Ti foil and to obtain a fresh surface for NTs growth. Afterwards the samples were masked with a polyimide-based tape (exposed area 2 cm x 2 cm) and used as anode in a two-electrode electrochemical cell (a platinum foil was used as counter electrode) under continuous stirring in ambient conditions. Anodization was performed applying a 60 V potential for 5 min in order to obtain a NTs carpet with thickness ranging between 1.5 and 1.9 μm. Finally, the TiO<sub>2</sub> NTs were annealed

at 450 °C (30 min heating ramp, 30 min in temperature, cooling down in 2 h) to crystallize them into anatase phase. More details on the process are given elsewhere [16, 20].

### **3.2.1.3. ZnO nanowires grown by hydrothermal synthesis**

ZnO nanowires were obtained by hydrothermal route with a conventional approach [17] using two steps: first the preparation of a ZnO seed-layer on the FTO glass substrates (with an exposed area of 2 cm x 2 cm), and second the NWs growth. Briefly, the seeded substrates were obtained by dip coating (speed 375 mm/min) the FTO-covered glass in a 10 mM solution of zinc acetate (Sigma, purity 98%) in ethanol and then calcining them in air at 350 °C for 1 h (heating rate 5 °C/min). Afterwards, the ZnO NWs were grown by immersing the seeded substrates in a 100 mL water solution of zinc nitrate hexahydrate ( $\text{Zn}(\text{NO}_3)_2 \cdot 6\text{H}_2\text{O}$ , 25 mM, 98%, Sigma-Aldrich), hexamethyleneteramine (HMT, 12.5 mM, Sigma-Aldrich), polyethyleneimine (PEI, 5mM, average  $M_w \approx 800$ , Sigma-Aldrich) and ammonium hydroxide ( $\text{NH}_4\text{OH}$ , 28%, 320 mM, Sigma-Aldrich) for 2 h at 88 °C under stirring (300 rpm). The obtained ZnO NWs were then thermally treated in air at 500 °C for 1 h (heating rate 1°C/min).

### **3.2.1.4. ZnO@TiO<sub>2</sub> core-shell heterostructures prepared by sol-gel impregnation**

The ZnO@TiO<sub>2</sub> core-shell structures were obtained by immersing for 10 min the ZnO NWs grown on FTO glass substrate in a non-acid titania precursor solution constituted by 0.46 M titanium isopropoxide (TTIP, 97%, Sigma-Aldrich), 0.28 M acetylacetonone (99%, Fisher Aldrich) and 0.92 M bi-distilled water (from a Direct-Q, Millipore system) in 5 mL of 1-butanol (anhydrous, 99.8%, Sigma-Aldrich) under stirring at room temperature. The sample was then dried in horizontal position and thermally treated in air at 450 °C for 30 min (heating rate 1 °C/min) for the complete titania crystallization into anatase phase.

## **3.2.2. Morphological and optical characterization**

The morphology and the structural properties of the different nanostructures were investigated by means of Field Emission Scanning Electron Microscopy (FESEM) using either a ZEISS Auriga or a ZEISS Merlin, and by means of a FEI TECNAI F20ST Bright-Field Transmission Electron microscope (BF-TEM) and Scanning Transmission Electron Microscope (STEM, equipped with High-Angle Annular Dark Field (HAADF) detector). The samples for TEM/STEM characterization were prepared by detaching the nanostructures

from the substrate, dispersing them in ethanol employing an ultrasonic bath, and putting a drop of the dispersion on the top of a holey carbon copper grid. The mean geometrical dimensions of the different nanostructures, obtained by FESEM images, have also been used to calculate their geometrical surface (GS). The UV–visible spectra were recorded with a Cary 5000 Scan UV–visible spectrophotometer, using a diffuse reflectance integrating sphere. All spectra were recorded in both Kubelka-Munk function  $F(R)$  and total reflectance (% R) modes and background subtracted.

### 3.2.3. Photo-electrochemical characterization

The PEC experiments were performed in a Teflon reactor equipped with a quartz window for frontal illumination. All the tests were carried out in a three electrodes configuration using the TiO<sub>2</sub> NPs film, TiO<sub>2</sub> NTs, ZnO NWs or ZnO@TiO<sub>2</sub> core-shell heterostructures as the working electrodes for the water photo-electrolysis reaction, a platinum wire as the counter electrode, and an Ag/AgCl (KCl 3 M) as the reference electrode, in 0.1 M NaOH aqueous electrolyte (pH = 12.7). N<sub>2</sub> was bubbled through the electrolyte solution for 30 min before the tests. The electrochemical measurements were performed using a multi-channel VSP potentiostat/galvanostat (by BioLogic), with EC-Lab<sup>®</sup> software (version 10.1x) for data acquisition. The current-voltage ( $I$ - $V$ ) characteristic curves were recorded by means of Linear Sweep Voltammetry (LSV) at a scan rate of 10 mV/s, when a constant open circuit voltage was achieved, varying the applied potential from -0.9 V to 0.8 V vs. Ag/AgCl, in the dark and under AM1.5G simulated sunlight (using a 450 W Xe lamp by Newport with an AM1.5G filter and a water filter model 6123NS) using a power density of 100 mW/cm<sup>2</sup> (including 3.7 mW/cm<sup>2</sup> in the UV range: 280 to 400 nm). The irradiance was measured by means of a Delta Ohm Photo-radiometer model HD2102.1. Chrono-amperometric ( $I$ - $t$ ) tests were carried out to examine the photo-response of the nanostructures over time at -0.1 V vs. Ag/AgCl (0.86 V<sub>RHE</sub>) under continuous ON-OFF light cycles, with the same illumination condition used for the LSV. Further LSV were recorded with the TiO<sub>2</sub> NTs and the ZnO@TiO<sub>2</sub> core-shells with a higher light intensity than in the previous tests, using 220 mW/cm<sup>2</sup> (having an UV contribution of 14 mW/cm<sup>2</sup>). The measured potentials versus the Ag/AgCl reference electrode were converted to the reversible hydrogen electrode (RHE) scale via the Nernst Equation (1):

$$E_{RHE} = E_{Ag/AgCl} + 0.059 \cdot pH + E_{Ag/AgCl}^{\circ} \quad (3.1)$$

where  $E_{\text{RHE}}$  is the converted potential vs. RHE in V vs. RHE ( $V_{\text{RHE}}$ ),  $E_{\text{Ag/AgCl}}$  is the experimental potential measured against the Ag/AgCl reference electrode in V vs. Ag/AgCl ( $V_{\text{Ag/AgCl}}$ ), and  $E^{\circ}_{\text{Ag/AgCl}}$  is the standard potential of Ag/AgCl (KCl 3 M) at 25 °C (*i.e.* 0.21 V). EIS curves were recorded using the same potentiostat described above, from 0.1 Hz to 100 kHz, with AC amplitude of 25 mV, at different applied potentials from -0.5 to 0.5 V vs. Ag/AgCl, in the dark and under AM1.5G simulated solar light (100 mW/cm<sup>2</sup>). EIS for Mott-Schottky plots were performed at a frequency of 5 kHz, with AC amplitude of 20 mV, from -0.8 to 0.7 V vs. Ag/AgCl with a scan step of 0.1 V.

### 3.3. Results and discussion

#### 3.3.1. Morphology and structure

Figure 3.1 reports the 45° tilted FESEM views of the TiO<sub>2</sub> NPs and of the different vertically aligned nanostructures. All the four considered nanostructures have a comparable thickness (see Figure 3.1), which is about 1.5 μm. Figure 3.1a shows the TiO<sub>2</sub> NPs film, which is uniform and continuous, characterized by nanoparticles with a size between 7 to 13 nm, interconnected in a mesoporous network [15]. As shown in Figure 3.1b, the TiO<sub>2</sub> NTs grown by anodic oxidation are vertically arranged with respect to the Ti foil. The TiO<sub>2</sub> NTs are closely packed, with an outer diameter (o.d.) in the range 100 - 130 nm and inner diameter (i.d.) around 70 nm [16]. The ZnO NWs, shown in Figure 3.1c, are almost vertically aligned, with a diameter ranging between 100 and 200 nm. Finally, Figure 3.1d put in evidence the good coverage of the ZnO NWs with the titania shell made of crystalline anatase nanoparticles [18, 19].

The different nanostructures have also been investigated with the TEM technique, both in BF-TEM and in STEM modes, as shown in the Figure 3.2.

In Figure 3.2a, two BF-TEM images at different magnification show the TiO<sub>2</sub> nanoparticles in the anatase crystalline form, as put in evidence by the selected area electron diffraction (SAED) analysis (not reported here) and by the Fast Fourier Transform (FFT) in the inset. The size of the particles is in the range 10-20 nm, in agreement with the previously reported FESEM characterization.

In Figure 3.2b, the BF-TEM characterization of the TiO<sub>2</sub> NTs is reported with different magnifications. The lower magnification put in evidence the shape of the TiO<sub>2</sub> NTs, where the wall, with a thickness of about 25 nm, is clearly visible. The high-magnification images

collected in two distinct regions of the NTs confirm the poly-crystallinity of the  $\text{TiO}_2$  NTs, which are constituted by anatase phase [16].

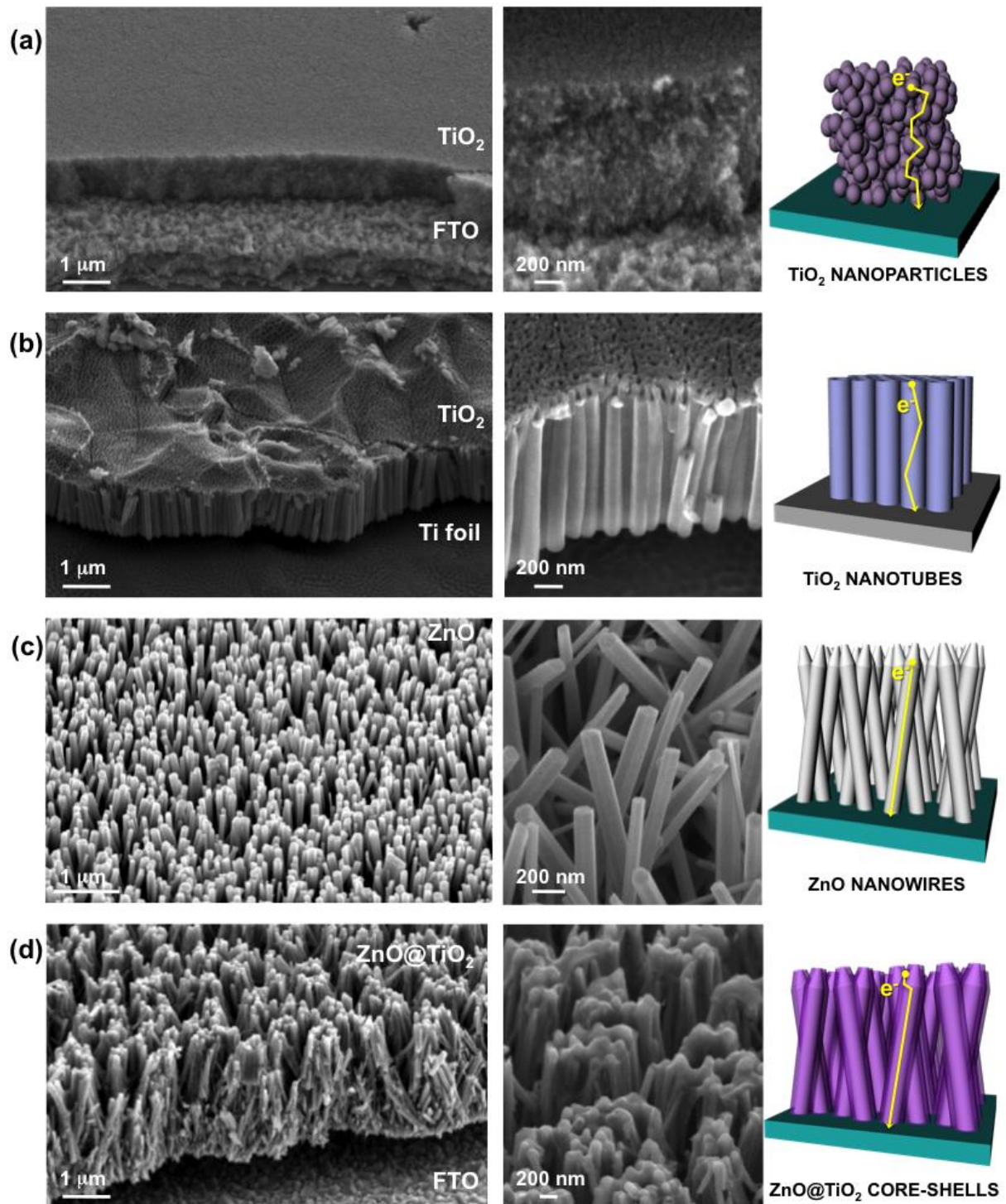


**Figure 3.1.** 45° tilted view FESEM characterization at two different magnifications and schematic representation indicating the  $e^-$  flow path of the different nanostructures: (a)  $\text{TiO}_2$  NPs, (b)  $\text{TiO}_2$  NTs, (c) ZnO NWs and (d) ZnO@ $\text{TiO}_2$  core shells

Figure 3.2c shows two ZnO NWs BF-TEM images at two different magnifications, in which it is clear in the good crystallinity and the preferential orientation along the (002) direction of the ZnO NWs [18], as put in evidence by the FFT in the inset.

For what concerns the ZnO@TiO<sub>2</sub> core-shell structures, the HAADF STEM images at two different magnifications in Figure 3.2d evidence the good coverage of the ZnO NWs (brighter color, higher atomic number) with the titania shell (darker color, lower atomic number) with an average thickness of about 20-50 nm, made of crystalline anatase nanoparticles [18, 19].

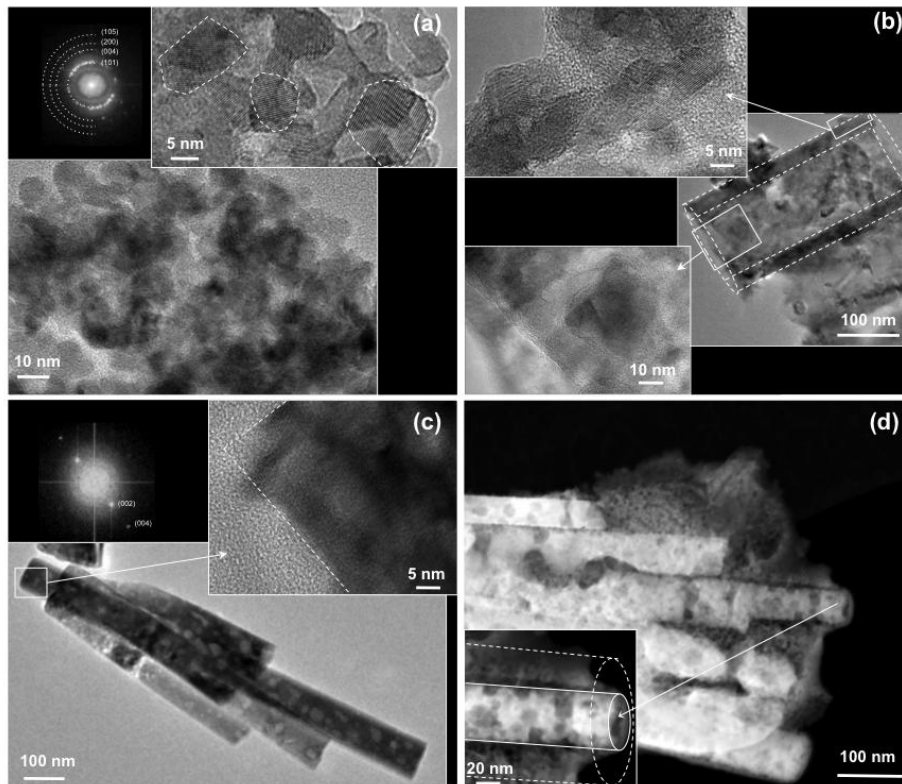


**Figure 3.2.** TEM characterization of the different nanostructures. (a) BF-TEM images at two different magnifications of TiO<sub>2</sub> NPs; in the inset, the FFT of the high magnification image is reported. (b) BF- TEM of TiO<sub>2</sub> NTs at different magnifications. (c) Bright Field TEM of a group of ZnO NWs; in the inset, the FFT of the high magnification image is reported. (d) HAADF STEM of ZnO@TiO<sub>2</sub> core shell: in the inset, a detail of the core-shell with an higher magnification is put in evidence

### 3.3.2. Optical properties

The UV–Vis spectra of the four studied TiO<sub>2</sub> and ZnO nanostructures, in Kubelka-Munk function  $F(R)$  and total reflectance (% R) modes are reported in Figures 3.3a and 3.3b.

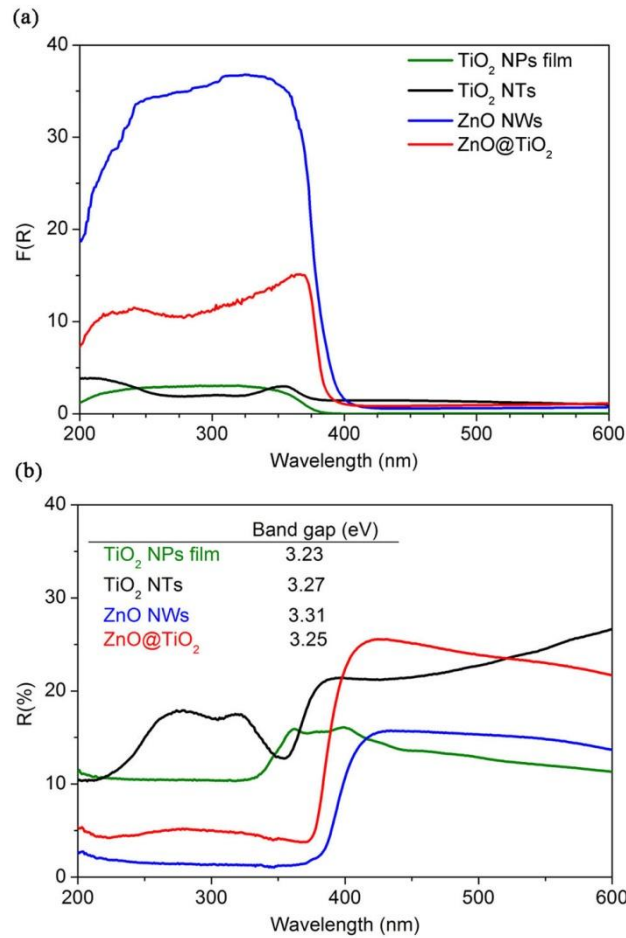


**Figure 3.3.** Optical measurements: (a) Kubelka-Munk spectra, (b) total reflectance and optical band gap for the samples: TiO<sub>2</sub> NPs film (green line), TiO<sub>2</sub> NTs (black line), ZnO NWs (blue line) and ZnO@TiO<sub>2</sub> core-shell structures (red line)

As it is well known,  $F(R)$  is directly proportional to the absorbance. In the range from 200 to 400 nm, the  $F(R)$  is higher for the bare ZnO NWs than for the ZnO@TiO<sub>2</sub> core-shell sample and even for the pure titania nanomaterials, *i.e.* TiO<sub>2</sub> NTs and NPs film. Consistently, the spectra recorded in total reflectance mode (Figure 3.3b) of both titania materials (NTs and NPs film) show a strong increase of the light scattering in the UV range (from 200 to 400 nm), whereas lower scattering is observed for the core-shell sample and is even lower for the bare ZnO NWs. This behavior is attributed to the high degree of crystallinity of the titania-based nanostructures and of the TiO<sub>2</sub> shell deposited on the ZnO NWs (consistent with the TEM and X-ray diffraction patterns reported elsewhere [18, 19]), thanks to the thermal treatment at relatively high temperature (see the experimental section for details). In addition, high scattering levels are expected for rough nanostructures with a high surface area. This is the case of the TiO<sub>2</sub> NPs film [15], the TiO<sub>2</sub> NTs [20] and of the core-shell structure [19] due

to the titania nanoparticles that constitute the shell. The optical band gap values were estimated by using the Tauc's method (see Section 2.3.2) and are reported in the inset of Figure 3.3b. The bare ZnO NWs shows a higher  $E_g$  value (3.31 eV) than both the core-shell material (3.25 eV) and the nanostructured titania samples, *i.e.* TiO<sub>2</sub> NTs (3.27 eV) and TiO<sub>2</sub> NPs film (3.23 eV). The lower band gap values obtained for the core-shell, the TiO<sub>2</sub> NTs and TiO<sub>2</sub> NPs samples are attributed to the presence of anatase TiO<sub>2</sub>, which  $E_g$  has been reported to be about 3.2 eV [4]. Therefore, the narrowing of the  $E_g$  in the core-shell nanostructure with respect to the pure ZnO NWs is easily explained [18].

### 3.3.3. Photo-electrochemical activity for the water splitting reaction

The PEC behavior of the TiO<sub>2</sub> NPs, TiO<sub>2</sub> NTs, ZnO NWs and the ZnO@TiO<sub>2</sub> core-shell heterostructures was evaluated using the prepared photoanodes, which have the same active area (4 cm<sup>2</sup>), for the water photo-electrolysis reaction in 0.1 M NaOH solution (pH = 12.7). Figure 3.4a reports the LSV behavior recorded with the four photoanodes. From the LSV scans in dark conditions, from 0.1 to 1.8 V<sub>RHE</sub>, a tiny current in the range of 10<sup>-4</sup> mA/cm<sup>2</sup> was obtained for all the nanostructures until reaching the onset potential ( $E^o$ ) for the water oxidation reaction at about 1.75 V<sub>RHE</sub>. As expected, the  $E^o$  is reached at potential higher than the theoretical one ( $E^o = 1.23$  V<sub>RHE</sub>), due to the high overpotential effect of TiO<sub>2</sub> and ZnO semiconductors. In contrast, during the LSV under simulated sunlight irradiation (AM1.5G, 100 mW/cm<sup>2</sup>), a sudden increase of the photocurrent is observed at potentials more negative than the redox potential  $E^o$ , because part of the energy required for the oxidation is provided by the light. These results are in agreement with the behavior expected for a n-type semiconductor [21]. Under sunlight illumination, the photocurrent density ( $J$ ) of the TiO<sub>2</sub> NPs and TiO<sub>2</sub> NTs showed an important rise starting at about 0.17 and 0.19 V<sub>RHE</sub>, respectively, reaching a maximum  $J$  value of 0.02 and 0.12 mA/cm<sup>2</sup> at about 0.3 V<sub>RHE</sub> and 0.6 V<sub>RHE</sub>, respectively, which is associated with the saturation of the TiO<sub>2</sub> semiconductor [15, 22]. In contrast, the ZnO NWs showed a pronounced increase of the photocurrent starting at about 0.40 V<sub>RHE</sub>, which continues to rise until reaching a maximum  $J$  of 0.45 mA/cm<sup>2</sup> at 1.7 V<sub>RHE</sub>. The ZnO@TiO<sub>2</sub> core-shell electrodes showed similar behavior, but with an enhanced photo-response, reaching a maximum photocurrent density of 0.63 mA/cm<sup>2</sup> at 1.7 V<sub>RHE</sub>, value that is about 1.5 times higher than the one obtained for the ZnO NWs. The larger photocurrents observed with the 1D-nanostructures (TiO<sub>2</sub> NTs, ZnO NWs and ZnO@TiO<sub>2</sub>) with respect to the TiO<sub>2</sub> NPs film (even if they have a similar thickness) could be explained by a more efficient electron injection at the semiconductor-electrolyte interface and a faster

electron transport from the photoanode to the substrate, which results in a higher number of collected photoelectrons [18, 19, 23].

Additionally, it is worth to note that by coupling the ZnO NWs with a shell of TiO<sub>2</sub> NPs a significant increase of the photocurrent density during the water photo-electrolysis reaction is obtained. Indeed, this is related to the absence of a photocurrent saturation region, as occurs with TiO<sub>2</sub> NPs and TiO<sub>2</sub> NTs photoanodes upon illumination [24]. Therefore, these results are promising in comparison with other results reported in the literature for the water photo-electrolysis using TiO<sub>2</sub> and ZnO nanostructures [24, 25]. For instance, a  $J$  lower than 0.3 mA/cm<sup>2</sup> at 1.8 V<sub>RHE</sub> was reported by using nanocoral structures of ZnO [26] and N-doped ZnO NWs [24]. The photo-activity demonstrated by the ZnO@TiO<sub>2</sub> core-shell sample is also in-line with recent results on pure and N-doped rutile TiO<sub>2</sub> NWs (~ 1.6 μm) [27]. Even though, these values are still smaller than those recently obtained by the coupling of ZnO with visible light absorbing semiconductors, e.g. ZnO-CdS core-shell NWs [28] and ZnO NWs sensitized with CdS/Se quantum dots [29].

The solar-to-hydrogen efficiency (STHE) of each sample type under sunlight illumination was calculated from the  $I$ - $V$  data according to the expression [30]:

$$STHE = J_i (1.23 - E_{RHE}) / I_{light} \quad (3.2)$$

where  $J_i$  is the photocurrent density at the measured bias,  $E_{RHE}$  is the applied bias vs. RHE, and  $I_{light}$  is the irradiance intensity (100 mW/cm<sup>2</sup>). The STHE curves in Figure 3.4b show that the maximum of the curves for the four studied samples increases in the following order: TiO<sub>2</sub> NPs, ZnO NWs, TiO<sub>2</sub> NTs and ZnO@TiO<sub>2</sub>, according to the following values: 0.013 %, 0.047 %, 0.071 % and 0.073 %, respectively. A significant increase of the STHE was obtained using the 1D-nanostructures with respect to TiO<sub>2</sub> NPs, due to their higher photocurrent densities [18, 19, 23].

It is worth to note that both the TiO<sub>2</sub> NTs and the ZnO@TiO<sub>2</sub> samples gave similar maximum STHE but at different applied potentials, being lower for the NTs (*i.e.* 0.5 V<sub>RHE</sub>) than for the core-shell sample (*i.e.* 0.9 V<sub>RHE</sub>). This feature could likely be explained by the different photo-catalytic and transport properties of these two materials. In fact, the open circuit voltage (OCV), *i.e.* the voltage corresponding to  $J = 0$ , is an approximated measure of the flat band potential, which is an important parameter for semiconductor electrodes. Actually, this determines the band edge positions at the semiconductor–electrolyte interface, thus fixing the energies of conduction band electrons and valence band holes reacting with the electrolyte

solution [31]. So, the shift of the OCV towards lower values is another indication of a better photocatalytic activity. The results in the inset of the Figure 3.4a indicate that both the TiO<sub>2</sub> NPs and the TiO<sub>2</sub> NTs samples have a lower flat band potential than the ZnO-based materials. Indeed, the TiO<sub>2</sub> NTs and NPs report almost the same OCV (about 0.20 V<sub>RHE</sub>). Therefore, both the TiO<sub>2</sub> nanostructures present the onset  $E^o$  at a lower value with respect to both the ZnO-based materials, as well as the coating of the ZnO NWs with the TiO<sub>2</sub> anatase shell results in an improved photocatalytic performance compared to the bare ZnO NWs. In fact, the increased photocurrent density of the ZnO@TiO<sub>2</sub> sample is reflected by both its higher STHE with respect to the ZnO NWs and the left-shift in the OCV, from 0.45 V<sub>RHE</sub> (for ZnO NWs) to 0.34 V<sub>RHE</sub> (for core-shell sample). The origin of this effect can rely on different reasons. First, well crystallized TiO<sub>2</sub> nanoparticles on the TiO<sub>2</sub> NPs, TiO<sub>2</sub> NTs or deposited on the surface of the ZnO NWs (in the core-shell sample) could effectively diminish the surface recombination sites, thus increasing the recombination resistance between electrons in the photoanode and holes in the electrolyte, leading to longer charge life-time [14, 32]. On the other hand, electron transport within single crystalline ZnO NWs in the core-shell sample must be faster than in the pure NWs, due to a better charge separation induced by the formation of an heterojunction at the interface between the well crystallized ZnO and TiO<sub>2</sub> materials [14], which was confirmed by TEM and diffuse reflectance analysis (explained above).

In order to investigate the photo-corrosion properties of the TiO<sub>2</sub> and ZnO nanostructures, the stability of the photoanodes was investigated as a function of time. Figure 3.4c shows the  $I-t$  curves of all samples working at -0.1 V vs. Ag/AgCl (0.86 V<sub>RHE</sub>). This potential was chosen since it is a representative value after the photocurrent saturation for both the TiO<sub>2</sub> nanostructures and is, as well, the potential of the maximum STHE for the ZnO NWs and ZnO@TiO<sub>2</sub> samples. The maximum photocurrent densities reached at this potential for all the samples increase in the order: TiO<sub>2</sub> NPs, TiO<sub>2</sub> NTs, ZnO NWs and ZnO@TiO<sub>2</sub>, according to the following values: 0.016, 0.12, 0.14 and 0.19 mA/cm<sup>2</sup>, respectively, which are in agreement with the  $J$  values reported in the LSV (see Figure 3.4a). The same trend was also found at higher potentials. Moreover, a good photo-current stability was observed for all the four samples under numerous light ON-OFF cycles for a long period of time (38 min). However, an initial stage of photo-degradation of the pristine ZnO NWs was observed by FESEM analysis [19], in contrast with both the TiO<sub>2</sub> NPs and the ZnO@TiO<sub>2</sub> samples. This fact is due to the low photo-corrosion resistance of the ZnO directly exposed to the NaOH electrolyte.

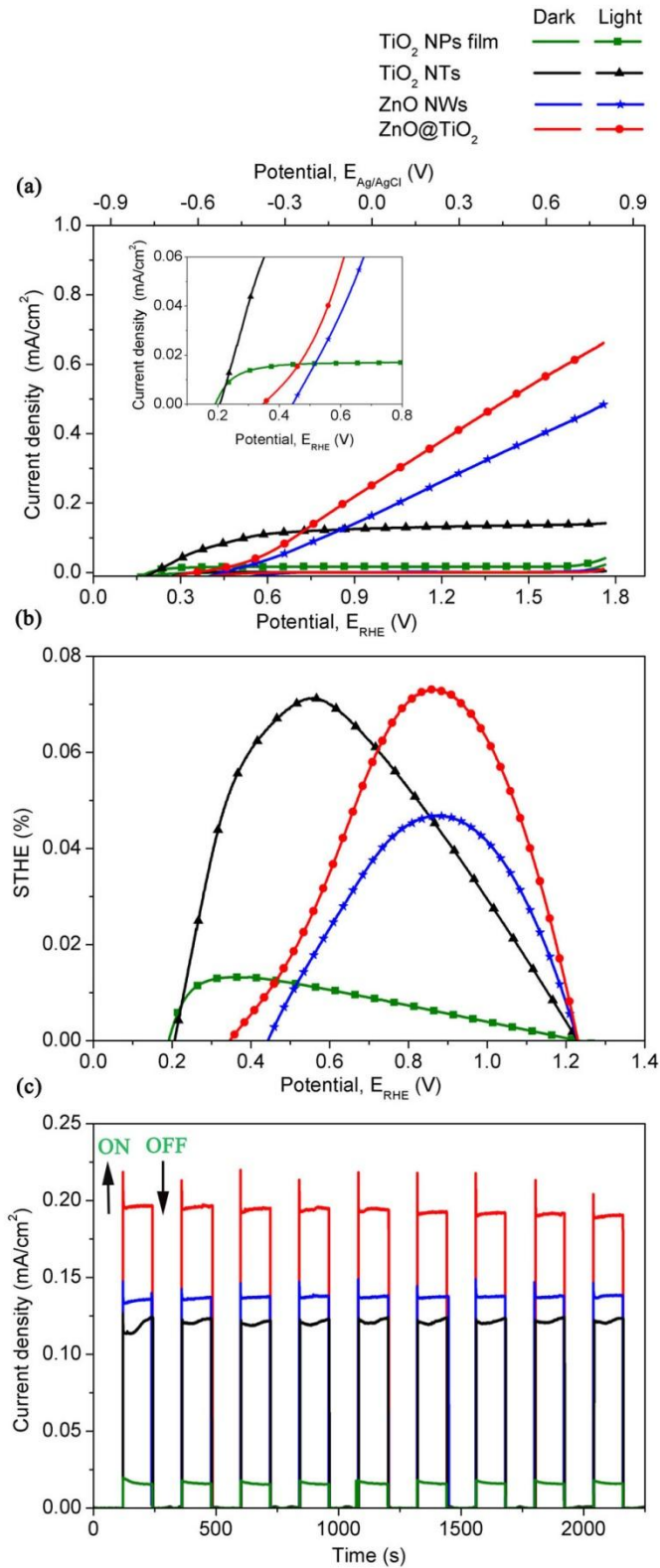


**Figure 3.4.** Photoelectrochemical characterizations for the samples: TiO<sub>2</sub> NPs film (green line), TiO<sub>2</sub> NTs (black line), ZnO NWs (blue line) and ZnO@TiO<sub>2</sub> core-shell structures (red line). (a) LSV collected with a scan rate of 10 mV/s in the dark and under illumination (AM1.5G, 100 mW/cm<sup>2</sup>); (b) Solar-to-hydrogen efficiency as a function of the applied potential; and (c) Chrono-amperometric (*I-t*) curves at an applied potential of -0.1 V vs. Ag/AgCl under illumination with 120 s light ON/OFF cycles

It is important to point out that for a feasible application of a water photo-electrolysis device, the anodic photo-electrodes should present: (i) a high UV-Vis light absorption, (ii) a reduced overpotential for the water oxidation reaction, and (iii) efficient charge transport properties to be able to sustain high photo-current densities. If these conditions are satisfied, the photo-electrodes would be able to reach STHE values of 10 – 15 % with the minimum applied bias [33]. The best performing materials here studied, the TiO<sub>2</sub> NTs and the ZnO@TiO<sub>2</sub> core-shell samples, have different advantages and constrains that must be taken into consideration. With this aim, the relationship between the transport and the photo-catalytic properties of the studied nanostructures, and in particular of the TiO<sub>2</sub> NTs and of the ZnO@TiO<sub>2</sub> core-shell materials, are deeper investigated and discussed in the following sections.

#### 3.3.4. Electrochemical impedance spectroscopy analysis

In order to further analyze what is the most important process responsible for the different performances of the four TiO<sub>2</sub> and ZnO investigated nanostructures, the PEC behavior of the studied photo-electrodes has been investigated by EIS technique. The results of the EIS measurements performed at 1.23 V<sub>RHE</sub> are reported in the Figure 3.5. In accordance with the LSV curves, the impedance modulus of both the TiO<sub>2</sub> photoelectrodes are larger than the ZnO-based ones (see Figure 3.5a). Concerning the phase spectra, two features can be recognized, related to the two different processes occurring in the analyzed systems: a high frequency peak, associated to the charge transport properties of the photoelectrode material, and a low frequency peak associated with the charge transfer at the photoelectrode/electrolyte interface [15]. For the TiO<sub>2</sub>-based and pure ZnO NWs photoanodes the two processes partially overlaps, thus resulting in the formation of a one broad peak; on the other hand, the core-shell sample exhibits two well-distinguished peaks, one centered at about 4 Hz and the other one at about 200 Hz. In order to evaluate the time constants associated to the different processes for all the analyzed samples, the EIS data were modeled through the equivalent circuit shown in Figure 3.5b [15] composed of: a series resistance  $R_s$  (accounting for the resistances of the conductive substrate, of the external electrical contacts and of the liquid electrolyte), a parallel between the resistance  $R_H$  and the capacitance  $C_H$  at the Helmholtz double layer (related to the low frequency process), and a parallel between the resistance  $R_{dl}$  and the capacitance  $C_{dl}$  in the depletion layer in the semiconductor (related to the high frequency process). For all the samples, the computed curves match well with the experimental data, as it is evident in Figure 3.5. Starting for the fitting parameters, the time constants  $\tau_H$  and  $\tau_{dl}$ , related to the charge transfer at the semiconductor/electrolyte interphase

and to the charge transport in the semiconductor, respectively, were calculated through the following equations and their values are summarized in Table 3.1.

$$\tau_H = R_H C_H \quad (3.3)$$

$$\tau_{dl} = R_{dl} C_{dl} \quad (3.4)$$

Moreover, with the aim to evaluate the influence of the surface area on the photoelectrochemical properties of the materials, the geometric surface (GS) of the nanostructures (calculated by considering the dimensions measured through FESEM images) is also reported in the Table 3.1.

By looking at the calculated parameters, as expected, the  $R_s$  value obtained for the TiO<sub>2</sub> NTs sample is one-order of magnitude lower than the  $R_s$  obtained for the other samples, due to the higher conductivity of the Ti foil substrate with respect to the FTO film. Moreover, the TiO<sub>2</sub> NPs film is characterized by slower processes, if compared to the other nanostructures. In particular, it exhibits time constants which are 4 times larger with respect to the NTs-based photoelectrode, although the TiO<sub>2</sub> NPs GS is about 2.5 times higher than the one of the NTs. Regarding the  $\tau_{dl}$  values, this difference can be attributed to the faster electronic transport inside the 1D nanostructure, if compared to the charge transfer by hopping among the nanoparticles [20]. Therefore, even if the photo-catalytic activity of the anatase crystalline phase found in both TiO<sub>2</sub>-based materials should be similar (*i.e.* both these materials have similar flat-band, as previously discussed), the transfer of charges at the TiO<sub>2</sub>-electrolyte interphase is fastened due to the lower accumulation of charges in the NTs than in the NPs nanostructure. As a consequence, the recombination of e<sup>-</sup>/h<sup>+</sup> pairs is reduced, with a resulting increase in the kinetics of the water oxidation reaction in the NTs with respect to the NPs sample, which is observed through the fastening of the charge-transfer at the semiconductor-electrolyte interphase (*i.e.*  $\tau_H$  value). This hence explains the higher saturation photo-current evidenced with the TiO<sub>2</sub> NTs in comparison with the NPs film (shown in Figure 3.4a). In addition, as expected, the charge transport inside the ZnO NWs results even faster with the respect to the polycrystalline TiO<sub>2</sub> NPs and NTs samples, being the NWs characterized by a monocrystalline structure [34]. Finally, the core-shell sample exhibited a five-times lower  $\tau_{dl}$  value if compared to the bare nanowires. This feature can be explained by both the improvement in the electronic transport and in the efficient separation of charge-carriers at the ZnO@TiO<sub>2</sub> interphase [18] induced by the double annealing process performed in the

heterostructures sample, which enhances the crystalline quality and favors the interconnection between the TiO<sub>2</sub> nanoparticles in the shell and the ZnO core.

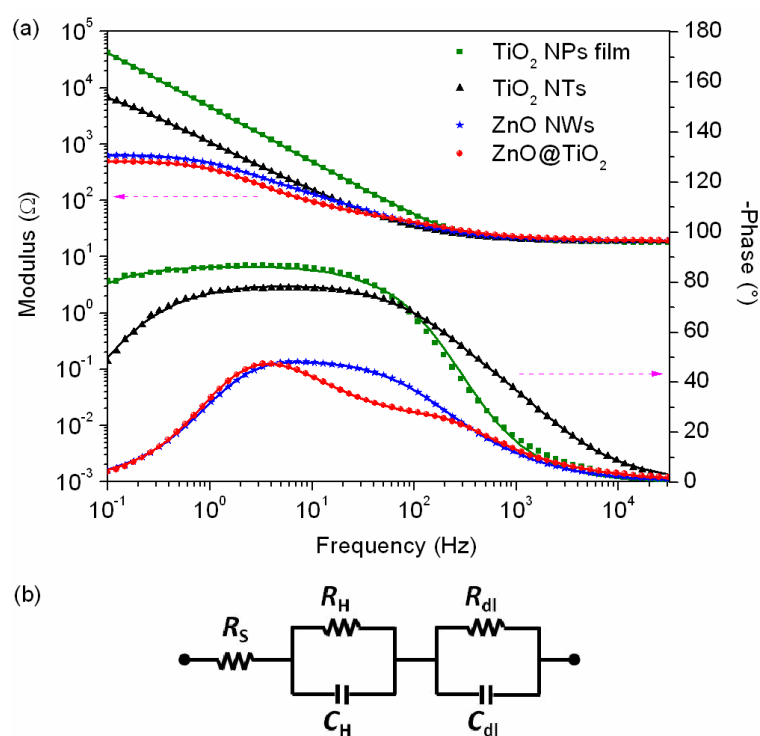


**Figure 3.5.** (a) Bode plots of modulus (left axis) and phase (right axis) of the impedance of TiO<sub>2</sub> NPs, TiO<sub>2</sub> NTs, ZnO NWs and the ZnO@TiO<sub>2</sub> core-shell heterostructures acquired at an applied potential of 0.3 V<sub>Ag/AgCl</sub> (1.23 V<sub>RHE</sub>) under illumination. The points represent the experimental data while the solid lines are the fitting curves. (b) Equivalent circuit used to fit the EIS data

**Table 3.1.** Time constants related to the charge transfer processes involved in the water splitting reaction on the different TiO<sub>2</sub> and ZnO studied nanostructures, evaluated through EIS analysis at 1.23 V<sub>RHE</sub>, under AM1.5G simulated sunlight (100 mW/cm<sup>2</sup>)

Sample	Geometric surface, GS (cm <sup>2</sup> )	R <sub>s</sub> (Ω)	τ <sub>H</sub> (s)	τ <sub>dl</sub> (ms)
TiO <sub>2</sub> NPs	1500	17.92	10.75	333
TiO <sub>2</sub> NTs	600	2.78	2.530	76.0
ZnO NWs	100	19.25	0.150	16.0
ZnO@TiO <sub>2</sub>	110	19.09	0.130	3.00

### 3.3.5. Electronic properties vs. PEC behavior of TiO<sub>2</sub> NTs and ZnO@TiO<sub>2</sub> core-shells

Even if the core-shell material is characterized by better transport properties than the TiO<sub>2</sub> NTs, the latter demonstrated to achieve a STHE similar to the first one at a lower potential (see Section 3.3). In order to analyze the reason of such feature, the EIS measurements on these two materials were analyzed in all the range of studied potentials, under sunlight illumination, and the results are reported in the Figure 3.6.

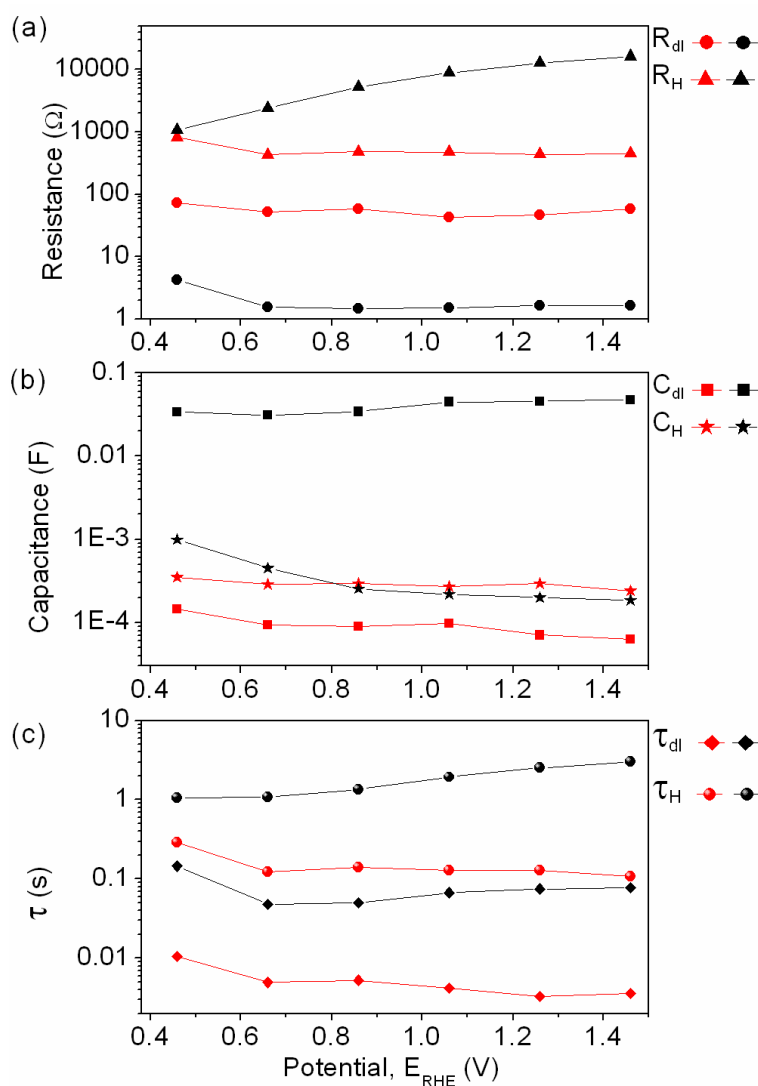


**Figure 3.6.** Transport parameters from the fitting of EIS data obtained with the TiO<sub>2</sub> NTs (black points) and the ZnO@TiO<sub>2</sub> core-shell (red points) at different potentials under sunlight illumination: (a) resistance, (b) capacitance and (c) time constants

Both the materials evidenced almost constant charge transport parameters (*i.e.*  $R_{dl}$  and  $C_{dl}$ ) after 0.6 V<sub>RHE</sub>, indicating a quasi-conductive behavior of both the semiconductors under the

electric field induced by the applied bias potential. In all the range of studied potentials, it is moreover confirmed the faster electron transport (lower  $\tau_{dl}$ ) within the ZnO@TiO<sub>2</sub> core-shells than in the TiO<sub>2</sub> NTs. On the other hand, in contrast with the core-shell material in which both the charge transfer parameters  $R_H$  and  $C_H$  remains constant after 0.6 V<sub>RHE</sub>, in the TiO<sub>2</sub> NTs the  $R_H$  increases and the  $C_H$  slightly decreases with the potential. Since the capacitance at the Helmholtz double layer is related to the reaction rate at the surface of the photo-catalyst under illumination, the  $C_H$  decreasing after 0.5 V<sub>RHE</sub> must be correlated with the achievement of the maximum STHE at such potential for the TiO<sub>2</sub> NTs. In addition, the charge-transfer resistance ( $R_H$ ) of the NTs increases with the potential, leading to a simultaneous increase of the charge-carrier recombination at the surface of the TiO<sub>2</sub> photo-catalyst, due to the reduction of the  $e^-/h^+$  separation efficiency [35]. In fact, this can explain the saturation of the photocurrent often observed with pure TiO<sub>2</sub> materials [22]. As a consequence of this and of the polycrystalline nature of the TiO<sub>2</sub> NTs, even if their exposed GS is six times higher than the one of the ZnO@TiO<sub>2</sub> sample, the  $\tau_H$  (which is correlated to the reaction kinetics) remains 10-fold larger in the NTs than in the core-shells for all the range of applied potentials.

These findings evidence that not always the benefits of material nanostructuration could outweigh the disadvantages. The advantages are the high surface area and absorption volume close to the semiconductor-electrolyte interface, allowing the effective collection and reaction of photo-generated holes. The disadvantages are the partial loss of electric field for charge separation and the increased opportunity for electrons to recombine with species at the electrode surface or in the electrolyte before being collected at the conductive substrate [36]. For such reason, the other two major factors that can affect photocurrent efficiency of the nanostructured electrodes must be properly tuned: (i) the band gap energy, and (ii) the density of surface states and defects.

Regarding the first factor, the TiO<sub>2</sub> NTs has a slightly higher band gap (3.27 eV) than the ZnO@TiO<sub>2</sub> sample (3.25 eV), and thus the core-shells ability to exploit the visible component of sunlight illumination is slightly better than for the NTs. However, when these materials are illuminated in the UV-Vis range with the doubled of the intensity previously used (about 220 mW/cm<sup>2</sup>), the  $J$  at 1.23 V<sub>RHE</sub> is increased of 5 times with the NTs and only of 2.4 times with the core-shells (as observed by comparing the Figures 3.4a and 3.7a). In addition, it is interesting to notice that under such conditions the maximum STHE are proportionally enhanced in both the materials, but with a different factor: 2.4 times for the NTs and of only 1.2 times for the core-shell. These results could be justified by the higher IPCE of the NTs under UV illumination (maximum of 85%) than for the core-shell sample

(maximum of 50%) at 1.23 V<sub>RHE</sub> (data not shown): in fact, in the tests reported in Figure 3.7a the UV component is about 4 times larger than in the previous ones (Figure 3.4a). Moreover, these results are in agreement with the recent work of Qorbani et al. [37] in which TiO<sub>2</sub> NTs were tested with different intensities of simulated sunlight up to 600 mW/cm<sup>2</sup> and yielded a linear dependency between the generated photo-current density and the applied illumination intensity, suggesting that charge-carriers (e<sup>-</sup>/h<sup>+</sup> pair) generation rate is the limiting step for the PEC water splitting. Regarding the second factor, the charge carrier density was calculated according to the Mott-Schottky equation [31], in order to evaluate the surface properties of these two nanostructures:

$$\frac{1}{C_{SC}^2} = \frac{2}{e \cdot \epsilon \cdot \epsilon_0 \cdot N_d} \left( E - E_{FB} - \frac{kT}{e} \right) \quad (5)$$

where  $C_{SC}$  is the capacitance of the space charge region,  $\epsilon_0$  is the permittivity of the free space,  $\epsilon$  is the dielectric constant of the semiconductor (100 for TiO<sub>2</sub> and 19 for the core-shell sample, calculated as a weighted volume value between the  $\epsilon$  of both ZnO and TiO<sub>2</sub>),  $N_d$  is the donor density,  $e$  is the electron charge value,  $E$  is the applied potential,  $E_{FB}$  is the flat band potential and  $kT/e$  is the temperature dependent correction term (25 mV at room temperature).

The  $N_d$  values obtained from the linear fitting process are  $7.05 \times 10^{19} \text{ cm}^{-3}$  for the TiO<sub>2</sub> NTs and  $5.71 \times 10^{19} \text{ cm}^{-3}$  for the core-shells (see Figure 3.7b), which are comparable with those usually observed for ZnO NWs and TiO<sub>2</sub> NTs [22, 38]. The materials have similar  $N_d$ ; however, if these values are normalized by the GS, it results that the core-shells ( $5.19 \times 10^{17}$ ) have a higher donor density per unit of active surface with respect to the TiO<sub>2</sub> NTs ( $1.18 \times 10^{17}$ ). A higher  $N_d$  can also shift the Fermi level of semiconductors toward its conduction band, which further facilitates the charge separation at the semiconductor/electrolyte interface. Thus, this enhanced charge separation and the most favorable charge transport are the most probable reasons for the higher photocurrent values reached with the core-shell samples at high potentials ( $> 0.9 \text{ V}_{RHE}$ ) than the ones obtained with the pure TiO<sub>2</sub> nanostructure with the saturation of the photo-current.

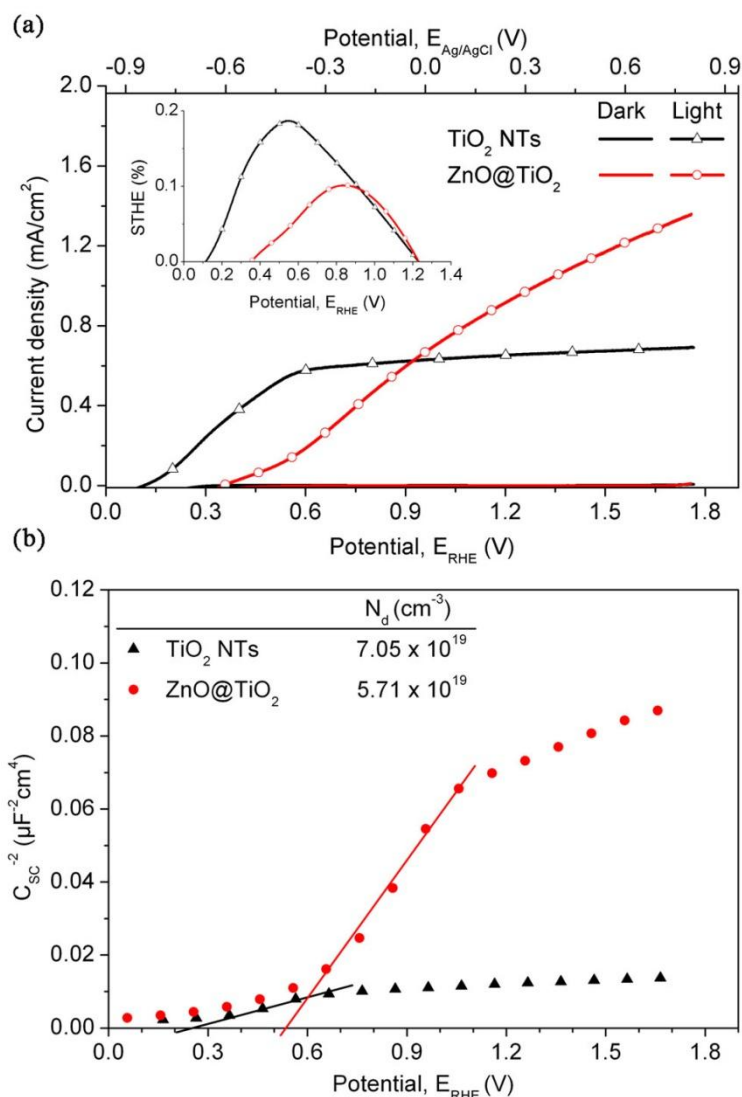


**Figure 3.7.** (a) LSV in the dark and under UV-Vis illumination (intensity of 220 mW/cm<sup>2</sup>), inset: STHE calculated from the data in (a). (b) Mott-Schottky plots of TiO<sub>2</sub> NTs (black triangles) and ZnO@TiO<sub>2</sub> core-shell structures (red circles)

These results, together with the ones reported in the previous sections 3.3 and 3.4, evidence the promising photo-electrochemical ability of both the TiO<sub>2</sub> NTs and ZnO@TiO<sub>2</sub> core-shell nanostructures. In addition, they indicate that different possible strategies for optimizing the solar-induced water splitting activity of these nanostructured photoelectrodes can be suggested. In particular:

- First, the main advantage of the TiO<sub>2</sub> NTs is the low flat-band potential, which allows obtaining high photo-currents with a reduced bias. This intrinsic property of the TiO<sub>2</sub> NTs contributes in obtaining high STHE with a low consumption of extra energy in the PEC water splitting system. The deposition of a co-catalysis could be for example

a key solution to improve the charge-carriers separation at the TiO<sub>2</sub> NTs-electrolyte interphase, which has been identified from our results to be the factor limiting their photocurrent. For example, the deposition of Pt nanoparticles in the top and walls of 10 μm-long TiO<sub>2</sub> nanotube arrays made by Lai et al. [39] yielded to an enhancement of the  $J$  from 16.3 to 24.2 mA/cm<sup>2</sup> in 2 M Na<sub>2</sub>CO<sub>3</sub> - ethylene glycol solution with 320 mW/cm<sup>2</sup> of simulated sunlight illumination. However, there are few examples in which low-cost and earth-abundant catalyst (e.g. Co-, Mn- or Cu-based materials) have been deposited on TiO<sub>2</sub> NTs [40]. Similarly, the deposition of a co-catalyst in the high available surface of the TiO<sub>2</sub> in the shell of the ZnO@TiO<sub>2</sub> electrode can be exploited to reduce its onset potential.

- Second, both the TiO<sub>2</sub> NTs and the core-shells can be prepared having different sizes and lengths with a low-cost process and in few synthesis steps. However, there are few examples in the literature of ZnO@TiO<sub>2</sub> electrodes prepared and tested for the PEC water oxidation [18, 41] and the ZnO NWs length is often < 2 μm. In contrast, the anodic oxidation process commonly used for the synthesis of the NTs renders easy the increase in their length and, thus, the enhancement of the active surface available for the reaction. It is important to point out that the results here reported with the ZnO@TiO<sub>2</sub> ( $J < 0.7$  mA/cm<sup>2</sup>) are in-line with or even more performing than some literature values obtained for both pure and doped ZnO NWs [42] and for 1D TiO<sub>2</sub>-ZnO nanostructures [25] tested under AM-1.5G sunlight. Even though, good performances have also been reached with other TiO<sub>2</sub>-based nanostructures: e.g. Pan *et al* reported 2 mA/cm<sup>2</sup> obtained with 2 - 4 μm-long hierarchical TiO<sub>2</sub> nanobelt/ZnO nanorod in 0.5 M Na<sub>2</sub>SO<sub>4</sub> (120 mW/cm<sup>2</sup>) and Wang *et al* [30] obtained ~ 2.8 mA/cm<sup>2</sup> with H<sub>2</sub>-treated rutile TiO<sub>2</sub> NWs (2-3 μm length). The latter was the most performing values reached with TiO<sub>2</sub> NWs. Instead, TiO<sub>2</sub> nanotube arrays with a length ranging from hundreds of nm up to 45 μm, with different aspect-ratios, were reported with even better results for the water photo-electrolysis [43-45]. For instance, Sun *et al* [43] reached 5 mA/cm<sup>2</sup> in KOH (110 mW/cm<sup>2</sup>) with TiO<sub>2</sub> NTs with an optimized length of 7 μm, made in 1 h of electrochemical anodization; Gong *et al* [44] prepared highly ordered TiO<sub>2</sub> nanotube arrays by a three-step electrochemical anodization process with a length up to 18 μm (i.d. 50 nm), and reached a maximum  $J$  of about 24 mA/cm<sup>2</sup> with the 1.2 μm-long sample in 0.5 M KOH.
- Third, the photo-catalytic properties of both the TiO<sub>2</sub> NTs and the ZnO@TiO<sub>2</sub> can be further enhanced by modifying their optical or surface properties [46]. In this regard,

one approach that has been often used is the doping (e.g. with C, N, S etc) or the creation of bilayered systems with low band-gap semiconductors (e.g. WO<sub>3</sub>, CdSe, CdS, etc) [46, 47], in order to enhance visible light absorption, charge separation and charge transport. Good examples are the C-doped TiO<sub>2</sub> NTs prepared by Park *et al* [48] (~ 2 μm length, i.d. 70 nm) obtaining a *J* close to 1 mA/cm<sup>2</sup>, or the TiO<sub>2-x</sub>C<sub>x</sub> nanotubes annealed in H<sub>2</sub> atmosphere by Monhapatra *et al* [49] reaching about 3 mA/cm<sup>2</sup>, both under sunlight conditions in 1M KOH electrolyte. Nonetheless, really impressive results were recently reported by combining the use of heterostructures with high visible light absorber and concentrated sunlight. For instance, Qorbani *et al* [37] made CdS-sensitized TiO<sub>2</sub> NTs (2.9 μm length, 125 nm i.d.) yielding up to 28 mA/cm<sup>2</sup> with an illumination of 4 suns (400 mW/cm<sup>2</sup>), and Li *et al* [50] prepared ZnO/CuS and ZnO/CuInS<sub>2</sub> core/shell nanorod arrays producing about 8 and 16.9 mA/cm<sup>2</sup>, respectively, by using 5 suns of incident light and Na<sub>2</sub>S electrolyte.

- Finally, as shown in the Figure 3.7a and discussed above, the illumination with concentrated light is an operative condition that could really mark the difference for the performance of a TiO<sub>2</sub>- or ZnO- based device, due not only to the high amount photo-generated holes that can enhance the inherent activity of these materials, but also to the low-cost availability of solutions to produce concentrated light (*i.e.* through the use of polymeric Fresnel lens).

### 3.4. Conclusions

Four TiO<sub>2</sub> and ZnO – based nanostructures, having the same active area and similar thicknesses, were deeply characterized and compared in terms of their structural and photo-electrochemical properties. FESEM and TEM analysis evidenced the structural differences and the high degree of crystallinity of the various materials. Optical measurements allowed to evaluate the energy gap values and to appreciate the occurrence of scattering effects due to the high surface area of the different structures coupled with their characteristic dimensions. Photo-electrochemical activity measurements and electrochemical impedance spectroscopy analysis showed an improvement in charge collection efficiency of 1D-nanostructures, related to a more efficient electron transport in the materials. The highest photocurrent density and photo-conversion efficiency in our system were obtained with the ZnO@TiO<sub>2</sub> core-shells and with the TiO<sub>2</sub> NTs. The core-shell heterostructured material reached up to 0.63 mA/cm<sup>2</sup> at 1.7 V<sub>RHE</sub> and had a maximum STHE of 0.073 % (at 0.9 V<sub>RHE</sub>) under sunlight illumination of AM1.5G (100 mW/cm<sup>2</sup>), thus being the best performance ever reported for

ZnO@TiO<sub>2</sub> for this application. In addition, the TiO<sub>2</sub> NTs attained a saturation photocurrent of 0.12 mA/cm<sup>2</sup> from about 0.5 V<sub>RHE</sub>, potential at which yielded a maximum STHE of 0.071 %, similar to what obtained with the core-shell sample under the same operative conditions but at a lower applied bias. EIS analysis evidenced that the TiO<sub>2</sub> NPs exhibited time constants 4 times larger with respect to the NTs-based photoelectrode, which justified the worse performance of the 3D NPs nanostructure with respect to the 1D TiO<sub>2</sub> NTs. Moreover, the increase of the charge-carrier recombination at the TiO<sub>2</sub>-electrolyte interphase in the TiO<sub>2</sub> NTs with the applied potential indicated a reduction of the e<sup>-</sup>/h<sup>+</sup> separation efficiency in this polycrystalline TiO<sub>2</sub> material, explaining the reason for the photocurrent saturation. Therefore, the charge transfer time constant obtained for the TiO<sub>2</sub> NTs was 10-fold larger than in the core-shells, for all the range of applied potentials: this occurrence was identified as the main responsible for the lower photo-currents of the TiO<sub>2</sub> NTs with respect to the core-shell material at high bias. In contrast, the enhanced performance of the core-shell samples was attributed to the high electron mobility within the monocrystalline 1D ZnO nanostructure (*i.e.* five-times lower  $\tau_{dl}$  value if compared to the bare nanowires due to the efficient separation of charge-carriers at the ZnO@TiO<sub>2</sub> interphase) coupled to the high specific surface area of the TiO<sub>2</sub> polycrystalline shell, which fasten of about 13% the charge-transport and thus the kinetics for the water photo-electrolysis in this material with respect to the bare ZnO NWs. In conclusion, the efficient application of both the TiO<sub>2</sub> NTs and the ZnO@TiO<sub>2</sub> core-shell photoanodes opens important perspectives, not only in the water splitting application field, but also for other photo-catalytic applications (e.g. photovoltaic cells, degradation of organic substances), due to their chemical stability, easiness of preparation and improved transport properties. Different optimization strategies (*i.e.* co-catalysis, surface modifications to adsorb visible light, increase of thickness, use of concentrated solar light) were identified for each of the studied materials in order to increase their effectiveness and to achieve the efficiency values required for commercial applications.

### 3.5. References

- [1] A. Fujishima, K. Honda, Nature, 238 (1972) 37-38.
- [2] A.A. Ismail, D.W. Bahnemann, Solar Energy Materials and Solar Cells, 128 (2014) 85-101.
- [3] J.R. McKone, N.S. Lewis, H.B. Gray, Chemistry of Materials, 26 (2013) 407-414.
- [4] A.L. Linsebigler, G. Lu, J.T. Yates, Chemical Reviews, 95 (1995) 735-758.
- [5] M. Gratzel, Nature, 414 (2001) 338-344.

- [6] C. Bauer, G. Boschloo, E. Mukhtar, A. Hagfeldt, *The Journal of Physical Chemistry B*, 105 (2001) 5585-5588.
- [7] D. Fattakhova-Rohlfing, A. Zaleska, T. Bein, *Chemical Reviews*, doi: 10.1021/cr500201c (2014).
- [8] C. Xiaobo, S.M. Samuel, *Chem Rev*, 107 (2007) 2891-2959.
- [9] T.P. Chou, Q. Zhang, G. Cao, *The Journal of Physical Chemistry C*, 111 (2007) 18804-18811.
- [10] T. Zhao, Y. Zhao, L. Jiang, *Philosophical Transactions of the Royal Society A: Mathematical, Physical and Engineering Sciences*, 371 (2013) 20130263.
- [11] A. Wolcott, J.Z. Zhang, *Multidimensional Nanostructures for Solar Water Splitting: Synthesis, Properties, and Applications*, in: *On Solar Hydrogen & Nanotechnology*, John Wiley & Sons, Ltd, 2010, pp. 459-505.
- [12] G. Wang, Y. Ling, H. Wang, L. Xihong, Y. Li, *Journal of Photochemistry and Photobiology C: Photochemistry Reviews*, 19 (2014) 35-51.
- [13] C. Xu, Y. Song, L. Lu, C. Cheng, D. Liu, X. Fang, X. Chen, X. Zhu, D. Li, *Nanoscale Research Letters*, 8 (2013) 391.
- [14] D. Chen, H. Zhang, S. Hu, J. Li, *The Journal of Physical Chemistry C*, 112 (2007) 117-122.
- [15] D. Hidalgo, R. Messina, A. Sacco, D. Manfredi, S. Vankova, E. Garrone, G. Saracco, S. Hernández, *International Journal of Hydrogen Energy*, doi: 10.1016/j.ijhydene.2014.02.163 (2014).
- [16] A. Lamberti, A. Sacco, S. Bianco, D. Manfredi, M. Armandi, M. Quaglio, E. Tresso, C.F. Pirri, *Solar Energy*, 95 (2013) 90-98.
- [17] V. Farías Rivera, F. Auras, P. Motto, S. Stassi, G. Canavese, E. Celasco, T. Bein, B. Onida, V. Cauda, *Chemistry – A European Journal*, 19 (2013) 14665-14674.
- [18] S. Hernández, V. Cauda, A. Chiodoni, S. Dallorto, A. Sacco, D. Hidalgo, E. Celasco, C.F. Pirri, *ACS Applied Materials & Interfaces*, 6 (2014) 12153–12167.
- [19] S. Hernández, V. Cauda, D. Hidalgo, V. Farías Rivera, D. Manfredi, A. Chiodoni, F.C. Pirri, *Journal of Alloys and Compounds*, 615 (2014) S530 – S537.
- [20] A. Lamberti, A. Sacco, S. Bianco, D. Manfredi, F. Cappelluti, S. Hernandez, M. Quaglio, C.F. Pirri, *Physical Chemistry Chemical Physics*, 15 (2013) 2596-2602.
- [21] J.J. Kelly, Z. Hens, D. Vanmaekelbergh, Z. Hensalso, *Photoelectrochemical Systems Characterization*, in: *Encyclopedia of Electrochemistry*, Wiley-VCH Verlag GmbH & Co. KGaA, 2007.

- [22] Z. Zhang, P. Wang, *Energy & Environmental Science*, 5 (2012) 6506-6512.
- [23] A. Lamberti, A. Sacco, D. Hidalgo, S. Bianco, D. Manfredi, M. Quaglio, E. Tresso, C.F. Pirri, *Acta Physica Polonica, A.*, 123 (2013) 376.
- [24] X. Yang, A. Wolcott, G. Wang, A. Sobo, R.C. Fitzmorris, F. Qian, J.Z. Zhang, Y. Li, *Nano Letters*, 9 (2009) 2331-2336.
- [25] I.A. Ji, M.-J. Park, J.-Y. Jung, M.J. Choi, Y.-W. Lee, J.-H. Lee, J.H. Bang, *Bull. Korean Chem. Soc*, 33 (2012) 2201.
- [26] K.-S. Ahn, Y. Yan, S. Shet, K. Jones, T. Deutsch, J. Turner, M. Al-Jassim, *Applied Physics Letters*, 93 (2008) -.
- [27] S. Hoang, S. Guo, N.T. Hahn, A.J. Bard, C.B. Mullins, *Nano Letters*, 12 (2011) 26-32.
- [28] Y. Myung, D.M. Jang, T.K. Sung, Y.J. Sohn, G.B. Jung, Y.J. Cho, H.S. Kim, J. Park, *Acs Nano*, 4 (2010) 3789-3800.
- [29] G. Wang, X. Yang, F. Qian, J.Z. Zhang, Y. Li, *Nano Letters*, 10 (2010) 1088-1092.
- [30] G. Wang, H. Wang, Y. Ling, Y. Tang, X. Yang, R.C. Fitzmorris, C. Wang, J.Z. Zhang, Y. Li, *Nano Letters*, 11 (2011) 3026-3033.
- [31] K. Rajeshwar, *Encyclopedia of electrochemistry*, (2002).
- [32] C. Xu, J. Wu, U.V. Desai, D. Gao, *Nano Letters*, 12 (2012) 2420-2424.
- [33] J. Newman, P.G. Hoertz, C.A. Bonino, J.A. Trainham, *Journal of The Electrochemical Society*, 159 (2012) A1722-A1729.
- [34] I. Gonzalez-Valls, M. Lira-Cantu, *Energy Environ. Sci.*, 2 (2009) 19-34.
- [35] M.-S. Lee, I.-C. Cheon, Y.-I. Kim, *Bulletin of the Korean Chemical Society*, 24 (2003) 1155-1162.
- [36] W.H. Leng, P.R.F. Barnes, M. Juozapavicius, B.C. O'Regan, J.R. Durrant, *The Journal of Physical Chemistry Letters*, 1 (2010) 967-972.
- [37] M. Qorbani, N. Naseri, O. Moradlou, R. Azimirad, A.Z. Moshfegh, *Applied Catalysis B: Environmental*, 162 (2015) 210-216.
- [38] I. Mora-Seró, F. Fabregat-Santiago, B. Denier, J. Bisquert, R. Tena-Zaera, J. Elias, C. Lévy-Clément, *Applied Physics Letters*, 89 (2006) 203117-203117-203113.
- [39] Y. Lai, J. Gong, C. Lin, *International Journal of Hydrogen Energy*, 37 (2012) 6438-6446.
- [40] G. Dai, S. Liu, Y. Liang, T. Luo, *Applied Surface Science*, 264 (2013) 157-161.
- [41] J. Fan, R. Zamani, C. Fábrega, A. Shavel, C. Flox, M. Ibáñez, T. Andreu, A. López, M., J. Arbiol, J.R. Morante, A. Cabot, *J. Phys. D: Appl. Phys.*, 45 (2012) 415301.

- [42] X. Yang, A. Wolcott, G. Wang, A. Sobo, R.C. Fitzmorris, F. Qian, J.Z. Zhang, Y. Li, *Nano Lett.*, 9 (2009) 2331-2336.
- [43] Y. Sun, G. Wang, K. Yan, *International Journal of Hydrogen Energy*, 36 (2011) 15502-15508.
- [44] J. Gong, Y. Lai, C. Lin, *Electrochimica Acta*, 55 (2010) 4776-4782.
- [45] Z. Zhang, M.F. Hossain, T. Takahashi, *International Journal of Hydrogen Energy*, 35 (2010) 8528-8535.
- [46] S. Choudhary, S. Upadhyay, P. Kumar, N. Singh, V.R. Satsangi, R. Shrivastav, S. Dass, *International Journal of Hydrogen Energy*, 37 (2012) 18713-18730.
- [47] K.R. Reyes-Gil, D.B. Robinson, *ACS Applied Materials & Interfaces*, 5 (2013) 12400-12410.
- [48] J.H. Park, S. Kim, A.J. Bard, *Nano Letters*, 6 (2005) 24-28.
- [49] S.K. Mohapatra, M. Misra, V.K. Mahajan, K.S. Raja, *The Journal of Physical Chemistry C*, 111 (2007) 8677-8685.
- [50] Y. Li, Z. Liu, Y. Wang, Z. Liu, J. Han, J. Ya, *International Journal of Hydrogen Energy*, 37 (2012) 15029-15037.

## Chapter 4

### Enhanced performance of PANI-TiO<sub>2</sub> nanocomposite mesoporous films for sun-driven water splitting

#### 4.1. Introduction

Photochemical and photoelectrochemical (PEC) water splitting have been widely investigated in the last decades as a means of converting solar to chemical energy in the form of fuels. Hydrogen is a key solar fuel since it can be used directly in PEM fuel cells or combustion engines, or combined catalytically with CO<sub>2</sub> to make carbon containing fuels [1].

Different semiconductors (e.g. ZnO, Fe<sub>2</sub>O<sub>3</sub>, BiVO<sub>4</sub>, WO<sub>3</sub>) have been reported for the sun-driven water photoelectrolysis [2]. However, the interest on the application of the TiO<sub>2</sub> as water splitting photocatalyst and for other uses (e.g. photodegradation of contaminants, photovoltaics, electrical energy storage, paint pigments, etc.) is still high, due to its non-toxicity, abundance, low-cost, good stability, excellent photocatalytic performance, easy availability and possibility to structure at the nano- and micro-scales [3]. Indeed, several recent reviews deal with the general approaches toward the fabrication of 3D-titania morphologies, [2, 4-6] with a particular interest in porous titania materials [7-11] porous spheres [12, 13], shells [14], nanosheets [15], nanorods [16], fibers [17], and nanotubes [18-20], are focused on various applications of 3D-titania materials in solar cells [13, 21], photocatalysis and photoelectrochemistry [22-26] or electrochemical energy storage [11]. Nevertheless, the disadvantages of TiO<sub>2</sub> with respect to its application as water oxidation photocatalyst are its limited absorption of solar light (wavelengths below ~ 380 nm) due to its large bandgap (3.20 eV), and its reduced photocatalytic activity because of the fast recombination of charge carriers [27]. Efforts to overcome such issues have been made by modifying TiO<sub>2</sub> with methods such as metal and non-metal doping [23], noble metal deposition [28], forming composites with both narrow band gap inorganic semiconductors or through dye sensitization [4, 26]. Regarding the last approach, in order to warranty a good electron/hole transfer, the conduction band (CB) and valence band (VB) of the semiconductor (or the highest occupied molecular orbital (HOMO) and the lowest unoccupied molecular orbital (LUMO) of the dye) must have at a higher energy level than the ones of the TiO<sub>2</sub>. There a few inorganic materials satisfying such requirements (e.g. CdS [29], Fe<sub>2</sub>O<sub>3</sub> [30]), which in some cases have stability issues, and the application of dye-sensitized TiO<sub>2</sub> is

restricted due to the employment of noble-metal-containing dyes (e.g. Ru-, Rh- or Pd-containing dyes) or because of dissolution and degradation of dyes during photocatalytic processes [31-33].

In recent years, polymers with extended  $\pi$ -conjugated electron systems have attracted considerable attention because of their absorption coefficients in the visible region and high conductivity, allowing high mobility of charge carriers. Among conductive polymer, polyaniline (PANI) have been widely used to improve electronic conductivity as well as solar energy transfer and photocatalytic activity of  $\text{TiO}_2$ , due to its easiness of preparation and excellent environmental stability. A high number of works exploit the role of PANI- $\text{TiO}_2$  composites for photocatalytic degradation or organic matrix [28, 31, 34-38] or for photovoltaic solar cells [39]. On the other hand, there are some examples of PANI combined with other semiconductors for  $\text{H}_2$  generation, such as the case of PANI-CdS composite nanoparticles synthesized by He et al. [40] for direct  $\text{H}_2$  evolution in the presence of  $\text{SO}_3^{2-}/\text{S}^{2-}$  sacrificial reactant. Nevertheless, there are few examples of PANI-semiconductor based photoelectrodes tested for the PEC water splitting reaction. Only recently, Jing et al. [27] reported on a ternary polyaniline-graphene- $\text{TiO}_2$  hybrids for water oxidation in  $\text{Na}_2\text{SO}_4$  (pH=7) electrolyte under visible light illumination generating up to  $10 \mu\text{A}/\text{cm}^2$  at 0.8 V vs. SCE ( $\sim 1.4$  V vs. RHE).

From a chemical point of view, PANI can be considered as being derived from two different repeating units, which are alternatively reduced and oxidized, whose base form is given in Figure 4.1 [41-43]. The average oxidation state can be varied continuously, as indicated in the Figure 1, where  $y = 1$  is the completely reduced polymer,  $y = 0.5$  the “half-oxidized” polymer,  $y = 0$  the completely oxidized polymer (Figure 4.1b to 4.1d). As inferred from the generalized formula of PANI (Figure 4.1a), the polymer could in principle exist in a continuum of oxidation states ranging from the completely reduced ( $y = 1$ ) to the completely oxidized material in the pernigraniline oxidation state ( $y = 0$ ). However, at the solid state, in the range  $y = 1$  to  $y = 0.5$  only the two chromophores characteristic of  $y = 1$  and  $y = 0.5$  species are present, thus at the molecular level all intermediate oxidation states consist of mixtures of the chromophores characteristic of these two states [41, 44]. The same phenomenon is true in the  $y = 0.5$  to  $y = 0$  oxidation state range [45, 46]. At the molecular level all intermediate oxidation states consist only of mixtures of the chromophores characteristic of the two states defining the beginning and end of each range. The terms leucoemeraldine, emeraldine and pernigraniline refer to the oxidation states where  $y = 1, 0.5$

and 0 respectively, either in the base form, or in the protonated salt form [41, 43]. The differences in oxidation states are obtained by the formal oxidation of the carbons directly linked to the nitrogen atoms in the main chain. The difference between leucoemeraldine and emeraldine is of two electrons every four aniline monomers. The same result can be obtained for the difference between emeraldine and pernigraniline.

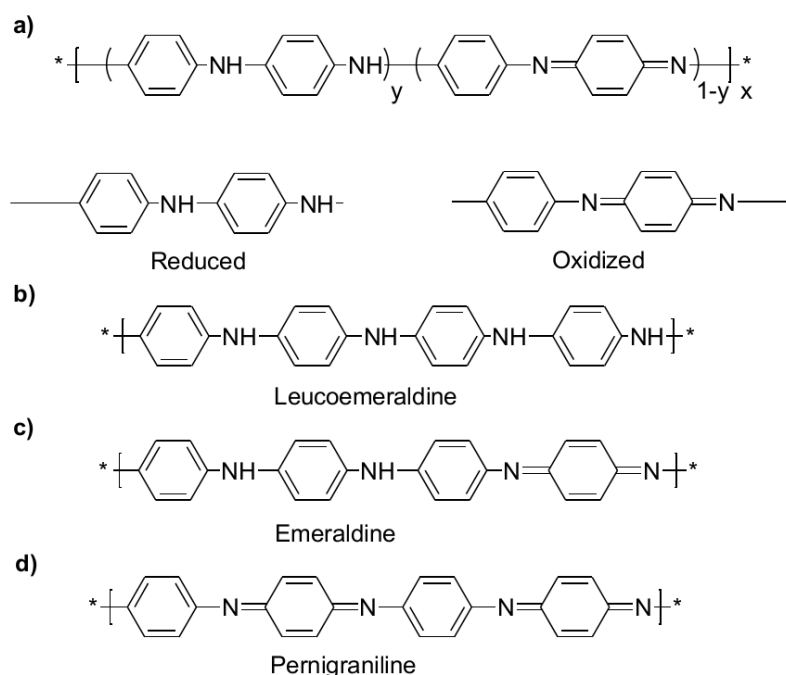


**Figure 4.1.** Generalized composition of polyanilines indicating the reduced and oxidized repeating units (a), the completely reduced polymer (b), the half-oxidized polymer (c) and the fully oxidized polymer (d). Reproduced from [48]

Of the different oxidation states of PANI only emeraldine was proved to be electrical conductive, the mechanism of doping is linked to the protonation of the emeraldine form that is called basic form or emeraldine base (EB). In principle, the imine nitrogen atoms can be protonated in whole or in part to give the corresponding salts (Figure 4.2a and 4.2b), the degree of protonation of the polymeric base depending on its oxidation state and on the pH of the aqueous acid, because complete protonation of the imine nitrogen atoms in EB results in the formation of a delocalized polysemiquinone radical cation [42, 43, 47] (Figure 4.2c and 4.2d) and is accompanied by an increase in conductivity of about ten orders of magnitude. The partly protonated emeraldine salt can be synthesized easily either by the chemical or electrochemical oxidative polymerization of aniline [41, 43]. It can be deprotonated by aqueous ammonium hydroxide to give emeraldine base powder (a semiconductor).

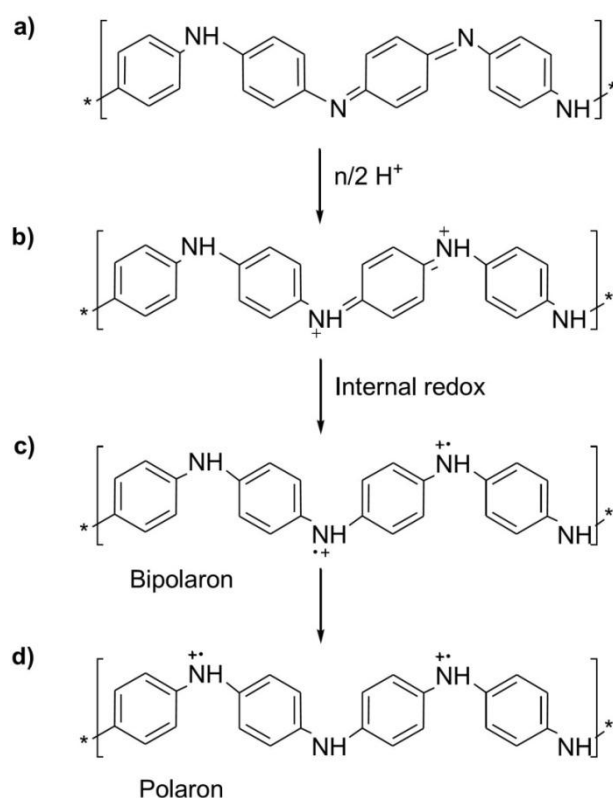


**Figure 4.2.** PANI Emeraldine base before protonation (a), after 50% protonation (b) and formation of bipolaron (c) and polaron (d) forms. Reproduced from [48]

In the available literature different ways to produce PANI have been demonstrated, however, aniline is classically chosen as the starting monomer. In previous works, which have been conducted by different research group at Istituto Italiano di Tecnologia [49, 50], a method to produce polyaniline in the EB form starting from the aniline dimer (DANI), which on the contrary to aniline is non-toxic and low-cost was developed. Such method produces PANI soluble in organic solvents, which thus can be used to functionalize other materials (e.g. titanium oxide) by drop casting and impregnation, among other techniques.

In this Chapter the main contribution was the use of PANI to increase the photocatalytic response of the development  $\text{TiO}_2$  NPs films previously described in Chapter 2. This Chapter reports for the first time the synthesis of PANI- $\text{TiO}_2$  nanocomposite mesoporous films prepared through a fast, safe, low cost and environmentally friendly technique that employs DANI as the PANI precursor [49, 50]. On difference with other methods [51], a 3D mesoporous  $\text{TiO}_2$  nanoparticles film supported on fluorine-doped Tin Oxide (FTO) was impregnated in a solution of PANI, obtaining the uniform coverage of the mesoporous

substrate after only ten minutes. The PANI-TiO<sub>2</sub> nanocomposites were fully characterized in their physico-chemical characteristics, and PEC behavior for the water splitting reaction under simulated solar light (AM 1.5G). UV-Vis spectroscopy and Incident-Photon-Current-Efficiency (IPCE) measurements were used to identify the principal parameters playing a role in the enhanced performance of the PANI-modified films with respect to the TiO<sub>2</sub> ones. The obtained results were analyzed in comparison with the existing literature regarding PANI-TiO<sub>2</sub> composites for different photocatalytic applications.

The results of this research are part of the publication entitled: “Enhanced performance of PANI-TiO<sub>2</sub> nanocomposite mesoporous films for sun-driven water splitting”. D. Hidalgo, S. Bocchini, M. Fontana, F. C. Pirri, G. Saracco, S. Hernández. (2015) Energy. Submitted.

## **4.2. Experimental**

### **4.2.1. Sol-gel synthesis and deposition of TiO<sub>2</sub> nanoparticles**

Titanium (IV) isopropoxide (TTIP, 97 %), glacial acetic acid (99.7 %) and Tween 20, all from Sigma Aldrich, were used as purchased for the preparation of the sol of TiO<sub>2</sub> nanoparticles. The synthesis procedure used to obtain the nano-TiO<sub>2</sub> sol is as follows: TTIP, glacial acetic acid and water were maintained in molar ratios 1:10:300 [7], whereas a molar ratio (R) between Tween 20/TTIP of 0.5/1 was used. Firstly, the TTIP was hydrolyzed into the glacial acetic acid and then, surfactant Tween 20 was added under vigorous stirring. Subsequently, the mixture was added drop wise into the DI-water and the final solution was aged under continuous stirring for 48 h at ambient temperature. Then, the TiO<sub>2</sub> sol was treated in a rotary evaporator at 40 °C for 2 h under vacuum. The final solution was homogeneous and stable for weeks and it was used to the preparation of TiO<sub>2</sub> nanoparticles (NPs) films. TiO<sub>2</sub> films were supported into fluorine-doped tin oxide glass (FTO, 7 Ω/sq) substrates in an effective surface area of 4 cm<sup>2</sup>. First, the support was cleaned in acetone using an ultrasonic bath and then rinsed with ethanol. A “piranha” solution 3:1 (Sulfuric Acid: Hydrogen Peroxide) was then employed to remove organic residues on the surface. The concentrated TiO<sub>2</sub> solution, obtained after the rotary evaporator treatment, was spin-coated with a spinner model Spin 150 by using a program in two steps: 1500 rpm for 10s followed by 3000 rpm for 10s. Finally, TiO<sub>2</sub> films were annealed in a programmable furnace at 500 °C for 15 min in air, using a heating rate of 1 °C/min, and were cooled down naturally. Further details of the characterization of the TiO<sub>2</sub> films are described in Chapter 2.

#### **4.2.2. Polyaniline synthesis**

N-phenyl-1,4-phenyldiamine 98 %, that is the aniline dimer (DANI), poly(sodium 4-styrenesulfonate) (PSS), ammonium persulfate (APS) 98 %, sodium persulfate (SPS) 98 %, hydrochloric acid 37 wt%, dimethylsulfoxide (DMSO) 99.9 % and dimethylformamide (DMF) were purchased from Aldrich and used as received.

The synthesis of PANI PSS-doped was already presented elsewhere by Bocchini et al. [49]. 40 ml of a solution of DANI (4 mmol, 0.9212 g) in DMSO was added drop by drop to 360 mL of a solution of PSS (0.915 g) in HCl 0.1 M. APS (5 mmol, 1.141 g) dissolved in 100 mL of HCl 0.1 M was poured slowly. After 3 hours, the precipitate was filtered and washed several times with distilled water. The product was a green powder. The product was firstly separated by filtration, then washed with both double distilled water and ethanol, and finally dried at 60 °C until constant weight.

#### **4.2.3. Deposition of polyaniline on TiO<sub>2</sub> films**

PANI was deposited in the TiO<sub>2</sub> films by impregnation method. The PANI was dispersed in DMSO at the concentration of 2 wt% (instead different stated) by alternative mechanical mixing and ultrasonication. Just before to use the PANI solution, it was ultrasonicated for one hour in order to re-disperse it. The TiO<sub>2</sub> film was dipped into the PANI solution and then removed after 10 min of impregnation. Finally, PANI/TiO<sub>2</sub> composites films were dried at 80 °C under vacuum for 24 h to remove all the residual DMSO. Oxidized PANI/TiO<sub>2</sub> (PANIO<sub>x</sub>/TiO<sub>2</sub>) was obtained by immersion of the previous produced PANI/TiO<sub>2</sub> in a solution 0.018 M of SPS in water for 1 h.

#### **4.2.4. Materials and characterization**

X-ray diffraction (XRD) analysis was performed by using a X-ray diffractometer Cu-K $\alpha$  x-ray tube ( $\lambda=1.54 \text{ \AA}$ ) with an accelerating voltage of 40 KV, in order to determine the crystal structure and crystallinity of the TiO<sub>2</sub> particles. Field Emission Scanning Electron Microscope (FESEM) examinations were performed with a Zeiss SupraTM 40 equipped with Energy Dispersive Spectroscopy (EDS, Inca XSight; Oxford Instrument). Attenuated Total Reflectance (ATR) spectra were collected on a Nicolet 5700 FTIR Spectrometer (ThermoFisher) equipped with a ZnSe single crystal. A spectrophotometer model Cary 500 by Varian was used to obtain the transmittance spectra of the samples, which were recorded in the wavelength range of 300 - 800 nm at room temperature.

#### 4.2.5. Photoelectrochemical tests of TiO<sub>2</sub> and PANI-TiO<sub>2</sub> composites films

The PEC experiments were performed in a glass reactor equipped with a quartz window for frontal illumination [7]. All the tests were carried out in a three electrodes configuration using the TiO<sub>2</sub> NPs, PANI/TiO<sub>2</sub> and PANI<sub>ox</sub>/TiO<sub>2</sub> nanocomposite films as the working electrodes for the water photo-electrolysis reaction, a platinum wire as the counter electrode, and an Ag/AgCl (KCl 3 M) as the reference electrode, in 0.1 M NaOH aqueous electrolyte (pH = 12.7). The electrochemical measurements were performed using a multi-channel VSP potentiostat/galvanostat (by BioLogic), with EC-Lab<sup>®</sup> software (version 10.1x) for data acquisition. The current-voltage (*I-V*) characteristic curves were recorded by means of Linear Sweep Voltammetry (LSV) at a scan rate of 10 mV/s, when a constant open circuit voltage was achieved, varying the applied potential from -0.7 V to 0.7 V vs. Ag/AgCl, in the dark and under simulated sunlight (using a 450 W Xe lamp by Newport with an AM 1.5G filter and a water filter model 6123NS) using a power density of 100 mW/cm<sup>2</sup>. The irradiance was measured by means of a Delta Ohm Photo-radiometer model HD2102.1. Chronoamperometric (*I-t*) tests were carried out to examine the photo-response of the nanostructures over time at -0.1 V vs. Ag/AgCl (0.86 V<sub>RHE</sub>) under continuous ON-OFF light cycles, with the same illumination condition used for the LSV. The measured potentials versus the Ag/AgCl reference electrode were converted to the reversible hydrogen electrode (RHE) scale via the Nernst Equation (1):

$$E_{RHE} = E_{Ag/AgCl} + 0.059 \cdot pH + E_{Ag/AgCl}^{\circ} \quad (1)$$

where  $E_{RHE}$  is the converted potential (V vs. RHE),  $E_{Ag/AgCl}$  is the experimental potential measured against the Ag/AgCl reference electrode (V vs. Ag/AgCl), and  $E_{Ag/AgCl}^{\circ}$  is the standard potential of Ag/AgCl (KCl 3 M) at 25 °C (*i.e.* 0.21 V). Incident photon-to-electron conversion efficiency (IPCE) spectra were recorded using a Newport Xe lamp (150 W) coupled to a monochromator (Cornestone 130 by Newport), by varying the wavelength of the incident light from 300 nm to 550 nm (step size: 10 nm), at an applied potential of 0.26 V vs. Ag/AgCl (1.23 V vs. RHE). In this case, the electrode illuminated area was 1 cm<sup>2</sup> and the light power density was about 1 mW/cm<sup>2</sup> (measured at 390 nm).

### 4.3. Results and discussion

#### 4.3.1. Physico-chemical characterization of TiO<sub>2</sub> and PANI-TiO<sub>2</sub> films

X-ray diffraction spectra of TiO<sub>2</sub> film is illustrated in Figure 4.3. In this figure is reported the film prepared with 1 spin coating layers using a molar ratio between Tween 20/TTIP of 0.50/1 in the sol. The XRD patterns present obvious peak at 25.4° (101) and 47.7° (200), corresponding to the anatase phase which is the mainly used for photocatalytic applications [7, 34]. From XRD, it was also observed that the diffraction pattern of the PANI/TiO<sub>2</sub> and PANIox/TiO<sub>2</sub> nanocomposite films is the same as TiO<sub>2</sub> NPs film as shown in Figure 4.3. This results means the PANI deposited has no influence on crystallinity of the TiO<sub>2</sub> NPs film.

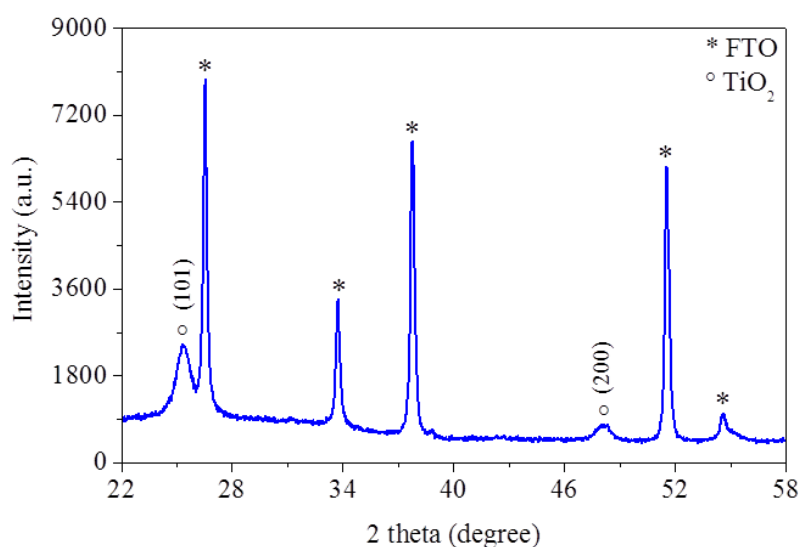


**Figure 4.3.** XRD spectra for immobilized TiO<sub>2</sub> films calcined at 500°C

FESEM analysis was used to investigate the morphology and the adhesion of the TiO<sub>2</sub> nanoparticles in the substrate. The estimated TiO<sub>2</sub> film thickness was measured in cross section as shown in Figure 4.4a, which showing TiO<sub>2</sub> films with a thickness of about 530 nm. As shown on Figure 4.4b, the crystallites of TiO<sub>2</sub> films exhibited a nearly round shape with an average crystal size around 7 - 8 nm. Through the incorporation of Tween 20, the prepared transparent TiO<sub>2</sub> films were very reproducible, homogeneous and crack-free, with a mesoporous structure [7]. Figures 4.4c and 2d showed the surface coating of PANI/TiO<sub>2</sub> and PANIox/TiO<sub>2</sub> nanocomposite films, respectively. There were almost no significant changes with respect to TiO<sub>2</sub> NPs films, which suggested that PANI layer on the TiO<sub>2</sub> was very thin. The rough and mesoporous structure of the samples exhibit a high active surface area, which have been demonstrated to be beneficial for photocatalytic reactions (Chapter 2) [7].

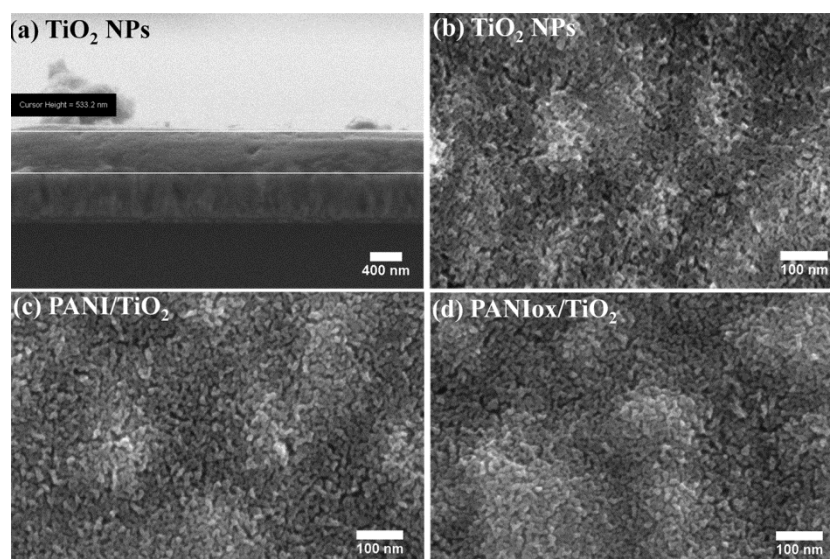


**Figure 4.4.** FESEM images of TiO<sub>2</sub> film in cross-section (a) and top view (b), of PANI/TiO<sub>2</sub> (c) and PANIox/TiO<sub>2</sub> (d) films in top view

The experimental FT-IR spectrum in ATR mode of both the TiO<sub>2</sub> film and the PANI-TiO<sub>2</sub> films before and after preliminary oxidation are reported in Figure 4.5. Due to the low signal obtained on ATR with the TiO<sub>2</sub> films impregnated in 2 wt% of PANI solution, the FT-IR spectra reported in Figure 4.5 correspond to TiO<sub>2</sub> films impregnated with a 10 wt% PANI solution, which were used only for characterization purposes. These spectra confirm the successful modification of the TiO<sub>2</sub> films through the PANI impregnation and allow the analysis of PANI oxidation state.

The TiO<sub>2</sub> is well identified by two main absorbance peaks in the (OH) stretching region (3100–4000 cm<sup>-1</sup>). The broad band at 3400 cm<sup>-1</sup> is associated with weakly bonded hydroxyl groups, instead absorbance peak at 3745 cm<sup>-1</sup> is characteristic of non-hydrogen bonded hydroxyl groups [52]. The other band with a maximum at 818 cm<sup>-1</sup> is associated to vibration of bulk TiO<sub>2</sub> skeletal frequency region [41].

In addition, the spectra of PANI and oxidized PANI deposited on TiO<sub>2</sub> are well distinguishable but practically super-imposable, thus meaning that the oxidation process does not degrade the skeletal structure of PANI. On the other hand, it is quite difficult to discriminate between the different oxidation states of PANI using infrared analyses. Both spectra present the absorbances already described for TiO<sub>2</sub>. The 1308 cm<sup>-1</sup> band is a fingerprint associated with the C-N stretching typical of PANI [42]. In both spectra the PANI exhibits a band at 1567 cm<sup>-1</sup> attributed to C=N stretching of quinoid diimine unit (the oxidised form of PANI). C-C aromatic ring stretching of the benzenoid diamine unit (the reduced form of PANI) appears at

1494  $\text{cm}^{-1}$  [53]. Based on previous reports, the intensities presented by these two bands should identify the oxidation state of PANI [51] the intensity ratio of these two absorption bands is indicative of the extent of oxidation state of the polymer, which evidence the content of the quinoid diimine and benzene ring structure. The ratio is calculated as following: R (intensity ratio) =  $(I_{\text{quinoid}}) / (I_{\text{benzenoid}})$ , where I is absorption intensity, obviously the higher is the ratio the higher is oxidation number. In our case R is equals to 0.6 for the PANI/TiO<sub>2</sub> sample and 0.65 for the PANIOx/TiO<sub>2</sub> film, thus indicating a partial transformation from emeraldine form to pernigraniline form after the pre-oxidation of the sample. This finding is supported by the fact that the PANI/TiO<sub>2</sub> changed its color from green (typical of emeraldine salt) to violet (distinctive of penigraniline form of PANI) after oxidation. In such case it can be supposed that pernigraniline is in the base form, mainly because it is stable only in really acidic conditions (e.g. at pH near to 0) [54]. Although this analysis is only qualitative because this method have been used and checked only for the absorbance of FT-IR in transmittance mode, it could provide a good approximation for the analysis of the ATR infrared spectra for comparative purposes.

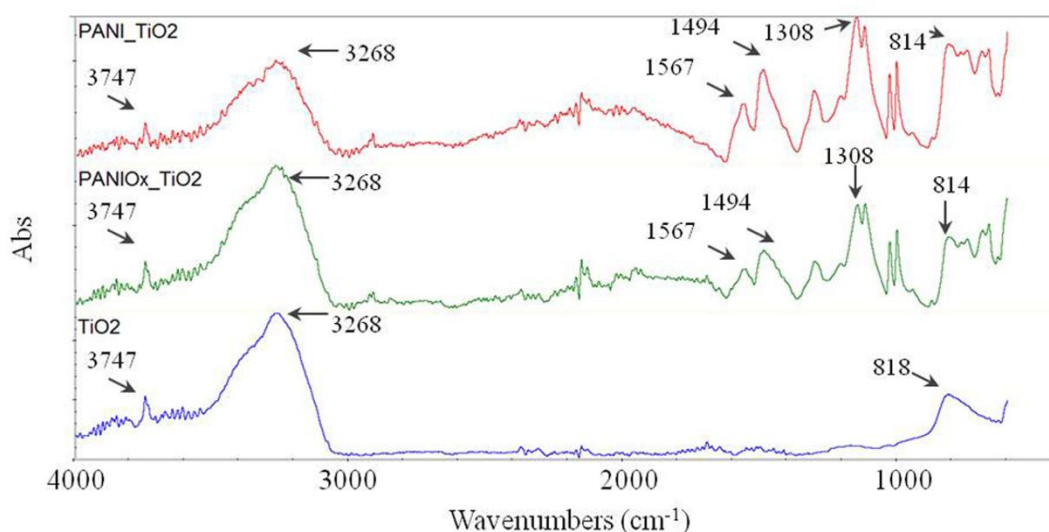


**Figure 4.5.** ATR infrared spectra of TiO<sub>2</sub> and PANI-TiO<sub>2</sub> films

#### 4.3.2. Photoelectrochemical characterization of TiO<sub>2</sub> and PANI-TiO<sub>2</sub> films

The PEC behavior of the TiO<sub>2</sub> NPs, PANI/TiO<sub>2</sub> and PANIOx/TiO<sub>2</sub> composite films were evaluated using the prepared photoanodes for the water photo-electrolysis reaction in 0.1 M NaOH solution (pH = 12.7). From LSV scans in dark conditions in Figure 4.6a only a slight current ( $< 0.1 \mu\text{A}/\text{cm}^2$ ) was obtained for all the samples due to the high overpotential effect of both TiO<sub>2</sub> semiconductor and PANI-TiO<sub>2</sub> composites in absence of illumination. In

contrast, under simulated sunlight irradiation (AM 1.5G, 100 mW/cm<sup>2</sup>), a sudden increase of the photocurrent is observed at potentials more negative than the theoretical redox potential for water oxidation ( $E^0 = 1.23$  V vs. RHE) in all the samples, indicating that part of the energy required for the reaction is provided by the light. These results are in agreement with the expected behavior for a n-type semiconductor [55].

The photocurrent density ( $J$ ) of the TiO<sub>2</sub> NPs photoelectrode showed an important rise starting at about 0.56 V vs. RHE, reaching a maximum  $J$  value of 6.08  $\mu\text{A}/\text{cm}^2$  at about 1.68 V vs. RHE, which is associated with the saturation of the TiO<sub>2</sub> semiconductor [7, 56]. In contrast, the PANI/TiO<sub>2</sub> photoelectrode showed a pronounced increase of  $J$  starting at about 0.58 V vs. RHE, which continues to rise until reaching a maximum of 12.10  $\mu\text{A}/\text{cm}^2$  at 1.68 V vs. RHE. Such result is of high relevance if compared with the recently reported PANI-graphene-TiO<sub>2</sub> ternary composite electrode, with which a maximum photocurrent of 10  $\mu\text{A}/\text{cm}^2$  was obtained at about 1.4 V vs. RHE for the water photoelectrolysis reaction [27], thanks to the faster electron transfer rate attributed to the introduction of well-conductive graphene and PANI.

The PANIox/TiO<sub>2</sub> electrodes showed similar behavior, but with a reduced PEC performances. The PANIox/TiO<sub>2</sub> electrodes showed a pronounced increase of the photocurrent starting at about 0.77 V vs. RHE, reaching a maximum photocurrent density  $J$  of 10.03  $\mu\text{A}/\text{cm}^2$  at 1.68 V vs. RHE. This feature could likely be explained by the different photo-catalytic and transport properties of both PANI/TiO<sub>2</sub> and PANIox/TiO<sub>2</sub> with respect to TiO<sub>2</sub> NPs as discussed below.

In addition, Figure 4.6b shows the photocurrent density of the photoanodes investigated as a function of time, after different cycles of darkness and UV-Vis illumination. The anodic photocurrent appeared immediately after the light was turned on, due to instantaneous photo-induced electron transition from the VB to the CB, and then a slightly decrease is observed until a quasi-steady-state value is reached. The steady state photocurrent for the PANI/TiO<sub>2</sub> sample doubled the TiO<sub>2</sub> NPs film performance and is about 30% higher than the one of the PANIox/TiO<sub>2</sub> film, in accordance with LSV results. As expected, when the light was turned off, the photocurrent decreased quickly down to zero, confirming the effective photocatalytic (and not only catalytic) activity of all the studied materials.

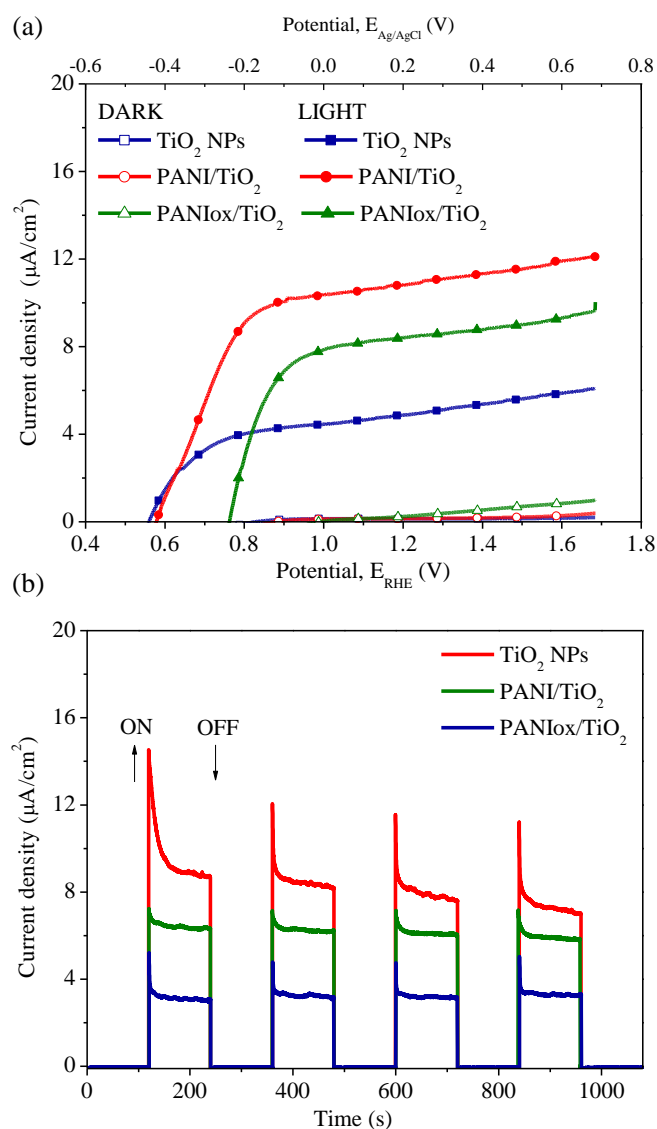


**Figure 4.6.** Photoelectrochemical characterizations for the samples: TiO<sub>2</sub> film (blue line), PANI/TiO<sub>2</sub> film (red line) and PANIox/TiO<sub>2</sub> (green line). (a) LSV collected with a scan rate of 10 mV/s in the dark and under illumination (AM 1.5G, 100 mW/cm<sup>2</sup>) and (b) Chronoamperometric ( $I-t$ ) curves at an applied potential of -0.1 V vs. Ag/AgCl under illumination with 120 s light ON/OFF cycles

The increase in the photocatalytic activity of PANI/TiO<sub>2</sub> and PANIox/TiO<sub>2</sub> compare to TiO<sub>2</sub> NPs should be essentially attributed to the efficient separation of electron and hole pairs, as already discussed in previous works on photocatalytic degradation of organic compounds [28, 35]. When the TiO<sub>2</sub> was coated with PANI, the interface between the two phases may act as a rapid separation site for the photogenerated electrons and holes, because of the difference in the energy levels of their conduction and valence bands. In the case of the PANI/TiO<sub>2</sub>

sample, in which PANI is in the emeraldine salt (ES) form (see Section 3.1), the HOMO of PANI is the polaron band, while its LUMO is the  $\pi^*$  band. In Figure 4.7 is illustrated the processes of photoexcitation and charge separation in the PANI-TiO<sub>2</sub> composite film system, under UV-Vis illumination. When the PANI-TiO<sub>2</sub> composite film is irradiated with UV-Vis light, PANI absorb photons, and electrons in the HOMO can be excited to the LUMO. In the same manner, TiO<sub>2</sub> absorb UV photons, and electrons in the VB of TiO<sub>2</sub> can be excited to its CB, thereby leaving holes at its surface.

Since the LUMO of PANI is at a potential level higher than such of TiO<sub>2</sub> [57], electrons can be easily injected into the CB of TiO<sub>2</sub>, which is advantageous for efficient charge carrier separation and electron transport. In fact, electrons in the CB of TiO<sub>2</sub> are transferred into the FTO conductive substrate, and then conducted through the external electrical circuit to be used for the H<sub>2</sub> formation reaction at the Pt cathode. Because of their strong oxidation ability, photogenerated holes in TiO<sub>2</sub> NPs and PANI species can migrate to the surface to be then consumed in the oxygen formation reaction. Alternatively, as shown in Figure 4.7, taking into account the position of redox potentials [21, 36, 39], the holes generated in the VB of TiO<sub>2</sub> most likely migrate to the HOMO of PANI so diminishing the  $e^-/h^+$  pairs recombination and contributing with the water oxidation reaction [37, 38]. Therefore, the larger photocurrents observed with the PANI-TiO<sub>2</sub> nanocomposite films with respect to the TiO<sub>2</sub> NPs film (see Figure 4.6) could be explained by a more efficient charge transfer at the semiconductor-electrolyte interface and a faster electron transport, which results in a lower recombination and a higher number of collected photoelectrons [58-60].

The sample PANI<sub>ox</sub>/TiO<sub>2</sub> was prepared and tested with the aim to discern if the PANI in the NaOH solution is oxidized, being such the reason for the highest photo-catalytic activity of the PANI/TiO<sub>2</sub> film. On the contrary, the results reported in Figure 4.6 shown that the PANI<sub>ox</sub>/TiO<sub>2</sub> perform worst than its original counterpart. The difference between PANI/TiO<sub>2</sub> and PANI<sub>ox</sub>/TiO<sub>2</sub> can be easily explained taking into account the presence of some pernigraniline base (PNB) form of PANI in the oxidized material (see Section 3.1). In the case of PNB, the PANI structure is composed from quinoid structures and thus the HOMO level are the quinoid orbitals that has lower energy with respect to polaron band [61]. Thus the migration of holes from TiO<sub>2</sub> to PANI is less favorable. On the other hand, the benzenoid orbitals are in this case the LUMO [61], that have an energy much lower than the  $\pi^*$  band previously considered for the ES and even lower than the TiO<sub>2</sub> CB. Hence, when the PANI<sub>ox</sub>

absorbs UV-Vis light, the electron in the  $\pi^*$  band can undergo more easily to internal relaxation to the benzenoid orbital, thus causing internal recombination.

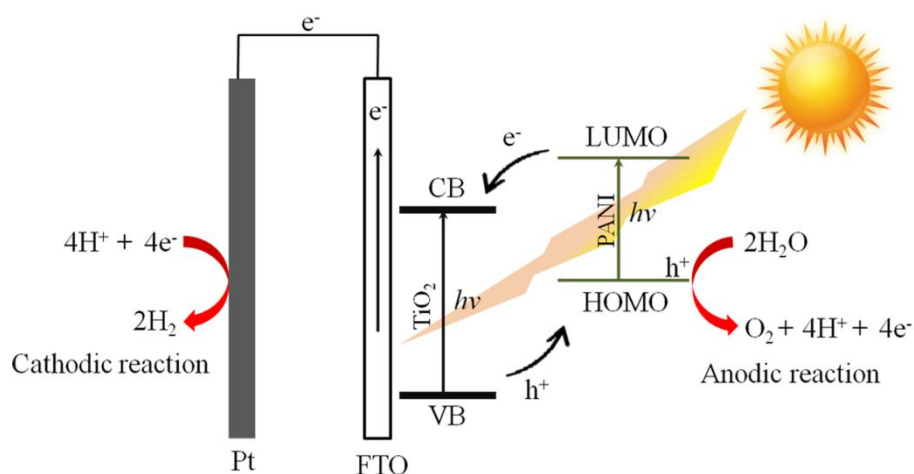


**Figure 4.7.** The mechanism of absorption of the UV component in the presence of PANI-TiO<sub>2</sub> composite film

In addition, the open circuit voltage (OCV) of the LSV measurements, *i.e.* the voltage corresponding to  $J = 0$ , is an approximated measure of the flat band potential, which is close to the CB on n-type semiconductors such as the titania [62]. From Figure 4.6a is worth of notice the change on the OCV after the oxidation of the PANI/TiO<sub>2</sub> film. In fact, the shift towards higher OCV values for PANI<sub>ox</sub>/TiO<sub>2</sub> is another indication of the lower energy level of the CB of this composite film with respect to PANI/TiO<sub>2</sub>, and is another index of its worst photocatalytic activity.

In order to identify what is the portion of the solar spectra actually working in the TiO<sub>2</sub> and PANI-TiO<sub>2</sub> films, both UV-Vis and IPCE spectra were recorded and are reported in Figure 4.8. From the UV-Vis spectra in transmittance mode shown in Figure 4.8a, it is possible to observe that no significant difference were presented for the TiO<sub>2</sub> NPs, PANI/TiO<sub>2</sub> and PANI<sub>ox</sub>/TiO<sub>2</sub> composite films between 300 and 330 nm. In this region, high UV light absorption (low transmittance) is observed for all the samples. Between 330 and 420 nm the transmittance increased, indicating a provably related reduction of absorption of the TiO<sub>2</sub> NPs. However, the PANI impregnated samples evidenced a higher absorption than the TiO<sub>2</sub> NPs, in the following order: PANI/TiO<sub>2</sub> > PANI<sub>ox</sub>/TiO<sub>2</sub> > TiO<sub>2</sub> NPs.

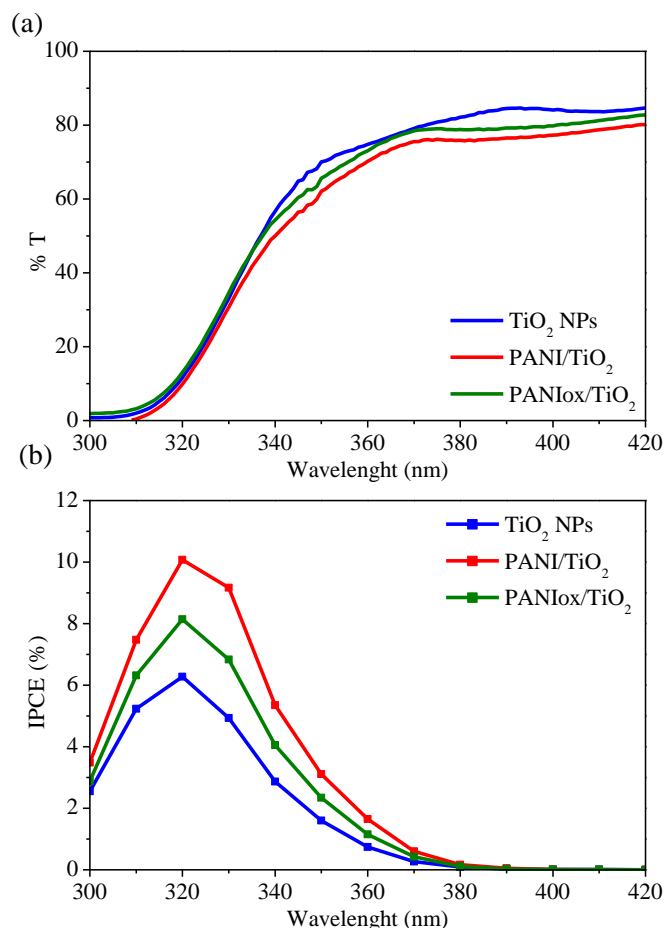


**Figure 4.8.** Optical properties for the samples: TiO<sub>2</sub> film (blue line), PANI/TiO<sub>2</sub> film (red line) and PANIox/TiO<sub>2</sub> (green line). (a) UV-Vis spectra recorded in transmittance mode and (b) IPCE spectra recorded by varying the wavelength of the incident light from 300 nm to 420 nm at an applied potential of 0.26 V vs. Ag/AgCl (1.23 V vs. RHE)

The photo-response of the different photoanodes evaluated through the IPCE spectra at an applied potential of 0.26 V vs. Ag/AgCl (1.23 V vs. RHE) are reported in Figure 4.8b. IPCE curves revealed that either the TiO<sub>2</sub> NPs or the PANI-TiO<sub>2</sub> nanocomposites here prepared have a relevant efficiency only in the UV region up to maximum 390 nm. The maximum IPCE was obtained at 320 nm for all the samples being 6.27 %, 8.17 % and 10.07 %, respectively for the TiO<sub>2</sub> NPs, PANIox/TiO<sub>2</sub> and PANI/TiO<sub>2</sub> samples. These results are in agreement with the highest UV absorption of the PANI impregnated samples but suggest that for the water splitting reaction the role of PANI in the PANI-TiO<sub>2</sub> composite is most important in the UV than in the visible region of the light. Indeed, in the literature is reported that the role of PANI as sensitizer plays also a role in the visible region but only for another redox reactions. For instance, PANI-TiO<sub>2</sub> composite particles, photoexcited with either UV or

visible light, has been reported to be effective for the photodegradation of organic compounds (i.e. Rhodamine B and Methylene blue) which involves the oxidation of water to OH<sup>·</sup> radicals [35]. In the present case, since the water oxidation to oxygen requires holes with a higher oxidation potential than in the previous case, it is possible that holes generated in the PANI under visible illumination are not able to perform the water splitting reaction. Therefore, the here reported results suggest that the main role of PANI, in the system PANI/TiO<sub>2</sub> for the PEC water splitting, is as sensitizer of TiO<sub>2</sub> NPs in the UV light and in significantly reducing the recombination losses which result in an improved photocatalytic activity.

Finally, the stability of the PANI/TiO<sub>2</sub> nanocomposite photoanode was investigated as a function of time and Figure 4.9 shows the *I-t* curves after various hours of operation at -0.1 V vs. Ag/AgCl (0.86 V vs. RHE). This potential was chosen as a representative value in the region of photocurrent saturation of the sample. A good photo-current stability was observed under numerous light ON-OFF cycles for a long period of time (190 min), so confirming a high degree of electrochemical durability, the not photodegradation of the emeraldine salt form of PANI under a highly oxidizing media, and the good adhesion of the PANI/TiO<sub>2</sub> nanocomposite material to the substrate.

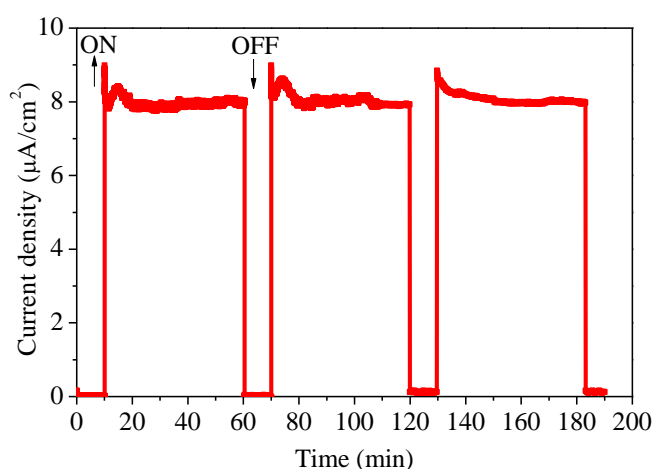


**Figure 4.9.** Photocurrent stability vs. time of PANI/ TiO<sub>2</sub> film obtained by chrono-amperometric (*I-t*) technique at an applied potential of 0.26 V vs. Ag/AgCl (1.23 V vs. RHE) under illumination with ON/OFF cycles

#### 4.4. Conclusions

In order to improve the photocatalytic activity of TiO<sub>2</sub> NPs film, PANI-TiO<sub>2</sub> nanocomposite films have been successfully prepared by a simple impregnation method. According to FESEM observations, a thin film of PANI was deposited on the TiO<sub>2</sub> NPs film, which not

significantly modified the morphology and crystallinity of TiO<sub>2</sub> NPs, as was also confirmed by XRD analysis. ATR results confirmed the present of PANI under the form of emeraldine salt (ES) and pernigraniline base (PNB) in PANI/TiO<sub>2</sub> and PANI<sub>ox</sub>/TiO<sub>2</sub> nanocomposite films, respectively. A remarkable enhancement of photocatalytic capacity was achieved by employing PANI-TiO<sub>2</sub> nanocomposite films for the PEC water splitting reaction. The PANI/TiO<sub>2</sub> and PANI<sub>ox</sub>/TiO<sub>2</sub> nanocomposite films showed a pronounced increase of the photocurrent under simulated sunlight irradiation (AM 1.5G, 100 mW/cm<sup>2</sup>), reaching maximum photocurrent density around 2 and 1.6 fold higher with respect to TiO<sub>2</sub> NPs. These results are in good agreement with IPCE measurements, which revealed that the PEC activity of both PANI/TiO<sub>2</sub> and PANI<sub>ox</sub>/TiO<sub>2</sub> films was enhanced in 1.6 and 1.3 fold higher with respect to the pristine TiO<sub>2</sub> NPs film at 1.23 V vs. RHE. The best performance of the PANI/TiO<sub>2</sub> sample can be associated to highly stable structure due to the present of un-oxidized part of polymer chain, which may give a high degree of electrochemical durability. PANI/TiO<sub>2</sub> film showed an exceptional stability under illumination with ON/OFF cycles during 190 min of test, also confirming the good adhesion of the composite material to the substrate. The synergic effect between emeraldine salt form of PANI and TiO<sub>2</sub> caused a rapid charge separation and a slow charges recombination of the photogenerated e<sup>-</sup>/h<sup>+</sup> pairs. Thus, the present PANI/TiO<sub>2</sub> film is a promising photocatalyst material for the PEC water splitting reaction.

#### 4.5. References

- [1] A. Fujishima, K. Honda, *Nature*, 238 (1972) 37-38.
- [2] X. Hu, G. Li, J.C. Yu, *Langmuir*, 26 (2009) 3031-3039.
- [3] D. Fattakhova-Rohlfing, A. Zaleska, T. Bein, *Chemical Reviews*, doi: 10.1021/cr500201c (2014).
- [4] X. Chen, S.S. Mao, *Chemical Reviews*, 107 (2007) 2891-2959.
- [5] C. Yu, B. Tian, D. Zhao, *Current Opinion in Solid State and Materials Science*, 7 (2003) 191-197.
- [6] M.L.K. Hoa, M. Lu, Y. Zhang, *Advances in Colloid and Interface Science*, 121 (2006) 9-23.
- [7] D. Hidalgo, R. Messina, A. Sacco, D. Manfredi, S. Vankova, E. Garrone, G. Saracco, S. Hernández, *International Journal of Hydrogen Energy*, doi: 10.1016/j.ijhydene.2014.02.163 (2014).

- [8] C. Boissiere, D. Grosso, A. Chaumonnot, L. Nicole, C. Sanchez, *Advanced Materials*, 23 (2011) 599-623.
- [9] P. Innocenzi, L. Malfatti, *Chemical Society Reviews*, 42 (2013) 4198-4216.
- [10] R. Zhang, A.A. Elzatahry, S.S. Al-Deyab, D. Zhao, *Nano Today*, 7 (2012) 344-366.
- [11] M.C. Orilall, U. Wiesner, *Chemical Society Reviews*, 40 (2011) 520-535.
- [12] W. Li, D. Zhao, *Advanced Materials*, 25 (2013) 142-149.
- [13] F. Zhu, D. Wu, Q. Li, H. Dong, J. Li, K. Jiang, D. Xu, *RSC Advances*, 2 (2012) 11629-11637.
- [14] J.B. Joo, Q. Zhang, M. Dahl, F. Zaera, Y. Yin, *Journal of Materials Research*, 28 (2013) 362-368.
- [15] Q. Xiang, J. Yu, M. Jaroniec, *Nanoscale*, 3 (2011) 3670-3678.
- [16] W. Zhou, H. Liu, R.I. Boughton, G. Du, J. Lin, J. Wang, D. Liu, *Journal of Materials Chemistry*, 20 (2010) 5993-6008.
- [17] W.S. Tung, W.A. Daoud, *Journal of Materials Chemistry*, 21 (2011) 7858-7869.
- [18] N. Liu, X. Chen, J. Zhang, J.W. Schwank, *Catalysis today*, 225 (2014) 34-51.
- [19] P. Roy, S. Berger, P. Schmuki, *Angewandte Chemie International Edition*, 50 (2011) 2904-2939.
- [20] A. Lamberti, A. Sacco, S. Bianco, D. Manfredi, F. Cappelluti, S. Hernandez, M. Quaglio, C.F. Pirri, *Physical Chemistry Chemical Physics*, 15 (2013) 2596-2602.
- [21] J. Yue, Z.H. Wang, K.R. Cromack, A.J. Epstein, A.G. MacDiarmid, *Journal of the American Chemical Society*, 113 (1991) 2665-2671.
- [22] D.P. Debecker, V. Hulea, P.H. Mutin, *Applied Catalysis A: General*, 451 (2013) 192-206.
- [23] W. Zhou, H. Fu, *ChemCatChem*, 5 (2013) 885-894.
- [24] H. Tong, S. Ouyang, Y. Bi, N. Umezawa, M. Oshikiri, J. Ye, *Advanced Materials*, 24 (2012) 229-251.
- [25] X. Wang, R.A. Caruso, *Journal of Materials Chemistry*, 21 (2011) 20-28.
- [26] J.Z. Zhang, *MRS Bulletin*, 36 (2011) 48-55.
- [27] L. Jing, Z.-Y. Yang, Y.-F. Zhao, Y.-X. Zhang, X. Guo, Y.-M. Yan, K.-N. Sun, *Journal of Materials Chemistry A*, 2 (2014) 1068-1075.
- [28] J. Wei, Q. Zhang, Y. Liu, R. Xiong, C. Pan, J. Shi, *J Nanopart Res*, 13 (2011) 3157-3165.
- [29] M. Qorbani, N. Naseri, O. Moradlou, R. Azimirad, A.Z. Moshfegh, *Applied Catalysis B: Environmental*, 162 (2015) 210-216.

- [30] S. Kuang, L. Yang, S. Luo, Q. Cai, *Applied Surface Science*, 255 (2009) 7385-7388.
- [31] F. Deng, L. Min, X. Luo, S. Wu, S. Luo, *Nanoscale*, 5 (2013) 8703-8710.
- [32] D. Pei, J. Luan, *International Journal of Photoenergy*, 2012 (2012) 13.
- [33] W.J. Youngblood, S.-H.A. Lee, K. Maeda, T.E. Mallouk, *Accounts of Chemical Research*, 42 (2009) 1966-1973.
- [34] G.A.O. Jinzhang, L.I. Shengying, Y. Wu, Z. Guohu, B.O. Lili, S. Li, *Rare Metals*, 26 (2007) 1-7.
- [35] M. Radoičić, Z. Šaponjić, I.A. Janković, G. Ćirić-Marjanović, S.P. Ahrenkiel, M.I. Čomor, *Applied Catalysis B: Environmental*, 136–137 (2013) 133-139.
- [36] J. Li, L. Zhu, Y. Wu, Y. Harima, A. Zhang, H. Tang, *Polymer*, 47 (2006) 7361-7367.
- [37] X. Li, D. Wang, G. Cheng, Q. Luo, J. An, Y. Wang, *Applied Catalysis B: Environmental*, 81 (2008) 267-273.
- [38] H. Zhang, R. Zong, J. Zhao, Y. Zhu, *Environmental science & technology*, 42 (2008) 3803-3807.
- [39] G. Senadeera, T. Kitamura, Y. Wada, S. Yanagida, *Journal of Photochemistry & Photobiology, A: Chemistry*, 164 (2004) 61-66.
- [40] K. He, M. Li, L. Guo, *International Journal of Hydrogen Energy*, 37 (2012) 755-759.
- [41] A.G. MacDiarmid, A.J. Epstein, *Faraday Discussions of the Chemical Society*, 88 (1989) 317-332.
- [42] J.-C. Chiang, A.G. MacDiarmid, *Synthetic Metals*, 13 (1986) 193-205.
- [43] A. MacDiarmid, J. Chiang, A. Richter, A. Epstein, *Synthetic Metals*, 18 (1987) 285-290.
- [44] A.G. MacDiarmid, A.J. Epstein, *Faraday Discuss. Chem. Soc.* 1989,88, 317, and refs therein; A. G. MacDiarmid, A. J. Epstein in *Science and Applications of Conducting Polymers* (Eds.: W. R. Salaneck, D. T. Clark, E. J. Samuelsen), Adam Hilger, Bristol, (1989) 117.
- [45] F. Lu, F. Wudl, M. Nowak, A. Heeger, *Journal of the American Chemical Society*, 108 (1986) 8311-8313.
- [46] Y. Sun, A.G. MacDiarmid, A.J. Epstein, *J. Chem. Soc., Chem. Commun.*, (1990) 529-531.
- [47] A.G. MacDiarmid, J.-C. Chiang, A.F. Richter, N.L.D. Somasiri, A.J. Epstein, *Conducting Polymers* (Ed.: L. Alcazar), Reidel, Dordrecht, (1987) 105.
- [48] S. Bhadra, D. Khastgir, N.K. Singha, J.H. Lee, *Progress in Polymer Science*, 34 (2009) 783-810.

- [49] S. Bocchini, A. Chiolerio, S. Porro, D. Accardo, N. Garino, K. Bejtka, D. Perrone, C. Pirri, *Journal of Materials Chemistry C*, 1 (2013) 5101-5109.
- [50] A. Chiolerio, S. Bocchini, S. Porro, *Advanced Functional Materials*, 24 (2014) 3472-3472.
- [51] T. Abdiryim, Z. Xiao-Gang, R. Jamal, *Materials Chemistry and Physics*, 90 (2005) 367-372.
- [52] P. Madhu Kumar, S. Badrinarayanan, M. Sastry, *Thin solid films*, 358 (2000) 122-130.
- [53] J. Tang, X. Jing, B. Wang, F. Wang, *Synthetic Metals*, 24 (1988) 231-238.
- [54] G. D'Aprano, M. Leclerc, G. Zotti, *Macromolecules*, 25 (1992) 2145-2150.
- [55] J.J. Kelly, Z. Hens, D. Vanmaekelbergh, Z. Hensalso, *Photoelectrochemical Systems Characterization*, in: *Encyclopedia of electrochemistry*, Wiley-VCH Verlag GmbH & Co. KGaA, 2007.
- [56] Z. Zhang, P. Wang, *Energy & Environmental Science*, 5 (2012) 6506-6512.
- [57] M.-S. Liu, Y.-Z. Hao, X.-B. Qiao, M. Yang, M. Cai, Y. Li, *Electrochemistry (in Chinese)*, 4 (1998) 246.
- [58] A. Lamberti, A. Sacco, D. Hidalgo, S. Bianco, D. Manfredi, M. Quaglio, E. Tresso, C.F. Pirri, *Acta Physica Polonica, A.*, 123 (2013) 376.
- [59] S. Hernández, V. Cauda, A. Chiodoni, S. Dallorto, A. Sacco, D. Hidalgo, E. Celasco, C.F. Pirri, *ACS Applied Materials & Interfaces*, 6 (2014) 12153–12167.
- [60] S. Hernández, V. Cauda, D. Hidalgo, V. Farías Rivera, D. Manfredi, A. Chiodoni, F.C. Pirri, *Journal of Alloys and Compounds*, 615 (2014) S530 – S537.
- [61] W. Huang, A. MacDiarmid, *Polymer*, 34 (1993) 1833-1845.
- [62] K. Rajeshwar, *Encyclopedia of electrochemistry*, (2002).

## Chapter 5

### Literature review - Microbial fuel cell for electricity generation

#### 5.1. Introduction

Bioelectrochemical systems (BESs) are a new and exciting area in biotechnology. BESs are able to catalyze various electrochemical reactions with the aid of microorganisms. A typical BES consists of an anode and a cathode compartments which are separated by a proton exchange membrane (PEM). Generally, in the anode compartment a substrate is oxidized by microorganisms activity, while in the cathode compartment an electron acceptor is reduced. Microbial fuel cells (MFCs) are a specific type of BES which can be defined as a system in which microorganisms function as catalysts to convert chemical energy comprised in different substrates into electricity. In this chapter, an overview of the development of MFC is described as well as the most important parameters involved in the physic-chemical characterization of the system. Finally, the main objectives related with the improvement of the MFC systems are summarized.

#### 5.2. History of microbial fuel cell development

The earliest microbial fuel cells (MFCs) concept was demonstrated by Potter in 1910 [1]. In 1911, Potter described how microbial conversions could create reducing power, and thus electrical current from living cultures of *Escherichia coli* and *Saccharomyces cerevisiae* by using platinum electrodes [2]. In 1931, Cohen investigated the capacity of bacteria to create reducing power, and noted that the main limitation of the current generation was the small capacity that microorganisms could deliver [3]. It took until the 1960s before this microbial capacity was truly combined with fuel cells and the first microbial fuel cells emerged [4, 5]. This didn't generate much interest until 1980s when it was discovered that current density and the power output could be greatly enhanced by the addition of electron mediators. Unless the species in the anodic chamber are anodophiles, the microbes are incapable of transferring electrons directly to the anode. Typical synthetic exogenous mediators include dyes and metallorganics such as neutral red (NR), methylene blue (MB), thionine, meldola's blue (MeIb), 2-hydroxy-1,4-naphthoquinone (HNQ), and Fe(III)EDTA [1, 6-9]. Unfortunately, the toxicity and instability of synthetic mediators limit their applications in MFCs and only are used in laboratory researches. A real breakthrough was made when some microbes were

found to transfer electrons directly to the anode [10, 11]. These microbes are operationally stable and yield a high Coulombic efficiency [11, 12]. *Shewanella putrefaciens* [13], *Geobacteraceae sulfurreducens* [14], *Geobacter metallireducens* and *Rhodospirillum rubrum* [11] are all bioelectrochemically active and can form a biofilm on the anode surface and transfer electrons directly by conductance through the membrane. When they are used, the anode material acts as the final electron acceptor in the dissimilatory respiratory chain of the microbes in the biofilm. Biofilms forming on a cathode surface may also play an important role in electron transfer between the microbes and the electrodes. Cathodes can serve as electron donors for *Thiobacillus ferrooxidans* suspended in a catholyte [15] for an MFC system that contained microbes in both anodic and cathodic chambers. *G. metallireducens* and *G. sulfurreducens* [16] or other seawater biofilms [17] may all act as final electron acceptors by grabbing the electrons from cathode as electron donors. Since the cost of a mediator is eliminated, mediator-less MFCs are advantageous in wastewater treatment and in power generation [14]. At present, however, one of the problems for the application of this methodology is the low output of power. Principally, the output power depends on the rate of substrate degradation, the rate of electron transfer from the bacteria to the anode, the circuit resistance, the proton mass transfer in the liquid [18], the performance of the electrode and the external operating conditions and so on. Different electrode materials vary in their physical and chemical properties (e.g., surface area, electric conductivity, and chemical stability), thus, they also vary in their impact on microbial attachment, electron transfer, electrode resistance and the rate of electrode surface reaction. Therefore, it is of great significance to select and develop suitable electrode materials to optimize and promote the performance of MFCs. Moreover, as a main component, the electrode materials determine the price of MFCs and thus influence the wastewater treatment cost and energy production. In this way, many efforts related to electrode preparations and designs have been made, unfortunately, the low output power continues to be one of the bottleneck problems for the commercial application of MFC.

### **5.3. Bioelectricity generation using microbial fuel cell**

Microbial fuel cells (MFCs) are devices that use bacteria as the catalysts to oxidize organic and inorganic matter and generate current [2, 4]. The reasons for this recent interest in using bacteria to generate electricity are a combination of the need for new sources of energy, discoveries about microbial physiology related to electron transport, and advancement of fuel cell technologies.

A typical microbial fuel cell consists of anode and cathode compartments as shown in Figure 5.1. In the anode compartment, fuel (substrate) is oxidized by microorganisms activity, generating electrons and protons, while in the anode compartment an electron acceptor is reduced. Electrons produced by the bacteria from these substrates are transferred to the anode and flow to the cathode linked by a conductive electrode material containing a resistor, or operated under an external load. A great variety of substrates can be used in MFCs for electricity production ranging from pure compounds such as glucose [11], acetate [19] to complex mixtures of organic matter present in wastewater [20]. When microorganisms consume a substrate in the anode compartment under anaerobic conditions they produce carbon dioxide, protons and electrons according to the following reactions [21]:

- If glucose is used as substrate



- If acetate is used as substrate



Electrons can be transferred to the anode material by electron mediators or shuttles [22, 23], by direct membrane associated electron transfer [14], or by so-called nanowires [24] produced by the bacteria, or perhaps by other as yet undiscovered means. Chemical mediators, such as neutral red, methylene blue or anthraquinone-2,6-disulfonate (AQDS), can be added to the system to allow electricity production by bacteria unable to otherwise use the electrode [25, 26]. If no exogenous mediators are added to the system, the MFC is classified as a “mediator-less” MFC even though the mechanism of electron transfer may not be known [27]. MFCs operated using mixed cultures currently achieve substantially greater power densities than those with pure cultures [22, 23]. Community analysis of the microorganisms that exist in MFCs has so far revealed a great diversity in composition [28, 29].

In most MFCs the electrons that reach the cathode combine with protons that diffuse from the anode through a cation exchange membrane (CEM) and oxygen provided from air; the resulting product is water [20, 25]. Chemical oxidizers, such as ferricyanide or Mn (IV), can also be used although these must be replaced or regenerated [22]. In the case of metal ions, such as Mn that are reduced from Mn (IV) to Mn (II), bacteria located in the cathode can help to catalyze the reoxidation of the metal using dissolved oxygen [30, 31]. In this way, when oxygen and ferricyanide are used as electron acceptor, the reaction occurring at the cathode is as follows [21, 32]:

- If oxygen is used as electron acceptor



- If ferricyanide is used as electron acceptor



From the above equations, ferricyanide in the cathode compartment is reduced to ferrocyanide; thus, the chemical must be replaced after it is depleted. However, oxygen can be constantly replenished by bubbling the water with air; thus, energy production from organic matter is sustainable in these systems. MFCs are being constructed using a variety of materials, and in an ever increasing diversity of configurations. These systems are operated under a range of conditions that include differences in temperature, pH, electron acceptor, electrode surface areas, reactor size, and operation time. The final characterization of the systems are common carried out by the interpretation of data obtained through electrochemical characterization i.e. power densities derived from polarization curves and many others electrochemical techniques that allow to interpret and compare results among these systems in term of power density and energy generation [33].

Applications for MFCs might include: wastewater treatment, electricity generation, biohydrogen production and as a sensor for pollutant analysis [34]. More specifically, in wastewater treatment, waste or more specific wastewater needs to be treated to the levels specified in the discharge regulations before it can be discharged into the environment. Two main classes of biological wastewater treatment processes are currently the most widely used: aerobic and anaerobic treatment. Both technologies have their own niche in environmental technology, are commercially available and are worldwide implemented [29]. In contrast to anaerobic digestion, a MFC creates electrical current and an off-gas containing mainly carbon dioxide. MFCs have operational and functional advantages over the technologies currently used for generating energy from organic matter. First, the direct conversion of substrate energy to electricity enables high conversion efficiency. Second, MFCs operate efficiently at ambient, and even at low, temperatures distinguishing them from all current bio-energy processes. Third, an MFC does not require gas treatment because the off-gases of MFCs are enriched in carbon dioxide and normally have no useful energy content. Fourth, MFCs do not need energy input for aeration provided the cathode is passively aerated [33]. Fifth, MFCs have potential for widespread application in locations lacking electrical infrastructures and also to expand the diversity of fuels we use to satisfy our energy requirements.

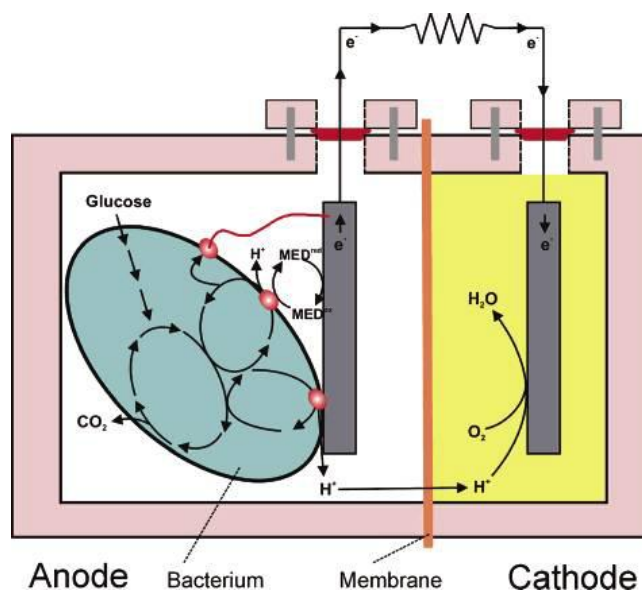


**Figure 5.1.** Operating principles of a MFC. A bacterium in the anode compartment transfers electrons obtained from an electron donor (glucose) to the anode electrode. This occurs either through direct contact, nanowires, or mobile electron shuttles (small spheres represent the final membrane associated shuttle). During electron production protons are also produced in excess. These protons migrate through the cation exchange membrane (CEM) into the cathode chamber. The electrons flow from the anode through an external resistance (or load) to the cathode where they react with the final electron acceptor (oxygen) and protons [33]

#### 5.4. Electron transfer in microbial fuel cell

Some microbes are electrochemically active, capable of accepting electrons from an external source or donating electrons to an external object such as an electrode. These microbes are known as electrogenic microbes [35]. Not all microbes are electrogenic, but non electrogenic microbes may still be part of a synergistic electrogenic biofilm consortium because they perform other functions such as providing certain organic nutrients to the electrogenic microbes in the consortium. Microbial cells are generally non-conductive because their cell membranes mostly contain non-conductive materials such as polysaccharides, lipids and peptidoglycans. Electron transfer between microbes and electrodes rely on two mechanisms, namely direct electron transfer (DET) and mediated electron transfer (MET) (see Figure 5.2) [36].

DET requires direct physical contact between the microbial cell membrane or a membrane organelle and the anode electrode surface, without the need for any diffusional redox species in the electron transfer process Both c-type cytochromes associated with bacterial outer

membrane (Figure 5.2a) and conductive nanowires or pili (Figure 5.2b) can be used for DET [37]. Thus, pili can be formed on demand to facilitate electron transfer between microbial cells and a solid surface [38]. Gorby *et al.* [24] suggested that formation of pili may be a common strategy used by electrogenic bacteria for efficient electron transfer and energy distribution. For MFC operations, this means that some microbes purposefully develop a network of pili to facilitate electron donation to an anode or electron acceptance from a biocathode in MFC operations [39]. After all, allowing the electron flow enables respiratory metabolism that benefits the biofilms bioenergetically.

While some microbes perform DET, other microbes need redox-active chemical species (mediators) to carry out indirect electron transfer; this is known as MET. An electron mediator is a molecule that functions as an electron shuttle between microbes and an electrode. In MET, direct contact between the bacterial cell membrane and the electrode surface is not required. In the early studies on MFCs, exogenous mediators like neutral red, hexacyanoferrate, thionin or 2-hydroxy-1,4-naphthoquinone (HNQ) were generally added to the systems in order to increase the electron transfer rate of non-enriched microbial communities as evidence the electron transfer mechanism in Figure 5.2c [6, 40]. In a synergistic biofilm consortium, it is possible that a non electrogenic microbe may secrete their own mediators that help the electrogenic microbe perform better such as phenazine, 2-amino-3carboxy-1,4-naphthoquinone, 1,2-dihydroxynaphthalene and 2,6-di-tertbutyl-p-benzoquinone, as evidenced in Figure 5.2d [23, 41-43].

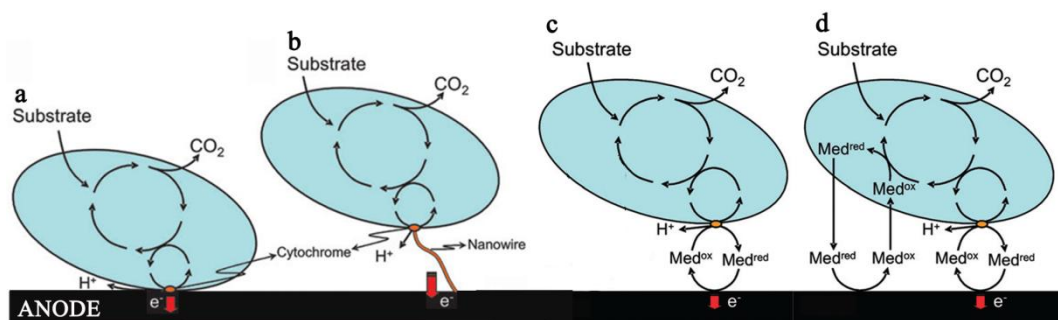


**Figure 5.2.** Electron transfer mechanisms between microbes and electrodes: (a) DET, via membrane bound cytochromes, (b) DET, via electronically conducting pili, (c) MET, via redox-active chemical species as mediator and (d) MET, via secreted mediators from microorganisms [36]

## 5.5. Microbes used in microbial fuel cells

Many microorganisms possess the ability to transfer the electrons derived from the metabolism of organic matters to the anode. A list of them is shown in Table 5.1 together with their substrates. Marine sediment, soil, wastewater, fresh water sediment and activated sludge are all rich sources for these microorganisms [19, 44]. A number of recent publications discussed the screening and identification of microbes and the construction of a chromosome library for microorganisms that are able to generate electricity from degrading organic matters [45-47]. The anodic electron transfer mechanism in MFC is a key issue in understanding the theory of how MFCs work. As mentioned above, microbes transfer electrons to the electrode through an electron transport system that either consists of a series of components in the bacterial extracellular matrix or together with electron shuttles dissolved in the bulk solution such as mediator.

The anodic reaction in mediator-less MFCs constructed with metal reducing bacteria belonging primarily to the families of *Shewanella*, *Rhodospirillum rubrum*, and *Geobacter* is similar to that in this process because the anode acts as the final electron acceptor just like the solid mineral oxides. *Geobacter* belongs to dissimilatory metal reducing microorganisms, which produce biologically useful energy in the form of ATP during the dissimilatory reduction of metal oxides under anaerobic conditions in soils and sediments. The electrons are transferred to the final electron acceptor such as  $\text{Fe}_2\text{O}_3$  mainly by a direct contact of mineral oxides and the metal reducing microorganisms [48, 49]. *S. putrefaciens*, *G. sulfurreducens*, *G. metallireducens* and *R. ferrireducens* transfer electrons to the solid anode electrode using the same system. Though most of the real mediator-less MFCs are operated with dissimilatory metal reducing microorganisms, an exception was reported with *Clostridium butyricum* [50, 51]. Mediators such as dye molecules and humic substances also have some effects on the mediator-less MFCs even though the anodophiles can transfer the electrons to the anode directly especially in the early stage of biofilm formation. Electron mediators like  $\text{Mn}^{4+}$  or neutral red (NR) incorporated into the anode noticeably enhance the performance of MFCs using anodophile *S. putrefaciens* [52]. *Actinobacillus succinogenes*, *Desulfovibrio desulfuricans*, *E. coli*, *Proteus mirabilis*, *Proteus vulgaris* and *Pseudomonas fluorescens* need extraneous mediators while some microbes can provide their own. For example, *Pseudomonas aeruginosa* produces pyocyanin molecules as electron shuttles. When an MFC is inoculated with marine sediments or anaerobic sludge, mixed cultured microbes are in the anode chamber. Usually mixed culture MFCs have good performances. Using complex mixed cultures (anodic microcosm) allows much wider substrate utilization. It means that the

MFCs have much wider substrate specificity when mixed than do pure cultures. In mixed culture MFCs (with anaerobic sludge) there are both electrophiles/anodophiles and groups that use natural mediators together in the same chamber.

**Table 5.1.** Microbes used in MFCs [34]

Microbes	Substrate	Applications
<i>Actinobacillus succinogenes</i>	Glucose	Neutral red or thionin as electron mediator (Park and Zeikus, 2000; Park and Zeikus, 1999; Park et al., 1999)
<i>Aeromonas hydrophila</i>	Acetate	Mediator-less MFC Pham et al. (2003)
<i>Alcaligenes faecalis</i> , <i>Enterococcus gallinarum</i> , <i>Pseudomonas aeruginosa</i>	Glucose	Self-mediate consortia isolated from MFC with a maximal level of 4.31 W m <sup>-2</sup> . Rabaey (2004)
<i>Clostridium beijerinckii</i>	Starch, glucose, lactate, molasses	Fermentative bacterium Niessen et al. (2004b)
<i>Clostridium butyricum</i>	Starch, glucose, lactate, molasses	Fermentative bacterium (Niessen et al., 2004b; Park et al., 2001)
<i>Desulfovibrio desulfuricans</i>	Sucrose	Sulphate/sulphide as mediator (Ieropoulos et al., 2005a; Park et al., 1997)
<i>Erwinia dissolven</i>	Glucose	Ferric chelate complex as mediators Vega and Fernandez, (1987)
<i>Escherichia coli</i>	Glucose sucrose	Mediators such as methylene blue needed. (Schroder et al., 2003; Ieropoulos et al., 2005a; Grzebyk and Pozniak, 2005)
<i>Geobacter metallireducens</i>	Acetate	Mediator-less MFC Min et al. (2005a)
<i>Geobacter sulfurreducens</i>	Acetate	Mediator-less MFC (Bond and Lovley, 2003; Bond et al., 2002)
<i>Gluconobacter oxydans</i>	Glucose	Mediator (HNQ, resazurin or thionine) needed Lee et al. (2002)
<i>Klebsiella pneumoniae</i>	Glucose	HNQ as mediator biomineralized manganese as electron acceptor (Rhoads et al., 2005; Menicucci et al., 2006)
<i>Lactobacillus plantarum</i>	Glucose	Ferric chelate complex as mediators (Vega and Fernandez, 1987)
<i>Proteus mirabilis</i>	Glucose	Thionin as mediator (Choi et al., 2003; Thurston et al., 1985)
<i>Pseudomonas aeruginosa</i>	Glucose	Pyocyanin and phenazine-1-carboxamide as mediator (Rabaey et al., 2004, 2005a)
<i>Rhodospirillum rubrum</i>	Glucose, xylose sucrose, maltose	Mediator-less MFC (Chaudhuri and Lovley, 2003; Liu et al., 2006)
<i>Shewanella oneidensis</i>	Lactate	Anthraquinone-2,6-disulfonate (AQDS) as mediator (Ringeisen et al., 2006)
<i>Shewanella putrefaciens</i>	Lactate, pyruvate, acetate, glucose	Mediator-less MFC (Kim et al., 1999a,b); but incorporating an electron mediator like Mn (IV) or NR into the anode enhanced the electricity production (Park and Zeikus, 2002)
<i>Streptococcus lactis</i>	Glucose	Ferric chelate complex as mediators (Vega and Fernandez, 1987)

## 5.6. MFC reactor components

Most MFC designs consist of two compartments (anode and cathode), containing the electrodes and the electrolyte, which are separated by a PEM membrane. Each MFC component has a specific function and needs to fulfill several requirements in order to maximize the energy generation in MFCs. As MFCs are a rather new technology, there are still many opportunities to improve its components or specifically develop new materials. An overview of the materials used and the recent innovations are given below.

### 5.6.1. Electrodes

The electrodes of MFCs are not only the backbone of the MFC designs; they also represent the physical medium by which one can collect or donate electrons to or from the bacteria. Therefore, specifically for the anode, the electrode material should have the following properties: (a) good electrical conductivity and low resistance; (b) strong biocompatibility;

(c) chemical stability and anti-corrosion; (d) large surface area; and (e) appropriate mechanical strength and toughness in order to minimize energy losses during current generation [53].

#### **5.6.1.1. Surface properties**

Carbon materials are the most widely used anodes in the present MFCs studies; they traditionally including graphite rod, graphite fiber brush, carbon cloth, carbon paper, carbon felt, and reticulated vitreous carbon (RVC) [27]. To improve the catalytic and surface properties of graphite and carbon, these materials have been modified with various electron mediating molecules or catalytic layers. In 2002, Park and Zeikus [52] proposed the use of graphite that was coated with electron mediators, such as  $Mn^{4+}$  or neutral red, which could increase the power output 10 fold. In 2006, Rosenbaum et al. [54] presented tungsten carbide coated carbon electrodes, which increased the power of a glucose fed MFC two-fold. Polytetrafluoroethylene (PTFE), a polymer frequently used in chemical fuel cell, has also been suggested to be able to increase the active surface area [55]. In 2007, Scott et al. [56] thoroughly investigated several methods to modify graphite electrodes, including the use of polyaniline, carbon nanofibers, activated carbon and combinations of these. All modified carbon materials worked better than unmodified graphite felt and graphite felt modified with quinone groups (by  $C/HNO_3$  treatment) showed the greatest improvement and resulted in a three-fold improvement. An ammonia treatment is another efficient modification method to improve the reactivity of the anode graphite [57]. By this treatment, the startup time of the MFC was shortened by 50% and the power output increased by 48%. The improvement is attributed to the increased surface charge of the treated carbon electrodes. In the present, the modification of electrode materials proved to be an effective way to improve the performance of MFCs because it changed the physical and chemical properties to provide for better microbial attachment and electron transfer.

#### **5.6.1.2. Structure**

Next to the surface properties, the structure of the electrodes determines the performance of MFCs. A switch from electrode materials with mainly two-dimensional properties, such as graphite plates, to three-dimensional materials, which completely fill the anode compartment, such as graphite granules, allowed a significant increase of the active surface of the anode, i.e. the ratio between its surface and volume, and has resulted in a two-fold increase of the power output [58]. It was previously reported that the use of graphite felt as the electrode

material could increase the power output three-fold compared to the use of a graphite rod in the same reactor. Another approach i.e. the use a graphite brush electrode, which consists of graphite fibers that are wound around a conductive but noncorrosive metal current collector, significantly (2.5 fold) improved the performance of the bioanode and the entire MFC compared to the use of two-dimensional carbon cloth or carbon paper electrodes [59]. In addition, the use of porous anodes or anode foam structures have also been reported to enhance the contact area between the substrate and the anodic bacteria and to subsequently improve the anode performance [60, 61].

### **5.6.1.3. Base material**

In the study of MFCs, carbon-based materials are generally regarded as the most versatile electrodes materials. Although carbon and graphite have good properties as an electrode material, their resistivity toward the flow of electrons is typically 1000 times higher compared to metals [62]. Stainless steel, which had been suggested as an electrode material [63], exerted a great performance when used as the cathode material, but was considerably less effective as an anode [64]. The reasons for this low effectiveness remain to be investigated. Recently, ter Heijne et al. [65] reported that that uncoated titanium was unsuitable as an anode material. Kargi and Eker [66] suggested the use of copper or copper alloys as potential anode materials, but their performance was largely comparable to that of graphite. Moreover, due to its solubility, copper is toxic for anodic bacteria.

### **5.6.2. Electrolyte**

In classical electrochemical systems, higher electrolyte conductivity ensures higher performance system, but in microbial systems this parameter should not go beyond the salinity tolerance level of microbes [67]. Typical power densities of MFCs vary from 2 to 3 W/m<sup>2</sup> projected area of cathode, at 30 °C with neutral to slightly alkaline well buffered electrolyte of about 20 mS/cm conductivity [68]. In addition, current density per volume of electrolyte solution should be used only for well-defined practical objectives, for instance to compare the compactness of different set-ups. The combination of inoculum and substrate/electrolyte selected plays a key role on the performance of microbial electrochemical systems [67].

### 5.6.3. Membrane

The majority of MFC designs require the separation of the anode and the cathode compartments by a cation exchange membrane (CEM). Exceptions are naturally separated systems such as sediment MFCs [69] or specially designed single-compartment MFCs [70, 71]. The most commonly used CEM is Nafion (Dupont Co., USA), which is available from numerous suppliers (e.g., Aldrich and Ion Power, Inc.). Alternatives to Nafion, such as Ultrex CMI-7000 (Membranes International Incorp., Glen Rock, NJ) also are well suited for MFC applications [22] and are considerably more cost-effective than Nafion. When a CEM is used in an MFC, it is important to recognize that it may be permeable to chemicals such as oxygen, ferricyanide, other ions, or organic matter used as the substrate. The market for ion exchange membranes is constantly growing, and more systematic studies are necessary to evaluate the effect of the membrane on performance and long-term stability [72].

### 5.7. MFC design

Many different configurations are possible for MFCs (Figures 5.3 and 5.4). A widely used and inexpensive design is a two chamber MFC built in a traditional “H” shape, consisting usually of two bottles connected by a tube containing a separator which is usually a cation exchange membrane (CEM) such as Nafion [25, 26, 28, 45] or Ultrex [73], or a plain salt bridge [28] (Figure 5.3a to 5.3f). The key to this design is to choose a membrane that allows protons to pass between the chambers (the CEM is also called a proton exchange membrane, PEM), but optimally not the substrate or electron acceptor in the cathode chamber. As long as the two chambers are kept separated, they can be pressed up onto either side of the membrane and clamped together to form a large surface (Figure 5.3b). The amount of power that is generated in these systems is affected by the surface area of the cathode relative to that of the anode [32] and the surface of the membrane [50]. In contrast, the salt bridge MFC produces little power due the high internal resistance observed [28]. Using ferricyanide as the electron acceptor in the cathode chamber increases the power density due to the availability of a good electron acceptor at high concentrations, but its use is restricted to fundamental laboratory studies. The cathode can also be placed in direct contact with air (Figures 5.3e, 5.4c, 5.4d), either in the presence or absence of a membrane [70]. Much larger power densities have been achieved using oxygen as the electron acceptor when aqueous-cathodes are replaced with air-cathodes. Several variations on these basic designs have emerged in an effort to increase power density or provide for continuous flow through the anode chamber (in contrast to the above systems which were all operated in batch mode). Systems have been designed with an

outer cylindrical reactor with a concentric inner tube that is the cathode [74, 75] (Figure 5.4d), and with an inner cylindrical reactor (anode consisting of granular media) with the cathode on the outside [76] (Figure 5.4a). Another variation is to design the system like an upflow fixed-bed biofilm reactor, with the fluid flowing continuously through porous anodes toward a membrane separating the anode from the cathode chamber [77] (Figure 5.4b). Systems have been designed to resemble hydrogen fuel cells, where a CEM is sandwiched between the anode and cathode (Figure 5.4c). To increase the overall system voltage, MFCs can be stacked with the systems shaped as a series of flat plates or linked together in series [29] (Figure 5.4e).

Due to their complex designs, two-compartment MFCs are difficult to scale-up even though they can be operated in either batch or continuous mode. One compartment MFCs (see Figure 5.4d) offer simpler designs and cost savings. They typically possess only an anodic chamber without the requirement of aeration in a cathodic chamber. Park and Zeikus [78] designed a one compartment MFC consisting of an anode in a rectangular anode chamber coupled with a porous air-cathode that is exposed directly to the air. Protons are transferred from the anolyte solution to the porous air-cathode [78]. Many designs of one compartment MFCs have been proposed and studied [70, 76, 78], its application is of great interest to practical implementation of scale-up of MFCs.

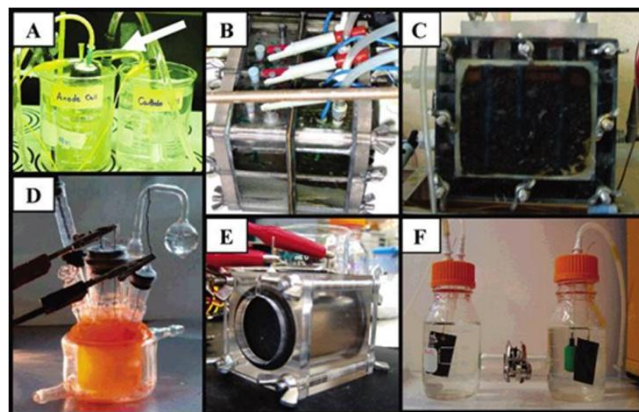


**Figure 5.3.** Types of MFCs used in studies [79]: (a) easily constructed system containing a salt bridge [28]; (b) four batch-type MFCs where the chambers are separated by the membrane (without a tube) and held together by bolts [23]; (c) same as B but with a continuous flow-through anode (granular graphite matrix) and close anode-cathode placement [58]; (d) photoheterotrophic type MFC [80]; (e) single-chamber, air-cathode system in a simple “tube” arrangement [70]; (f) two-chamber H-type system showing anode and cathode chambers equipped for gas sparging [45]

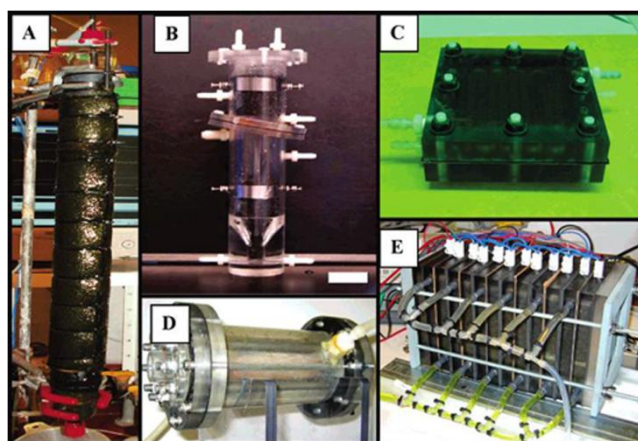


**Figure 5.4.** MFCs used for continuous operation [79]: (a) upflow, tubular type MFC with inner graphite bed anode and outer cathode [76]; (b) upflow, tubular type MFC with anode below and cathode above, the membrane is inclined [77]; (c) flat plate design where a channel is cut in the blocks so that liquid can flow in a serpentine pattern across the electrode [20]; (d) single-chamber system with an inner concentric air cathode surrounded by a chamber containing graphite rods as anode [75]; (e) stacked MFC, in which 6 separate MFCs are joined in one reactor block [29]

## 5.8. Effect of operating conditions

So far, performances of laboratory MFCs are still much lower than the ideal performance. There may be several possible reasons. Power generation of an MFC is affected by many factors including microbe type, fuel biomass type and concentration, ionic strength, pH, temperature, and reactor configuration [18]. With a given MFC system, the following operating parameters can be regulated to decrease the polarizations in order to enhance the performance of an MFC.

### 5.8.1. Substrate

To date, many organic substrates have been investigated as possible energy sources to generate electricity using MFCs ranging from carbohydrates (glucose, sucrose, cellulose, starch), volatile fatty acids (formate, acetate, butyrate), alcohols (ethanol, methanol), amino acids, proteins and even inorganic components such as sulfides or acid mine drainages [45, 57, 81-83]. In order to benchmark new MFC components, reactor designs or operational conditions, acetate is commonly used as a substrate because of its inertness towards

alternative microbial conversions (fermentations and methanogenesis) at room temperature. This results in high Coulombic efficiencies of up to 98% [76] and high power outputs of up to  $115 \text{ W/m}^3$  [57] for mixed anodophilic cultures.

Although the use of a pure or single substrate allows to study the metabolic processes and conversion products during the microbial conversion, it is not feasible to power full scale MFCs with pure substrates from an economical point of view. In that perspective, the use of second generation bio-fuels or organic waste streams is highly promising because it allows to combine the actual treatment of the waste stream with the generation of energy. A range of more complex organics, containing a large variety of different readily and non-readily degradable molecules such as domestic wastewater [70], brewery wastewater [84], paper recycling wastewater [85] have been demonstrated to generate electrical power in MFCs. Nevertheless, the power outputs using wastewater are about a factor 10 lower compared to pure substrates [86, 87]. Moreover, the composition of the wastewater is strongly affecting the power output of MFCs.

The type of substrate fed to a MFC potentially has an impact on the structure and composition of the microbial community. The more reduced the substrate is, the more energy there is available to divide across the community. This may lead to an increase of the possible interactions and niches. Up till now, no clear image of the effect of the type of substrate on the microbial community is available [75].

### **5.8.2. pH buffer and electrolyte**

If no buffer solution is used in a working MFC, there will be an obvious pH difference between the anodic and cathodic chambers, though theoretically there will be no pH shift when the reaction rate of protons, electrons and oxygen at the cathode equals the production rate of protons at the anode. The PEM causes transport barrier to the cross membrane diffusion of the protons, and proton transport through the membrane is slower than its production rate in the anode and its consumption rate in the cathode chambers at initial stage of MFC operation thus brings a pH difference [88]. However, the pH difference increases the driving force of the proton diffusion from the anode to the cathode chamber and finally a dynamic equilibrium forms. Some protons generated with the biodegradation of the organic substrate transferred to the cathodic chamber are able to react with the dissolved oxygen or electron acceptor while some protons are accumulated in the anodic chamber when they do not transfer across the PEM or salt bridge quickly enough to the cathodic chamber. Gil et al. [88] detected a pH difference of 4.1 (9.5 at cathode and 5.4 in anode) after 5-hour operations

with an initial pH of 7 without buffering. With the addition of a phosphate buffer (pH 7.0), pH shifts at the cathode and anode were both less than 0.5 unit and the current output was increased about 1 to 2 folds. It was possible that the buffer compensated the slow proton transport rate and improved the proton availability for the cathodic reaction. In 2004, Jang et al. [89] supplied an HCl solution to the cathode and found that the current output increased by about one fold. This again suggests that the proton availability to the cathode is a limiting factor in electricity generation. Increasing ionic strength by adding NaCl to MFCs also improved the power output [18, 89], possibly due to the fact that NaCl enhanced the conductivity of both the anolyte and the catholyte.

### **5.8.3. Proton exchange system**

Proton exchange system can affect an MFC system's internal resistance and concentration polarization loss and they in turn influence the power output of the MFC. Despite attempts by researchers to look for less expensive and more durable substitutes, Nafion is still the best choice. However, side effect of other cations transport is unavoidable during the MFC operation even with Nafion. In a batch accumulative system, for example, transportation of cation species other than protons by Nafion dominates the charge balance between the anodic and cathodic chambers because concentrations of  $\text{Na}^+$ ,  $\text{K}^+$ ,  $\text{NH}_4^+$ ,  $\text{Ca}^{2+}$ ,  $\text{Mg}^{2+}$  are much higher than the proton concentrations in the anolyte and catholyte [72]. In this sense, Nafion as well as other PEMs used in the MFCs are not a necessarily proton specific membranes but actually cation specific membranes (CEM). The ratio of PEM surface area to system volume is important for the power output. The PEM surface area has a large impact on maximum power output if the power output is below a critical threshold. The MFC internal resistance decreases with the increase of PEM surface area over a relatively large range [50]. Membrane-less MFCs are desired if fouling or cost of the membrane becomes a problem in such applications.

### **5.8.4. Operating conditions in the anodic chamber**

Fuel type, concentration and feed rate are important factors that impact the performance of an MFC. With a given microbe or microbial consortium, power density varies greatly using different fuels. Table 5.1 shows the performances of some MFCs operated using different microbes and substrates [34]. Many systems have shown that electricity generation is dependent on fuel concentration both in batch and continuous-flow mode MFCs. Usually a higher fuel concentration yields a higher power output in a wide concentration range. Park

and Zeikus [52] reported that a higher current level was achieved with lactate (fuel) concentration increased until it was in excess at 200 mM in a single-compartment MFC inoculated with *S. putrefaciens*. Moon et al. [90] investigated the effects of fuel concentration on the performance of an MFC. Their study also showed that the power density was increased with the increase in fuel concentration [90]. Gil et al. [88] found that the current increased with a wastewater concentration up to 50 mg/L in their MFC. Interestingly, the electricity generation in an MFC often peaks at a relatively low level of feed rate before heading downward. This may be because a high feed rate promoted the growth of fermentative bacteria faster than those of the electrochemically active bacteria in a mixed culture [73, 90, 91]. However, if microbes are growing around the electrodes as biofilms, the increased feed rate is unlikely to affect the flora. One possible reason is that the high feed rate brings in other alternate electron acceptors competing with the anode to lower the output.

#### **5.8.5. Operating conditions in the cathodic chamber**

Oxygen is the most commonly used electron acceptor in MFCs for the cathodic reaction. Power output of an MFC strongly depends on the concentration level of electron acceptors. Several studies [32, 88] indicated that oxygen demand (DO) was a major limiting factor when it remained below the air-saturated level. Surprisingly, a catholyte sparged with pure oxygen that gave 38 mg/L DO did not further increase the power output compared to that of the air-saturated water (at 7.9 mg/L DO) [20, 32]. Rate of oxygen diffusion toward the anode chamber goes up with the DO concentration. Thus, part of the substrate is consumed directly by the oxygen instead of transferring the electrons through the electrode and the circuit [92]. Power output is much greater using ferricyanide as the electron acceptor in the cathodic chamber. So far, reported cases with very high power outputs such as 7200 mW/m<sup>2</sup>, 4310 mW/m<sup>2</sup> and 3600 mW/m<sup>2</sup> all used ferricyanide in the cathodic chamber [32, 93], while less than 1000 mW/m<sup>2</sup> was reported in studies using DO regardless of the electrode material. This is likely due to the greater mass transfer rate and lower activation energy for the cathodic reaction offered by ferricyanide [32]. Using hydrogen peroxide solution as the final electron acceptor in the cathodic chamber increased power output and current density according to [94]. As a consequence, aeration is no longer needed for single compartment MFCs with a cathode that is directly exposed to air. Rhoads et al. [30] measured the cathodic polarization curves for oxygen and manganese and found that reducing manganese oxides delivered a current density up to 2 orders of magnitude higher than that by reducing oxygen. Surely changing operating conditions can improve the power output level of the MFCs. However, it

is not a revolutionary method to upgrade the MFCs from low power system to an applicable energy source at the very present. The bottleneck lies in the low rate of metabolism of the microbes in the MFCs. Even at their fastest growth rate (i.e.  $\mu_{\max}$  value) microbes are relatively slow transformers. The biotransformation rate of substrates to electrons has a fixed ceiling which is inherently slow. Effort should be focused on how to break the inherent metabolic limitation of the microbes for the MFC application. High temperature can accelerate nearly all kinds of reactions including chemical and biological ones.

## **5.9. Electrochemical characterization techniques**

Electrochemical/analytical techniques have an essential role in this continuing process; they are vitally important in analyzing the limiting performances of each component, to optimize MFC operation, and to allow continued innovation. The following sections briefly introduce MFCs from an electrochemical point of view, before discussing the suitability of the various techniques that can be used in studying these complicated systems.

### **5.9.1. Choice of electrode configuration**

Two- and three-electrode configurations are commonly employed to determine MFC and electrode performances; a four-electrode configuration is sometimes used when the conductivity of an electrolyte (membrane) or electrode material is tested by electrochemical impedance spectroscopy (EIS) [95]. In practice, a MFC only needs two electrodes for electricity generation, an anode and a cathode. The measurement of a cathode–anode two electrode configuration represents the overall MFC performance, which will be limited by many factors and is rarely completely reproducible due to changes in the growth, evolution, and metabolism of the consortium of microbes present. In order to avoid unwanted perturbations to the system and to simplify studies, a reference electrode (RE) and a counter electrode (CE, sometimes called an auxiliary electrode) are often introduced into a MFC in order to analyze the behavior of an individual working electrode (WE), which can either be the anode or cathode: this is then a three-electrode configuration.

### **5.9.2. Open Circuit voltage**

The open circuit voltage (OCV) is the voltage of a MFC under a no-load condition (no current generation) and can be measured with a high impedance voltmeter or potentiometer in a two-electrode configuration between anode-cathode chambers. For example, a typical measured potential of a cathode using oxygen at pH 7 is about 0.2 V. This is clearly lower

than the expected value of 0.805 V, indicating the large energy loss occurring at the cathode. This energy loss is often referred to as overpotential, or the difference between the potential under equilibrium conditions and the actual potential, which for this case is 0.605 V (0.805 V - 0.2 V). This illustrates that the main application of thermodynamic calculations is to identify the size and nature of energy losses [79, 95].

### 5.9.3. MFC polarization techniques

The term “polarization” is the change of electrode potential or MFC voltage from its equilibrium state due to a flow of current. Polarization curves are plots of electrode potential (or MFC voltage) as a function of current or current density. There are four options for the measurement of MFC polarization discharge curves: (a) constant resistance discharge measured by connecting different resistors to the MFC and measuring the resulting currents and voltages; (b) potentiodynamic polarization, i.e. linear sweep voltammetry (LSV) where current is measured with slow voltage scan rate (e.g. 1 mV/s); (c) galvanostatic discharge, where the current is controlled and the resulting voltages measured; and (d) potentiostatic discharge, where the voltage is controlled and the resulting currents measured.

The factors affecting the steady state operation for MFCs are much more complicated than for traditional electrochemical systems. It is difficult to record a credible steady state polarization curve with a MFC for the following principal reasons: (a) the nature of the microbial species/communities is evolving with time and electrode potential, with concurrent changes in the biofilm (for chemical fuel cells, the composition and structure of catalysts change only very slowly with time via various degradation reactions, < 100  $\mu$ V/h in the best systems); (b) the concentrations of electroactive metabolites and/or substrate may also be constantly changing with time and potential (chemical fuel cells supplied with gases can be tested or operated with very precise and constant fuel/oxidant supplies); finally (c) the mechanisms of electrode reactions and operational conditions may be different for each different type of MFC, each requiring different sampling rates. MFCs can exhibit stable behavior in simple time-related voltage and current experiments using fixed resistance load, but long-term polarization testing requires caution as there is a continual risk of the presence of the above changes [79, 96].

An ideal polarization curve for a power generation device (MFC or chemical fuel cell) includes three characteristic regions located at different current ranges (either well segregated, as is typical with chemical fuel cells, or with varying and significant levels of overlap, as is more typical with MFCs) as shown in Figure 5.3a and summarized below [79]:

(a) the region of activation losses (region A), (b) the region of ohmic losses (region B) and (c) the region of mass transfer losses. For more details see Section 6.9.

#### 5.9.4. Current interruption (CI)

Current interruption (CI) techniques have been used extensively to measure the internal ohmic resistance of chemical fuel cells and more recently of MFCs [96]. As shown in Figure 5.5, the basic principle of the CI is to interrupt the current flow and to observe the resulting voltage transients. On current interruption, the ohmic overpotential is separated from other overpotentials as the former is a near instantaneous process, whereas the relaxation times for other voltage loss phenomena are significantly longer. CI measurements can be conducted using low cost electronic equipment, and resulting data are easily interpreted. The primary disadvantage is that very short duration ( $< 10 \mu\text{s}$ ) measurements of the perturbation to the system are required for precise and accurate determinations, and it is possible to overestimate the voltage changes if data collection is not rapid enough (sample rate is too low). Another disadvantage of using CI is that it is difficult to distinguish between charge transfer and mass transfer impedances [95].

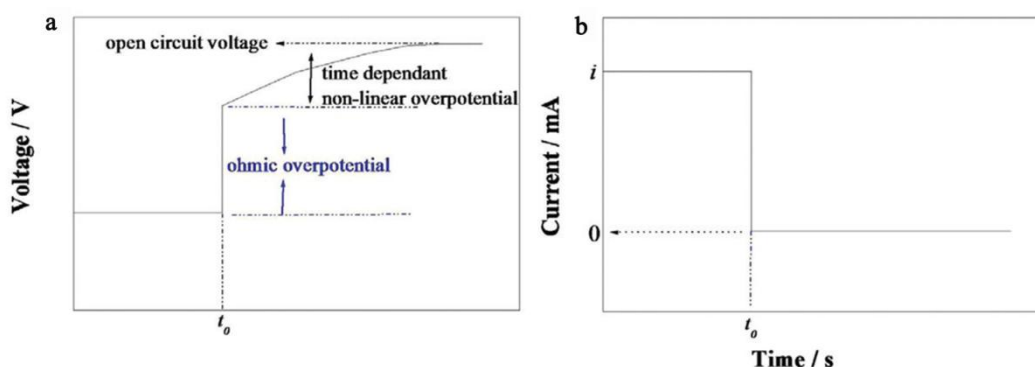


**Figure 5.5.** An ideal voltage transient in a MFC after current interruption. The MFC is firstly operated at a fixed current, and then current is interrupted at  $t_0$  [95]

#### 5.9.5. Electrochemical impedance spectroscopy

Electrochemical impedance spectroscopy (EIS) takes advantage of the large spectrum of time scales over which different processes occur in the system being studied. It is a powerful tool for examining chemical and physical processes in solutions, at solid–liquid interfaces and at solid–solid interfaces, as it allows the separation of the different voltage loss phenomena [97–99]. There are two common graphical representations used in EIS: Nyquist plots and Bode plots as is shown in Figure 5.6. The main shortcoming of Nyquist plots is that they do not

show the frequency represented by each data point (each point being a representation of the impedance vector in the complex plane at a particular frequency); Bode plots show this frequency information as they are plots of the magnitude and phase angle of the impedance vector versus frequency [95]. EIS data collection and analysis, especially when equivalent circuit modelling is used to interpret results and the reaction mechanism of electrode is not well known. Each EIS equivalent circuit element introduced (resistor, capacitance or inductor) must represent something in the real system. The use and analysis of EIS in MFCs context are still emerging. For this propose, detailed information on the internal ohmic resistances, and on the charge and mass transfer impedances, can be obtained on the analysis of correctly collected EIS spectra. For example, the Nyquist plot and the Bode plots of a single chamber MFC with an air cathode developed for wastewater treatment are shown in Figure 5.6. The internal ohmic resistance is often determined by the high frequency intercept of the curve with the real impedance axis ( $Z_{re}$ —the  $x$ -axis) [97]. The internal ohmic resistances recorded using EIS data are much more accurate than when using simple single frequency resistance measurements. EIS can, like CI, overestimate internal ohmic resistances, especially at high d.c. discharge current densities; however, this overestimation tends to occur at current densities of  $> 0.5 \text{ A/cm}^2$  (geometric) achievable in  $\text{H}_2/\text{O}_2$  chemical fuel cells, which are unlikely to be achieved with MFCs. With EIS technique the conductivity of electrode materials and membranes can be easily measured [95]. EIS has been applied additionally for the detection of the environmental limiting processes in MFCs, such as the effect of pH and biofilm formation on the electrodes [99, 100].

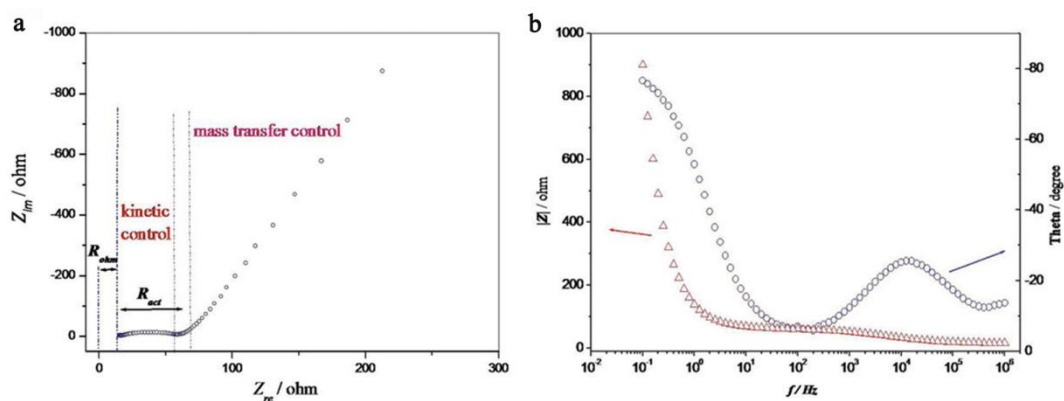


**Figure 5.6.** (a) A Nyquist plot and (b) a Bode plot of the impedance spectrum of a single chamber MFC measured with two-electrode configuration under open circuit voltage. The frequency range was  $10^6$ – $0.1 \text{ Hz}$  with a potential perturbation signal of  $10 \text{ mV rms}$ .  $R_{ohm}$  was the internal ohmic resistance,  $R_{act}$ , was the charge transfer “resistance” [95]

### 5.9.6. Cyclic voltammetry

In MFC studies, CV experiments have been used extensively to: (i) investigate the mechanisms of electrode reactions involving both direct and indirect electron transfer between the biofilm and the electrode; (ii) determine the redox potentials of the chemical or biological species involved at the anode or cathode (for a reversible redox couple, the average of the cathodic and anodic peak gives the reversible potential for that couple referenced against the RE being employed); and (iii) to evaluate the performance of the catalysts being studied [95].

CV is a simple technique and results are obtained in a relatively short time. However, background experiments (with blank electrolyte) are mandatory for high quality mechanistic studies. When microbial communities are present in MFC chambers, the peak current and the peak potential coming from the electrode interface reactions might involve direct electron transfer and/or indirect electron transfer. For complex systems, where there are many unknowns (especially relevant to wastewaters), the following CV testing protocols are recommended, as a minimum, to aid understanding: (a) Effects of electrode and electrolyte: Employ a biofilmless electrode in un-inoculated or abiotic electrolyte; (b) Effect of the biofilm: Employ a biofilm-coated electrode in the un-inoculated or abiotic electrolyte; (c) Effect of the substrate: Employ a biofilm-less and a biofilm-coated electrode in the un-inoculated or abiotic electrolyte with the addition of fresh substrate; (d) Effects of the suspended cells: Employ a biofilm-less electrode in an inoculated electrolyte; (e) Effect of the metabolites: Employ a biofilm-less electrode in the inoculated electrolyte with consumed substrate(s) [79, 95].

The characteristics of CV depend on several factors, such as the electrode surface pretreatment, the rate of the electron transfer reactions, the chemical and biological species present and their thermodynamic properties, the concentration of electroactive species and their rates of diffusion and the sweep rate. It should be noted that many electrode materials used in MFCs cannot produce reversible electrochemical reactions even for the classic reversible redox couple  $\text{Fe}(\text{CN})_6^{3-}/\text{Fe}(\text{CN})_6^{4-}$ . The main reason for this is that the heterogeneous processes of electrode reactions can be significantly affected by the microstructure, roughness and function groups present on the electrode surface [79, 95].

Electrochemical/analytical techniques have an essential role in this continuous process; they are vitally important in analyzing the limiting performances of each component, to optimize MF operation, and to allow continued innovation. More details with respect to the common electrochemical characterization used in MFC system are discussed in [79, 95, 99].

## 5.10. Factors limiting the electrical energy generation

The microbial conversion of substrates is a key process to generate electricity in MFCs. Despite, the microbial nature of the process, it is affected by electrochemical laws and principles which generally results in a lowering of the attainable voltage. The main electrical principles and the processes governing these losses are briefly described. Subsequently, the various conversions efficiencies are discussed.

### 5.10.1. Electrical parameters

Due to the positive potential difference ( $\Delta E$ ) between the poles of the MFC, the flow of electrons ( $I$ ) generates a useful power ( $P$ ) according to:  $P = I \times \Delta E$ . The ratio between the voltage and the current is determined by the external resistance ( $R_{ext}$ ) according to Ohms law:  $\Delta E = I \times R_{ext}$ . When the external resistance is infinite (open circuit conditions) no current flows and the open circuit voltage (OCV) is obtained. Conversely, when the  $R_{ext}$  is zero (short circuit conditions;  $\Delta E = \text{zero}$ ) the short circuit current ( $I_{SCC}$ ) is generated [101].

Alternatively, the relation between the cell voltage and the current (density) can be visualized by a polarization curve (Figure 5.7). From the polarization curve, the power performance curve can be calculated (Figure 5.7). The latter presents the relation between the power generation for a given current. The power delivered by a fuel cell is maximized when the external load matches the internal resistance of the fuel cell system [102]. Due to losses of any kind (see below), these curves are unfortunately not straight lines but they have a typical pattern (Figure 5.7).

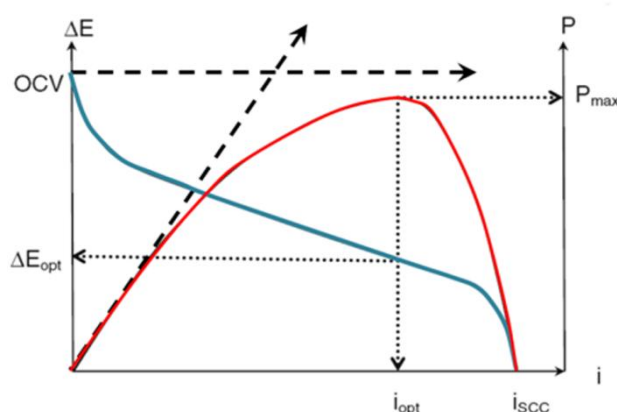


**Figure 5.7.** The polarization curve (blue), with the respective open circuit voltage (OCV) and  $i_{SCC}$  (short circuit current density) and the power performance curve (red), with the maximum power density ( $P_{max}$ ). From the point of maximum power density, the optimal voltage ( $E_{opt}$ ) and optimal current density ( $i_{opt}$ ) can be deduced. The striped lines indicate the ideal theoretical polarization curve and power performance curve in case no losses occur [87]

### 5.10.2. Activation losses

In order to start the transfer of electrons from the electrochemical active microorganisms (EAM) towards the electrode or to transfer electrons towards a final electron acceptor, an energy barrier needs to be overcome, which results in a voltage loss or activation overpotential [27, 101]. Activation losses are characterized by an initial steep decrease of the cell voltage at the onset of the electricity generation (region A of Figure 5.8). As the current steadily increases, the other losses e.g. ohmic and mass transfer losses become proportionally more important. Low activation losses can be achieved by increasing the electrode surface area, improving the electrode catalysis, increasing the operating temperature, and in case of the microbial catalysis, through the establishment of an enriched biofilm on the electrode(s). It is hypothesized that microorganisms can lower the activation overpotential and thus increase their metabolic energy gain by optimizing their electron transferring strategies [79, 101].

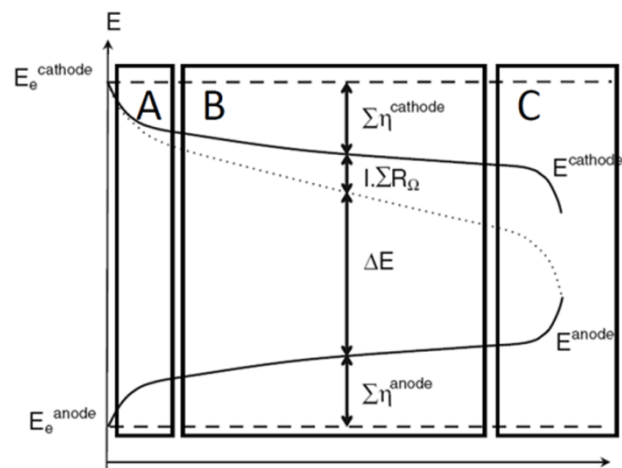


**Figure 5.8.** A cathodic ( $E^{\text{cathode}}$ ) and anodic ( $E^{\text{anode}}$ ) polarization curve indicating the region of activation losses (region A), the ohmic losses (region B) and mass transfer losses (region C). The cell voltage is represented by  $\Delta E$ , the losses by  $\eta$  and the ohmic loss by  $I \cdot \Sigma R_{\Omega}$ . The equilibrium potentials of the electrodes are indicated by  $E_e^{\text{cathode}}$  and  $E_e^{\text{anode}}$ . It is assumed that the reference electrode is placed near the anode [87]

### 5.10.3. Ohmic losses

The flow of electrons is hampered by the resistance of the electrode material, which introduces an ohmic voltage loss. The higher the conductivity of the electrode material and the lower the contact losses and travel distance of the electrons within the electrode, the more efficient are the electron conduction and the lower the ohmic loss. In general the ohmic losses are proportionally most determinative in region B of Figure 5.8. There are several techniques

to characterize the ohmic losses in an MFC, such as polarization curve, the current interrupt method and electrochemical impedance spectroscopy [79, 87, 101].

#### **5.10.4. Mass transfer**

The supply of sufficient substrate to the anodic biofilm and electron acceptor to the cathode surface at rates of at least the equivalent of the current generation is crucial to sustain the current generation. In addition, the accumulation of waste products in the biofilm, *e.g.* oxidized intermediates or protons, needs to be prevented as this might change the redox conditions and hamper the metabolic activity of the biofilm. A limited mass transfer of substrate or electron acceptors towards the anode or cathode respectively, can result in concentration or mass transfer losses [27]. Generally, mass transfer losses are characterized by a steep decrease of the cell voltage at near maximum current densities during polarization (Region C of Figure 5.8). In addition, a poor transfer of protons can cause the development of a pH gradient on the electrodes and between the anode and the cathode compartments. Both seriously affect the MFC performance [101, 103, 104].

#### **5.10.5. Electron quenching reactions and energy efficiency**

Substrate competing processes, such as fermentation or methanogenesis and respiration (if oxygen intrudes), result in a loss of electrons [70, 77]. Also, part of the substrate is inherently converted into anodophilic biomass. Moreover, a leakage of substrate towards the cathode results in a potential electron loss. All these processes lower the conversion of substrate into current which is expressed by the Coulombic efficiency (CE). The CE is defined as the ratio of the amount of substrate administered and the amount of electrons recovered. The ratio between the actual cell voltage ( $\Delta E$ ) and the OCV is determined as the potential efficiency (PE) [105]. By multiplying the CE and the PE, the energy conversion efficiency (ECE) is obtained. It is not possible to simultaneously maximize both the power density and the energy conversion efficiency. As a consequence, the energy conversion efficiency of a fuel cell is only 50% when power density is maximized [102]. In general, the fuel efficiency increases as the ratio of the external load to the internal resistance increases, however in this case the power output decreases [101].

### **5.11. References**

[1] I.A. Ieropoulos, J. Greenman, C. Melhuish, J. Hart, *Enzyme and microbial technology*, 37 (2005) 238-245.

- [2] M.C. Potter, Proceedings of the Royal Society of London. Series B, Containing Papers of a Biological Character, (1911) 260-276.
- [3] B. Cohen, Journal of Bacteriology, 21 (1931) 18-19.
- [4] R.S. Berk, J.H. Canfield, Applied microbiology, 12 (1964) 10-12.
- [5] W. van Hees, Journal of The Electrochemical Society, 112 (1965) 644.
- [6] D.H. Park, J.G. Zeikus, Applied and Environmental Microbiology, 66 (2000) 1292-1297.
- [7] T. Ikeda, K. Kano, Biochimica et Biophysica Acta (BBA) - Proteins and Proteomics, 1647 (2003) 121-126.
- [8] C.A. Vega, I. Fernández, Bioelectrochemistry and Bioenergetics, 17 (1987) 217-222.
- [9] R.M. Allen, H.P. Bennetto, Applied Biochemistry and Biotechnology, 39 (1993) 27-40.
- [10] B.-H. Kim, H.-J. Kim, M.-S. Hyun, D.-H. Park, Journal of Microbiology and Biotechnology, 9 (1999) 127-131.
- [11] S.K. Chaudhuri, D.R. Lovley, Nature biotechnology, 21 (2003) 1229-1232.
- [12] F. Scholz, U. Schröder, Nature biotechnology, 21 (2003) 1151-1152.
- [13] H.J. Kim, H.S. Park, M.S. Hyun, I.S. Chang, M. Kim, B.H. Kim, Enzyme and microbial technology, 30 (2002) 145-152.
- [14] D.R. Bond, D.R. Lovley, Applied and Environmental Microbiology, 69 (2003) 1548-1555.
- [15] D. Prasad, T.K. Sivaram, S. Berchmans, V. Yegnaraman, Journal of Power Sources, 160 (2006) 991-996.
- [16] K.B. Gregory, D.R. Bond, D.R. Lovley, Environmental microbiology, 6 (2004) 596-604.
- [17] A. Bergel, D. Féron, A. Mollica, Electrochemistry Communications, 7 (2005) 900-904.
- [18] H. Liu, S. Cheng, B.E. Logan, Environmental science & technology, 39 (2005) 5488-5493.
- [19] E. Zhang, W. Xu, G. Diao, C. Shuang, Journal of Power Sources, 161 (2006) 820-825.
- [20] B. Min, B.E. Logan, Environmental science & technology, 38 (2004) 5809-5814.
- [21] S. Das, N. Mangwani, Journal of Scientific and Industrial Research, 69 (2010) 727-731.
- [22] K. Rabaey, N. Boon, S.D. Siciliano, M. Verhaege, W. Verstraete, Applied and Environmental Microbiology, 70 (2004) 5373-5382.
- [23] K. Rabaey, N. Boon, M. Höfte, W. Verstraete, Environmental science & technology, 39 (2005) 3401-3408.
- [24] Y.A. Gorby, S. Yanina, J.S. McLean, K.M. Rosso, D. Moyles, A. Dohnalkova, T.J. Beveridge, I.S. Chang, B.H. Kim, K.S. Kim, Proceedings of the National Academy of Sciences, 103 (2006) 11358-11363.

- [25] D.R. Bond, D.E. Holmes, L.M. Tender, D.R. Lovley, *Science*, 295 (2002) 483-485.
- [26] D. Park, J. Zeikus, *Journal of Bacteriology*, 181 (1999) 2403-2410.
- [27] B.E. Logan, J.M. Regan, *TRENDS in Microbiology*, 14 (2006) 512-518.
- [28] B. Min, S. Cheng, B.E. Logan, *Water research*, 39 (2005) 1675-1686.
- [29] P. Aelterman, K. Rabaey, H.T. Pham, N. Boon, W. Verstraete, *Environmental science & technology*, 40 (2006) 3388-3394.
- [30] A. Rhoads, H. Beyenal, Z. Lewandowski, *Environmental science & technology*, 39 (2005) 4666-4671.
- [31] A. Shantaram, H. Beyenal, R.R.A. Veluchamy, Z. Lewandowski, *Environmental science & technology*, 39 (2005) 5037-5042.
- [32] S. Oh, B. Min, B.E. Logan, *Environmental science & technology*, 38 (2004) 4900-4904.
- [33] K. Rabaey, W. Verstraete, *TRENDS in Biotechnology*, 23 (2005) 291-298.
- [34] Z. Du, H. Li, T. Gu, *Biotechnology Advances*, 25 (2007) 464-482.
- [35] B.E. Logan, J.M. Regan, *Environmental science & technology*, 40 (2006) 5172-5180.
- [36] U. Schröder, *Physical Chemistry Chemical Physics*, 9 (2007) 2619-2629.
- [37] L. Peng, S.-J. You, J.-Y. Wang, *Biosensors and Bioelectronics*, 25 (2010) 1248-1251.
- [38] D. Xu, T. Gu, *Corrosion/2011 Paper*, (2011).
- [39] B. Sherar, I. Power, P. Keech, S. Mitlin, G. Southam, D. Shoesmith, *Corrosion Science*, 53 (2011) 955-960.
- [40] N. Kim, Y. Choi, S. Jung, S. Kim, *Biotechnology and bioengineering*, 70 (2000) 109-114.
- [41] S. Freguia, M. Masuda, S. Tsujimura, K. Kano, *Bioelectrochemistry*, 76 (2009) 14-18.
- [42] L. Deng, F. Li, S. Zhou, D. Huang, J. Ni, *Chinese Science Bulletin*, 55 (2010) 99-104.
- [43] A. Keck, J. Rau, T. Reemtsma, R. Mattes, A. Stolz, J. Klein, *Applied and Environmental Microbiology*, 68 (2002) 4341-4349.
- [44] J. Niessen, F. Harnisch, M. Rosenbaum, U. Schröder, F. Scholz, *Electrochemistry Communications*, 8 (2006) 869-873.
- [45] B.E. Logan, C. Murano, K. Scott, N.D. Gray, I.M. Head, *Water research*, 39 (2005) 942-952.
- [46] D. Holmes, D. Bond, R. O'neil, C. Reimers, L. Tender, D. Lovley, *Microbial ecology*, 48 (2004) 178-190.
- [47] J.H. Back, M.S. Kim, H. Cho, I.S. Chang, J. Lee, K.S. Kim, B.H. Kim, Y.I. Park, Y.S. Han, *FEMS microbiology letters*, 238 (2004) 65-70.
- [48] D.R. Lovley, *microbiological reviews*, 55 (1991) 259.

- [49] M. Vargas, K. Kashefi, E.L. Blunt-Harris, D.R. Lovley, *Nature*, 395 (1998) 65-67.
- [50] S.-E. Oh, B.E. Logan, *Applied Microbiology and Biotechnology*, 70 (2006) 162-169.
- [51] H.S. Park, B.H. Kim, H.S. Kim, H.J. Kim, G.T. Kim, M. Kim, I.S. Chang, Y.K. Park, H.I. Chang, *Anaerobe*, 7 (2001) 297-306.
- [52] D. Park, J. Zeikus, *Applied Microbiology and Biotechnology*, 59 (2002) 58-61.
- [53] M. Zhou, M. Chi, J. Luo, H. He, T. Jin, *Journal of Power Sources*, 196 (2011) 4427-4435.
- [54] M. Rosenbaum, F. Zhao, U. Schröder, F. Scholz, *Angewandte Chemie International Edition*, 45 (2006) 6658-6661.
- [55] T. Zhang, C. Cui, S. Chen, X. Ai, H. Yang, P. Shen, Z. Peng, *Chemical communications*, (2006) 2257-2259.
- [56] K. Scott, G. Rimbu, K. Katuri, K. Prasad, I. Head, *Process Safety and Environmental Protection*, 85 (2007) 481-488.
- [57] S. Cheng, B.E. Logan, *Electrochemistry Communications*, 9 (2007) 492-496.
- [58] K. Rabaey, W. Ossieur, M. Verhaege, W. Verstraete, *Water Science & Technology*, 52 (2005) 515-523.
- [59] B. Logan, S. Cheng, V. Watson, G. Estadt, *Environmental science & technology*, 41 (2007) 3341-3346.
- [60] S. Cheng, H. Liu, B.E. Logan, *Environmental science & technology*, 40 (2006) 2426-2432.
- [61] A. Morozan, I. Stamatina, L. Stamatina, A. Dumitru, K. Scott, *Journal of Optoelectronics and Advanced Materials*, 9 (2007) 221.
- [62] R.A. Serway, R.J. Beichner, J.W. Jewett, (2000).
- [63] S. Tanisho, N. Kamiya, N. Wakao, *Journal of electroanalytical chemistry and interfacial electrochemistry*, 275 (1989) 25-32.
- [64] C. Dumas, A. Mollica, D. Féron, R. Basséguy, L. Etcheverry, A. Bergel, *Electrochimica Acta*, 53 (2007) 468-473.
- [65] A. ter Heijne, H.V. Hamelers, M. Saakes, C.J. Buisman, *Electrochimica Acta*, 53 (2008) 5697-5703.
- [66] F. Kargi, S. Eker, *Journal of Chemical Technology and Biotechnology*, 82 (2007) 658-662.
- [67] M. Sharma, S. Bajracharya, S. Gildemyn, S.A. Patil, Y. Alvarez-Gallego, D. Pant, K. Rabaey, X. Dominguez-Benetton, *Electrochimica Acta*, 140 (2014) 191-208.
- [68] B.E. Logan, K. Rabaey, *Science*, 337 (2012) 686-690.

- [69] C.E. Reimers, L.M. Tender, S. Fertig, W. Wang, *Environmental science & technology*, 35 (2001) 192-195.
- [70] H. Liu, B.E. Logan, *Environmental science & technology*, 38 (2004) 4040-4046.
- [71] S. Cheng, H. Liu, B.E. Logan, *Electrochemistry Communications*, 8 (2006) 489-494.
- [72] R.A. Rozendal, H.V. Hamelers, C.J. Buisman, *Environmental science & technology*, 40 (2006) 5206-5211.
- [73] K. Rabaey, G. Lissens, S.D. Siciliano, W. Verstraete, *Biotechnology letters*, 25 (2003) 1531-1535.
- [74] W. Habermann, E. Pommer, *Applied Microbiology and Biotechnology*, 35 (1991) 128-133.
- [75] H. Liu, R. Ramnarayanan, B.E. Logan, *Environmental science & technology*, 38 (2004) 2281-2285.
- [76] K. Rabaey, P. Clauwaert, P. Aelterman, W. Verstraete, *Environmental science & technology*, 39 (2005) 8077-8082.
- [77] Z. He, S.D. Minteer, L.T. Angenent, *Environmental science & technology*, 39 (2005) 5262-5267.
- [78] D.H. Park, J.G. Zeikus, *Biotechnology and bioengineering*, 81 (2003) 348-355.
- [79] B.E. Logan, B. Hamelers, R. Rozendal, U. Schröder, J. Keller, S. Freguia, P. Aelterman, W. Verstraete, K. Rabaey, *Environmental science & technology*, 40 (2006) 5181-5192.
- [80] M. Rosenbaum, U. Schröder, F. Scholz, *Environmental science & technology*, 39 (2005) 6328-6333.
- [81] P. Clauwaert, D. van der Ha, W. Verstraete, *Biotechnology letters*, 30 (2008) 1947-1951.
- [82] J. Heilmann, B.E. Logan, *Water Environment Research*, 78 (2006) 531-537.
- [83] S.i. Ishii, T. Shimoyama, Y. Hotta, K. Watanabe, *BMC microbiology*, 8 (2008) 6.
- [84] Y. Feng, X. Wang, B.E. Logan, H. Lee, *Applied Microbiology and Biotechnology*, 78 (2008) 873-880.
- [85] L. Huang, B. Logan, *Applied Microbiology and Biotechnology*, 80 (2008) 349-355.
- [86] P. Aelterman, K. Rabaey, P. Clauwaert, W. Verstraete, *Water Science & Technology*, 54 (2006) 9-15.
- [87] P. Clauwaert, P. Aelterman, L. De Schamphelaire, M. Carballa, K. Rabaey, W. Verstraete, *Applied Microbiology and Biotechnology*, 79 (2008) 901-913.
- [88] G.-C. Gil, I.-S. Chang, B.H. Kim, M. Kim, J.-K. Jang, H.S. Park, H.J. Kim, *Biosensors and Bioelectronics*, 18 (2003) 327-334.

- [89] J.K. Jang, T.H. Pham, I.S. Chang, K.H. Kang, H. Moon, K.S. Cho, B.H. Kim, *Process Biochemistry*, 39 (2004) 1007-1012.
- [90] H. Moon, I.S. Chang, B.H. Kim, *Bioresource Technology*, 97 (2006) 621-627.
- [91] B. Kim, H. Park, H. Kim, G. Kim, I. Chang, J. Lee, N. Phung, *Applied Microbiology and Biotechnology*, 63 (2004) 672-681.
- [92] J.K. JANG, I.S. CHANG, B.H. KIM, *Journal of Microbiology and Biotechnology*, 14 (2004) 324-329.
- [93] U. Schröder, J. Nießen, F. Scholz, *Angewandte Chemie International Edition*, 42 (2003) 2880-2883.
- [94] B. Tartakovsky, S. Guiot, *Biotechnology progress*, 22 (2006) 241-246.
- [95] F. Zhao, R.C. Slade, J.R. Varcoe, *Chemical Society Reviews*, 38 (2009) 1926-1939.
- [96] P. Aelterman, S. Freguia, J. Keller, W. Verstraete, K. Rabaey, *Applied Microbiology and Biotechnology*, 78 (2008) 409-418.
- [97] A.J. Bard, L.R. Faulkner, *Electrochemical methods: fundamentals and applications*, Wiley New York, 1980.
- [98] J.R. Varcoe, R.C. Slade, G.L. Wright, Y. Chen, *The Journal of Physical Chemistry B*, 110 (2006) 21041-21049.
- [99] X. Dominguez-Benetton, S. Sevda, K. Vanbroekhoven, D. Pant, *Chemical Society Reviews*, 41 (2012) 7228-7246.
- [100] Z. He, Y. Huang, A.K. Manohar, F. Mansfeld, *Bioelectrochemistry*, 74 (2008) 78-82.
- [101] P. Aelterman, *Microbial fuel cells for the treatment of waste streams with energy recovery*, Ghent University, 2009.
- [102] J.B. Benziger, M.B. Satterfield, W.H.J. Hogarth, J.P. Nehlsen, I.G. Kevrekidis, *Journal of Power Sources*, 155 (2006) 272-285.
- [103] S. Freguia, K. Rabaey, Z. Yuan, J. Keller, *Water research*, 42 (2008) 1387-1396.
- [104] R.A. Rozendal, H.V. Hamelers, G.J. Euverink, S.J. Metz, C.J. Buisman, *International Journal of Hydrogen Energy*, 31 (2006) 1632-1640.
- [105] H.-S. Lee, P. Parameswaran, A. Kato-Marcus, C.I. Torres, B.E. Rittmann, *Water research*, 42 (2008) 1501-1510.

## Chapter 6

### New approach for low-cost microbial fuel cells for energy sustainable waste-streams treatment

#### 6.1. Introduction

The actual bottlenecks of the MFCs technology are mainly a low power density per unit of volume and a low Coulombic yield i.e. the efficiency in converting chemical energy into electricity [1]. The research towards a significant enhancement of the MFCs performance involves two key topics: (1) the electrodes features (chemical and physical properties, micro and macro structures) and (2) the selection of the microorganisms used at the anode compartment. The material used for electrodes manufacturing should have excellent electrical conductivity, full biocompatibility, high corrosion resistance, sufficient mechanical strength and high surface area per unit volume. During the past decade, a variety of materials have been investigated, including graphite fiber brushes, graphite rods, carbon paper, carbon mesh, and carbon felt [2-5]. Carbon-based electrodes can be prepared in different configurations: planar structures, packed structures or brush structure. Examples of flat-plate structure are: carbon paper and mesh, graphite plates or sheets and carbon cloth or felt [3, 6-9]. Packed-structures are becoming increasingly common in MFC [10-15] since they increase the surface area available for bacteria growth. It is of great significance to select and develop suitable electrodes materials to optimize and promote the performances of MFCs. Moreover, as a main component, the electrode materials determine the price of MFCs and thus influence in the final wastewater treatment and output power cost.

To this purpose, this Chapter presents an experimental investigation aimed to test several low-cost commercial carbon-based materials used as electrodes of MFC. Experimental tests were carried out using a two-compartment prototype MFC. *Saccharomyces cerevisiae* (baker's yeast) was used as "model microorganism", first of all for its fair reproducibility, that permit easily to compare the performance of the different anode electrode tested and secondly for its rapid startup, easy preparation and low cost [16]. All the tests were performed at the same operating conditions using commercial carbon-based materials as anode electrode. Most of the tested materials are designed and intended for other uses [17], however their relatively low cost and easy availability might contribute significantly to the scale-up of the MFCs sustainable energy generation. The electrode materials examined

included: different carbon textiles, granules graphite, active carbon, carbon sheet, carbon felt and graphite rods. Materials were characterized from a morphological point of view in order to evaluate the available surface for microorganisms growth. Electrochemical experiments were performed and results were analyzed through the use of polarization curves which gave information on the dynamics of the electron transfer and hence about the output generation. Finally, the electrodes were compared in terms of global performance, criticism, application range and possibility of future modification of the electrode surface in order to increase the power density.

The results of this research are part of the publication entitled: “New approach for low-cost microbial fuel cells for energy sustainable waste-streams treatment”. T. Tommasi, D. Hidalgo, I. Mazzarino, E. Celasco, A. Sacco, B. Ruggeri. Under preparation.

## **6.2. Experimental**

### **6.2.1. Electrodes materials and preparation**

The carbon-based conductive materials tested as anode electrode in an MFC were: carbon mesh: C200-T, NCT-200, C200-D, NCUD-150 (all produced by Prochima, Italy), carbon sheet (Carolina, USA), carbon felt (SGL Group, Germany) and granules graphite (1 - 4 mm, MGT s.r.l. Italy). For all experiments, carbon sheet (Carolina, USA) was used as cathode electrode. The preparation of the electrode material depends on the shape of material to be tested. For granular material, it has been weighed the required amount of material to completely fill the anode chamber. Instead, in the case of carbon textiles, carbon felt and carbon sheet, it has been cut the required amount of conductive material in order to ensure an entire covering of the anode compartments. The electrical connection was assured by using a graphite rod (2 mm of diameter) inserted in both anode and cathode chambers, in order to ensure an effective current carrying as showed in Figure 6.1.

### **6.2.2. MFC configuration and operation**

The MFC device consists of two rectangular chambers, i.e. the anode and the cathode, in plexiglass with dimension (4 cm x 3 cm x 1cm) separated by a cation exchange membrane (CEM, CMI 7000, Membranes International Inc.) as shown in Figure 6.1. Both anode and cathode chamber were filled with the conductive material as is described in Section 6.2.1. All the investigations have been conducted under the same operational conditions, in batch mode at room temperature ( $22 \pm 2$  °C) using *Saccharomyces cerevisiae* (baker's yeast) as active

microorganism. The anode chamber was filled with baker's yeast ( $100 \text{ g}\cdot\text{L}^{-1}$ ), glucose ( $60 \text{ g}\cdot\text{L}^{-1}$ ) used as synthetic substrate and methylene blue ( $1.22 \text{ g}\cdot\text{L}^{-1}$ ) used as redox mediator for the transport of electrons from *Saccharomyces cerevisiae* to the anode electrode surface. The cathodic compartment was filled by potassium ferricyanide ( $6.58 \text{ g}\cdot\text{L}^{-1}$ ) used as oxidant compound. To prepare anodic and cathodic solutions, a buffer solution of phosphate minerals salts:  $\text{Na}_2\text{HPO}_4$  ( $8.2 \text{ g}\cdot\text{L}^{-1}$ ) and  $\text{NaH}_2\text{PO}_4$  ( $5.2 \text{ g}\cdot\text{L}^{-1}$ ) was used.

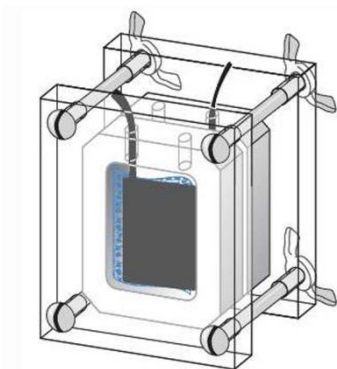


**Figure 6.1.** Miniaturized microbial fuel cells configuration

### 6.2.3. Characterization and electrochemical measurements

The surface morphologies of the anode before incubation with microorganisms were examined by a Field Emission Scanning Electron Microscope (FESEM, ZEISS supra 40) and Optical microscope (Axio Scope A1 POL) as shown in Figure 6.2. Resistivity measurements have been performed in a size material of  $2 \text{ cm} \times 2 \text{ cm}$  using a Keithley 2635 Source Measure Unit in four-point probe configuration.

All electrochemical experiments were performed by a multi-channel VSP potentiostat/galvanostat produced by BioLogic. Measurements were recorded by using EC-Lab software version 10.1x for data acquisition. All tests were carried out using a two electrode configuration, where the working electrode was coupled to the anode and both counter and reference electrodes were connected to the cathode. The electrochemical performance of the MFC was carried out using polarization curves. Experiments were characterized in terms of open circuit voltage (OCV), current density and power density of the MFC in order to gain information on the dynamics of electron transfer and hence, on power production.

Polarization curves were performed at a scan rate of  $1 \text{ mV}\cdot\text{s}^{-1}$  when a constant OCV was achieved, from the open-circuit cell voltage  $V_0$  (where  $I = 0$ ) to the short-circuit cell voltage  $V_{sc} = 0$  (where  $I = I_{\text{max}}$ ). The measurements were carried out from time  $t_{20\text{min}}$  to  $t_{24\text{h}}$  in order

to examine *S. cerevisiae* ability to consume the substrate. From the  $I$ - $V$  curves, the power density was calculated by  $P = I \cdot V \cdot v^{-1}$ , where  $I$ ,  $V$  and  $v$  represent current recorded, voltage output and the total anode volume ( $10 \pm 2$  mL), respectively.

### 6.3. Results and discussion

#### 6.3.1. Properties of commercial carbon-based materials as electrode in MFC

In MFC applications, a good anode material should have the following properties: good electrical conductivity, strong biocompatibility, chemical stability and anti-corrosion, large surface area to support microorganisms growth; and appropriate mechanical strength and toughness. Due to its excellent electrical conductivity and chemical stability carbon based materials have become the most used electrode in MFC although several reports have attempted to use non-carbon materials in order to develop new promising electrodes [18-20]. In terms of configuration, carbon-based electrodes can be divided into a plane structure, a packed structure and brush structure. In this section are discussed in detail carbon-based materials with flat-plane and packed structure configuration. The structure of the carbon-based materials tested are shown in Figure 6.2, with a plane structure were: carbon mesh (C200-T, NCT-200, C200-D, NCU-D-150), carbon sheet (C-SHEET) and carbon felt (C-FELT), while granules graphite (G-GRAPHITE) present a packed structure.

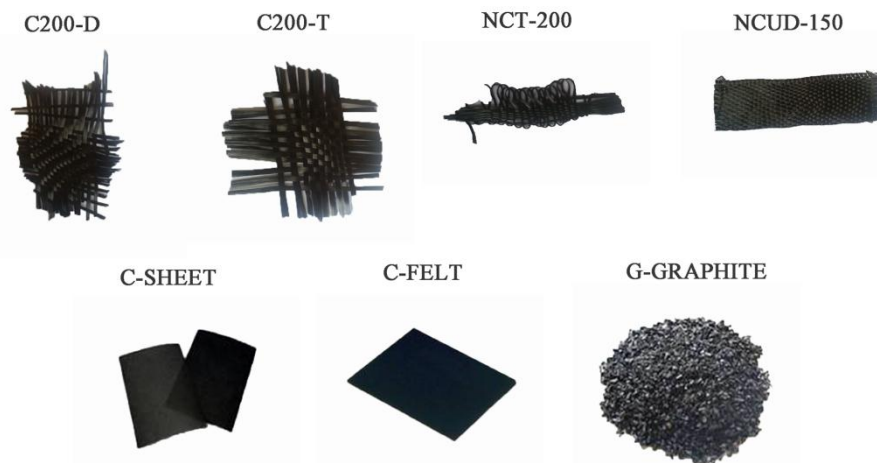


**Figure 6.2.** Images of the commercial carbon-based materials used as anode electrode in MFC

Carbon mesh produced by Prochima are usually used for the building of products that require high mechanical resistance and rigidity, e.g. airplane and car components, sports equipment and bike frames. For these ends, these textiles are normally used together with epoxy matrices,

obtaining extreme rigid and light laminated textile, with an elastic modulus similar to steel, high tensile strength and low elongation percentage. For MFC applications, these carbon meshes seem to offer a suitable support for microorganisms support and proliferation as well as large resistance which could be beneficial in large-scale MFCs. In addition, carbon mesh materials are produced by a relatively easy procedure and for that reason they could represent a low-cost option.

Carbon sheet is very thin and relatively stiff but slightly brittle (see Table 6.1). It offers a compact structure and a relatively smooth surface, both of which facilitate the quantitative measurement of biomass per unit of surface area. However, its low specific area and high cost with respect to carbon mesh could inhibit the application of this electrode in scale-up MFC. In comparison with carbon sheet, carbon felt is much more thick and flexible, giving to the materials high large resistance. Its loose texture confers more space for bacteria growth although the growth of bacteria is more likely to be restricted by the mass transfer of substrate and products on its inner surface. In addition, the plane structure of carbon sheet and carbon felt offer a beneficial solution to the reduction in the distance between the two electrodes which have been demonstrated to improve the performances of MFCs [21].

Packing electrodes such as granules graphite offer larger resistance with respect to carbon mesh and carbon sheet. The use of carbon-based electrodes in packing form is becoming increasingly common in MFC [10-14] since it's obtained a substantial increase in the available surface area for microorganisms growth [22-24]. In order to make the complete bed conductive, the granules must be tightly packed next to each other, although dead zones for current collection may still exist after long term running [25]. Using packing materials problems of biofouling can occur because of granules are heavy and could clog after long-term running, and as a consequence both the gaseous products ( $\text{CO}_2$ ) and nutrients does not permeate and flow easily.

In Table 6.1 are reported the electrical resistivity of the tested carbon-based materials, which is intrinsic property that quantifies how strongly a given material opposes the flow of electric current. Thus, a low resistivity indicates a material that readily allows the movement of electric charge. In this way, the electrical resistivities of the tested materials increase in the following order: C-FELT, C200-D, NCT-200, NCUD-150, C-SHEET and C200-T. For G-GRAPHITE are not reported the electrical resistivity due to the difficult to perform the measurement in the packed material.

**Table 6.1.** Thickness and resistivity of the commercial carbon-based materials used as anode electrode

Anode material	Thickness (mm)	Resistivity ( $\Omega/\text{cm}^2$ )
C200-T	0.6	0.170
NCT-200	0.7	0.048
C200-D	0.7	0.045
NCUD-150	0.8	0.083
C-SHEET	0.5	0.092
C-FELT	10	0.015

### 6.3.2. Power generation

Electrochemical characterization of the commercial carbon-based materials were conducted in an MFC in order to give information on which materials are suitable to be used or not as electrode in a MFC. The tested materials were: carbon mesh (C200-T, NCT-200, C200-D, NCUD-150), carbon sheet (C-SHEET), carbon felt (C-FELT) and granules graphite (G-GRAPHITE). Figure 6.3 shows the polarization curves ( $I, V$ ) obtained by Linear Sweep Voltammetry technique, varying the potential from Open Circuit Voltage (OCV) till to 0 V, which correspond to the Short Circuit Current (SCC) condition. After feeding each chamber with anodic and cathodic solutions, MFC required at least 2 h to reach pseudo-steady-state conditions after a start-up period in which open circuit voltage of the MFC increased. For this reason, comparison of the materials was performed considering the results obtained after two hours of operation as shown in Table 6.2.

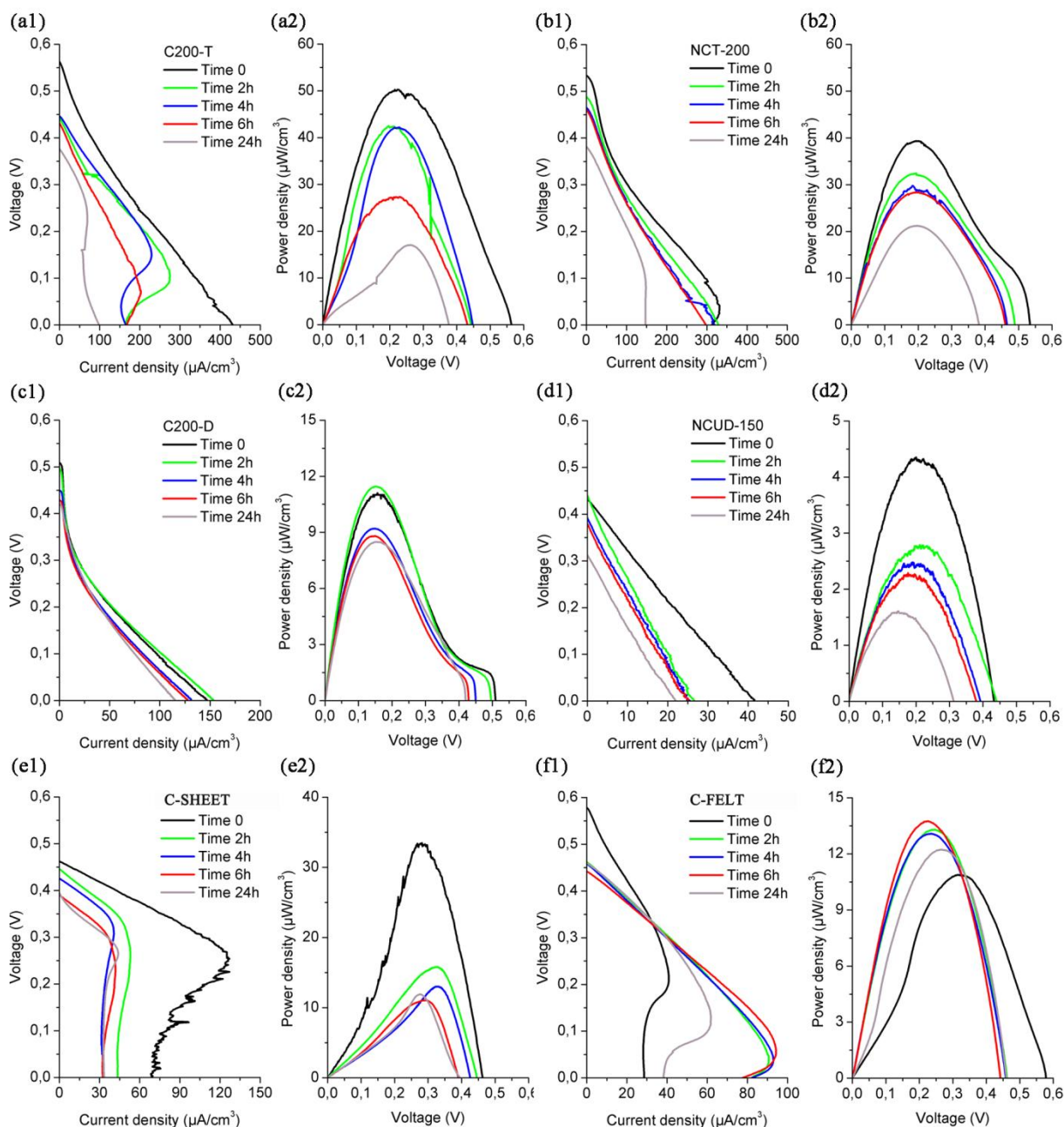


**Figure 6.3.** Polarization curves of commercial carbon-based materials: (a1,a2) C200-T; (b1,b2) NCT-200; (c1,c2) C200-D; (d1,d2) NCUD-150; (e1,e2) C-SHEET and (f1,f2) C-FELT at OCV conditions with respect to the maximum current density and power density obtained, respectively

Electrochemical results showed that low-cost carbon mesh materials C200-T (Figures 6.3a1 and 6.3a2) and NCT-200 (Figures 6.3b1 and 6.3b2) gave the best performance, producing after 2 h of operation a maximum power densities of  $42.4 \mu\text{W}/\text{cm}^3$  ( $164.3 \mu\text{A}/\text{cm}^3$ ) and  $32.3 \mu\text{W}/\text{cm}^3$  ( $330.3 \mu\text{A}/\text{cm}^3$ ), respectively. It is worth to noting that C200-T (Figure 6.3a1) showed

a sudden reduction of the current density at low potentials with respect to NCT-200 (Figure 6.3b1). This phenomenon could be explained taking into account that to supply high current, all the electrons from the anode are transported to the cathode and that at the anode surface predominate mass transfer phenomena [26]. Moreover, carbon mesh materials C200-D (Figures 6.3c1 and 6.3c2) and NCUD-150 (Figures 6.3d1 and 6.3d2) gave the lowest performance with respect to the previous carbon mesh, producing after 2 h of operation a maximum power densities of  $11.4 \mu\text{W}/\text{cm}^3$  ( $152.7 \mu\text{A}/\text{cm}^3$ ) and  $2.8 \mu\text{W}/\text{cm}^3$  ( $26.4 \mu\text{A}/\text{cm}^3$ ), respectively. This could be associated due to the present of the so called “activation zone” [26], at high potential and low current. In this zone, where the electrons coming from the active microorganisms need to overcome an energy barrier to generate electricity lowering the cell voltage; this is more evident in the case of C200-D in Figure 6.3c1.

In spite of the activation losses and mass transfer phenomena, it is worth noting that the mesh structure of these materials allowed a good contact of anode solution in their porosity created by overlapping of the carbon-fibers. In this way, anode solution can easily come in contact with the electrode material which favors the electron transport from microorganisms to the electrode. However, all these materials tend to lose strength and therefore its shape after being in contact for long periods of operation.

Results obtained to C-SHEET (Figures 6.3e1 and 6.3e2) showed a maximum power density of  $15.8 \mu\text{W}/\text{cm}^3$  ( $44.1 \mu\text{A}/\text{cm}^3$ ) while that C-FELT (Figures 6.3f1 6.3f2) produced a maximum power density around  $13.2 \mu\text{W}/\text{cm}^3$  ( $82.4 \mu\text{A}/\text{cm}^3$ ). The sudden decrease of the current density for C-SHEET at voltages  $< 0.35 \text{ V}$  (Figure 6.3e1) could be associated to ohmic losses [26], in which ohmic electrolyte resistance and the resistance of the membrane are the dominated phenomenon. In addition, due to C-SHEET is slightly brittle its lose strength which hinders a complete coverage of the anode chamber after some time of operation. Moreover, the suddenly reduction on the current density at low voltage for C-FELT is related to mass transfer phenomena as was explained above for carbon mesh C200-T. In spite of this, C-FELT due to its loose texture confers more space for bacteria growth and because of its large resistance has been used in a large number of MFC studies [15].

Finally, by using graphite granules we obtained that important problems of biofouling can occur because granules are heavy and could clog after long-term running: both the gaseous products ( $\text{CO}_2$ ) and nutrients does not permeate and flow easily inside the MFC. For this reason, it was found that graphite granules was not suitable materials to be use as electrode in an MFC. In particular, Figure 6.3 shows that both current and potential density tend to decrease during test evolution, lowering the power output of the cell: this behavior, which

was repeated for most of the carbon-materials used, is due to the consumption of reagents including carbon source by microorganisms activity and hence the lower microorganisms growth during time even if some accumulation of toxic substances able to inhibit the metabolism cannot be excluded considering that the tests were performed in batch conditions.

**Table 6.2.** Open circuit voltage, maximum current density and maximum power obtained after 2 h of operation by using different commercial carbon-based materials as anode electrode in an MFC operated with *Saccharomyces cerevisiae* as active microorganism and methylene blue as redox mediator

<b>Anode material</b>	<b>OCV (V)</b>	<b>Maximum current density (<math>\mu\text{A}/\text{cm}^3</math>)</b>	<b>Maximum power density (<math>\mu\text{W}/\text{cm}^3</math>)</b>
C200-T	0.44	164.3	42.4
NCT-200	0.48	330.3	32.3
C200-D	0.49	152.7	11.4
NCUD-150	0.45	26.4	2.8
C-SHEET	0.44	44.1	15.8
C-FELT	0.45	82.4	13.2

#### 6.4. Conclusions

This study demonstrated that commercial materials are suitable electrodes for MFC; their use could either reduce MFC costs or improve the energy sustainability of the process, promoting the MFC technology as possible alternative in waste water treatment. Commercial carbon mesh gave the best results producing maximum power density around  $42.4 (\mu\text{W}/\text{cm}^3)$  by using C200-T. However, these materials tended to fray and lose strength during batch operation hindering their use in long-term evaluation test MFC. Moreover, even if the electrical performance of C-FELT was lower than to carbon meshes, it has a great application potential thanks to its great mechanical resistance, surface area, adaptability and flexibility that gives greater possibilities expectation for long-term application. Due to these reason that during this work C-FELT is considered as reference electrode material. In order to increase

power generation in MFC by using low-cost and commercial carbon-based materials several strategies can be adopted. For example, some important future directions of the research could be the treatment of the surface of commercial materials in order to facilitate electron recovery, hence lowering the electrical resistance of the materials and in the same time to evaluate the best behavior of material in contact with a consortium of microorganisms in the transferring electrons from the cell of bacteria to the anode electrode.

## 6.5. References

- [1] M. Rahimnejad, N. Mokhtarian, G. Najafpour, W. Daud, A. Ghoreyshi, *World Appl Sci J*, 6 (2009) 1585-1588.
- [2] J. Wei, P. Liang, X. Huang, *Bioresource Technology*, 102 (2011) 9335-9344.
- [3] X. Wang, S. Cheng, Y. Feng, M.D. Merrill, T. Saito, B.E. Logan, *Environmental science & technology*, 43 (2009) 6870-6874.
- [4] X. Xie, L. Hu, M. Pasta, G.F. Wells, D. Kong, C.S. Criddle, Y. Cui, *Nano letters*, 11 (2010) 291-296.
- [5] N. Mokhtarian, W. Wan Ramli, M. Rahimnejad, G. Najafpour, *World Applied Sciences Journal*, 18 (2012) 559-567.
- [6] S. Cheng, B.E. Logan, *Electrochemistry Communications*, 9 (2007) 492-496.
- [7] Y. Liu, F. Harnisch, K. Fricke, U. Schröder, V. Climent, J.M. Feliu, *Biosensors and Bioelectronics*, 25 (2010) 2167-2171.
- [8] Q. Deng, X. Li, J. Zuo, A. Ling, B.E. Logan, *Journal of Power Sources*, 195 (2010) 1130-1135.
- [9] A. Morozan, L. Stamatina, F. Nastase, A. Dumitru, S. Vulpe, C. Nastase, I. Stamatina, K. Scott, *physica status solidi (a)*, 204 (2007) 1797-1803.
- [10] K. Rabaey, P. Clauwaert, P. Aelterman, W. Verstraete, *Environmental science & technology*, 39 (2005) 8077-8082.
- [11] M. Di Lorenzo, K. Scott, T.P. Curtis, I.M. Head, *Chemical Engineering Journal*, 156 (2010) 40-48.
- [12] P. Aelterman, M. Versichele, M. Marzorati, N. Boon, W. Verstraete, *Bioresource Technology*, 99 (2008) 8895-8902.
- [13] P.R. Bandyopadhyay, D.P. Thivierge, F.M. McNeilly, A. Fredette, *Oceanic Engineering, IEEE Journal of*, 38 (2013) 32-42.
- [14] F. Li, Y. Sharma, Y. Lei, B. Li, Q. Zhou, *Applied Biochemistry and Biotechnology*, 160 (2010) 168-181.

- [15] D. Hidalgo, T. Tommasi, V. Cauda, S. Porro, A. Chiodoni, K. Bejtka, B. Ruggeri, *Energy*, 71 (2014) 615-623.
- [16] A.L. Walker, C.W. Walker Jr, *Journal of Power Sources*, 160 (2006) 123-129.
- [17] V. Oliveira, M. Simões, L. Melo, A. Pinto, *Biochemical engineering journal*, 73 (2013) 53-64.
- [18] C. Dumas, A. Mollica, D. Féron, R. Basséguy, L. Etcheverry, A. Bergel, *Electrochimica Acta*, 53 (2007) 468-473.
- [19] H. Richter, K. McCarthy, K.P. Nevin, J.P. Johnson, V.M. Rotello, D.R. Lovley, *Langmuir*, 24 (2008) 4376-4379.
- [20] A. ter Heijne, H.V. Hamelers, M. Saakes, C.J. Buisman, *Electrochimica Acta*, 53 (2008) 5697-5703.
- [21] J.R. Kim, S.H. Jung, J.M. Regan, B.E. Logan, *Bioresource Technology*, 98 (2007) 2568-2577.
- [22] D. Jiang, B. Li, *Biochemical engineering journal*, 47 (2009) 31-37.
- [23] S. You, Q. Zhao, J. Zhang, J. Jiang, C. Wan, M. Du, S. Zhao, *Journal of Power Sources*, 173 (2007) 172-177.
- [24] B. Erable, N. Duteanu, S. Kumar, Y. Feng, M.M. Ghangrekar, K. Scott, *Electrochemistry Communications*, 11 (2009) 1547-1549.
- [25] B. Logan, S. Cheng, V. Watson, G. Estadt, *Environmental science & technology*, 41 (2007) 3341-3346.
- [26] B.E. Logan, B. Hamelers, R. Rozendal, U. Schröder, J. Keller, S. Freguia, P. Aelterman, W. Verstraete, K. Rabaey, *Environmental science & technology*, 40 (2006) 5181-5192.

## Chapter 7

### Surface modification of commercial carbon felt used as anode for Microbial Fuel Cells (MFCs)

#### 7.1. Introduction

Several investigations have been conducted in order to increase power densities in MFC. Up to date, one of the bottlenecks of MFCs technology is the electron transfer from microorganisms to the electrode. In order to obtain a significant enhancement of the MFCs performance, an ideal anode material should promote bacterial attachment and facilitate electron transfer. In order to improve bacterial adhesion and electron transfer, electrode surface modification and/or activation have become a new topic of interest in the research field of MFCs. To address these issues, several strategies have been developed on carbon-based materials to improve the performances of MFC anode, such as metal and non-metal materials modification [1], conductive polymers deposition [2], carbon nanotubes coating [3], ammonium treatment [4] and self-made metal-graphite composite [5].

Recently, nitrogen groups incorporation in carbon-based materials has been studied as anode-modification in MFC, which was reported to be beneficial in facilitating the electron transfer from the microorganisms to the electrode. The results reported in literature evidence that high temperature treatments in presence of air or ammonia gas on carbon mesh can produce an increase on power density of 14% and 25%, respectively than untreated commercial carbon mesh, likely due to an increase in the N/C ratio at the surface of the material [6]. Heating carbon cloth surfaces at high temperatures with ammonia gas (700 °C for 1 h) showed an increase in power density of 20% compared to untreated carbon cloth and a reduction of the start-up time of the MFCs, likely due to an increase of the amine groups on the surface of the carbon cloth [4]. Power density of 28.4 mW·m<sup>-2</sup> has been obtained using graphite felt after HNO<sub>3</sub> treatment, in a single chamber MFCs configuration with brewery wastewater diluted with sewage [7]. Carbon cloth anodes treated by concentrated nitric acid and high temperature resulted in improved power generation around 1.4 and 2 fold higher, respectively with respect to the untreated carbon cloth by a microbial fuel cell [8].

Conductive polymer materials such as polyaniline (PANI), polypyrrole (PPy) and composite materials based on them, in combination with carbon materials, have been studied for the same purpose: improvement of MFC performance [2, 9, 10]. PANI can be produced by

simple processes, it has good conductivity and it is biochemically stable in the microbial fuel cell working conditions, thus it has great application potential in the MFC. In previous works reported in literature, PANI was obtained by direct polymerization of the aniline in aqueous solution and then used as surface modifier of the electrode materials in the MFCs [2, 10]. Results obtained in a two-chamber MFC using a microbial community of *Clostridiales* and two conductive polymers: polyaniline (PANI) and polyaniline-co-o-aminophenol (PAOA) to modify carbon felt anode reached a maximum power density of  $27.4 \text{ mW}\cdot\text{m}^{-2}$  and  $23.8 \text{ mW}\cdot\text{m}^{-2}$ , and compared with unmodified carbon felt, i.e. increased by 35% and 18%, respectively [2]. In addition, power density of  $26.5 \text{ mW}\cdot\text{m}^{-2}$  was achieved by deposition of polymer based material (PANI) on graphite felt as support in an MFC operated in batch mode, with brewery wastewater diluted with sewage [7]. However, besides the interesting potentialities of PANI, there are some drawbacks related to its preparation methods. In fact, these methods included the precipitation of already formed PANI on the carbon materials without any specific linking procedure and with the use of a mutagen substance such as aniline. Moreover, the doping agent was hydrochloric acid and thus the PANI at the operational conditions inside the MFC was in the basic non conductive form [11].

In this Chapter are reported the surface modification of carbon felt either with nitrogen groups incorporation or polymer deposition, in order to increase the electrochemical performances of commercial carbon felt (C-FELT) as anode electrode in MFCs. The new strategies include:  $\text{HNO}_3$  activation at low temperature (C- $\text{HNO}_3$ ) and in situ deposition of PANI (C-PANI) on commercial carbon felt. Furthermore, it is proposed a new and chemically safe synthesis procedure and an in-situ deposition of PANI on carbon materials, starting from the aniline dimer (non toxic/mutagenic substance) and using polystyrenesulfonate (PSS) as an emulsifying/doping agent which provide the necessary conditions for the use of PANI as surface modifier for electrode materials in the MFCs. The development of the PANI synthesis procedure have previously development and optimized by Bocchini and Chiolerio et al., at Istituto Italiano di Tecnologia as is reported in [12, 13].

The surface properties of the C-FELT, C- $\text{HNO}_3$  and C-PANI were analyzed and characterized by several methods: Field Emission Scanning Electron Microscopy, Energy Dispersive Spectroscopy, Fourier Transformed Infrared Spectra, resistivity measurements and impedance spectroscopy. The electrochemical performances of the anode materials were evaluated in a dual-chamber MFC using *Saccharomyces cerevisiae* as active microorganism, in terms of the dynamics of electron transfer and power generation.

The results of this research are part of the publication entitled: “Chemical pre-treatment of commercial carbon felt used as anode of Microbial Fuel Cells”. D. Hidalgo, T. Tommasi, S. Bocchini, A. Chiolerio, A. Chiodoni, I. Mazzarino, B. Ruggeri. (2015) Energy. Submitted.

## **7.2. Experimental**

### **7.2.1. Materials**

Commercial carbon felt (C-FELT) (Soft felt SIGRATHERM GFA5, SGL Carbon, Germany) and carbon paper (Carolina, USA) were used as electrode materials for anode and cathode chambers, respectively. Nitric acid (HNO<sub>3</sub>, 70%), N-phenyl-1,4-phenylenediamine (DANI, 98%), poly (sodium 4-styrenesulfonate) (PSS), ammonium persulfate (APS, 98%), chloridric acid (HCl, 37%) and methanol (CH<sub>4</sub>O, 99.9%) were used to perform nitric acid activation and polyaniline deposition (PANI) on C-FELT. Baker’s yeast (*Saccharomyces cerevisiae*) was used as active microorganism.  $\alpha$ -D-glucose (96%), methylene blue, potassium ferricyanide ( $\geq 99\%$ ), sodium phosphate dibasic dihydrate ( $\geq 98\%$ ) and sodium phosphate monobasic monohydrate ( $\geq 98\%$ ) were used to conduct electrochemical experiments in the MFC. All reagents used were purchased from Sigma Aldrich.

### **7.2.2. Anode material preparation**

#### **7.2.2.1. Activation of commercial carbon felt by nitric acid**

C-FELT was cleaned in acetone for 10 min to remove organic residues on the surface and then it was dried in air at room temperature. Subsequently, it was dipped in 500 mL of nitric acid (5% v/v) and maintained under agitation for 10 h at 80 °C. After the draining of the acid solution, the treated C-FELT was washed with distilled water until a neutral pH was achieved. Finally, treated C-FELT was dried in an oven at 110 °C for 12 h.

#### **7.2.2.2. Synthesis and deposition of PANI on carbon felt**

The deposition of PANI on C-FELT was made by using a similar technique to layer by layer deposition, where the PANI doped by PSS was grown in successive steps by alternating immersion in positively charged monomer solution and negatively charged polystyrenesulfonate solution. The oxidizing agent was also included, thus providing a layer by layer successive polymerization-deposition as described below.

PANI deposition was performed in situ on C-FELT adapting a synthesis methodology that was developed for the realization of a conductive ink [12, 13] starting from the aniline dimer

as follows: (1) the C-FELT was treated with a solution of 0.01 M of PSS in a solution 0.1 M of HCl for 15 min, (2) rinsed in distilled water and thus immersed in a solution 0.01 M of DANI in methanol for 15 min, and (3) rinsed again in distilled water and immersed in a solution of 0.01 M in APS, 0.01 M of PSS and 0.1 M of HCl for 15 min. The material was slightly pressed on absorbent paper to remove the excess of solution between stages. Steps (2) and (3) were repeated 8 times each, and at the end of the deposition the modified carbon material was washed in distilled water. Finally, the material was dried in air at room temperature for at least 12 h before being used in the MFCs.

### **7.2.3. Characterizations of anode materials**

The surface morphologies of the different anodic materials before incubation were examined using a ZEISS Auriga Field Emission Scanning Electron Microscope (FESEM) equipped with an OXFORD INCA Energy Dispersive X-ray Spectroscopy (EDS) detector. In order to assess the functionalization with PANI, Fourier Transformed Infrared Spectra (FT-IR) measurement was performed on a Nicolet 5700 FTIR Spectrometer (ThermoFisher). From a small piece of the functionalised C-FELT, PANI was extracted with dimethylsulfoxide (DMSO) by dipping for 24 h. The resulting solution was casted on a silicon wafer and scanned with a signal resolution of  $2\text{ cm}^{-1}$  in the range of  $(4000 - 400)\text{ cm}^{-1}$ . Resistivity measurements on carbon felt before and after treatment were performed using  $4\text{ cm}^2$  of material by a Keithley 2635 Source Measure Unit. For this purpose, each sample was characterized in two different configurations: (1) placing the probes on the same plane of the material, “in-plane” configuration, and (2) placing the probes on opposite sides of the material, “out-of-plane” configuration mode. Materials were tested in both two point contact and four point contact configuration in order to evaluate the contact resistance. Impedance spectroscopy measurements on C-FELT before and after treatment were performed in out of plane configuration by submitting materials to a 100 mV signal using a precision impedance analyzer (LCR-meter Agilent E4980A) from 20 Hz up to 2 MHz.

### **7.2.4. MFCs configuration and operation**

The MFC device consists of two square chambers in polymethylmethacrylate (PMMA) with dimension  $8\text{ cm} \times 8\text{ cm} \times 2\text{ cm}$  separated by a cation exchange membrane (CEM, CMI 7000, Membranes International Inc.) as shown in Figure 7.1. In each chamber, the conductive material was introduced and connected with a graphite rod (5 mm in diameter) to ensure an effective current carrying capacity. The anodic materials tested were: (1) commercial carbon

felt (C-FELT), (2) HNO<sub>3</sub>-treated carbon felt (C-HNO<sub>3</sub>) and (3) PANI-deposited carbon felt (C-PANI), all with the same dimensions 8 cm x 8 cm x 0.5 cm. In each cathodic chamber, carbon paper with dimensions of 8 cm x 8 cm x 0.1 cm was used as cathode electrode. All the experiments were conducted in batch mode at room temperature (22 ± 2 °C). The anodic compartment was filled by a solution containing baker's yeast (*Saccharomyces cerevisiae*) (50 g·L<sup>-1</sup>) used as active microorganisms, glucose (60 g·L<sup>-1</sup>) used as synthetic substrate and methylene blue (1.22 g·L<sup>-1</sup>) used as redox mediator for the transport of electrons from the microorganisms to the electrode surface. The cathodic compartment was filled by potassium ferricyanide (6.58 g·L<sup>-1</sup>) used as final electron acceptor compound. A buffer solution of phosphate mineral salts: Na<sub>2</sub>HPO<sub>4</sub>·2H<sub>2</sub>O (8.2 g·L<sup>-1</sup>) and NaH<sub>2</sub>PO<sub>4</sub>·H<sub>2</sub>O (5.2 g·L<sup>-1</sup>) was used to prepare both anodic and cathodic solutions.

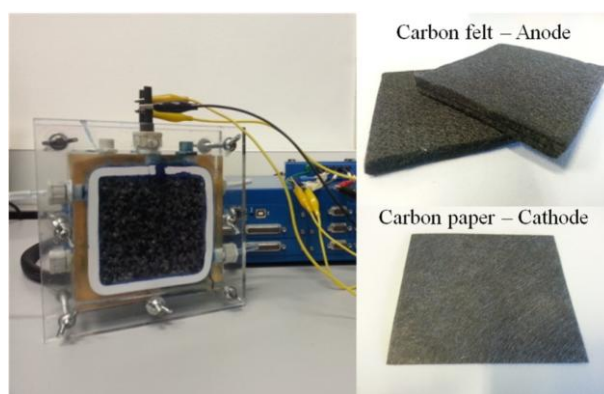


**Figure 7.1.** Microbial Fuel Cell configuration

#### 7.2.5. Electrochemical characterizations

Experiments were carried out in terms of Open Circuit Voltage (OCV), Linear Sweep Voltammetry (LSV) and Current Interrupt (CI) techniques. Electrochemical experiments were performed using a multi-channel VSP potentiostat/galvanostat produced by BioLogic. Measurements were recorded by using EC-Lab<sup>®</sup> software version 10.1x for data acquisition. All tests were carried out using a two-electrode setup, where the working electrode was connected to the anode and both counter and reference electrodes were connected to the cathode. Polarization curves were performed at a scan rate of 1 mV·s<sup>-1</sup> when constant OCV was achieved, from the open-circuit cell voltage  $V_0$  (where  $I = 0$ ) to the short-circuit cell voltage  $V_{sc} = 0$  (where  $I = I_{max}$ ). From the  $I$ - $V$  curves, the power density was calculated by  $P = I \cdot V \cdot v^{-1}$ , where  $I$ ,  $V$  and  $v$  represent the current, the voltage output recorded and the medium anode volume, respectively. CI measurement was employed to evaluate the electrical

resistance of the MFC [14]. CI tests were performed for each tested anode materials at a voltage  $V_{CI}$  equal to 90 % of OCV in the following manner: when the MFC produced a stable current output  $I_0$  under an applied voltage  $V_{CI}$ , the circuit was opened causing a steep potential ( $V_R$ ) in the firsts 50  $\mu$ s, followed by a progressive increase in voltage until to reach stable OCV conditions. The electrical resistance of the MFC was calculated as  $R = V_R/I_0$  and a mean value of several measures were evaluated.

### 7.3. Results and discussion

#### 7.3.1. Characterizations of anode materials

FESEM analysis was used to investigate the morphological properties of the anode materials: C-FELT, C-HNO<sub>3</sub> and C-PANI. In Figure 7.2a and 7.2b, the results obtained for C-FELT before treatments are reported in two different magnifications. The C-FELT was constituted by randomly arranged cylindrical fibers with a smooth surface. It is also possible to observe that the loose texture confers a suitable space for bacterial growth, despite the fact that the growth of bacteria is more likely to be controlled by mass transfer phenomena of substrate between liquid bulk and microorganisms surface [15]. In Figure 7.2c, the result obtained for C-HNO<sub>3</sub> is reported. It turns out that the HNO<sub>3</sub>-treatment increases the roughness of the single carbon fiber, but do not damage the structure of the fiber itself. Figure 7.2d evidences that carbon fibers are covered with a PANI film, which makes the fibers pretty rough with respect to the commercial carbon felt, reported in Figure 7.2b. Also in the case of the PANI deposition, the integrity of the fibers is preserved.

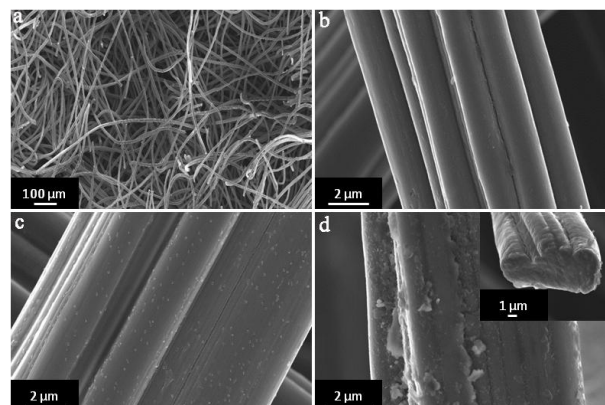


**Figure 7.2.** FESEM images of anode materials: (a,b) C-FELT, (c) C-HNO<sub>3</sub> and (d) C-PANI

The EDS elemental analysis reported in Figure 7.3 evidences the chemical composition of the anode materials used: C-FELT (black line), C-HNO<sub>3</sub> (red line) and C-PANI (blue line). The

C-FELT is mainly composed by carbon (C) and oxygen (O), while in the case of C-HNO<sub>3</sub>, the appearance of the nitrogen (N) peak and the increase of the oxygen peak intensity confirm the presence of superficial functional groups such as nitrogen [16] or oxygenated ones [17], which would favour the electrical conductivity between electrode materials and microorganisms. The presence of PANI on the C-PANI material was confirmed through the presence of sulphur (S), sodium (Na) and nitrogen (N) peaks, derived respectively from the sulphuric functional groups of PSS, the residual sodium salt of PSS and the presence of polyaniline which could increase the conductivity of the C-PANI with respect to C-FELT. The FT-IR spectrum of the extracted PANI obtained as described in the synthesis procedure (Section 7.2.3) after the in-situ formation on carbon felt, is reported in Figure 7.4. The PANI FT-IR spectrum shows the main PSS absorbance peaks confirming the formation of the PANI/PSS salt. PSS showed both the characteristic peaks of polystyrene and of sulfonation. The 3100 - 3000 cm<sup>-1</sup> wavenumbers zone showed the stretching of aromatic carbon hydrogen bonds ( $\nu_{\text{CHarom}}$ ) while in the 3000 - 2800 cm<sup>-1</sup> zone the stretching carbon hydrogen bonds of the aliphatic chain ( $\nu_{\text{CHaliph}}$ ) are shown [18]. The carbon-carbon stretching of benzene ring is presented at 1596 and 1453 cm<sup>-1</sup>. Antisymmetric and symmetric vibrational adsorption peaks of SO<sup>3-</sup> group can be assigned at 1224 and 1034 cm<sup>-1</sup>, respectively. The presence of PANI was assessed by the nitrogen-hydrogen bond stretching ( $\nu_{\text{NH}}$ ) of secondary aromatic amine at 3250 cm<sup>-1</sup>. In the aromatic ring stretching region, the PANI exhibited a band at 1574 cm<sup>-1</sup> attributed to C=N stretching of quinoid diimine unit (the oxidised form of PANI). C-C aromatic ring stretching of the benzenoid diamine unit (the reduced form of PANI) appeared at 1509 cm<sup>-1</sup> [19]. The 1308 cm<sup>-1</sup> corresponded to the stretching C-N of benzenoid rings of PANI and the C=N of quinoid rings appeared at 1173 cm<sup>-1</sup>. The FTIR results obtained from the extracted PANI are in good agreement with the EDS report of C-PANI showed in Figure 7.3.

In order to complete the characterization of the carbon felts, resistivity measurements were performed in two different testing configurations: (1) “in-plane” and (2) “out-of-plane”, using two point contacts configuration, as reported in Section 7.2.3. The results of multiple measurements allowing computing the average and standard deviation of each experimental point (*I* versus *V*) is shown in Figure 7.5, in semilogarithmic scale (hence only the positive part of the *I-V* curves is visible).

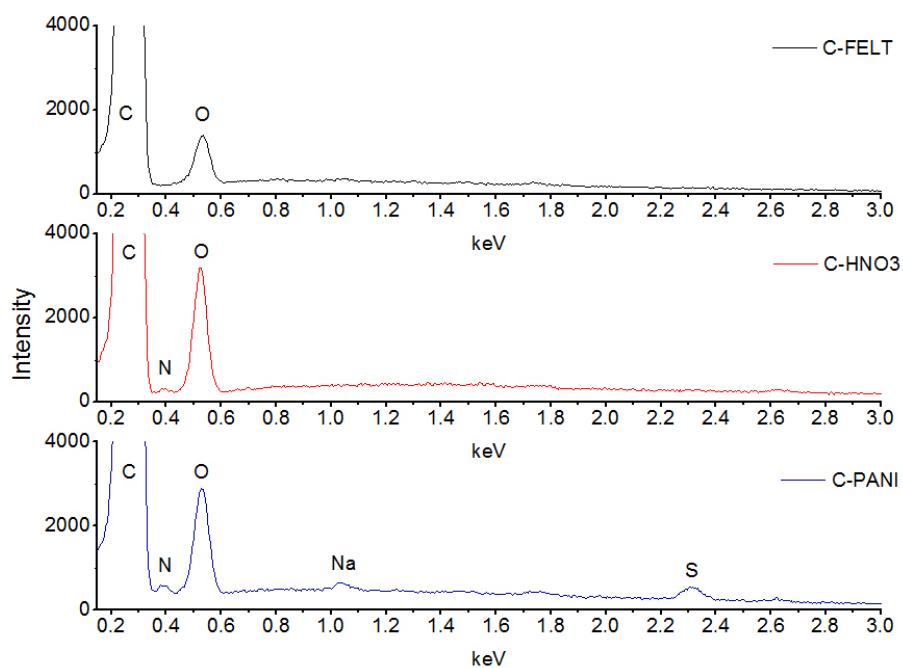


**Figure 7.3.** EDS spectrum of C-FELT (black line), C-HNO<sub>3</sub> (red line) and C-PANI (blue line)

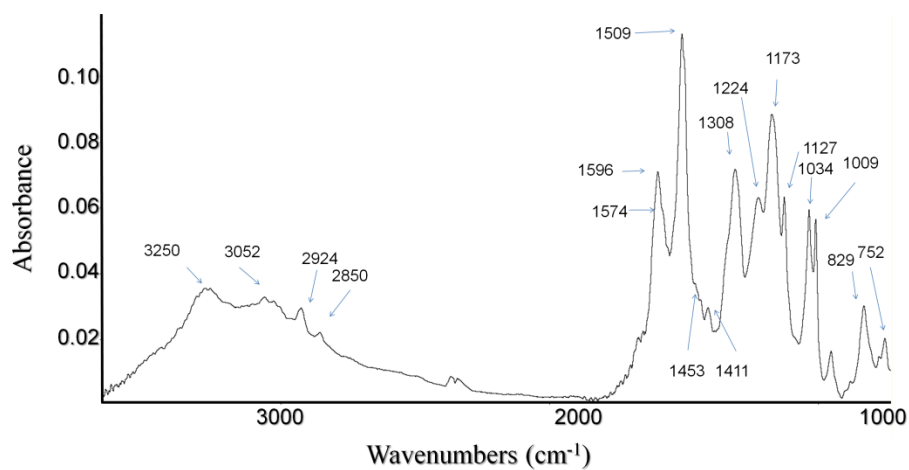


**Figure 7.4.** FTIR spectra of PANI from the carbon felt after PANI deposition

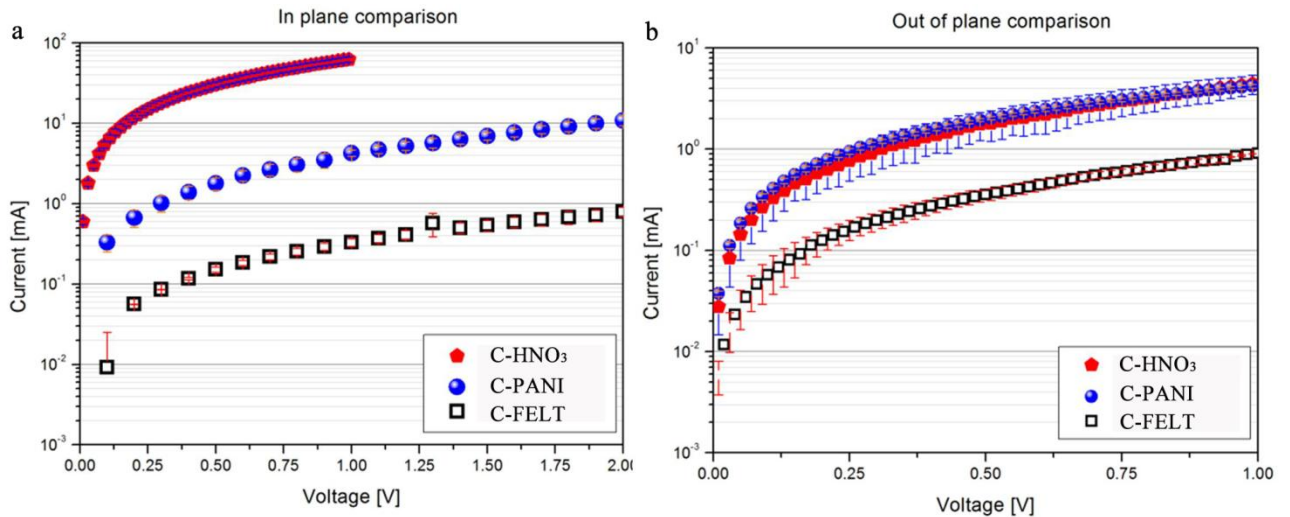


**Figure 7.5.** *I-V* curves in log scale for two different testing configurations: (a) in-plane and (b) out-of-plane using two point contacts configuration

Table 7.1 reports the values of the electrical resistance of C-FELT, C-HNO<sub>3</sub> and C-PANI. From the in-plane data (Figure 7.5a), it is clear that the C-HNO<sub>3</sub> experiences the highest conductivities, two orders of magnitude higher than the C-FELT and one order of magnitude higher than the C-PANI. From the out-of-plane data (Figure 7.5b), unexpectedly, the C-PANI gave the best result, overperforming the C-HNO<sub>3</sub> in terms of maximum sustainable current. This could be explained by considering the random distribution and irregular contact across the carbon fibers (Figure 7.2a), which were strengthened through the in-situ formation of PANI (Figure 7.2d), favouring a decrease of the resistance of the material and ensuring a more stable electrical contact between the fibers.

We also performed a comparison between out-of-plane two point contacts and out-of-plane four point contacts (not shown) measure approaches, in order to evaluate the contact resistance. The four point contacts measurement configuration is normally used to characterize metals (very low resistivity systems), as shown in Chiolerio et al [20]. Results indicate a variation of less than 10% in resistance between the two measures, thus suggesting that the contact resistance is estimated to be around 100  $\Omega$  for the C-FELT and around 30  $\Omega$  for both C-HNO<sub>3</sub> and C-PANI. Furthermore, impedance spectroscopy study was conducted on the bare felts, again in the out-of-plane configuration, by submitting materials to a 100 mV signal. Figure 7.6a shows the real part of complex impedance (resistance) as a function of the measurement frequency, while Figure 7.6b shows the imaginary part of complex impedance (reactance). Resistance curves (Figure 7.6a) confirmed the results already disclosed by the *I-V* analysis (Out-of-plane resistance as reported in Table 7.1, with a slight reduction of the

absolute resistance values in the following order: C-FELT, C-HNO<sub>3</sub> and C-PANI. The reactance values are overall very low, showing that in the case of C-HNO<sub>3</sub> some negative reactance phenomena (capacitive behaviour) occur around 500 kHz, which disappears over 1 MHz.

**Table 7.1.** Resistance data collected from the *I-V* measurements performed in the anode materials under both in-plane and out-of-plane two point contacts configuration, and impedance spectroscopy measurements conducted in out-of-plane resistance configuration at 1 kHz

Material	<i>I-V</i> analysis		Impedance spectroscopy
	In plane resistance [ $\Omega$ ]	Out of plane resistance [ $\Omega$ ]	Out of plane resistance at 1 kHz [ $\Omega$ ]
C-FELT	$2530 \pm 30$	$1364 \pm 7$	$80.5 \pm 0.5$
C-HNO <sub>3</sub>	$15.70 \pm 0.02$	$311 \pm 2$	$72 \pm 1$
C-PANI	$137 \pm 2$	$247.5 \pm 0.5$	$14.0 \pm 0.5$

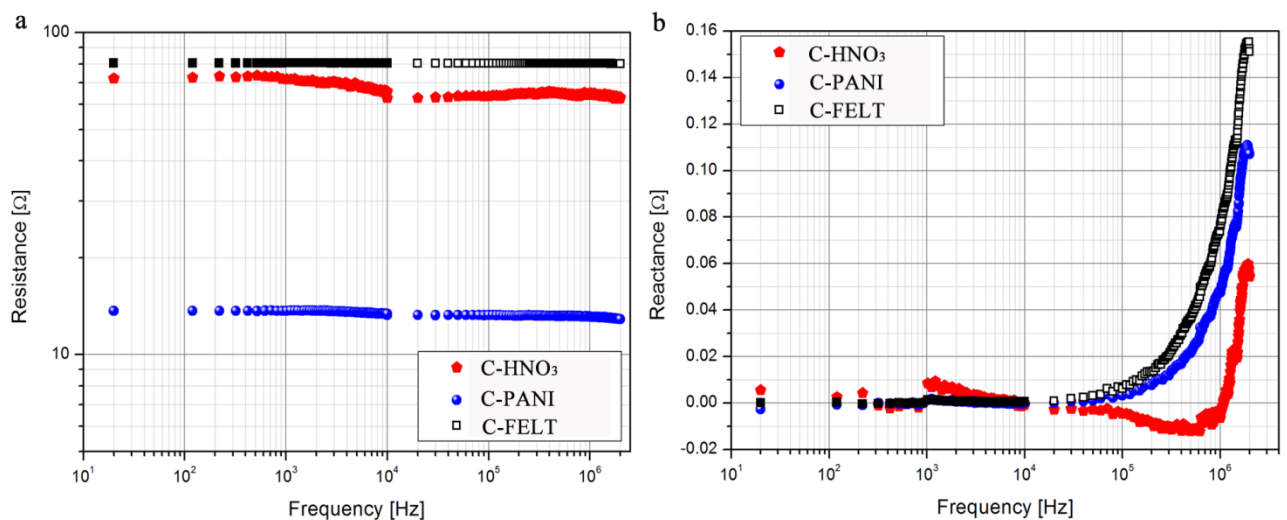


**Figure 7.6.** Impedance spectroscopy measurements (a) resistance and (b) reactance curves as a function of signal frequency

### 7.3.2. Power generation

Figure 7.7a shows the polarization curves ( $I, V$ ) obtained by Linear Sweep Voltammetry technique, varying the potential from Open Circuit Voltage (OCV) till to 0 V, which correspond to the Short Circuit Current (SCC) condition. The tests were conducted using C-FELT, C-HNO<sub>3</sub> and C-PANI as anode materials. After feeding each chamber with anodic and cathodic solutions, MFC required at least 2 h to reach pseudo-steady-state conditions after a start-up period in which open circuit voltage of the MFC increased.

The polarization curves of the anode materials after 2 h of operation show the usual behavior of others MFCs [21] and it can be divided in three zones: A, B and C as shown in Figure 7.7a.

The A zone, at high potential and low current, the so called “activation zone”, is the zone where the electrons coming from the active microorganisms need to overcome an energy barrier to generate electricity lowering the cell voltage; this is more evident in the case of C-HNO<sub>3</sub> than C-PANI. In fact, the highest OCV value was obtained with C-HNO<sub>3</sub> (0.63V against 0.46V of C-FELT), while in the test conducted with C-PANI the initial voltage of the MFC cell decreased from 0.46 of C-FELT to 0.40 V. This phenomenon could be explained considering the high difficulty of microorganisms adaptation, on the electrode surface, especially at the beginning of tests. In fact, in the case of C-PANI, due to the free chemical groups present on the surface, the electrochemical behaviour of cytoplasmic membrane of microorganisms is under stress and this could induce either some metabolic switch or damage [22]. Conversely, nitric acid treatment seems to permit an easier and fast adherence of microorganisms on the surface, probably thanks to increased roughness as well as to functional groups on the C-FELT surface, as it is possible to argue by comparing Figure 7.2b and Figure 7.2c. In the B zone, when the voltage falls more slowly, the phenomenon is dominated by the ohmic electrolyte resistance and by the resistance of the membrane. Here, both C-HNO<sub>3</sub> and C-PANI present similar behavior, which confirm that both materials undergo an ohmic decay.

In the third C zone, at very high current and approximately zero value of potential, the C-PANI shows a higher voltage drop, which means a higher electrical resistance. This phenomenon could be explained taking into account that to supply the very high current, all the electrons from the anode are conveyed to the cathode and that at the anode surface predominate mass transfer phenomena.

These processes involve the transfer of electrons from the bulk to the adhered microorganisms, as well as of electrons which need to move from outmembrane of microorganisms to the

electrode, in a very low electrical potential. In this situation the electron mobility is a crucial aspect. This phenomenon can be schematized by several mass transfers in series resistances: i) from the bulk of the liquid to microorganisms, ii) from the microorganisms to the electrode material, and iii) the electrical resistance of the electrode.

By comparing the polarization curves in B zone of C-HNO<sub>3</sub> and C-PANI, and by considering the items i) and ii) explained above, it is evident the higher resistance of C-HNO<sub>3</sub> as confirmed by the direct resistivity measurements reported in the Table 7.1.

Figure 7.7b shows the comparison of power generation using the three different materials. C-FELT before treatment could sustain a maximum power density of  $\sim 160 \text{ mW}\cdot\text{m}^{-2}$ . The system operated with C-HNO<sub>3</sub> generated a maximum power density of  $\sim 400 \text{ mW}\cdot\text{m}^{-2}$ , while using C-PANI a maximum value of  $\sim 460 \text{ mW}\cdot\text{m}^{-2}$  was observed. Results evidence that the oxidation of the carbon surface with HNO<sub>3</sub> improved the performance 2.5 times with respect to carbon felt. This could be related either to the increase of real surface area or due to the presence of superficial nitrogen functional groups, which is beneficial in the facilitation the electron transfer in MFCs [7, 8, 23, 24]. The highest power density in the case of C-PANI of 2.9 times with respect to C-FELT, could be attributed to several phenomena as: (1) reduction of the activation losses, which favors the start-up period, (2) high affinity of the microorganisms on the electrode surface and (3) an increase of the roughness of the material that facilitates the electron transfer from the microorganism to the electrode. These results are in good agreement with results present in literature, confirming that PANI treatment on carbon materials is effectively able to improve MFC performance [2, 7].

Figure 7.7c shows the maximum power density versus time for the duration of the tests. In the case of C-FELT, the power increased in the first 6 h of operation, and then remained constant around  $160 \text{ mW}\cdot\text{m}^{-2}$  until the end of the test (24 h). In the case of C-HNO<sub>3</sub> and C-PANI, the power densities decrease versus time with an unstable behavior around 2 h, probably due to the transition phenomenon present in the system. After this initial period, it is possible to observe that power density drops during the duration of the test, probably due to the rapid substrate and reagents depletion occurred in order to sustain the higher current, differently than what happens in the C-FELT case, as previously reported in literature [25, 26].

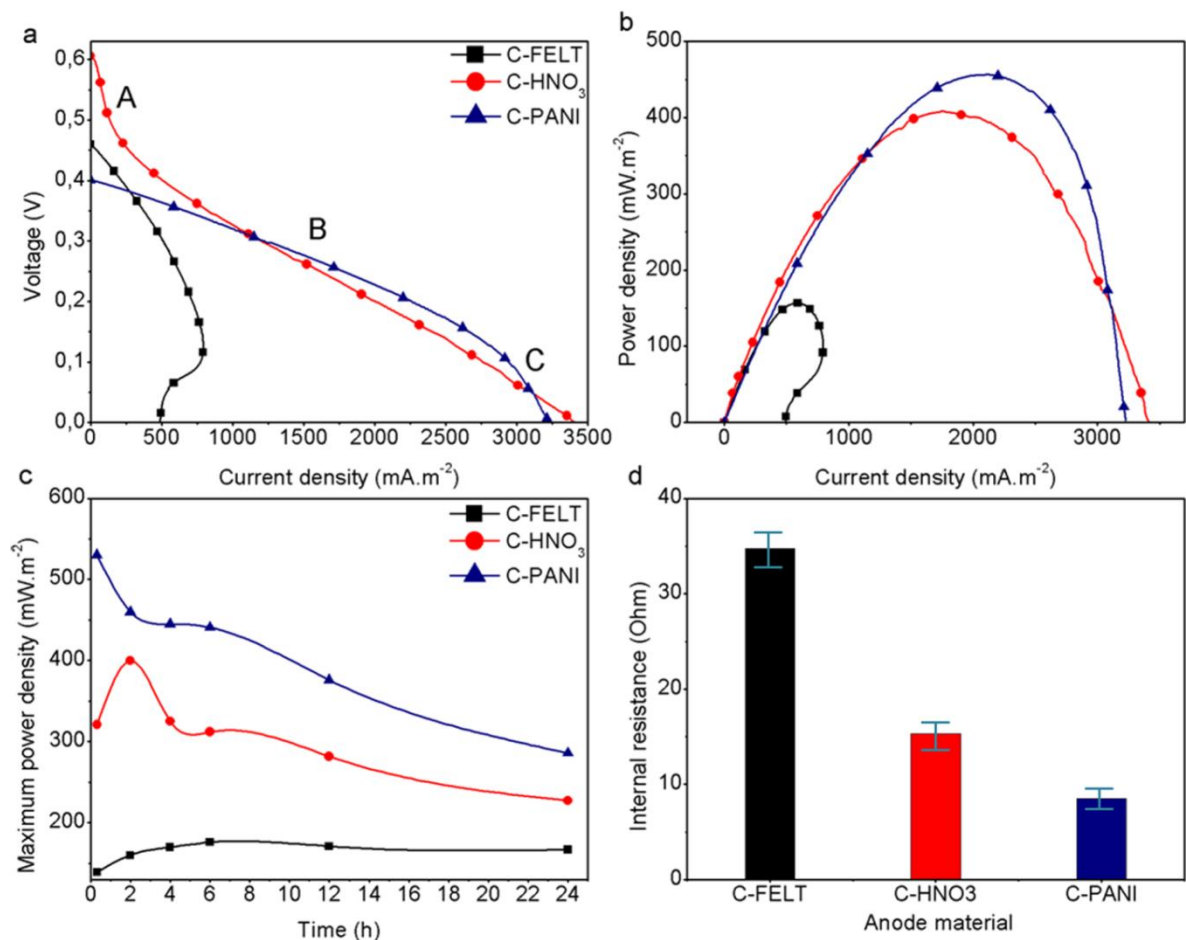


**Figure 7.7.** Electrochemical analysis of C-FELT (black line), C-HNO<sub>3</sub> (red line) and C-PANI (blue line) by means of (a) Polarization curves and (b) current density curves recorded at 2 h of operation, (c) power density curves vs. time recorded during 24 h of operation and (d) internal resistance measured through current interrupt method after 3 h of operation in an MFC

The total internal resistance ( $R_{int}$ ) of a MFC depends on many terms: the anodic resistance  $R_a$ , the cathodic resistances  $R_c$ , the ions exchange membrane resistance  $R_m$  and electrolyte resistance  $R_e$  [21]. In proximity of OCV, the current (the harvested electron) depends than the so called “activation” phenomena, while in proximity of maximum current “diffusive” phenomena prevails [21]. It is well known that activation and diffusive resistances can be neglected only in the so called “ohmic regime”, where the current is a linear function of the voltage [21]. Considering that both activation and diffusive losses are strongly dependent of electrode materials, the CI technique was used in the region of high  $V$  and low  $I$  in the non linear shape of polarization curve [27]. The obtained value is not the electrical resistance in the classic sense, but it is able to give us information on how the losses depend on the different electrode material and permit hence to compare then, which is the end of this study. The

internal resistance of the overall MFC (anode, cathode, electrolyte and membrane) was determined as reported in Section 7.2.5, and the comparison of the three different anodic materials studied: C-FELT, C-HNO<sub>3</sub> and C-PANI, after 3 h of operation are reported in Figure 7.7d. The internal resistance values were intended with a predominant contribution of the anode material effects, due to all the tests were conducted under the same operational conditions, and only anode material was changed. As shown in Figure 7.7d, the internal resistance obtained using C-FELT was of ~ 35 Ω, while the tests performed either with C-HNO<sub>3</sub> or with C-PANI evidenced a strong reduction to 15 Ω and 8 Ω, respectively. These results are in good agreement with respect to the results obtained through the resistance measurements as reported in Table 7.1.

**Table 7.2.** Comparison of the present results with literature data obtained using untreated and treated carbon based materials as anode electrode materials in MFCs

<b>Anode</b>	<b>Treatment</b>	<b>Microbe</b>	<b>Substrate</b>	<b>mW·m<sup>-2</sup></b>	<b>Reference</b>
C-FELT	Untreated	<i>S. cerevisiae</i>	Glucose	160	This work
Graphite	Untreated	<i>S. cerevisiae</i>	Hydrolyzed Lactose	4	[28]
Graphite plates	Untreated	<i>S. cerevisiae</i>	Glucose	8	[29]
C-HNO <sub>3</sub>	HNO <sub>3</sub>	<i>S. cerevisiae</i>	Glucose	400	This work
Carbon felt	HNO <sub>3</sub>	Domestic wastewater	Brewery wastewater	28.4	[7]
Carbon mesh	High-temperature ammonia gas process	Domestic wastewater	Sodium acetate	1015	[6]
C-PANI	PANI deposition	<i>S. cerevisiae</i>	Glucose	460	This work
Carbon felt	PANI deposition	Domestic wastewater	Brewery wastewater	26.5	[7]
Carbon felt	PANI deposition	<i>Clostridiales</i>	Sodium acetate	27.4	[2]

Finally, the Table 7.2 shows a representative set of power density data for MFC, data obtained by various researchers, using untreated and treated carbon based materials by  $\text{HNO}_3$  activation, high-temperature ammonia gas process and PANI deposition. It is possible to observe that the power density of the MFC remarkable improves by using different anode modification methods; the results of the present work are in average comparable with those reported in literature. The only difference is related to treated carbon mesh.

#### **7.4. Conclusions**

In this Chapter nitric acid activation and PANI deposition were performed in order to increase the performance of commercial carbon felt as anode material in MFC. Electrochemical determinations revealed a maximum power density of  $160 \text{ mW}\cdot\text{m}^{-2}$  using C-FELT, while power densities of  $400 \text{ mW}\cdot\text{m}^{-2}$  and  $460 \text{ mW}\cdot\text{m}^{-2}$  were obtained using C- $\text{HNO}_3$  and C-PANI, respectively. These results seem to be related to a strong reduction of the activation losses contribution and to an important decrease of the internal resistance of the cell using C- $\text{HNO}_3$  and C-PANI of about 2.3 and 4.4 times, respectively, with respect to C-FELT. The highest power generation results are obtained with polyaniline deposition, since the PANI deposited acts as an electrical contact between the random structures of the carbon material. Results evidence that nitric acid activation and PANI deposition on carbon felt offer a solution to improve the power generation of MFC, satisfying electrical requirements and improving the durability of the materials. The important increase on the power and current in all of these cases were likely to be a combination of factors including: (1) enhanced electrical conductivity, (2) increased surface area, and (3) increased affinity of the anode surfaces. Moreover, the proposed PANI deposition has multiple advantages with respect to the previous ones: i) increase of PANI conductivity in the soaker solution, ii) decrease of risk hazard during polymerization by use of non-toxic starting monomer and iii) more homogeneous and faster deposition method.

In order to improve further the MFCs technology, the obtained results suggest to conduct future tests with modified carbon felts in the presence of a consortium culture of microorganisms in order to check their possible applications in wastewater treatment process. Finally, tests on durability in continuous mode for long periods are necessary in order to verify not only the increase of the power density but also, the total electrical energy produced by MFCs device during its time-course of life, which is more stringent from an energy sustainability point of view. Both proposed strategies are reported in the following Chapter.

## 7.5. References

- [1] M. Rosenbaum, F. Zhao, M. Quaas, H. Wulff, U. Schröder, F. Scholz, *Applied Catalysis B: Environmental*, 74 (2007) 261-269.
- [2] C. Li, L. Zhang, L. Ding, H. Ren, H. Cui, *Biosensors and Bioelectronics*, 26 (2011) 4169-4176.
- [3] P. Liang, H. Wang, X. Xia, X. Huang, Y. Mo, X. Cao, M. Fan, *Biosensors and Bioelectronics*, 26 (2011) 3000-3004.
- [4] S. Cheng, B.E. Logan, *Electrochemistry Communications*, 9 (2007) 492-496.
- [5] D.H. Park, J.G. Zeikus, *Biotechnology and Bioengineering*, 81 (2003) 348-355.
- [6] X. Wang, S. Cheng, Y. Feng, M.D. Merrill, T. Saito, B.E. Logan, *Environmental Science & Technology*, 43 (2009) 6870-6874.
- [7] K. Scott, G.A. Rimbu, K.P. Katuri, K.K. Prasad, I.M. Head, *Process Safety and Environmental Protection*, 85 (2007) 481-488.
- [8] H. Cai, J. Wang, Y. Bu, Q. Zhong, *Journal of Chemical Technology and Biotechnology*, 88 (2013) 623-628.
- [9] Y. Zou, C. Xiang, L. Yang, L.-X. Sun, F. Xu, Z. Cao, *International Journal of Hydrogen Energy*, 33 (2008) 4856-4862.
- [10] M. Ghasemi, W.R.W. Daud, N. Mokhtarian, A. Mayahi, M. Ismail, F. Anisi, M. Sedighi, J. Alam, *International Journal of Hydrogen Energy*, 38 (2013) 9525-9532.
- [11] G.G. Wallace, P.R. Teasdale, G.M. Spinks, L.A. Kane-Maguire, *Conductive electroactive polymers: intelligent polymer systems*, 3 th ed., CRC press, 2008.
- [12] S. Bocchini, A. Chiolerio, S. Porro, D. Accardo, N. Garino, K. Bejtka, D. Perrone, C.F. Pirri, *Journal of Materials Chemistry C*, 1 (2013) 5101-5109.
- [13] A. Chiolerio, S. Bocchini, S. Porro, *Advanced Functional Materials*, 24 (2014) 3375-3383.
- [14] P. Aelterman, K. Rabaey, H.T. Pham, N. Boon, W. Verstraete, *Environmental science & technology*, 40 (2006) 3388-3394.
- [15] J. Wei, P. Liang, X. Huang, *Bioresource Technology*, 102 (2011) 9335-9344.
- [16] P.H. Matter, E. Wang, M. Arias, E.J. Biddinger, U.S. Ozkan, *Journal of Molecular Catalysis A: Chemical*, 264 (2007) 73-81.
- [17] T. Iwazaki, R. Obinata, W. Sugimoto, Y. Takasu, *Electrochemistry Communications*, 11 (2009) 376-378.
- [18] R. Silverstein, F. Webster, *Spectrometric identification of organic compounds*, 6 th ed., John Wiley & Sons, 1998.

- [19] J. Tang, X. Jing, B. Wang, F. Wang, *Synthetic Metals*, 24 (1988) 231-238.
- [20] A. Chiolerio, P. Allia, P. Tiberto, M. Coisson, *Journal of Physics: Condensed Matter*, 20 (2008) 345213.
- [21] B.E. Logan, B. Hamelers, R. Rozendal, U. Schröder, J. Keller, S. Freguia, P. Aelterman, W. Verstraete, K. Rabaey, *Environmental Science & Technology*, 40 (2006) 5181-5192.
- [22] S. Fulda, A.M. Gorman, O. Hori, A. Samali, *International Journal of Cell Biology*, 2010 (2010) 23.
- [23] B. Erable, N. Duteanu, S.M.S. Kumar, Y. Feng, M.M. Ghangrekar, K. Scott, *Electrochemistry Communications*, 11 (2009) 1547-1549.
- [24] T. Saito, M. Mehanna, X. Wang, R.D. Cusick, Y. Feng, M.A. Hickner, B.E. Logan, *Bioresource Technology*, 102 (2011) 395-398.
- [25] C. Feng, L. Ma, F. Li, H. Mai, X. Lang, S. Fan, *Biosensors and Bioelectronics*, 25 (2010) 1516-1520.
- [26] R. Ganguli, B.S. Dunn, *Fuel Cells*, 9 (2009) 44-52.
- [27] Y. Fan, E. Sharbrough, H. Liu, *Environmental science & technology*, 42 (2008) 8101-8107.
- [28] G. Najafpour, M. Rahimnejad, N. Mokhtarian, W.R.W. Daud, A. Ghoreyshi, *World Applied Sciences Journal*, 8 (2010) 1-5.
- [29] M. Rahimnejad, G. Najafpour, A.A. Ghoreyshi, *Mass transfer in chemical engineering processes*, 5 (2011) 233-250.

## Chapter 8

### Streamlining of commercial berl saddles: a new material to improve the performance of microbial fuel cells

#### 8.1. Introduction

The main classes of biological wastewater treatment approach are aerobic and anaerobic treatments; the first is highly energy consuming, whereas the anaerobic treatment, adequately designed and operated can produce a surplus of energy [1] under the form of either bioCH<sub>4</sub> or bioH<sub>2</sub>, or both, according to the biowaste characteristics [2, 3]. So, the main challenges for this technology are to replace the energy expensive aerobic wastewater treatment approach, finding an alternative to the most common technologies, such as activated sludge and aerobic biofilm processes [4]. Both aerobic and anaerobic processes have their own niche in environmental technology and are commercially available. In addition, they are worldwide implemented to treat either municipal or industrial wastewaters [5, 6]. Among wastewater treatment plants, both entrapped or immobilized biofilm processes permit to reach a very high efficiency for reactor unit volume, either under aerobic or anaerobic conditions [7, 8]. This is attributed to the high concentration of microorganisms per unit of volume, consequently smaller compact systems are necessary with respect to wastewater treatment plants using free microorganism. The high bacteria concentration in entrapped or immobilized biofilm is due to the very large surface area of the support material available for the microorganism [9]. Moreover, in order to prevent mass transport problems and high liquid pressure drop, the ideal candidate support material needs to have high bed void fraction (75% minimum), high specific surface area (200 m<sup>2</sup>/m<sup>3</sup> minimum) and negligible interferences with biological functionality to guarantee an optimal microbial adhesion and activity [6, 9]. Plastic or ceramic materials with different shapes and dimensions are often selected for biofilm reactors, such as fixed and fluidized beds. A traditional support for bacteria used in immobilized bioreactors is the so-called Berl saddle. This is a ceramic scaffold with the shape of a saddle “without inside and outside faces” [10, 11]. The Berl saddle performs better than Rasching rings with respect to distribution and low pressure drop of fluids. It provides relatively high useable contact surface area with high void bed fraction. These features are of fundamental importance in the bioreactor field because of the presence of gas phase either in anaerobic or aerobic conditions. In the case of MFC, at the anode chamber, where anaerobic

conditions are present, the microorganisms generate gas that should migrate easily out of the system, in order to avoid an increase of pressure in the anode chamber [12]: hence the need of high bed void fraction is of paramount importance. Another aspect of the MFC anode regards the requirement of having as many as possible microorganisms pressed on the surface of the anode, in order to decrease the electrical polarization necessary to harvest the electrons produced via the respiration chain [13, 14]. To address this challenge, it is important to have a material with high porosity, showing a pore diameter with the same order of magnitude of microorganisms size, in order to increase the surface colonization of the anode [15, 16]. The application of a three-dimensional electrode has resulted in the increase of the volumetric power densities, hence it is highly recommended, from a construction point of view, for the generation in future larger MFC systems. Sell et al. [17] were the first to report on the use of a packed bed of granular graphite as a three-dimensional electrode and showing an increase of power density. They supposed an increment of charge transfer rate and a decrement of polarization effects thanks to the better performance of cell in terms of higher current values. Meanwhile, other three-dimensional electrodes were tested, including reticulated vitreous carbon [18], granular activated carbon [19], carbon brushes [20] and graphite granules [21, 22]. In particular, Aelterman et al. [22] have conducted tests using graphite granules of different sizes (2 mm and 5 mm) as packed electrode: the 5 mm graphite granules generated a maximum power output of  $257 \text{ mW}\cdot\text{L}^{-1}$  of Total Anode Compartment (TAC). While, the reactor with the 2 mm granules had a less stable electricity generation, generating  $143 \text{ mW}\cdot\text{L}^{-1}$  of TAC; moreover the small granules were heavy and created a clogging due to their relatively low porosity, that obstructed liquid and gaseous fluxes.

For the above mentioned reasons, in this Chapter Berl saddles are considered as packing material that could help to reduce the biofouling for its large bed void fraction, and favor the growth of biofilm and its activity, by increasing the degassing of the produced gas inside the MFCs anode. By considering that MFCs combine a biological process with the traditional fuel cell concept, it is necessary to render conductive the packing material to be used as electrode in MFC, which according to our knowledge, up to date was not performed yet. Therefore, in this Chapter the creation of a conductive carbon layer on the surface of ceramic Berl saddles was carried out.  $\alpha$ -D-glucose was used as precursor material for the carbon layer; the conductive layer was obtained by the following consecutive steps on the Berl saddles: (i) impregnation in  $\alpha$ -D-glucose solution, (ii) caramelization, and (iii) pyrolysis. This strategy allows obtaining by a cost-effective and easy procedure, a good packing material for bacteria growth and proliferation, helping in reducing biofouling and having a low electrical

resistance for the direct recovery of electrons by bacteria metabolisms. It is therefore a good candidate for anode material in a MFC. The obtained carbon-coated Berl saddles were characterized from a structural, morphological and chemical point of view as well as tested as anode material by a laboratory MFC. A comparison in terms of production and process cost was also carried out between our carbon-coated Berl saddles and commercial carbon felt, showing the advantages of the former material as anode for MFCs.

The results of this research are part of the publication entitled: “Streamlining of commercial Berl saddles: a new material to improve the performance of microbial fuel cells”. D. Hidalgo, T. Tommasi, V. Cauda, S. Porro, A. Chiodoni, K. Bejtka, B. Ruggeri. (2014) *Energy*, 71, 615.

## 8.2. Experimental

### 8.2.1. Materials

Yeast (*Saccharomyces cerevisiae*, baker yeast) was used as active microorganisms. Commercial Berl saddles,  $\alpha$ -D-glucose (96%), Methylene blue, Sodium phosphate dibasic dihydrate ( $\text{Na}_2\text{HPO}_4 \cdot 2\text{H}_2\text{O}$ , 98%), Sodium phosphate monobasic monohydrate ( $\text{NaH}_2\text{PO}_4 \cdot \text{H}_2\text{O}$ , 98%) and Potassium ferricyanide ( $\text{K}_3\text{Fe}(\text{CN})_6$ , 99%) were purchased from Sigma Aldrich.

### 8.2.2. Deposition of conductive carbon layer on Berl saddles

$\alpha$ -D-glucose was used to prepare a conductive carbon layer on commercial Berl saddles. Berl saddles were first accurately cleaned in ultrasonic bath for 10 min at 60 Hz using ethanol to remove pollutants from the surface and then dried in air at room temperature. Subsequently, Berl saddles (250 g) were immersed in 200 mL of glucose solution ( $500\text{g} \cdot \text{L}^{-1}$ ) in water under gentle orbital shaking conditions for 24 h. Berl saddles were separated by filtration from the glucose solution, and caramelized at 185 °C under vacuum for 24 h. The caramelized material was then pyrolyzed at 800 °C under  $\text{N}_2$  flux ( $500\text{ mL} \cdot \text{min}^{-1}$ ) in a horizontal tube furnace for 2 h (heating rate of  $5\text{ }^\circ\text{C} \cdot \text{min}^{-1}$ ), and then let to cool down overnight. A scheme of the whole preparation process is shown in Figure 8.1, where a picture of the step-by-step procedure and of the energy involved is highlighted. On the basis of this scheme, an evaluation of the conductive layer production cost is presented.

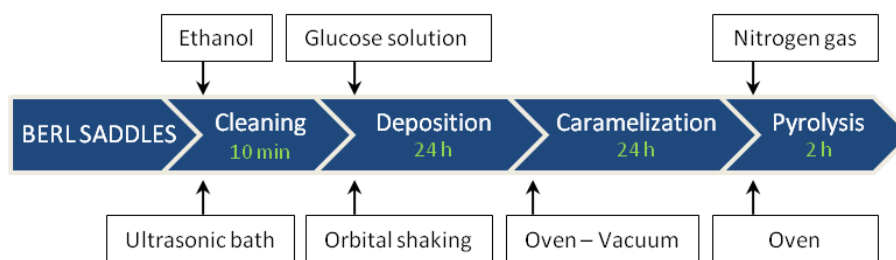


**Figure 8.1.** Scheme of the process flow for the deposition of conductive carbon layer on Berl saddles

### 8.2.3. Characterization of Berl saddles

The resistivity measurements were performed using a Keithley 2635 Source Measure Unit in a four-point probe configuration. The morphology of the Berl saddles before and after treatments were investigated by means of a Field Emission Scanning Electron Microscope (FESEM, ZEISS Dual Beam Auriga) equipped with Energy Dispersive Spectroscopy (EDS, Inca XSight; Oxford Instrument). Transmission Electron Microscopy (TEM) samples were prepared by collecting carbon flakes scraped from a coated Berl saddle after mild ultrasonic treatment in ethanol onto a holey carbon grid, and imaged using a FEI Tecnai F20ST operating at 200 kV. The crystalline structure of the carbon layer was analyzed by Philips X'Pert X-ray diffractometer in the Bragg-Brentano configuration with Cu-K $\alpha$  monochromatic radiation (1.54059 Å) as X-ray source. Raman spectra of the carbon layer deposited on Berl saddles were acquired using a standard Renishaw InVia micro-Raman spectrometer using laser excitation wavelength at 514 nm and laser spot size of 20  $\mu$ m. Nitrogen adsorption isotherm were obtained from a Quadrasorb instrument (Quantachrome) and Brunauer–Emmett–Teller (BET) specific surface area was measured by multipoint method within the relative pressure range of 0.1–0.3  $P/P_0$ . The pore size distribution was evaluated by the Density Functional Theory (DFT) method.

### 8.2.4. MFC configuration and operation

The MFC device consists of two rectangular chambers, i.e. the anode and the cathode. Both compartments were made in Plexiglas with dimension 0.08 m x 0.08 m x 0.02 m and separated by a cation exchange membrane (CEM, CMI 7000, Membranes International Inc.), as shown in Figure 8.2a. The conductive material was introduced in each chamber, by using the carbon-coated Berl saddles as anodic material (Figure 8.2b) and commercial carbon paper (Carolina, USA) as cathode. Each conductive material was connected with a graphite rod (5

mm in diameter) to ensure an effective current transport. All the investigations were carried out by using *Saccharomyces cerevisiae* as active microorganism, under the same operational conditions, in batch mode at room temperature  $22 \pm 2$  °C. The anodic chamber was filled with Yeast ( $50 \text{ g}\cdot\text{L}^{-1}$ ), Glucose ( $60 \text{ g}\cdot\text{L}^{-1}$ ) as feeding substrate and Methylene blue (MB) ( $1.22 \text{ g}\cdot\text{L}^{-1}$ ) as Red-Ox mediator for the transport of electrons from the microorganism to the electrode surface. The cathodic compartment was filled by Potassium ferricyanide ( $6.58 \text{ g}\cdot\text{L}^{-1}$ ) used as oxidant compound. To prepare anodic and cathodic solutions, a buffer of inorganic salts, i.e.  $\text{Na}_2\text{HPO}_4\cdot 2\text{H}_2\text{O}$  ( $8.2 \text{ g}\cdot\text{L}^{-1}$ ) and  $\text{NaH}_2\text{PO}_4\cdot \text{H}_2\text{O}$  ( $5.2 \text{ g}\cdot\text{L}^{-1}$ ) was used.

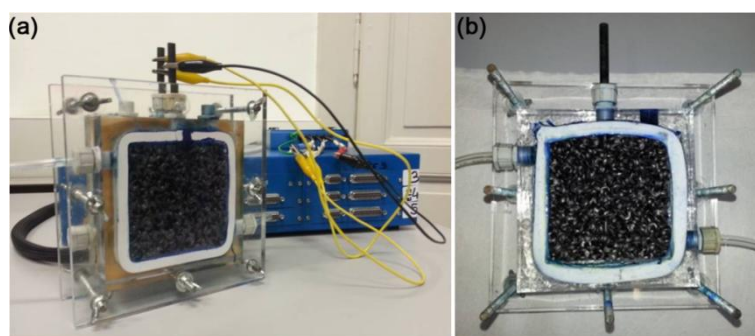


**Figure 8.2.** (a) Image of the MFC configuration and (b) anodic compartment filled with Berl saddles

### 8.2.5. Electrochemical measurements and analyses

The experiments were carried out in terms of Open Circuit Voltage (OCV), Linear Sweep Voltammetry (LSV), Cyclic Voltammetry (CV) and Current Interrupt (CI) techniques, in order to gain information on the dynamics of electron transfer and hence, on power production. Electrochemical experiments were performed on a multi-channel VSP potentiostat/galvanostat produced by BioLogic. Measurements were recorded by using EC-Lab software version 10.1x (BioLogic) for data acquisition. All tests were carried out using a two electrode setup, where the working electrode was coupled to the anode and both counter electrode and reference electrode were connected to the cathode. The anodic compartment was filled with 100 mL of anodic solution corresponding to 80% void fraction of the Berl saddles, which was calculated as the fraction of the void volume over the total volume in the anodic compartment. Polarization curves were performed at a scan rate of  $1 \text{ mV}\cdot\text{s}^{-1}$  when a constant OCV was achieved, from the open-circuit cell voltage  $V_0$  (where  $I = 0$ ) to the short-circuit cell voltage  $V_{sc} = 0$  (where  $I = I_{max}$ ). The measurements were carried out from  $t_{20min}$  to  $t_{24h}$  in order to examine *S. cerevisiae* ability to consume the substrate under anaerobic

conditions. From the  $I$ - $V$  curves, the power density was calculated by  $P = IVv^{-1}$ , where  $I$ ,  $V$  and  $v$  represent current, recorded voltage output and the total anode chamber (TAC), respectively. CV was performed at  $t_{2h}$  and  $t_{24h}$  with a scan rate of  $1 \text{ mV}\cdot\text{s}^{-1}$  from  $V_0$  to  $V_{sc}$ , continuing in the reverse direction until back to the starting potential in order to evaluate the electrochemical activity of microorganisms. CI measurement was performed to determine the internal resistance of the MFC through the interruption of the current flow and the resulting voltage transients [23]. The test was carried out using a very short perturbation to the system (10 ms) using a voltage  $V_0$  equal to 90% of OCV when the MFC produced stable current output  $I_o$ . The circuit was opened causing a steep potential ( $V_R$ ) followed of further low rise. The resistance was evaluated as  $R_{int} = V_R/I_o$  and a mean value of different tests were computed.

### 8.3. Result and discussion

#### 8.3.1. Characterization of Berl saddles

The pristine ceramic Berl saddles are mainly constituted of silica ( $\text{SiO}_2$ , >70%), alumina ( $\text{Al}_2\text{O}_3$ , 17-23%) and others oxides ( $\text{K}_2\text{O} + \text{Na}_2\text{O}$ ,  $\text{Fe}_2\text{O}_3$ ,  $\text{CaO}$ ); these are all non-conductive compounds, which makes the Berl saddles extremely inappropriate to be used as electrode in MFC. Therefore, to render Berl saddles a suitable electrode for MFC, deposition of conductive carbon layer is necessary. The process is summarized in Figure 8.1 and the results on the Berl saddle surface are shown in Figure 8.3. After the impregnation and caramelization steps, the Berl saddles resulted completely covered by glucose (Figure 8.3b). After pyrolysis, the formation of a carbon layer on the surface of the material was obtained, resulting in an evident color change, as shown in Figure 8.3c. The electrical properties of the material were evaluated in four-point probe configuration, obtaining a resistivity around  $50 \pm 10 \text{ } \Omega$  on the pyrolyzed Berl saddles.

The Berl saddles were imaged by FESEM before and after treatment including the final pyrolysis step. Pristine Berl saddles show a very rough surface (Figures 8.4a and 8.4b) whereas the impregnation with glucose, caramelization and further pyrolysis lead to a smoothing of the surface covered by carbon (Figures 8.4c and 8.4d). The thickness of the carbon layer is about 7-8  $\mu\text{m}$ , and the composition as shown in the inset of Figure 8.4c. EDS analysis was carried out on both surfaces (Figures 8.4e and 8.4f), showing that the amount of carbon after pyrolysis greatly increases on the surface of the Berl saddles. Also the amount of oxygen decreases after pyrolysis, confirming the formation of graphitic carbon. The relative

content of the other elements, mainly related to the saddle composition, remain nearly the same.



**Figure 8.3.** Image of the Berl saddles: (a) pristine (b) after caramelization (c) after pyrolysis of the glucose

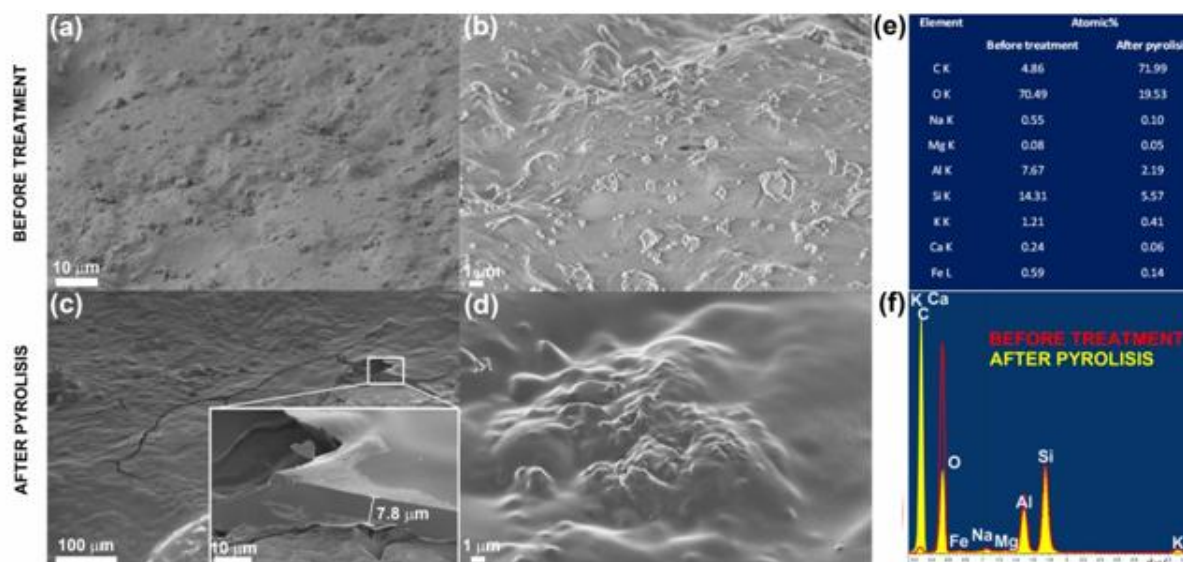


**Figure 8.4.** FESEM images of the Berl saddles (a,b) before any treatment; (c,d) after impregnation with glucose, caramelization and pyrolysis; (e) table of elements obtained by EDS analysis before and after treatment; and (f) graph of the relative amount (atomic %) of the elements on the Berl saddles surface before and after treatment

The crystalline nature of the carbon layer was investigated by both X-ray diffraction pattern (Figure 8.5a) and Raman spectroscopy (Figure 8.5b). It is worth to note that after caramelization (orange curve in Figure 8.5a) and even more after pyrolysis (red curve), a pronounced peak at  $26.6^\circ$ , assigned to the (002) reflection plane of graphite, appears. The broader FWHM of the (002) peak in the caramelized sample with respect to the pyrolyzed

one, is attributed to the small size of the graphitic crystals, which are nucleating but not completely formed at such low temperature (185 °C).

In contrast, the narrow and intense (002) peak of the sample after pyrolysis reveals the presence of larger graphitic crystal due to the high temperature treatment (800 °C). Peaks at higher angles are also clearly visible in the spectrum of pyrolyzed saddles and can be all assigned to polycrystalline graphite (JCPDS 41-1487). Figure 8.5b reports the Raman spectra of four different spots on the sample. No relevant differences are observed among them, so the covering of the saddles surface can be considered uniform, in agreement with FESEM analysis. The presence of G and D peaks typical of graphitic and amorphous carbon is observed [24, 25]. Table 8.1 reports the analysis of G and D peaks positions ( $\text{cm}^{-1}$ ) and intensities (arbitrary units), the intensities ratio ( $I_D/I_G$ ) and an estimation of the graphitic clusters dimension ( $L_a$ ) calculated by Tuinstra/Koenig model [26]. The reported Raman spectra are typical of polycrystalline graphitic carbon ( $\text{sp}^2$  hybridized), with a certain disorder arising from nanostructured clusters indicated by the presence of D peak. The position of G peak is shifted with respect to that of pure graphite ( $1581 \text{ cm}^{-1}$  to  $\sim 1593 \text{ cm}^{-1}$ ), confirming the presence of some degree of nanostructure graphitic clusters, with  $L_a$  calculated by the aforementioned model to be about 5.5 nm. The presence of tetrahedral carbon ( $\text{sp}^3$  hybridized) is minimal; however, a slight amorphization of the carbon clusters could not be excluded by this technique.

Nitrogen sorption isotherm reported in Figure 8.5c shows the presence of hysteresis and some microporosities either in Berl saddle as such (black curve) or after pyrolysis (red curve). This is indeed confirmed by the DFT pore size distribution (Figure 8.5d), showing a broad pore size range in both saddles before and after treatment. However, smaller nanopores size of about 2.6 and 4.1 nm are evidenced in the pyrolyzed material, with respect to the commercial one (pore size maximum at about 4.8 nm). The BET surface area shows an increase of more than 3 times from the pristine Berl saddles ( $0.13 \text{ m}^2 \cdot \text{g}^{-1}$ ) with respect to those covered by pyrolyzed graphitic carbon ( $0.46 \text{ m}^2 \cdot \text{g}^{-1}$ ). The increase of both surface area and pore volume are attributed to the polycrystalline graphitic carbon layer formation, both of them are key points for the overall anode performance and bacteria growth and proliferation.

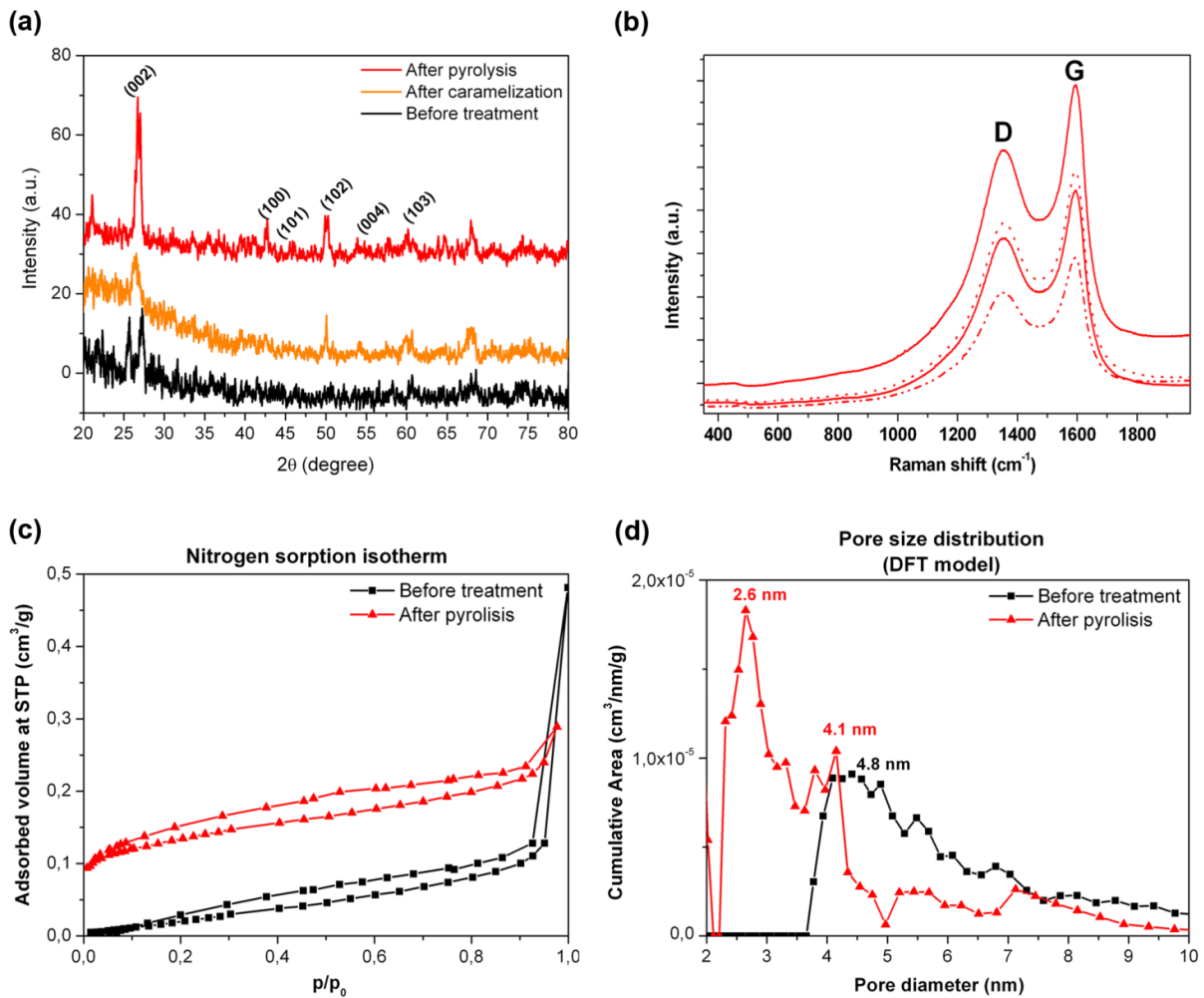


**Figure 8.5.** (a) XRD pattern of the commercial Berl saddles (black curve), after caramelization (orange curve) and pyrolysis (red curve); (b) Raman spectra of the pyrolyzed carbon-coated Berl saddle at four different spots (G and D peaks typical of graphitic and amorphous carbon); (c) Nitrogen sorption isotherms and (d) DFT pore size distribution of the Berl saddles before treatment (black curve) and after pyrolysis (red curve)

The presence of graphitic carbon was also confirmed by TEM analysis. Figure 8.6a shows a Bright Field TEM image of the edge of a graphitic flake. It contains numerous nanocrystals and the Fourier Transform of the crystalline area (shown in the inset) indicates the polycrystalline nature of the flakes, with a slight preferential orientation, as already pointed out with XRD analysis. Figure 8.6b shows graphite nanocrystals with dimension below 10 nm.

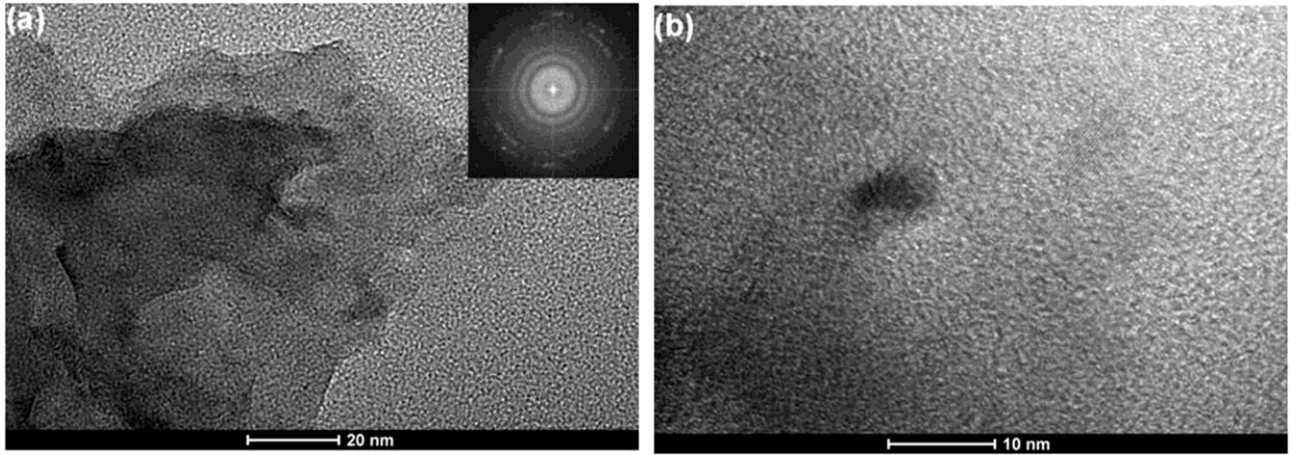


**Figure 8.6.** Bright Field TEM image of the carbon coating on Berl saddles: (a) edge of the coating and (b) graphite nanocrystals

**Table 8.1.** Analysis of carbon peaks at 4 different spots on the sample measured by Raman spectroscopy

Sample	D position ( $\text{cm}^{-1}$ )	G position ( $\text{cm}^{-1}$ )	$I_D$	$I_G$	$I_D/I_G$	$L_a$ (nm)
1	1352	1592	235668	294918	0.799	5.51
2	1351	1592	155334	194906	0.797	5.52
3	1353	1593	320111	395579	0.809	5.44
4	1352	1594	217071	272753	0.796	5.53
Average	$1352 \pm 1$	$1593 \pm 1$			$0.800 \pm 0.004$	5.5

### 8.3.2. Electrochemical characterization of carbon-coated Berl saddles in MFC

Figure 8.7a shows the polarization curves [27, 28] obtained by varying the scan rate of  $1 \text{ mV} \cdot \text{s}^{-1}$  for the whole MFC from  $t_{20\text{min}}$  to  $t_{24\text{h}}$  using the carbon-coated Berl saddles as anodic material. These polarization curves can be divided in three zones: (i) starting from the OCV where  $I = 0$ , there is an initial steep decrease of the voltage corresponding to the activation losses; (ii) the voltage then falls more slowly and the voltage drop is fairly linear with current indicating that ohmic losses are dominant; and finally (iii) the voltage falls rapidly at higher currents. This last effect could be attributed to the polarization effects inducing mass transfer phenomena [29]. Additionally, we observed that at least two hours were required to obtain a

proper characterization of the system and thus to achieve a complete stabilization of the operating conditions in the MFC.

Based on these data, power density curves were obtained as reported in Figure 8.7b. The maximum power density produced, respect to the total anode chamber (TAC) was  $8 \text{ mW}\cdot\text{L}^{-1}$  ( $130 \text{ mW}\cdot\text{m}^{-2}$ ) at a current density of  $29.6 \text{ mA}\cdot\text{L}^{-1}$  after 2 h of operation. It is also possible to observe that both power and current densities decrease during the test evolution due to the consumption of reagents by microorganisms, thus lowering the substrate availability for the microorganism activity.

Figure 8.7c shows cyclic voltammetric curves [30] obtained using the Berl saddles in MFC after 2 h and 24 h of operation, by applying a scan rate of  $1 \text{ mV}\cdot\text{s}^{-1}$ . The results showed that by decreasing the potential from OCV to the short-circuit cell voltage, the polarization curves exhibit the three main zones previously described. Continuing in the reverse direction, a slight decrease of the current was obtained with respect to the initial values. This can be explained by assuming that the biological systems require a few minutes to reach quasi-steady-state conditions after being disturbed to return at the start potential (OCV). Finally, through the CV measurement, it was also possible to confirm the activity of the microorganisms related with a reduction of the available substrate for the growth and the consequent decrease of the current after 24 h of operation.

The internal resistance was determined using the current interrupt method [21]. In this case, when the MFC produced a stable current output before interruption ( $I_o$ ) and potential approximately equal to 90% of OCV, the circuit was opened causing an initial steep potential ( $V_R$ ) during the first 10 ms of the perturbation to the system. The steep is referred to the ohmic losses caused by the internal resistance ( $R_{int}$ ) calculated as  $R_{int} = V_R/I_o$ . The obtained results showed internal resistance at 2 h and 24 h of operation around  $25 \Omega$  and  $23 \Omega$ , respectively. The reduction of the internal resistance with time could be explained by the growth of the microorganisms, which generate a biofilm around the Berl saddles improving their colonization and hence increasing the electron transport from the microorganisms to the electrode. A wide variety of electrode materials were studied in the literature in order to increase the power density of MFCs [31, 32]. However, up to date, the principal bottleneck limiting the efficiency of MFC continues to be the electron transfer from the bacteria to the anode.

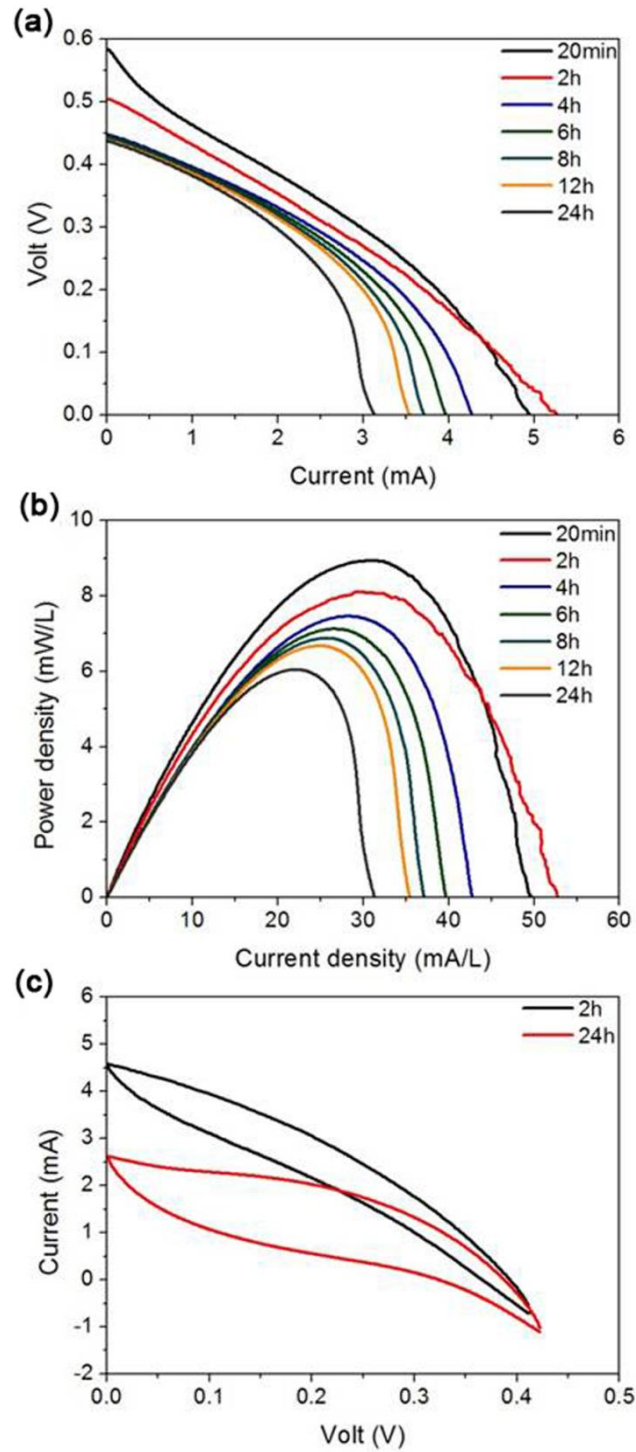


**Figure 8.7.** (a) Polarization curves and (b) power density curves referred to TAC carried out from  $t_{20\text{min}}$  to  $t_{24\text{h}}$ ; (c) Cyclic Voltammetry at  $t_{2\text{h}}$  (black curve) and  $t_{24\text{h}}$  (red curve) using Berl saddles during a single test in MFC device

The Table 8.2 shows a representative set of power density data for MFCs by various researchers using *Saccharomyces cerevisiae* with different electrode materials and electron

mediators [33-35]. It is possible to see that the obtained power density with carbon-coated Berl saddles increased of about 2-3 times higher compared to the literature data. Additionally, by the same MFC configuration, we tested a commercial carbon felt (data not reported) under the same operational conditions used for the Berl saddles artifact in MFCs, obtaining comparable results ( $180 \text{ mW}\cdot\text{m}^{-2}$ ). Authors working in different conditions (e.g. other microorganisms, design and operative conditions) but with packed electrode, have obtained comparable results: the maximum power density varies between 5 to  $90 \text{ mW}\cdot\text{L}^{-1}$  of anodic chamber volume, using granular activated carbon [19] and granular graphite [21], respectively.

**Table 8.2.** Comparison of literature data obtained using *Saccaromyces cerevisiae*, methylene blue as electron mediators with different electrode materials in MFCs

Reference	Microbe	Substrate	Anode	Mediator ( $\text{mW}\cdot\text{m}^{-2}$ )	
[33]	<i>S. cerevisiae</i>	Glucose	Platinum mesh	MB	65
[34]	<i>S. cerevisiae</i>	Hydrolyzed lactose	Graphite	MB	4
[35]	<i>S. cerevisiae</i>	Glucose	Graphite plates	MB	8
Our previous work <sup>a</sup>	<i>S. cerevisiae</i>	Glucose	Carbon felt	MB	180
Present work	<i>S. cerevisiae</i>	Glucose	Carbon-coated Berl saddles	MB	130

<sup>a</sup> Results obtained under the same operational conditions used to test the Berl saddles as anode material.

This confirms that carbon-coated Berl saddles show an outstanding potential applicability as electrode in MFC, matching either electrical requirements or bacteria activity. In addition, we verified that during the time of the test no clogging of the electrode as consequence of gas entrapment occurred, confirming the great potential in the use of the innovative carbon-coated Berl saddles as anode in MFCs and for scale-up purposes. Finally, the surface of the Berl Saddles was also investigated by FESEM after their operation in MFC. In Figure 8.8 a FESEM picture of the surface of Berl saddles after the operation in the MFC is reported. It shows that the graphite layer is nearly intact, after 24 hours of operation. In addition, the

presence of *S. cerevisiae* grown on top of the surface support is clearly observed. The presence of these bacteria demonstrates that a proper colonization of the graphite surface by microorganisms can take place, confirming that our innovative graphitized Berl saddles have a good potential applicability as electrode in MFCs.

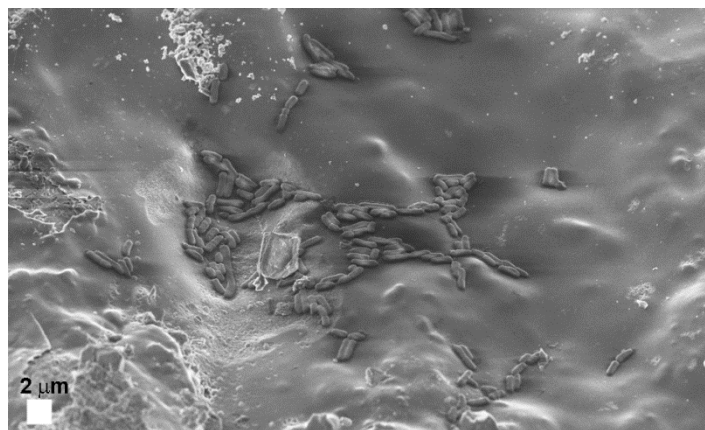


**Figure 8.8.** FESEM image of the Berl saddles surface after the electrochemical test in MFC

### 8.3.3. Cost analysis of carbon-coated Berl saddles

In order to evaluate the advantages of using Berl saddles with respect to commercial carbon felt as anode material in MFC, a comparison of those materials from an economic point of view is mandatory. These data are presented in Table 8.3. The cost of reagents used for the carbon layer deposition on Berl saddles was provided by the manufacturers of the raw materials. Similarly, the energy consumed during the preparation process was estimated using the European energy cost [36]. The cost of Berl saddles was calculated according with the quantity of material necessary to fill a MFC chamber (0.15 Kg) with dimensions 0.08 m x 0.08 m x 0.02 m.

The quantification of the energy consumed for each instrument employed in the different processes was estimated in two steps with the following considerations: i) the effective power consumption for the instruments used per each process step was estimated using a ratio of the full nominal power calculated considering the effective time of on-mode (e.g. the time slots in which a furnace was on to ramp and maintain the setup temperature); ii) in addition, the power consumption data were scaled considering that the instruments were not used at full volume capacity.

From the results obtained reported in Table 8.3, it was found that about 0.96 € will be required to produce the Berl saddles necessary to fill the anodic chamber. The cost of

commercial carbon felt is 130 €/m<sup>2</sup> (SGL group S.p.A). To fill a MFC chamber with the same dimension of that used for the Berl saddles, a surface area of 0.064 m<sup>2</sup> is necessary which is equivalent to 0.83 €. Therefore, the cost involved to produce the lab-scale Berl saddles is slightly higher than the cost of commercial carbon felt. However, a consistent decrease in the cost of the carbon-coated Berl saddle could be obtained in the production at the industrial scale. Also, the Berl saddle acts as a traditional support material for bacteria in immobilized bioreactors, which proves that this material is completely suitable for bacteria growth and proliferation. As a consequence from these considerations, a second generation of MFC reactor will consist in a single-compartment tubular chamber containing the Berl saddles as anode, which could be used for scale-up purposes, whereas the cathode will be a conductive foil wrapped on it. These results will be presented in a forthcoming work.

**Table 8.3.** Cost estimation analysis of carbon-coated Berl saddles

<b>Material</b>	<b>Unit cost</b>	<b>Quantity / MFC chamber</b>	<b>Cost / MFC chamber (€)</b>
Berl saddles	0.18 €/kg <sup>a</sup>	0.15 kg	0.03
Ethanol	1 €/L <sup>b</sup>	0.03 L	0.03
Glucose	1 €/kg <sup>b</sup>	0.08 kg	0.08
Nitrogen gas	2.37 €/m <sup>3,c</sup>	0.09 m <sup>3</sup>	0.21
Ultrasonic bath	0.17 €/kWh <sup>d</sup>	0.03 kWh	0.01
Orbital shaking	0.17 €/kWh	0.18 kWh	0.03
Oven – vacuum	0.17 €/kWh	2.31 kWh	0.40
Oven	0.17 €/kWh	1.00 kWh	0.17
Total cost per chamber (€)			0.96

<sup>a</sup> Purchased from Sigma Aldrich

<sup>b</sup> Italian Chambers of Commerce

<sup>c</sup> Sapio Group

<sup>d</sup> EUROSTAT, Price of electricity for non-domestic use in Europe in the second half of 2012

#### 8.4. Conclusions

In this Chapter a continuous and homogeneous graphite layer was deposited on commercial Berl saddles by subsequent steps of impregnation, caramelization and pyrolysis of glucose, used as carbon precursor. Morphological, structural and chemical properties of the carbon-coated Berl saddles were studied and the presence of graphitic carbon was confirmed. The conductive carbon-coated Berl saddles were successfully used as anode electrode in MFC using *S. cerevisiae* as active microorganism. After a period of stabilization of 2 h, an open circuit voltage between 440-600 mV was observed in the cell. The results revealed a maximum power density of  $8 \text{ mW}\cdot\text{L}^{-1}$  at a current density of  $29.6 \text{ mA}\cdot\text{L}^{-1}$ . These values are significantly higher than those of many carbon materials reported in the literature, and are in good agreement with the results obtained using commercial carbon felt under the same MFC operation. In addition, a production and processing cost estimation for carbon-coated Berl saddles shows that they can be very competitive with respect to industrially-produced carbon felt. The obtained results suggest that the carbon-coated Berl saddles offer a low-cost solution to satisfy either electrical or bioreactor requirements, increasing the reliability of the MFC processes. This new electrode material seems to be a valid candidate for scaled-up systems and for continuous mode application of MFC technology.

#### 8.5. References

- [1] T. Tommasi, B. Ruggeri, S. Sanfilippo, *Journal of Cleaner Production*, 34 (2012) 91-97.
- [2] G. Kvesitadze, T. Sadunishvili, T. Dudaury, N. Zakariashvili, G. Partskhaladze, V. Ugrehelidze, G. Tsiklauri, B. Metreveli, M. Jobava, *Energy*, 37 (2012) 94-102.
- [3] H. Ren, W. Zhou, K.i. Nakagami, W. Gao, *Energy*, 35 (2010) 2210-2222.
- [4] S.T. Oh, J.R. Kim, G.C. Premier, T.H. Lee, C. Kim, W.T. Sloan, *Biotechnology Advances*, 28 (2010) 871-881.
- [5] P. Aelterman, *Microbial fuel cells for the treatment of waste streams with energy recovery*, Ghent University, 2009.
- [6] P. Aelterman, K. Rabaey, P. Clauwaert, W. Verstraete, *Water Science & Technology*, 54 (2006) 9-15.
- [7] A. Luciano, P. Viotti, G. Mancini, V. Torretta, *Journal of environmental management*, 113 (2012) 51-60.
- [8] A. Cheikh, A. Yala, N. Drouiche, N. Abdi, H. Lounici, N. Mameri, *Ecological Engineering*, 53 (2013) 329-334.
- [9] C. Arnaiz, J. Gutierrez, J. Lebrato, *Biochemical engineering journal*, 27 (2006) 240-245.

- [10] Chemical and Engineering News. BERL SADDLES Tops Tower Pack, 22 (1944) 78.
- [11] Sigma Aldrich.  
<http://www.sigmaaldrich.com/catalog/product/aldrich/z169013?lang=it&region=IT> 2014.  
Last access: April 2014
- [12] V. Oliveira, M. Simões, L. Melo, A. Pinto, *Energy*, 61 (2013) 463-471.
- [13] X. Wang, H. Lin, J. Wang, B. Xie, W. Huang, *Materials letters*, 78 (2012) 174-176.
- [14] D.R. Lovley, *Geobiology*, 6 (2008) 225-231.
- [15] X. Xie, M. Ye, L. Hu, N. Liu, J.R. McDonough, W. Chen, H. Alshareef, C.S. Criddle, Y. Cui, *Energy & Environmental Science*, 5 (2012) 5265-5270.
- [16] M. Di Lorenzo, T.P. Curtis, I.M. Head, K. Scott, *Water research*, 43 (2009) 3145-3154.
- [17] D. Sell, P. Krämer, G. Kreysa, *Applied Microbiology and Biotechnology*, 31 (1989) 211-213.
- [18] Z. He, S.D. Minter, L.T. Angenent, *Environmental science & technology*, 39 (2005) 5262-5267.
- [19] D. Jiang, B. Li, *Biochemical engineering journal*, 47 (2009) 31-37.
- [20] B. Logan, S. Cheng, V. Watson, G. Estadt, *Environmental science & technology*, 41 (2007) 3341-3346.
- [21] K. Rabaey, P. Clauwaert, P. Aelterman, W. Verstraete, *Environmental science & technology*, 39 (2005) 8077-8082.
- [22] P. Aelterman, M. Versichele, M. Marzorati, N. Boon, W. Verstraete, *Bioresource Technology*, 99 (2008) 8895-8902.
- [23] B.E. Logan, B. Hamelers, R. Rozendal, U. Schröder, J. Keller, S. Freguia, P. Aelterman, W. Verstraete, K. Rabaey, *Environmental science & technology*, 40 (2006) 5181-5192.
- [24] A. Ferrari, J. Robertson, *Physical Review B*, 61 (2000) 14095.
- [25] A.C. Ferrari, J. Robertson, *Philosophical Transactions of the Royal Society of London. Series A: Mathematical, Physical and Engineering Sciences*, 362 (2004) 2477-2512.
- [26] F. Tuinstra, J.L. Koenig, *The Journal of Chemical Physics*, 53 (1970) 1126-1130.
- [27] A.K. Manohar, O. Bretschger, K.H. Nealson, F. Mansfeld, *Electrochimica Acta*, 53 (2008) 3508-3513.
- [28] T. Tommasi, A. Chiolerio, M. Crepaldi, D. Demarchi, *Microsystem Technologies*, 20 (2014) 1023-1033.
- [29] I.S. Kim, K.-J. Chae, M.-J. Choi, W. Verstraete, *Environmental Engineering Research*, 13 (2008) 51-65.

- [30] E. LaBelle, D. Bond, I.P. Lens, Bio-electrochemical Systems: from Extracellular Electron Transfer to Biotechnological Application, (2005).
- [31] M. Zhou, M. Chi, J. Luo, H. He, T. Jin, Journal of Power Sources, 196 (2011) 4427-4435.
- [32] J. Wei, P. Liang, X. Huang, Bioresource Technology, 102 (2011) 9335-9344.
- [33] A.L. Walker, C.W. Walker Jr, Journal of Power Sources, 160 (2006) 123-129.
- [34] G. Najafpour, M. Rahimnejad, N. Mokhtarian, W.R.W. Daud, A. Ghoreyshi, World Applied Sciences Journal, 8 (2010) 1-5.
- [35] M. Rahimnejad, G. Najafpour, A.A. Ghoreyshi, Mass transfer in chemical engineering processes, 5 (2011) 233-250.
- [36] Ronchi E, Barbabella A, Refrigeri L. I costi dell'energia in Italia. Fondazione per lo sviluppo sostenibile, Roma: 2013.  
[http://www.fondazionevilupposostenibile.org/f/Documenti/Costi\\_energia\\_in\\_Italia\\_web.pdf](http://www.fondazionevilupposostenibile.org/f/Documenti/Costi_energia_in_Italia_web.pdf)  
Last access: April 2014.

## Chapter 9

### Continuous electricity generation using microorganisms from seawater in microbial fuel cells (MFCs): long-term evaluation of promising anode materials

#### 9.1. Introduction

MFCs provides new opportunity for sustainable energy production from biodegradable compounds present in the wastewater, achieving simultaneous wastewater treatment [1]. Furthermore, MFCs operated using mixed cultures currently achieve substantially greater power densities than those with pure cultures [2, 3], mainly due to a much wider substrate utilization [4].

The ideal performance of an MFC depends on the electrochemical reactions that occur between the organic substrate at a low potential such as acetate and the final electron acceptor with a high potential, such as oxygen [5]. However, its ideal cell voltage is uncertain because the electrons are transferred to the anode from the organic substrate through a complex respiratory chain that varies from microbe to microbe and even for the same microbe when growth conditions differ. According to this, MFC voltages will remain limited; even neglecting the internal losses, the voltage will never exceed a theoretical open circuit voltage (OCV) of 1.14 V as determined by the NADH (-0.32 V) and pure oxygen (+0.82 V) redox potentials [4, 6]. The highest OCV (1.05 V) thus far reported using microbial anodes and Enzymatic Bilirubin Oxidase (BOx) Air-Breathing Cathode [7] illustrates this limitation. The maximum current on the other hand is determined by: (i) the MFC design which determines the electrochemical losses (e.g., internal resistance) and convective transport limitations [3, 8], (ii) the volumetric loading which represents the total amount of electrons delivered by the substrate for current production, and finally, (iii) the amount of substrate converted to electricity (the Coulombic efficiency) [9]. Despite this, improvements of the reactor design [10], the application of new electrode materials [11], improved cathode reactions [12, 13] and the enrichment of highly specialized microbial communities [14], have enabled that the performance and durability of MFCs increased over the last years.

Despite all efforts to increase the electron transfer from the bacteria to the anode, up to date it continues to be the principal bottleneck limiting the efficiency of MFCs. For this propose, a wide variety of electrode materials have been studied in the literature in order to increase the power density of MFCs [11, 15]. Modifying the electrode surface by the binding of mediators

such as neutral red and metals such as iron and manganese has resulted in an increased current generation [16]. Foam structured anodes with carbonized polymers with ferrocene catalyst result in a higher biocompatibility with *Escherichia coli* [17]. By using carbon electrodes modified with quinone/quinoid groups [18] and by combining a highly conductive electrolyte and an ammonium electrode treatment [19], a doubling of the maximum power density could be achieved compared to unmodified graphite and carbon felt. Conductive polymer materials such as polyaniline (PANI), polypyrrole (PPy) and composites materials based on them, in combination with carbon materials, have been studied to improve MFC performance [20-23]. Results obtained in a two-chamber MFC using a microbial community of *Clostridium* and two conductive polymers: polyaniline (PANI) and polyaniline-co-o-aminophenol (PAOA) to modify carbon felt anode reached a maximum power density of 27.4  $\text{mW}\cdot\text{m}^{-2}$  and 23.8  $\text{mW}\cdot\text{m}^{-2}$ , and compared with unmodified carbon felt, i.e. increased by 35% and 18%, respectively [20]. Specifically, however, the use of a three-dimensional electrode has resulted in the increase of the volumetric power densities [10, 24]. In 1989, Sell et al. [25] were the first to report the use of a packed bed of granular graphite as a three-dimensional electrode. Meanwhile, other three-dimensional electrodes have been tested, including reticulated vitreous carbon [26], granular activated carbon [27] and carbon brushes [13]. In comparison to the use of flat or two-dimensional electrodes, three-dimensional electrodes have higher surface to volume ratios of up to  $6.0 \times 10^6 \text{ m}^2\cdot\text{m}^{-3}$  [28, 29] which can support an increased attachment of biofilm. It also results in a lower surface based current density for a given flow of electrons. As most losses are related to the current density, this can result in an increased power output [30]. Under these considerations, the application of three-dimensional structures is inevitable for the generation of high currents in future larger MFC systems.

MFCs hitherto produce power densities up to 17-19  $\text{W}\cdot\text{m}^{-2}$  with respect to electrode surface area or volumetric power densities up to 2.87  $\text{kW}\cdot\text{m}^{-3}$ , admittedly at very small scale and artificial conditions [31-33]. Apart from energy recovery from wastewater, MFCs have also been investigated for other applications such as biosensors and energy-neutral desalination [34, 35]. The most important technological advance which expanded the application range for microbial electrocatalysis has been the possibility to apply the electricity produced by microbial fuel cells as the driving force to catalyze the production of high value chemicals such as hydrogen gas, caustic soda or hydrogen peroxide at the cathode, at a lower energy cost compared to more classical electrochemical production processes [36-38]. Electricity, now increasingly available at low cost from renewable sources, enables driving microbial conversions that are otherwise thermodynamically not feasible. The higher value of these

reduced final products relative to electricity makes the microbial fuel cells more economically attractive towards concrete industrial implementations [39].

This chapter presented a compressive study of the most promising anode materials studied previously in Chapters 6 to 8. The performance of different electrode materials (flat and three-dimensional structures) was studied under continuous operation in MFCs systems not only to obtain an increase on the power density, but rather for produce energy which could be effectively used in different industrial applications as described above. To this propose, the performance of the different anode materials in a two-chamber MFC were examined: (1) commercial carbon felt, due to its good performance have been used as electrode in several MFCs investigations reported in literature (more details see Chapter 6) [29, 40, 41], (2) polyaniline-deposited carbon felt, which have been recently studied and results shown an important increase of MFC performance (more details see Chapter 7) [20, 42]; however up to date according to our knowledge results of a long-term evaluation tests have not been reported, and finally (3) carbon-coated Berl saddles, a three-dimensional electrode developed during this work which offer a suitable support for biofilm growth and a promising material for scale up MFCs systems (more details see Chapter 8) [29]. A compressive characterization of our MFCs systems was performed for more than three months of operation under continuous operation mode. In order to contribute to a greater und understanding regarding to the MFCs performance, the Real Time quantitative Polymerase Chain Reaction (RT-qPCR) was used as a method for determining bacterial communities presented in the anode. RT-qPCR measurement were conducted by Armato (2014) in collaboration with Università degli Studio di Torino. Current generation was evaluated in term of the influence of operational parameters such as: anodic and cathodic behavior, substrate concentration or flow rate, external resistance, recirculation loop and operation time. Even, an accurate monitoring of the main operational conditions was conducted, including: pH, temperature, conductivity and substrate concentration due to their important contribution on the biofilm growth and hence in the electricity production by MFCs. The electrochemical performance was evaluated in term of polarizations curves including: Linear Sweep Voltammetry and Current Interrupt method. Finally, the continuous energy produced was calculated from voltage data recorder under an external load connected to each MFCs system.

The results of this research are part of the publication entitled: “Continuous electricity generation using microorganisms from seawater in microbial fuel cells (MFCs): long-term

evaluation of promising anode materials". D. Hidalgo, T. Tommasi, V. Karthikeyan, B. Ruggeri. Under preparation.

## 9.2. Experimental

### 9.2.1. Materials

**Electrode materials:** commercial carbon felt (Soft felt SIGRATHERM GFA5, SGL Carbon, Germany), polyaniline-deposited carbon felt and carbon-coated Berl saddles were using as anode electrode. All experiments were conducted using commercial carbon felt in the cathode chamber. **Anode modifications:** N-phenyl-1,4-phenyldiamine (DANI, 98%), ammonium persulfate (APS, 98%), poly (sodium 4-styrenesulfonate) (PSS), chloridric acid (HCl, 37%) and methanol (CH<sub>4</sub>O, 99.9%) were used to perform polyaniline (PANI) deposition on commercial carbon felt (C-FELT) following the deposition procedure explained in Chapter VII. Carbon-coated Berl saddles were obtained according to the procedure described in Hidalgo et al. [29].

**Reagents:** sodium acetate ( $\geq 99\%$ ), peptone (bacteriological for microbiology), potassium ferricyanide ( $\geq 99\%$ ), sodium phosphate dibasic dihydrate ( $\geq 98\%$ ) and sodium phosphate monobasic monohydrate ( $\geq 98\%$ ) were used to conduct electrochemical experiments in the MFC. All reagents used were purchased from Sigma Aldrich.

### 9.2.2. Bacterial growth conditions

The fresh sea water sample (Arma di Taggia, Sanremo, Italy), before to be used as inoculum in MFCs was previously enriched in 250 mL glass flasks in three following steps. In the first step, the fresh seawater was inoculated (10% v/v) into a synthetic substrate, with the following composition in g·L<sup>-1</sup>: 7 C<sub>6</sub>H<sub>12</sub>O<sub>6</sub>, 8.2 Na<sub>2</sub>HPO<sub>4</sub>, 5.2 NaH<sub>2</sub>PO<sub>4</sub>, 8 CH<sub>3</sub>CO<sub>2</sub>Na, 7 fructose and 10 peptone. These reagents were dissolved in 75% v/v filtered sea water and 25 % v/v distilled water. After that, the pH of culture was set-up in the range 7 - 7.5 by adding NaOH 2 N. Furthermore, in order to reach strictly anaerobic condition, the culture was purged by N<sub>2</sub> flow for 5 min. The "culture enrichment" was conducted at room temperature (24 ± 2 °C) and under gentle orbital shaking (150 rpm). The bacteria growth was monitored taking samples during time-course of the test by measuring the optical density (OD) at 600 nm. When OD was inside the range (0.5 - 0.8 ) A, that is inside the range of the exponential phase of bacteria growth, 10% culture was used as inoculum of the new fresh culture (second step), which contains the same medium described before and the same operative conditions.

Once again the culture reached an OD in the range (0.5 - 0.8) A was inoculated in the third fresh medium, repeating the same procedure. When OD was in the range (0.5 - 0.8) A, the inoculum was ready to be inoculated into MFC test, always in a ratio of 10% v/v of the total anode volume.

### **9.2.3. Determination of bacterial communities**

In order to evaluate microbial community variability for each MFC, DNA extraction was performed with a commercial kit (UltraClean™ Microbial DNA Isolation Kit, MO-BIO Laboratories Inc., Carlsbad, CA), and the fluorimetric quantification of each DNA sample was performed using Qubit™ Fluorometer and Qubit™ dsDNA HS Assay by Invitrogen (distributed by Life Technology Ltd. – Paisley, UK). After DNA extraction and purification, the Real Time quantitative Polymerase Chain Reaction (RT-qPCR) was used to identify and quantify the following genera of microorganisms: Total Bacteria, Total Sulfate-Reducing Bacteria (SRB), *Acetobacter*, *Clostridium*, *Geobacter*, *Saccharomyces*, and *Shewanella*. Gene target primers for each strain were selected by the international scientific literature and they have been tested in their functionality. First, all RT-qPCR were carried out using specific primer; each sample were tested in triplicate. The reactions were conducted using standard super-mix (Bio-Rad SsoFast\_EvaGreen SuperMix) and RT-qPCR Chromo4 (Bio-Rad) with Opticon Monitor 3 Software. After that, RT-qPCR protocols were tested with their specific primer, and a new common thermal protocol for RT-qPCR was drawn and tested. To quantify the Total Bacteria, the reaction was conducted using standard power-mix (Bio-Rad IQ™ Multiplex PowerMix) and RT-qPCR Chromo4 (Bio-Rad) with Opticon Monitor 3 Software. In order to obtain an absolute quantification of bacteria for each MFC samples, a standard curve of specific genomic DNA was performed, in this way, the quantification of bacteria could be expressed in terms of gene copies number as a useful and necessary parameter to compare different samples. After each PCR analysis, to confirm fragment amplification, gel electrophoresis on 2% agarose was performed. For further details about the experimental procedure followed for microorganisms identification and quantification consult the research work conducted by Armato (2014) [43] in collaboration with Università degli Studio di Torino.

### **9.2.4. MFC configuration and operation**

The MFC device consists of two circular chambers, i.e. the anode and the cathode. Both compartments were made in Plexiglas with dimension 12 cm of diameter and 1 cm of depth,

separated by a cation exchange membrane (CEM, CMI 7000, Membranes International Inc.) as shown in Figure 9.1. The total volume of each empty chamber was around 170 mL. Experiments were conducted in three identical MFC with the same operational conditions in which the mainly different is attributed to the performances of the anode material used as follow: (1) the first cell was operated using commercial carbon felt (C-FELT), (2) the second cell was operated using PANI-deposited carbon felt (C-PANI), and (3) the third cell was operated using carbon-coated Berl saddles (C-SADDLES). All experiments were conducted using commercial carbon felt as cathode material. The conductive materials were introduced to each chamber and connected with a graphite rod of 5 mm in diameter to ensure an effective current transport. The three MFCs were operated in a continuous mode at an external resistance of 1000  $\Omega$  during more than three months of operation at room temperature of  $24 \pm 2$  °C.

The MFCs were inoculated with the effluent of an active MFC which operated using sodium acetate as substrate and a mixed microbial population naturally present in sea water previously enriched as is described in Section 9.2.2. The anolyte consisted of inoculum (50 mL), sodium acetate ( $1 \text{ g}\cdot\text{L}^{-1}$ ) and peptone ( $1.25 \text{ g}\cdot\text{L}^{-1}$ ) in anode buffer solution composed of 30% v/v of fresh sea water and 70% v/v of inorganic salts buffer, i.e.  $\text{Na}_2\text{HPO}_4\cdot 2\text{H}_2\text{O}$  ( $8.2 \text{ g}\cdot\text{L}^{-1}$ ) and  $\text{NaH}_2\text{PO}_4\cdot \text{H}_2\text{O}$  ( $5.2 \text{ g}\cdot\text{L}^{-1}$ ). The total volume of the anolyte was 500 mL which was recirculated from the anode vessel through the anode matrix at a flow rate of  $1 \text{ L}\cdot\text{h}^{-1}$  by a peristaltic pump (ISMATEC - ISM404B, Germany). A  $\text{N}_2$  flow was used to ensure anaerobic conditions in the anode chamber.

A sterile and concentrate synthetic anode influent was continuously fed by a syringe pump (KF Technology, Italy) at a flow rate of  $0.42 \text{ mL}\cdot\text{h}^{-1}$  in order to provide to the individual MFCs  $1 \text{ g}\cdot\text{L}^{-1}$  sodium acetate and  $1.25 \text{ g}\cdot\text{L}^{-1}$  peptone (in anode buffer solution) per day respect to the total volume of the anolyte. During the experiments, the total anolyte volume was maintained in 500 mL by using a vessel system to the collection of the exceeding anolyte solution.

The catholyte consisted of potassium ferricyanide ( $500 \text{ mL}$  at  $6.58 \text{ g}\cdot\text{L}^{-1}$ ) aqueous solution in buffer solution of inorganic salts with the same concentration as is described above, which was recirculated from the cathode vessel through the cathode matrix at a flow rate of  $1 \text{ L}\cdot\text{h}^{-1}$  by using a peristaltic pump. The oxidation/reduction of the cathode was controlled by a periodic renewal of the cathode solution when the solution was decolorized.

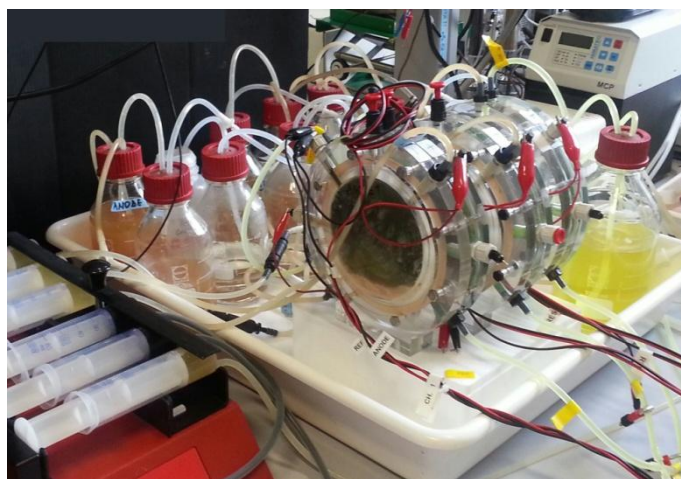


**Figure 9.1.** Microbial fuel cell configuration

### **9.2.5. Physical-chemical characterization of MFC parameters**

Anode solution samples were collected in the outflow of the cell using a 10 mL syringe. Redox potential and pH values of the anodic solution were measured using a pH-meter (model Crison Basic 20, Spain) provided with the suitable measuring electrodes. The pH of the anodic solution was adjusted manually every two days by the addition of diluted HCl 0.01 M to the anolyte solution in order to maintain the pH value around 7.5 – 8.3. The conductivity of the anodic solution was determined using conductimeter (CyberScan PCD 650, Singapore). UV-visible spectra was adopted to measure the optical density (OD) in order to explore the growth of the mixed microbial population present in the anodic solution. To this purpose, absorbance spectra of the anodic solution were recorded at 600 nm using an UV–visible spectrophotometer (PerkinElmer, Lambda 35, USA).

### **9.2.6. Electrochemical measurements and energy production using MFC**

Electrochemical experiments were performed on a multi-channel VSP potentiostat/galvanostat (BioLogic). Measurements were recorded by using EC-Lab software version 10.1x for data acquisition. All tests were carried out using a two electrode configuration, where the working electrode was coupled to the anode and both counter and reference electrodes were connected to the cathode. Linear Sweep Voltammetry (LSV) curves were recorded by imposing a linear potential decrease from the Open Circuit Voltage (OCV) of the cell ( $V_0$  where  $I = 0$ ) to the Short Circuit Voltage of the cell ( $V_{sc} = 0$  where  $I = I_{max}$ ) at a scan rate of  $1 \text{ mV} \cdot \text{s}^{-1}$ . From the  $I$ - $V$  curves, the power density was calculated by the following equation:  $P = (I \cdot V) \cdot A^{-1}$ , where  $I$ ,  $V$  and  $A$  represent current recorded, voltage output and the

total area chamber, respectively. The internal resistance was determined using the Current Interrupt (CI) method. When the MFC produced a stable current output ( $I_o$ ) and potential ( $V_o$ ), the circuit was opened causing an initial steep potential ( $V_R$ ) rise followed by a further slow increase of the potential ( $V_A$ ). The steep increase is referred to as the ohmic losses caused by the internal resistance ( $R_{int}$ ). The determination of the steep potential rise after current interrupting required the fastest possible recording of the potential during the first 50  $\mu$ s consequently  $R_{int}$  can thus be calculated as:  $R_{int} = V_R \cdot I_o$ .

To calculate the energy produce by MFCs, the cell voltage ( $\Delta V$ ) was continuously measured every 60 s using a data logger (Agilent, 34972A, The Netherlands) under an external resistance ( $R$ ) of 1000  $\Omega$ . The current ( $I$ ) was calculated from  $\Delta V$  and  $R$  using Ohms law:  $I = V \cdot R^{-1}$ . The current was average over a period of 24 h after the catholyte had been replenished to assure equal cathode performance for all tests. Thus, energy in joule (J) was calculated as the amount of electrons (amperes) with a driving force (volts) in a closed circuit system per unit of time (seconds) by the following equation:  $J = I \cdot \Delta V \cdot t$ .

### **9.3. Results and discussion**

#### **9.3.1. Physicochemical characterization of MFC parameters**

The optimization of MFCs requires an extensive exploration of the operating parameters that affect MFCs performances. A complete characterization of ours MFCs systems from a physicochemical point of view is presented including: pH, conductivity, redox potential and of microorganisms growth under MFCs operating in continuous mode.

Experiments were conducted using buffer solution in both chambers (anode and cathode) in order to maintain small variations in pH. However, due to the several reactions occurring during bacteria metabolisms, anolyte pH tended to increase especially in the initial stage of MFC operation. To avoid significantly variations on the anolyte pH, in this work HCl solution (0.01 M) was used to maintain the pH in the anode chamber around 7.5 – 8.3 as shown in Figure 9.2a taking as reference the typical pH values at which microorganism are exposed in natural seawater environmental [44]. Finally, it was possible also to observe that anolyte pH variations tended to reduce after around 80 days of operation due to the systems reached a dynamic equilibrium forms between anode, cathode and proton diffusion cross the membrane as previously reported [4].

Figure 9.2b shows the behavior of the conductivity in the three cells. At the beginning of the experiments, the conductivity of the solution was around  $27.4 \text{ mS}\cdot\text{cm}^{-1}$ . A continuous increase of the conductivity of the anode solution was observed which is intimately related with the continuous fed of mineral salts derived from the seawater and phosphate mineral salt present in the synthetic anode influent. After three months of operation, the conductivity of the anode solutions continuously increased reaching values around  $39 \text{ mS}\cdot\text{cm}^{-1}$  for C-FELT and C-PANI cells while that for C-SADDLES cell conductivity of  $36 \text{ mS}\cdot\text{cm}^{-1}$  was reached. In the development of MFCs two opposing goals consequently arise: (1) the salinity of the electrolyte must be as high as possible to decrease the ohmic drop, but also (2) it must not exceed the level that microorganisms can tolerate [45], and unfortunately, most microorganisms do not accept salinities higher than around  $100 \text{ mM}$  (a few  $\text{g}\cdot\text{L}^{-1}$ ). For this reason, most MFCs have so far been developed in solutions with low conductivities [46]. Typically, the higher power densities obtained with MFCs have been obtained around  $7 \text{ W}\cdot\text{m}^{-2}$  [47], and more commonly of the order of  $2$  to  $3 \text{ W}\cdot\text{m}^{-2}$ , for conductivity of the order of  $20 \text{ mS}\cdot\text{cm}^{-1}$  [48]. However, by avoiding acetate limitations and using salt marsh sediment as the inoculum, microbial bioanodes were able to give up to  $85 \text{ A}\cdot\text{m}^{-2}$  in electrolytes with conditions of  $104 \text{ mS}\cdot\text{cm}^{-1}$ , corresponding to 1.5 times the salinity of seawater [45]. From this elementary calculation, to be implemented on a large scale, microbial bioanodes must become able to operate at drastically higher conductivities, which is achievable considering that marine micro-flora is perfectly adapted to functioning in saline environmental ( $5.4 \text{ S}\cdot\text{m}^{-1}$ ). Thus, enough attention has not been paid so far on evaluation performance of MFC exposed to high conductivities and for this reason this work is aimed to investigate the performance of MFC operating using inoculum samples collected from seawater with the view to forming halo-tolerant electroactive biofilms which represent also an essential prerequisite if MFCs are to advance for industrial prospection.

In MFCs systems, the microbial activity is strongly dependent on the redox potential of the anode. For this reason, the oxidation or reduction character of the anodic solution was measured during the duration of the experiments and results are shown in Figure 9.2c. It is possible observe that the redox potential ranging from  $0 \text{ mV}$  in the initial state of the experiments until to reach redox potential below  $-200 \text{ mV}$  which demonstrated the strong oxidant potential of the anode solution. During respiration, microorganisms liberate electrons from an electron rich substrate at a low redox potential and transfer these electrons through a number of electron transport complexes through the cell membrane where a final electron acceptor is reduced [49]. Thus, the continuous reduction of the redox potential of the anodic

solutions in our experiments it is an indication of the proper activity of microorganisms to conduct the oxidation of substrate in the anode chamber.

Finally, the optical density or absorbance of the samples was measured for estimating the concentration of bacterial culture in the anodic solution. The measurement is based on the amount of light scattered by the culture rather than amount of light absorbed: higher is cells number bigger is the turbidity and the quantity of reflex light from bacterial culture.

Results shown in Figure 9.2d indicated a constant increase of the microorganisms population in all three cells. Despite the fact that the measurements were performed in the anodic solution, these results allowed obtaining an indication of the microorganisms growth in the anode chamber and hence an indication of the continuous growth of the biofilm formation on the electrode surface.

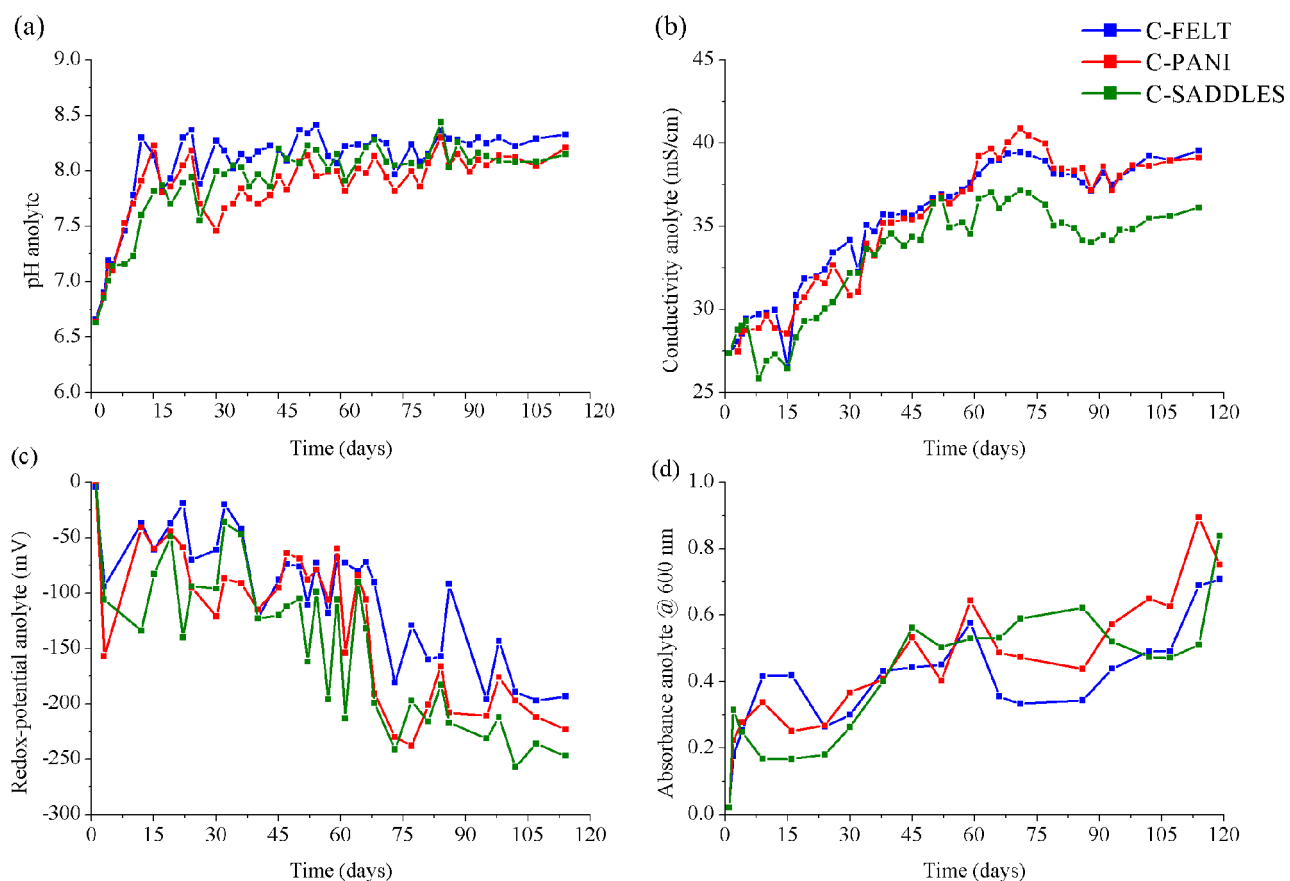


**Figure 9.2.** Physicochemical characterization of the anode solution in all three cells C-FELT (blue line), C-PANI (red line), and C-SADDLES (green line) including: (a) pH, (b) conductivity, (c) redox-potential, and (d) absorbance or optical density

### 9.3.2. Microorganisms identification

The microbial composition was analyzed with RT-qPCR method and Figure 9.3 gives an overview of the microbial communities presented during MFC operation. The analysis have been highlighted that the following microbial populations were present and quantifiable in each MFC: Total Sulfate-Reducing Bacteria (SRB), *Shewanella*, *Geobacter*, *Saccharomyces* and *Clostridium*. The higher number of microbial communities indicated that the MFC environment was suited for the growth and survival of a large variety of microorganisms from seawater and did not evolve to a mono-culture. The detected level in gene copies/mL of the various bacteria groups is displayed in Table 9.1. All groups varied in quantity during the MFC operation, but their presented in general an increase in the following order: *Clostridium* < *Saccharomyces* < *Geobacter* < *Shewanella*, and < *SRB*. From percentage analysis resulted 22% of Total Bacteria corresponding to: 16% for SRB, resulting the most present, 3.5% for *Shewanella*, 2.2% for *Geobacter*, 0.0007% for *Saccharomyces*, 0.0006% for *Clostridium* and 0.00% for *Acetobacter*, that resulted to be absent in all the samples probably owing to maintenance of the anaerobic conditions. Sulfate-Reducing bacteria resulted the most abundant microorganism and similar results were also presented in the research conducted by Logan using MFCs containing sediments [36].

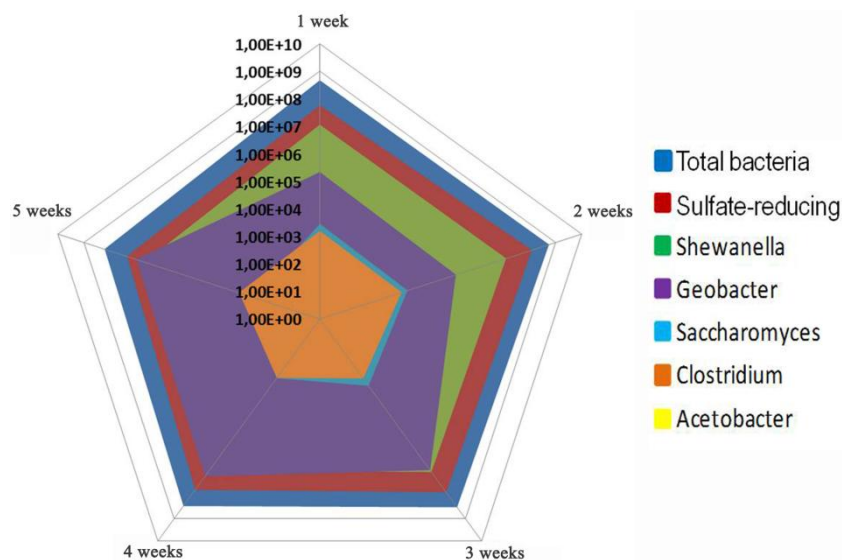


**Figure 9.3.** Radar graph of gene copies/mL average values of samples from all three cells C-FELT, C-PANI, and C-SADDLES for each strain by each probe during the time. Logarithmic scale was used [43]

**Table 9.1.** Descriptive analysis by each probe in MFC samples (n.d. not detected) [43]

Week	Acetobacter	T Bacteria	Clostridium	Geobacter	Saccharomyces	Shewanella	T. SRB
<b>C-FELT (gene copies/mL)</b>							
1 <sup>st</sup>	n.d.	1.03+09	3.28+03	2.77+05	4.21+03	1.84+07	1.24+08
2 <sup>nd</sup>	n.d.	1.15+09	2.18+03	2.46+05	4.28+03	1.86+07	3.06+08
3 <sup>rd</sup>	n.d.	6.90+08	5.28+02	1.85+07	1.79+03	1.32+07	1.51+08
4 <sup>th</sup>	n.d.	3.35+08	5.00+02	2.94+07	5.69+02	8.95+06	2.08+07
5 <sup>th</sup>	n.d.	2.54+08	1.53+02	1.99+07	6.25+02	6.05+06	1.31+07
<b>C-PANI (gene copies/mL)</b>							
1 <sup>st</sup>	n.d.	3.83+08	1.11+03	3.10+05	1.83+03	1.46+07	4.91+07
2 <sup>nd</sup>	n.d.	3.93+08	9.86+02	1.47+05	1.14+03	1.41+07	5.67+07
3 <sup>rd</sup>	n.d.	1.37+08	3.47+02	9.25+05	6.53+02	4.47+06	3.36+07
4 <sup>th</sup>	n.d.	3.03+08	4.17+02	4.71+06	4.91+02	6.21+06	1.11+08
5 <sup>th</sup>	n.d.	1.64+08	5.56+02	6.00+06	1.39+02	3.56+06	4.76+07
<b>C-SADDLES (gene copies/mL)</b>							
1 <sup>st</sup>	n.d.	3.10+07	3.61+02	7.13+04	2.54+03	1.88+06	4.04+06
2 <sup>nd</sup>	n.d.	1.45+08	8.06+02	7.78+04	1.25+03	6.30+06	1.24+07
3 <sup>rd</sup>	n.d.	8.08+07	5.69+02	5.65+04	6.53+02	5.85+06	6.77+06
4 <sup>th</sup>	n.d.	1.60+08	4.44+02	2.99+06	3.47+02	4.95+06	1.81+07
5 <sup>th</sup>	n.d.	7.56+07	2.92+03	4.94+06	2.22+02	5.11+06	8.47+06

Several studies have described the microbial composition in MFCs which revealed that the type and concentration of bacteria on anodes significantly affects current density in MFCs [49, 50]. Various species of *Geobacter* and *Shewanella* are the most studied microbes but a wide variety of bacteria species can transfer electrons to the anode without aid of redox mediators [32, 51]. For example, maximum current densities as low as  $0.6 \text{ mA}\cdot\text{cm}^{-2}$ ,  $3 \text{ mA}\cdot\text{cm}^{-2}$  and  $6.5 \text{ mA}\cdot\text{cm}^{-2}$  have been achieved for MFCs based on *Shewanella putrefaciens* [52], *Rhodospirillum rubrum* [53] and *Geobacter sulfurreducens* [54], respectively. Although most of the real mediator-less MFCs are operated with dissimilatory metal reducing microorganisms, an exception was reported with *Clostridium butyricum* [55, 56]. Comparing these data, several conclusions dealing with the microbial community composition can be derived. It is worth to note that RT-qPCR technique has some disadvantages: it does not

discriminate between alive and died microorganism, so it is not possible to characterize the active population in a MFC; moreover RT-qPCR only notices the target microorganism, so that the analysis have to be conducted based on decisions taken on the basis of the scientific literature, and it is impossible to characterize the whole MFC community. For more accurate determinations could be used a technique of DNA extraction which employs Ethidium Monoazide (EMA) or Propidium Monoazide (PMA), so to discriminate between alive microorganisms and dead ones; we could also combine this protocol of RT-qPCR with Denaturing Gradient Gel Electrophoresis (DGGE) analysis in order to identify species that are not expected by scientific literature. For further details about the results obtained regarding microorganisms identification and quantification consult the research work conducted by Armato (2014) [43] in collaboration with Università degli Studio di Torino.

### 9.3.3. Power generation

The Open Circuit Voltage (OCV) of the individual MFCs was monitored during 2 h periods after the disconnection of the external resistance in order to reach quasi-steady-state conditions before starting polarization techniques. In the initial stage, OCV values were around 0.76 V, 0.75 V and 0.64 V for C-FELT, C-PANI and C-SADDLES, respectively. The slightly different between the initial OCV values using flat-plate and three-dimensional materials could be associated to carbon-based materials offered a more continuous surface in which electron could be transferred with respect to C-SADDLES in which the contact point in the material are randomly organized (see Figure 9.6). After three months of operation, OCV reached values around 0.83 V, 0.77 V and 0.74 V for C-FELT, C-PANI and C-SADDLES, respectively, which indicated that the biological systems were properly adapted to all three anode materials and more specifically by using C-FELT.

Figure 9.4 shows the polarization curves obtained by varying the scan rate of  $1 \text{ mV}\cdot\text{s}^{-1}$  for the whole MFC from initial stage until three months of operation using C-FELT, C-PANI and C-SADDLES as anode material. As previously reported in literature, polarization curves can be divided in three zones [29, 41]: (i) starting from the OCV where  $I = 0$ , there is an initial steep decrease of the voltage corresponding to the activation losses; (ii) the voltage then falls more slowly and the voltage drop is fairly linear with current indicating that ohmic losses are dominant; and finally (iii) the voltage falls rapidly at higher currents. This last effect could be attributed to the polarization effects inducing mass transfer phenomena [57].

Figure 9.4a shows that by using C-FELT during the initial stage of the experiments, the system produced current density around  $390 \text{ mA}\cdot\text{m}^{-2}$  which increased continuously until to

reach  $740 \text{ mA}\cdot\text{m}^{-2}$  after three months of continuous operation. As a consequence, Figure 9.4b shows a significantly increase of the power density obtained from  $44 \text{ mW}\cdot\text{m}^{-2}$  to  $93 \text{ mW}\cdot\text{m}^{-2}$  under the same conditions. In spite of the increase of the current and power densities, it is worth to note that by using C-FELT the system was strongly dominated for ohmic losses, it is for this reason that many studies have been devoted in order to improve the performance of C-FELT through a wide variety of modification as is explained with more details in Chapter VII.

For this purpose: to improve C-FELT performance, the in-situ deposition of polyaniline on C-FELT was conducted following the procedure described in Chapter VII. Results shown in Figure 9.4c evidence that in the initial state of the experiments current density of  $4370 \text{ mA}\cdot\text{m}^{-2}$  were obtained using C-PANI which represented a raise in the current density of 11.2-folds with respect to untreated C-FELT under the same operational conditions. Additionally, Figure 9.4d shows that using C-PANI power density reached values around  $520 \text{ mW}\cdot\text{m}^{-2}$  which indicated an enhancement of 5.6-folds with respect to untreated C-FELT in the initial stage. This results are in good agreement with these reported in literature which evidence that conductive polymer materials such as polyaniline, polypyrrole and composites materials based on them in combination with carbon materials significant improved MFC performance [20-22, 58]. However most of these study have been conducted in batch operational mode and according to our knowledge, a complete characterization of these systems in continuous operation has not been performed yet. For this reason, in this study a long-term evaluation of the performance of C-PANI is reported.

In Figure 9.5a and 9.5b are reported current and power densities obtained during three months of continuous operation by using C-FELT, C-PANI and C-SADDLES. It was possible to observe that C-PANI initially shown the highest current and power densities, however it performance decreased continuously during time until to reach a similar performance with respect to C-FELT and C-SADDLES. This could be related to the effect of some operational conditions inside the MFC on C-PANI such as: (1) evident PANI losses over time which was detected by color changes in the piping system, (2)  $\text{pH} > 7$  could modify PANI into a non conductive form [59], and (3) possible degradation or deactivation of deposited PANI by microorganisms activity which have not been studied in depth up to date. Figure 9.4e and 9.4f show the current and power density produced by using C-SADDLES, respectively. Results evidenced current density around  $304 \text{ mA}\cdot\text{m}^{-2}$  and power density of  $51.3 \text{ mW}\cdot\text{m}^{-2}$  in an initial period. An important raise was obtained after three months of operation reaching current density around  $510 \text{ mA}\cdot\text{m}^{-2}$  and power density of  $102 \text{ mW}\cdot\text{m}^{-2}$ . Moreover, the performance

of C-SADDLES was compared with respect to C-FELT and results reported are in Figure 9.5a and 9.5b. Results indicated that also during a long-term evaluation of the performance both materials produced comparables results reaching power densities around  $93 \text{ mW}\cdot\text{m}^{-2}$  and  $102 \text{ mW}\cdot\text{m}^{-2}$  for C-FELT and C-SADDLES, respectively after three months of continuous operation.

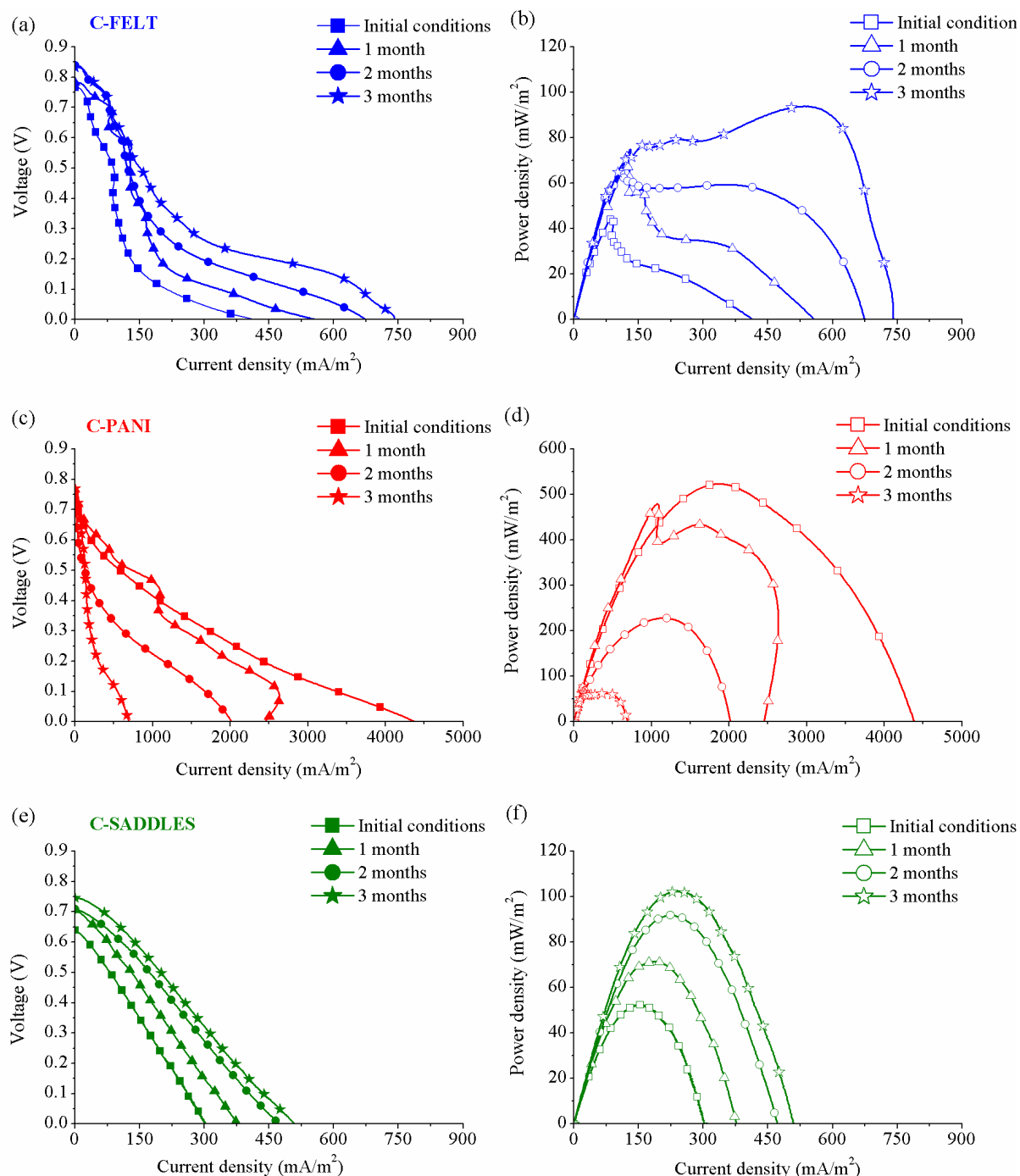


**Figure 9.4.** Polarization curves and power density curves carried out using (a,b) C-FELT, (c,d) C-PANI and (e,f) C-SADDLES, respectively as anode electrode from initial conditions until three months of continuous operation in MFC

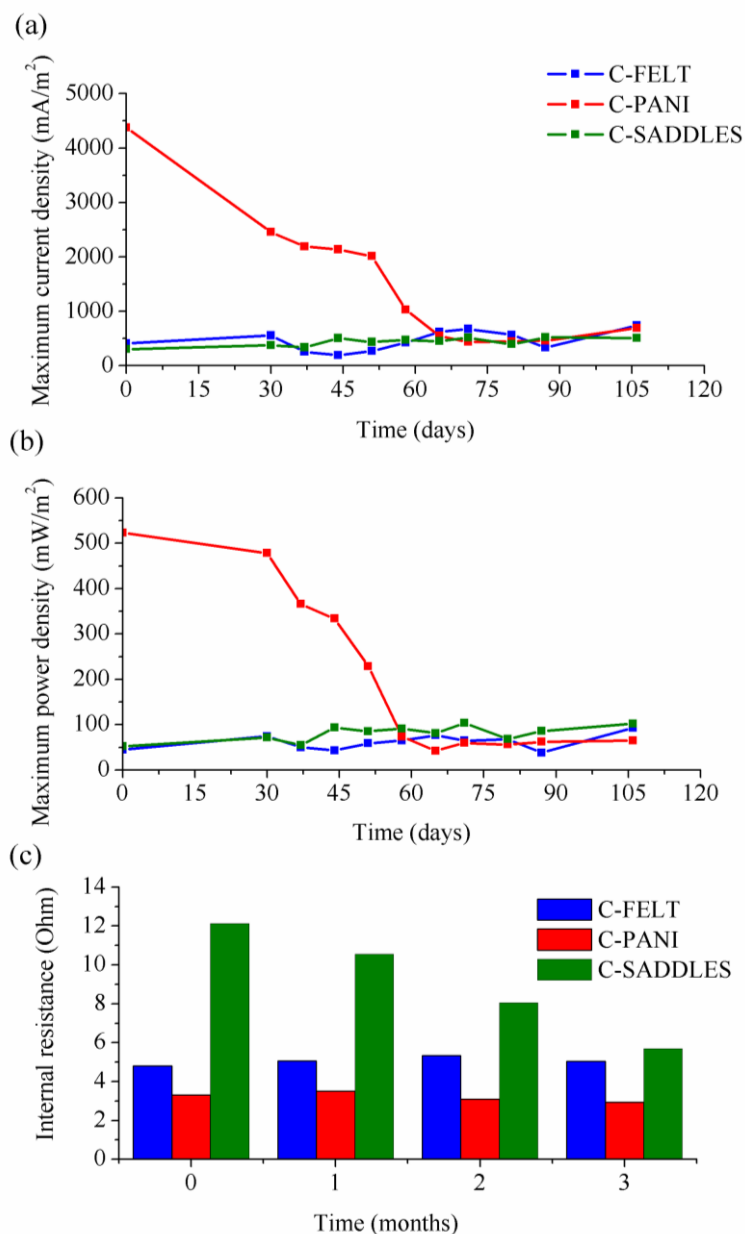


**Figure 9.5.** Long-term evaluation test of MFCs operated using C-FELT, C-PANI and C-SADDLES as anode electrode: (a) maximum current density, (b) maximum power density and (c) internal resistance obtained during three months of continuous operation

For more accurate characterization of our systems, the total internal resistance of the MFCs was determined. The total internal resistance ( $R_{int}$ ) of a MFC depends on many terms: the anodic resistance  $R_a$ , the cathodic resistances  $R_c$ , the ions exchange membrane resistance  $R_m$  and electrolyte resistance  $R_e$  [60]. The internal resistance of the overall MFC (anode, cathode, electrolyte and membrane) was determined as reported in Section 9.2.6, and the comparison of the three different anodic materials studied: C-FELT, C-PANI and C-SADDLES, for the

duration of the tests are reported in Figure 9.5c. The obtained value is not the electrical resistance in the classic sense, but it is able to give us information on how the losses depend on the different electrode material and permit hence to compare them, which is the end of this study. Considering that the internal resistances of MFCs depends on many factors including: electrodes separation distance, operation mode, ionic strength, and substrate properties, in this study the internal resistance values were intended with a predominant contribution of the anode material effects, due to all the tests were conducted under the same operational conditions, and only anode material was changed. As shown in Figure 9.5c, during the duration of the experiments, the internal resistance obtained using C-FELT and C-PANI not presented a significant variation showing values around 5  $\Omega$  and 3  $\Omega$ , respectively. This fact evidence that the operating conditions inside both cells were maintained. Thus, Figure 9.5c evidence a strong reduction of the internal resistance of the cell which operated using C-SADDLES. Results showed internal resistance around 12  $\Omega$  during the initial stage of the test, which decreased continuously until to reach internal resistance around 5.6  $\Omega$ . The important reduction of the internal resistance of the cell operated using C-SADDLES could be explained by the growth of the microorganisms which generate a biofilm around the Berl saddles improving their colonization and hence increasing the electron transport from the microorganisms to the electrode as shown in Figure 9.6, while C-FELT did not offer a proper microorganisms support for microorganisms growth and for this reason biomass tended to deposit on the bottom of the cells.

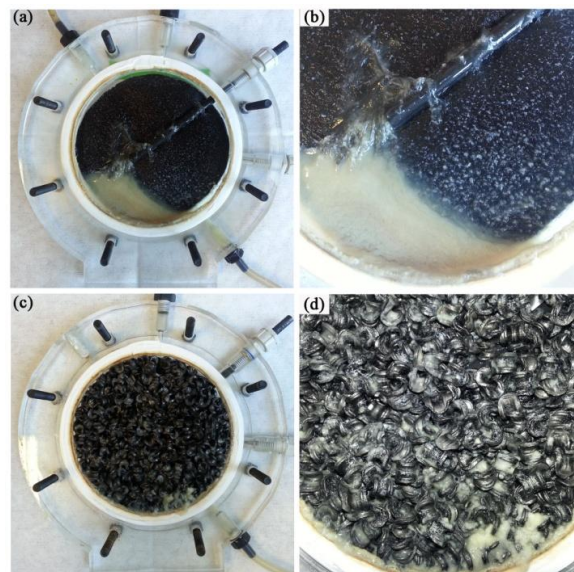


**Figure 9.6.** Biomass growth during continuous operation of MFCs using (a,b) C-FELT and (c,d) C-SADDLES as anode electrode

#### 9.3.4. Energy production using MFC

A wide range of bioelectrochemical process has been developed from electrical power generation to the production of biofuels and biochemicals. The most studied electrocatalysis-based process so far is the production of electricity in microbial fuel cells. Until now, MFCs produce power densities up to  $17 - 19 \text{ W}\cdot\text{m}^{-2}$  with respect to electrode surface area or volumetric power densities up to  $2.87 \text{ KW}\cdot\text{m}^{-3}$ , under small scale which involved many times artificial conditions [31-33]. This work is aimed to the calculation of the continuous electricity produced by MFCs systems operated under continuous mode. MFCs were continuously fed with synthetic influent ( $1\text{g}\cdot\text{L}^{-1}$  of acetate) under an external load of  $1000 \Omega$  during more than three months of operation. During this period, the systems were monitored and the calculation of the electricity produced was determined as is explained above in Section 9.2.6. Figure 9.7 shows the accumulated energy produced in Joules (J) during the first 90 days of operation. MFC operated with C-FELT produced around 1664 J of total electrical energy while that the MFC operated using C-SADDLES produced 1674 J. During the same period, both systems showed similar behavior with respect to the current and power densities generation (see Figure 9.5) which permit to validate that by using C-SADDLES comparable results can be obtained with respect to C-FELT which is one of the most common anode electrode used for MFC applications. Likewise, the energy produced by the MFC system operated using C-PANI was evaluated. In this case, due to the high performance of the material during the initial stage of the experiments, C-PANI showed an important improvement on the electricity produced reaching values around 1803 J after three months of operation, which represented an increase of 1.1-folds with respect to C-FELT. However, based on our results it is worth to note that the performance of C-PANI decreased during the period of testing reaching similar values to that obtained using C-FELT.

There have been many attempts to demonstrate that MFCs can produce electricity in marine environments. Reimers et al. (2001) simulated the marine environment in a laboratory and showed that the power produced by microbial fuel cells could be sufficient for oceanographic instruments deployed for long-term monitoring [61]. Tender et al. (2002) observed a potential gradient between an anode buried in marine sediment and a cathode in overlying seawater. They deployed two MFCs in coastal marine environments, in Tuckerton, New Jersey and Yaquina Bay Estuary, Oregon, and showed the possibility of power generation from marine sediment [62]. Reimers et al. (2006) showed that a cold seep has the potential to provide more power than neighboring ocean sediments in Monterey Canyon, California [63]. These studies demonstrate that microbial fuel cells deployed in natural waters can produce enough

energy to operate sensors requiring low power, however, a few work have been devoted to the direct application of the electricity produced by MFCs. In this direction, Donovan et al. (2008) demonstrated that microbial fuel cells with a microbial anode and cathode can be used as an effective renewable power source for remote monitoring using custom-designed electronics [34]. Crepaldi el al. (2013) demonstrated that the electrical energy produced by MFC systems have been effectively used to powered a wireless monitoring system for the transmission of the voltage level across a series of MFC plus an associated pressure level acquired using a piezoresistive nanostructured material and an associated read-out circuit [64]. In Spite of all the efforts made so far, it is worth noting that up to date microbial fuel cells produce a maximum cell potential around 0.8 V to 1.1 V which continues to be one of the major bottlenecks for the development and industrial application of MFC systems.

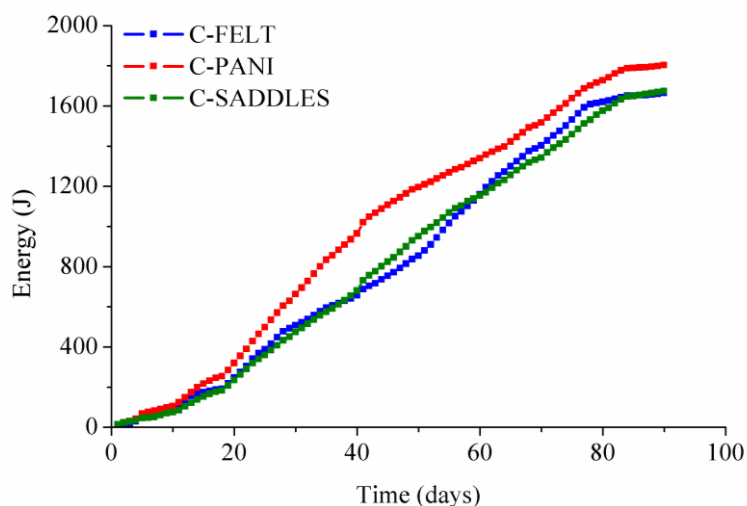


**Figure 9.7.** Accumulated energy produced by MFC systems operated under continuous operation mode using C-FELT, C-PANI and C-SADDLES as anode electrode

### 9.3.5. Variation of the applied external resistance

During subsequent periods of 2 h at a loading rate of  $1 \text{ g}\cdot\text{L}^{-1}$  of acetate, the external resistance of all reactors was lowered from  $8200 \ \Omega$  to  $10 \ \Omega$  as shown in Figure 9.8a. In the different steps, when the resistance was decreased an initial sudden rise of the current was produced and from which the systems got stabilized after 1 h. In order to maintain constant conditions in the cathode chamber, the cathodic solutions was replaced every day over the duration of the experiments before performing the change in the resistance. When all the systems operated with external resistance between  $8220 \ \Omega$  and  $2700 \ \Omega$  not remarkable different in the

current densities were obtained. Instead, significant variations on the current densities were obtained for all three cells with external resistance from 1800  $\Omega$  to 10  $\Omega$ , which resulted in a significant increase of the continuous current generation.

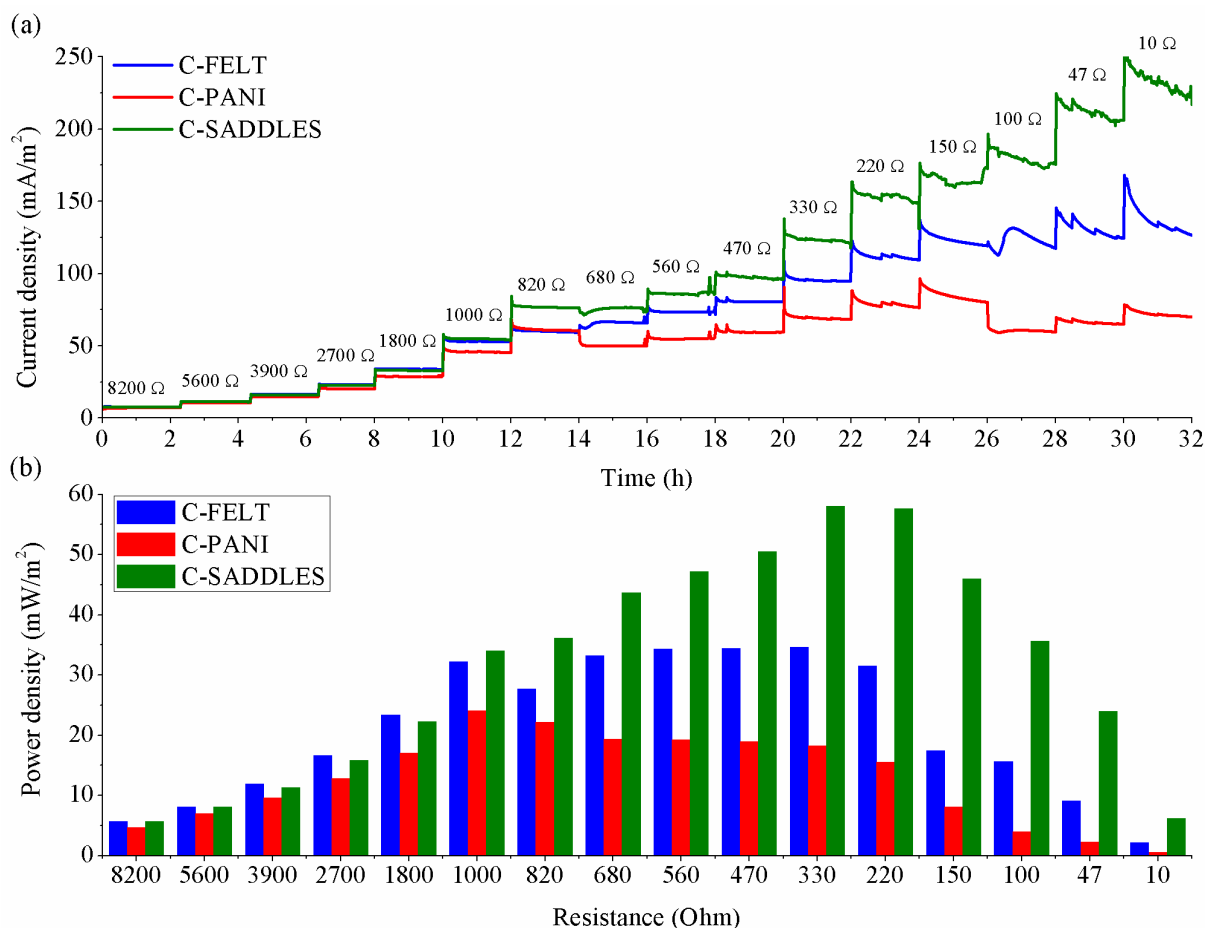


**Figure 9.8.** Overview of the continuous (a) current density and (b) power density during subsequent changes of the external resistance in MFC systems operated using C-FELT, C-PANI and C-SADDLES as anode electrode

Over this stage, with external resistance between 1800  $\Omega$  to 10  $\Omega$ , the maximum current density was produced by using C-SADDLES, conferring to the material a wide range of possibilities to be used under different conditions in long-term MFC tests. Similar to C-SADDLES, by using C-FELT an important increase of the current density was obtained, however in this case the system required higher periods of time (> 1 h) in order to reach new stabilized operational conditions. Finally, current density obtained using C-PANI showed to be less affected as a function of the external load, and as a result the increase of the current density was lower than that obtained for C-FELT and C-SADDLES. As a

consequence, the external resistance control de ratio between the current generation and the cell voltage [41]. Power generation was calculated with respect to the external load applied as shown in Figure 9.8b. It is possible to observe that maximum power density of around  $58 \text{ mW}\cdot\text{m}^{-2}$  was obtained using C-SADDLES under an external load of  $330 \Omega$ . In the test conducted using C-FELT and C-PANI the higher power densities were obtained at  $330 \Omega$  ( $34.60 \text{ mW}\cdot\text{m}^{-2}$ ) and  $1000 \Omega$  ( $24.03 \text{ mW}\cdot\text{m}^{-2}$ ), respectively. It is worth to note that by using C-FELT and C-PANI not remarkable difference in the power density were obtained between  $680 \Omega$  and  $330 \Omega$ . Similar results have been also obtained for other authors which concluded that: at lower external resistance higher current densities can be obtained [24, 41, 65], however a decrease of the external resistance needs to be accompanied by an increasing loading rate in order to increase the continuous current generation for prolonged tests [24].

#### 9.4. Conclusions

In this Chapter are presented the remarkable results obtained for MFCs systems operated with the most promising materials developed during this work and explained in the previous Chapters, including: C-FELT and C-PANI as flat-plate electrodes and C-SADDLES as new three-dimensional electrode. The performances of the different materials were evaluated in term of current density, power density and electrical energy production in a long-term test conducted in continuous mode for more than three months of operation. From RT-qPCR analysis was possible to identify and quantifiable the active microbial population involved in the electricity generation process which included: Total Sulfate-Reducing Bacteria (SRB), *Shewanella*, *Geobacter*, *Saccharomyces* and *Clostridium*. From polarization curves, the maximum power generation was obtained using C-SADDLES ( $102 \text{ mW}\cdot\text{m}^{-2}$ ) with respect to C-FELT ( $93 \text{ mW}\cdot\text{m}^{-2}$ ) and C-PANI ( $65 \text{ mW}\cdot\text{m}^{-2}$ ) after three months of operation. The important reduction of the internal resistance of the MFC operated using C-SADDLES with respect to C-FELT and C-PANI could be associated to a major colonization of the electrode surface, which results in an increase on the electron transport from the microorganisms to the electrode. The highest amount of electrical energy was produced by C-PANI (1803 J) with respect to C-FELT (1664 J) and C-SADDLES (1674 J). However, it is worth to note that PANI activity was reduced by the operating conditions inside the anode chamber such as: (1) PANI losses, (2)  $\text{pH} > 7$  possibly modified PANI into a non conductive form, and (3) possible degradation or deactivation of deposited PANI by microorganisms activity. The external resistance should be considered as an important factor in order to improve the performance of MFC systems. To this purpose, low external resistance accompanied by high

loading rate have to be considered in order to increase the continuous current generation and hence energy production for prolonged tests.

## 9.5. References

- [1] R.M. Allen, H.P. Bennetto, *Applied Biochemistry and Biotechnology*, 39 (1993) 27-40.
- [2] K. Rabaey, N. Boon, S.D. Siciliano, M. Verhaege, W. Verstraete, *Applied and Environmental Microbiology*, 70 (2004) 5373-5382.
- [3] K. Rabaey, N. Boon, M. Höfte, W. Verstraete, *Environmental science & technology*, 39 (2005) 3401-3408.
- [4] Z. Du, H. Li, T. Gu, *Biotechnology Advances*, 25 (2007) 464-482.
- [5] K. Rabaey, W. Verstraete, *TRENDS in Biotechnology*, 23 (2005) 291-298.
- [6] M. Madigan, J. Martinko, J. Parker, *Brock biology of microorganisms*, 9th ed. Prentice-Hall, Upper Saddle River, NJ, (2000) 113.
- [7] C. Santoro, S. Babanova, P. Atanassov, B. Li, I. Ieropoulos, P. Cristiani, *Journal of The Electrochemical Society*, 160 (2013) H720-H726.
- [8] H. Moon, I.S. Chang, J.K. Jang, B.H. Kim, *Biochemical engineering journal*, 27 (2005) 59-65.
- [9] P. Aelterman, K. Rabaey, H.T. Pham, N. Boon, W. Verstraete, *Environmental science & technology*, 40 (2006) 3388-3394.
- [10] K. Rabaey, P. Clauwaert, P. Aelterman, W. Verstraete, *Environmental science & technology*, 39 (2005) 8077-8082.
- [11] J. Wei, P. Liang, X. Huang, *Bioresource Technology*, 102 (2011) 9335-9344.
- [12] J.K. JANG, I.S. CHANG, B.H. KIM, *Journal of Microbiology and Biotechnology*, 14 (2004) 324-329.
- [13] B. Logan, S. Cheng, V. Watson, G. Estadt, *Environmental science & technology*, 41 (2007) 3341-3346.
- [14] B.E. Logan, J.M. Regan, *TRENDS in Microbiology*, 14 (2006) 512-518.
- [15] M. Zhou, M. Chi, J. Luo, H. He, T. Jin, *Journal of Power Sources*, 196 (2011) 4427-4435.
- [16] D. Park, J. Zeikus, *Applied Microbiology and Biotechnology*, 59 (2002) 58-61.
- [17] A. Morozan, I. Stamatina, L. Stamatina, A. Dumitru, K. Scott, *Journal of Optoelectronics and Advanced Materials*, 9 (2007) 221.
- [18] K. Scott, G. Rimbu, K. Katuri, K. Prasad, I. Head, *Process Safety and Environmental Protection*, 85 (2007) 481-488.

- [19] S. Cheng, B.E. Logan, *Electrochemistry Communications*, 9 (2007) 492-496.
- [20] C. Li, L. Zhang, L. Ding, H. Ren, H. Cui, *Biosensors and Bioelectronics*, 26 (2011) 4169-4176.
- [21] Y. Zou, C. Xiang, L. Yang, L.-X. Sun, F. Xu, Z. Cao, *International Journal of Hydrogen Energy*, 33 (2008) 4856-4862.
- [22] M. Ghasemi, W.R.W. Daud, N. Mokhtarian, A. Mayahi, M. Ismail, F. Anisi, M. Sedighi, J. Alam, *International Journal of Hydrogen Energy*, 38 (2013) 9525-9532.
- [23] U. Schröder, J. Nießen, F. Scholz, *Angewandte Chemie International Edition*, 42 (2003) 2880-2883.
- [24] P. Aelterman, M. Versichele, M. Marzorati, N. Boon, W. Verstraete, *Bioresource Technology*, 99 (2008) 8895-8902.
- [25] D. Sell, P. Krämer, G. Kreysa, *Applied Microbiology and Biotechnology*, 31 (1989) 211-213.
- [26] Z. He, S.D. Minter, L.T. Angenent, *Environmental science & technology*, 39 (2005) 5262-5267.
- [27] Z. He, N. Wagner, S.D. Minter, L.T. Angenent, *Environmental science & technology*, 40 (2006) 5212-5217.
- [28] S. Freguia, K. Rabaey, Z. Yuan, J. Keller, *Electrochimica Acta*, 53 (2007) 598-603.
- [29] D. Hidalgo, T. Tommasi, V. Cauda, S. Porro, A. Chiodoni, K. Bejtka, B. Ruggeri, *Energy*, 71 (2014) 615-623.
- [30] G. Hoogers, *Fuel Cell Technology Handbook*, (2002).
- [31] Y. Fan, S.-K. Han, H. Liu, *Energy & Environmental Science*, 5 (2012) 8273-8280.
- [32] B.E. Logan, *Nature Reviews Microbiology*, 7 (2009) 375-381.
- [33] Y. Fan, E. Sharbrough, H. Liu, *Environmental science & technology*, 42 (2008) 8101-8107.
- [34] C. Donovan, A. Dewan, D. Heo, H. Beyenal, *Environmental science & technology*, 42 (2008) 8591-8596.
- [35] X. Cao, X. Huang, P. Liang, K. Xiao, Y. Zhou, X. Zhang, B.E. Logan, *Environmental science & technology*, 43 (2009) 7148-7152.
- [36] B.E. Logan, D. Call, S. Cheng, H.V. Hamelers, T.H. Sleutels, A.W. Jeremiasse, R.A. Rozendal, *Environmental science & technology*, 42 (2008) 8630-8640.
- [37] R.A. Rozendal, E. Leone, J. Keller, K. Rabaey, *Electrochemistry Communications*, 11 (2009) 1752-1755.

- [38] K. Rabaey, S. Butzer, S. Brown, J.r. Keller, R.A. Rozendal, *Environmental science & technology*, 44 (2010) 4315-4321.
- [39] M. Sharma, S. Bajracharya, S. Gildemyn, S.A. Patil, Y. Alvarez-Gallego, D. Pant, K. Rabaey, X. Dominguez-Benetton, *Electrochimica Acta*, 140 (2014) 191-208.
- [40] R. Rousseau, X. Dominguez-Benetton, M.-L. Délia, A. Bergel, *Electrochemistry Communications*, 33 (2013) 1-4.
- [41] B.E. Logan, B. Hamelers, R. Rozendal, U. Schröder, J. Keller, S. Freguia, P. Aelterman, W. Verstraete, K. Rabaey, *Environmental science & technology*, 40 (2006) 5181-5192.
- [42] X.D. Benetton, S. Navarro-Avila, C. Carrera-Figueiras, (2009).
- [43] C. Armato, Ottimizzazione della metodica RT-qPCR applicata allo studio delle Microbial Fuel Cells - Tesi di Laurea in Biologia dell'Ambiente - Università degli Studi di Torino (2014)
- [44] R. Chester, *Marine geochemistry*, John Wiley & Sons, 2009.
- [45] R. Rousseau, X. Dominguez-Benetton, M.-L. Délia, A. Bergel, *Electrochemistry Communications*, 33 (2013) 1-4.
- [46] Y. Feng, X. Wang, B.E. Logan, H. Lee, *Applied Microbiology and Biotechnology*, 78 (2008) 873-880.
- [47] D. Pocaznoi, B. Erable, L. Etcheverry, M.-L. Delia, A. Bergel, *Physical Chemistry Chemical Physics*, 14 (2012) 13332-13343.
- [48] B.E. Logan, K. Rabaey, *Science*, 337 (2012) 686-690.
- [49] P. Aelterman, *Microbial fuel cells for the treatment of waste streams with energy recovery*, Ghent University, 2009.
- [50] M. Zhou, H. Wang, D.J. Hassett, T. Gu, *Journal of Chemical Technology & Biotechnology*, 88 (2013) 508-518.
- [51] P.D. Kiely, J.M. Regan, B.E. Logan, *Current Opinion in Biotechnology*, 22 (2011) 378-385.
- [52] H.J. Kim, H.S. Park, M.S. Hyun, I.S. Chang, M. Kim, B.H. Kim, *Enzyme and microbial technology*, 30 (2002) 145-152.
- [53] S.K. Chaudhuri, D.R. Lovley, *Nature biotechnology*, 21 (2003) 1229-1232.
- [54] D.R. Bond, D.R. Lovley, *Applied and Environmental Microbiology*, 69 (2003) 1548-1555.
- [55] S.-E. Oh, B.E. Logan, *Applied Microbiology and Biotechnology*, 70 (2006) 162-169.
- [56] H.S. Park, B.H. Kim, H.S. Kim, H.J. Kim, G.T. Kim, M. Kim, I.S. Chang, Y.K. Park, H.I. Chang, *Anaerobe*, 7 (2001) 297-306.

- [57] I.S. Kim, K.-J. Chae, M.-J. Choi, W. Verstraete, *Environmental Engineering Research*, 13 (2008) 51-65.
- [58] K. Scott, G.A. Rimbu, K.P. Katuri, K.K. Prasad, I.M. Head, *Process Safety and Environmental Protection*, 85 (2007) 481-488.
- [59] G.G. Wallace, P.R. Teasdale, G.M. Spinks, L.A. Kane-Maguire, *Conductive electroactive polymers: intelligent polymer systems*, 3 th ed., CRC press, 2008.
- [60] B.E. Logan, B. Hamelers, R. Rozendal, U. Schröder, J. Keller, S. Freguia, P. Aelterman, W. Verstraete, K. Rabaey, *Environmental Science & Technology*, 40 (2006) 5181-5192.
- [61] C.E. Reimers, L.M. Tender, S. Fertig, W. Wang, *Environmental science & technology*, 35 (2001) 192-195.
- [62] L.M. Tender, C.E. Reimers, H.A. Stecher, D.E. Holmes, D.R. Bond, D.A. Lowy, K. Pilobello, S.J. Fertig, D.R. Lovley, *Nature biotechnology*, 20 (2002) 821-825.
- [63] C. Reimers, P. Girguis, H. Stecher, L. Tender, N. Ryckelynck, P. Whaling, *Geobiology*, 4 (2006) 123-136.
- [64] M. Crepaldi, A. Chiolerio, T. Tommasi, D. Hidalgo, G. Canavese, S. Stassi, D. Demarchi, F. Pirri, in: *SPIE Microtechnologies*, International Society for Optics and Photonics, 2013, pp. 876311-876311-876319.
- [65] G. Jadhav, M. Ghangrekar, *Bioresource Technology*, 100 (2009) 717-723.

## Chapter 10

### **Application of the energy produced by MFCs: A low complexity wireless microbial fuel cell monitor using piezoresistive sensors and impulse-radio ultra-wide-band**

#### **10.1. Introduction**

Wireless microelectronics systems especially during the last decade have gained superior attention for a wide range of applications from Wireless Body Area Networks (WBAN), Wireless Sensor Networks (WSN), ubiquitous networking applied to Internet of Things (IoT). Thanks to the Microelectronics Process CMOS and Radio Frequency CMOS, a design can be aggressively scaled to meet ultra-small form factors and enable wireless connectivity to a huge range of objects. Among the available wireless technologies, Impulse Radio Ultra-Wide-Band (IR-UWB) attracts the research community thanks to its ultra-low power features combined to ease of implementation and low-complexity. In the US, (see the FCC Rules Part 15, subpart F) a signal which can be classified as Ultra-Wide-Band requires a fractional bandwidth of at least 0.2 or bandwidth of at least 500MHz. Thanks to this impulsive nature, an UWB signal can be easily generated using a small area CMOS integrated circuit, even all digital, enabling deep miniaturized wireless capabilities within a very small silicon die.

Traditionally, wireless sensors are powered by dry cell batteries [1]. The use of dry cell batteries is popular but problematic because of their limited lifetime. In remote locations replacing the batteries is costly, time consuming, and impractical. A possible solution to this problem is to produce power where it is needed, and microbial fuel cells (MFCs) can be used to produce energy to power them [2, 3]. MFCs are devices that generate electrical energy from organic wastes using exoelectrogenic bacteria on the anode [4, 5]. The application of MFCs for wastewater treatment or bioenergy production requires the use of inexpensive electrode materials [6-8] that are electrochemically and biologically stable, and that have a high specific surface area, electrical conductivity and appropriate mechanical strength [5, 6, 9]. Several researchers have been attempted to demonstrate the possibility of using a sediment microbial fuel cell as the power source for a remote sensor. These studies demonstrated that MFCs deployed in natural waters can produce enough energy to operate sensors requiring low power [10-12].

On the other hand, in the last decades the Micro-Electro-Mechanical Systems (MEMS) technology has matured and cornered the market of several application fields. In particular pressure sensors are the most investigated, developed and worldwide produced transducers [13]. The applications affected by the wide spread piezoresistive pressure sensors are varied and heterogeneous i.e. automotive, pipes and reservoirs monitoring, industrial and human robotics, smart phone, etc. Among different materials used in piezoresistive devices, the composites based on polymers and metal filler have several advantages, such as flexibility, mechanical robustness, insensitivity to overload, and can be prepared through cost effective processes [14]. As already reported for other metal-polymer hybrid systems with nickel [15, 16], silver [17] or gold particle fillers [18, 19], a giant piezo-resistive behavior can be obtained. Anyway although MFC generated energy, at current state, is not enough for high demands, it could be very useful to power sensors in remote terrestrial area where the human operation will be difficult or actually impossible to monitor the status of this biocell during use.

In this Chapter a fabricated flexible and conformable piezoresistive pressure sensor based on an innovative functional material has been employed. The conduction occurs by tunneling mechanisms in the copper-elastomer composite. This chapter reports on merging heterogeneous contributions and combining the advantages from these three separate fields in a system which enables the ultra-low-power monitoring of a microbial fuel cell voltage status and enables pressure monitoring features of the internal conditions of a cell. A UWB transmitter plus an ad-hoc read-out circuit connected to the piezoresistive material, enable two interesting features which can be potentially applied to an MFC, i.e., the wireless monitoring of the voltage level across an MFC plus the potential capability of reading out the pressure level of the chamber using a piezo-resistive sensor. Both signals are combined together in a pulse density modulation (PDM) format which is straightly related to both the voltage level of the MFC and the monitored pressure level. Both a UWB transmitter plus an ad-hoc read-out circuit connected to the piezoresistive material have been developed by different research group at Istituto Italiano di Tecnologia which were used in this work to evidence the application potential of the energy produced by the MFC.

The results of this research are part of the publication entitled: “A Low Complexity Wireless Microbial Fuel Cell Monitor using Piezoresistive Sensors and Impulse-Radio Ultra-Wide-Band”. M. Crepaldi, A. Chiolerio, T. Tommasi, D. Hidalgo, G. Canavese, S. Stassi, D. Demarchi, F. Pirri. (2013) SPIE Microtechnologies, International Society for Optics and Photonics, 876311.

## 10.2. Experimental

### 10.2.1. System Concept

An MFC can potentially be installed in not easily reachable environments where bacteria flowing in the cell can be self-sustained by the environment where it is installed. Even if not suitable for high demands, the MFC can give a large amount of power to dedicated ULP microelectronics systems to run specific tasks. The pressure inside the cell is an important information which needs to be considered as well. The membrane pressure can be directly related to the MFC metabolic activity of bacteria. Given an Ultra-Low-Power (ULP) read-out circuit combined to a nano-structured material plus an IR-UWB transmitter, a simple modulation format can transport the charge information over-the-air for a wireless monitoring system. Figure 10.1 shows a system concept block scheme.

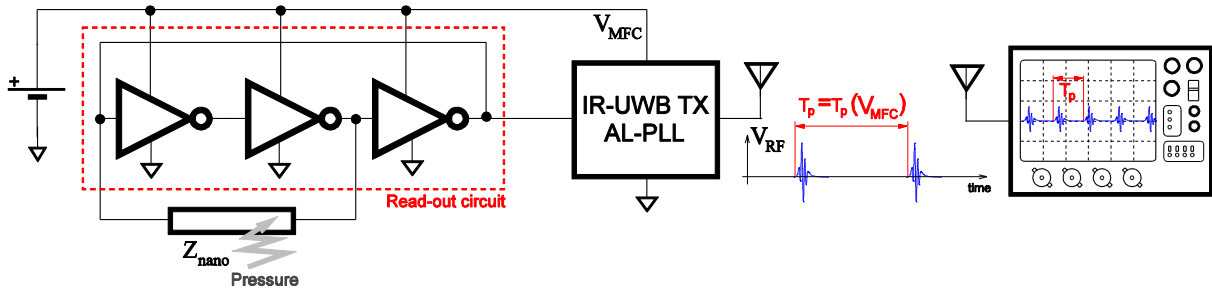


**Figure 10.1.** A microbial fuel cell powers an IR-UWB transmitter and an all-digital read-out circuit which generates digital triggers for the RF signal generation. Two MFC cells connected in series supply the microelectronic circuit

The battery depicted in the schematic identifies the MFC, voltage  $V_{MFC}$  which supplies both a read-out circuit and an asynchronous IR-UWB transmitter. The read-out circuit is a ring oscillator implemented with discrete components (74HC00 logic gates) undersupplied to 1V operation. The read-out circuit is connected to a piezoelectric nano-material sensor on which pressure can be applied. The read-out circuit oscillates at a given frequency  $f_p$ , period  $T_p$ , which depends on its supply voltage level. Frequency also varies as a function of the resistance across the generic impedance  $Z_{nano}$  because propagation delay of the inverter chain varies. Period is then a function of the MFC voltage level. The read-out circuit generates a square wave which triggers an IR-UWB transmitter. Every time a positive edge occurs at the input of the IR-UWB TX a pulse is radiated over-the-air and received by an oscilloscope with a connected antenna, emulating a receiver system. At the RX, the quantity  $T_p$  is measured.  $T_p$  is a function of both the supply voltage  $V_{MFC}$  and the applied pressure on the sensor. This

system enables wireless “charge” monitoring across the MFC without requiring expensive and power hungry electronics.

### **10.2.2. Microbial fuel cells**

Many bioenergy conversions exist including incineration, gasification, fermentation (e.g., bioethanol), anaerobic digestion for bioH<sub>2</sub> and biogas production [6, 20], etc., but MFCs have a number of attractive features such as direct electricity generation, high conversion efficiency and a reduced amount of sludge production. According to dimensions, MFCs may be divided into three groups, macro, meso and microscale MFCs. Microbes in the anodic chamber of an MFC oxidize added organic substrates and generate electrons and protons in the process (Figure 10.2). Carbon dioxide is produced as an oxidation product. Unlike in a direct combustion process, the electrons are absorbed by the anode and are transported to the cathode through an external circuit. After crossing a cation exchange membrane (CEM) or a salt bridge, the protons enter in the cathodic chamber where they combine with oxygen to form water. Microbes in the anodic chamber extract electrons and protons in the dissimilative process of oxidizing organic substrates [4]. Electric current generation is made possible by keeping microbes separated from oxygen or any other end terminal acceptor other than the anode and this requires an anaerobic anodic chamber. MFC is one approach to utilize biomass after appropriate pretreatments [21] and directly generates electricity from biomass. The materials of electrodes play an important role in MFC performance (e.g. power output), energy sustainable and costs. MFC technologies can potentially address both energy and water quality challenges because they can enable clean energy production while also purifying water, step generally very energy-expensive with traditional aerobic treatment. MFC principles have been demonstrated for lab scale devices, but scale-up to real full-scale applications is currently limited by power yield and long-term perform [5, 22, 23].

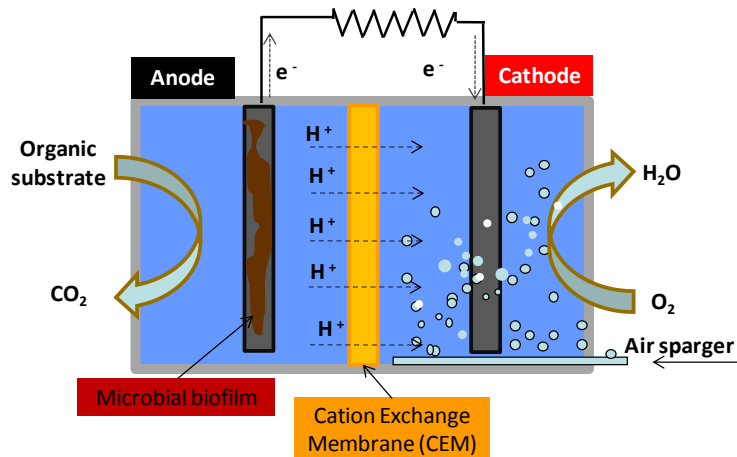


**Figure 10.2.** Schematic diagram of a typical two-chamber microbial fuel cell

### 10.2.3. Piezoresistive pressure sensor

A large area sensor (10mm x10mm) 1mm thick, based on piezoresistive composite material has been equipped with flexible metalized polyimide electrodes, details about the fabrication process flow can be find elsewhere [24]. In the prepared composite samples, copper particles are intimately coated by the silicone matrix that avoids any physical contact between them (see Figure 10.3). As a consequence, when no mechanical deformation is applied, piezoresistive specimens exhibit an insulating electric behavior even above the expected percolation threshold [25]. While during the application of a compressive strain to the functional material, the gap represented by the insulating layer between the metal particles is reduced, thus inducing an exponential rise of the probability for the electrons to tunnel between neighbor particles. This results in an increase of several orders of magnitude of the sample electrical conduction. This tunneling conduction mechanism is promoted by the characteristic shape of the particles, presenting multi-branched microstructures covered by very sharp nanometric spikes on the surface (see Figure 10.4). Moreover this micro corrugated morphology helps the polymeric matrix to intimately coat the filler, avoiding physical contact between close particles.

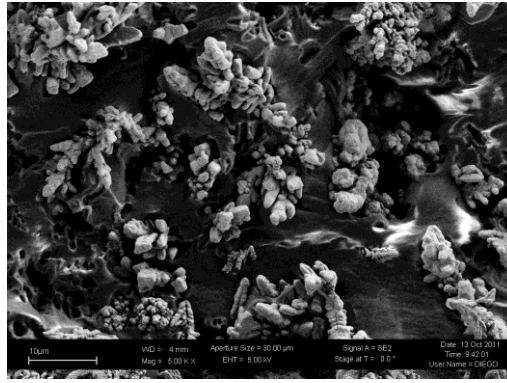


**Figure 10.3.** FESEM image of a PDMS-Cu composite showing the complete coverage of Cu particle by the polymeric matrix

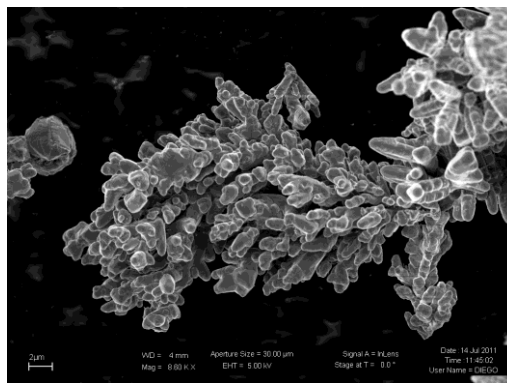


**Figure 10.4.** FESEM image of a conductive Cu filler powder showing multi branched microstructures covered by nano-tips

#### 10.2.4. IR-UWB transmitter

The integrated IR-UWB transmitter used in this work is all digital and it is fabricated in a 130nm RFCMOS technology process [26]. Basically it embeds a single-phase charge pump Phased Locked Loop (PLL) which generates an UWB pulse based on a single duty cycling reference input. The Asynchronous Logic Duty cycled PLL generates a UWB pulse in the low FCC band (0 - 960MHz) with a fractional bandwidth  $F$  larger than the minimum 0.2 required to radiate a UWB pulse. The AL-PLL UWB TX conceptual scheme is given in Figure 10.5. Based on a single duty cycling reference input, a Ring Oscillator (RO) synthesizes a Radio Frequency signal which is  $2N$  times faster than  $T_{ref}$ . Based on  $T_{ref}$  width, the circuit self adapts to synthesize a number of oscillations  $2N$  within a duty cycling duration.

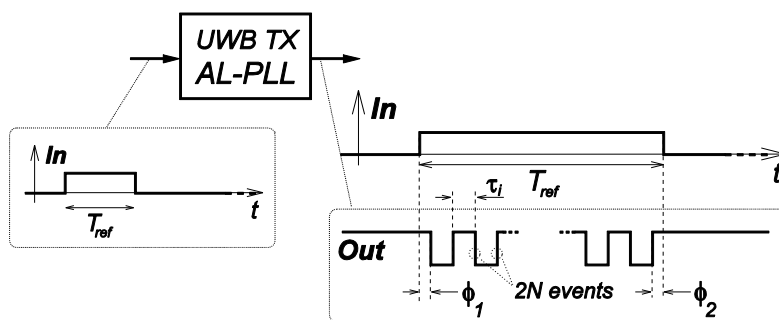


**Figure 10.5.** All-digital pulse synthesis based on an Asynchronous Logic-Phase Locked Loop (AL-PLL) [27]

### 10.3. Results and discussion

#### 10.3.2. MFC operation

Each MFC device comprises two circular chambers in Poly(methyl methacrylate) with internal diameter of 12 cm and 1 cm of thickness (internal volume for each chamber  $\sim 170$  ml) separated by a cation exchange membrane (CEM, CMI 7000, Membranes International Inc.). In each chamber carbon felt (Soft felt SIGRATHERM GFA5, SGL Carbon, Germany) was used as conductive material with a graphite rod (diameter 5 mm) to ensure an effective current conduction capability. Experiments were conducted in batch mode at room temperature ( $22 \pm 2^\circ\text{C}$ ), using *Saccharomyces cerevisiae* as active microorganism. The anode chambers were filled with yeast ( $50 \text{ g}\cdot\text{L}^{-1}$ ), glucose ( $60 \text{ g}\cdot\text{L}^{-1}$ ) and methylene blue ( $1.22 \text{ g}\cdot\text{L}^{-1}$ ) as redox mediator for the transport of electrons from the microorganisms to the electrode surface. The cathodic compartment was filled by potassium ferricyanide ( $6.58 \text{ g}\cdot\text{L}^{-1}$ ) used as oxidant compound. To prepare the anodic and the cathodic solution a buffer solution of minerals salts  $\text{Na}_2\text{HPO}_4$  ( $8.2 \text{ g}\cdot\text{L}^{-1}$ ) and  $\text{NaH}_2\text{PO}_4$  ( $5.2 \text{ g}\cdot\text{L}^{-1}$ ) was used. Two identical MFCs have been connected in series in order to power wireless sensor networks.

Beyond experiment set-up proposed in this paper, an electrochemical characterization of singular MFC has been conducted, in order to give an idea of electrical potentiality of these devices. All electrochemical experiments were run on a multi-channel VSP potentiostat (BioLogic) in a two-electrode set-up: where the working electrode was coupled to the anode and both counter and reference electrodes were connected to the cathode. Experiments were characterized in terms of open circuit voltage (OCV) and Linear Sweep Voltammetry (LSV) behavior, in order to gain information on the dynamics of electron transfer and hence, on power production. Polarization curves were measured a scan rate of  $1 \text{ mV}\cdot\text{s}^{-1}$ . Power was

indirectly calculated by  $P = I \cdot V$ , where  $I$ ,  $V$  represent the current and voltage output recorded, respectively. Figure 10.6 shows current ( $I, V$ ) and power ( $P, V$ ) curves obtained after 2 hrs MFC activity, before the measurements session with the IR-UWB piezo-resistive subsystem. Results showed a maximum power density of  $29.8 \text{ mW} \cdot \text{L}^{-1}$  and  $290 \text{ mW} \cdot \text{m}^{-2}$ , which slightly decrease from 2 h to 24h after the beginning of test.

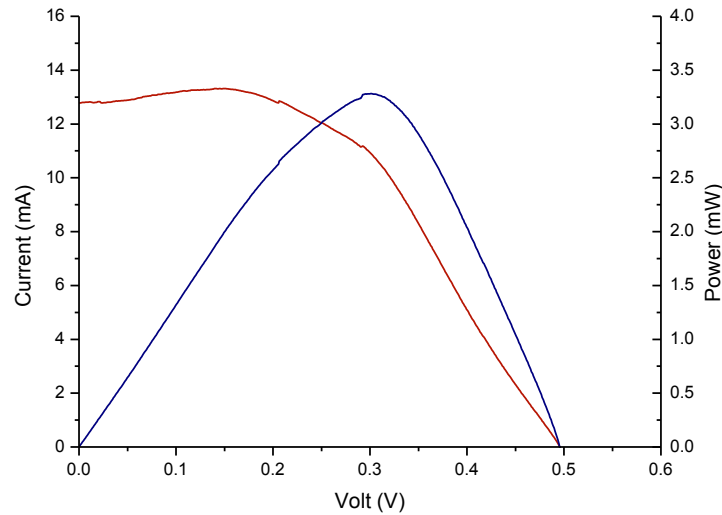


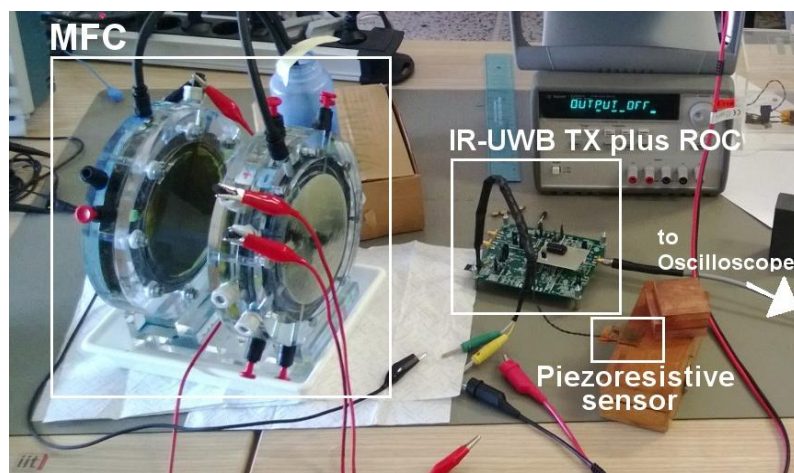
**Figure 10.6.** Polarization curve and power after 2 hrs operation from the beginning of test obtained by MFC working in batch mode with commercial carbon felt material as anode electrode

Particularly, Figure 10.6 shows that each MFC cell is able to reach about 3.2 mW as point of maximum power at 0.3 V, against 0.7 mW absorbed by the MFC/IR-UWB piezo-resistive demonstrator, even if the system requires two series MFCs to reach the supply voltage required (about 0.8 - 1 V). These results demonstrate that an MFC system, properly dimensioned and stacked in series could deliver enough power to sensors taking into account voltage input requirement and power absorption [28].

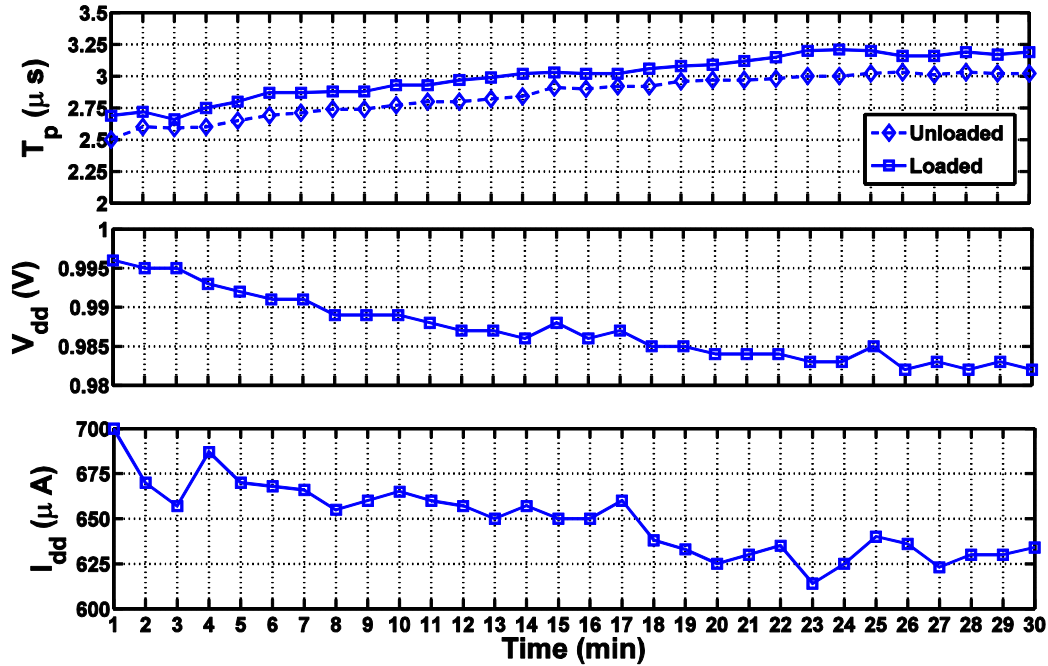
### 10.3.2. Complete system

Figure 10.7 shows the measurement set-up scheme for the combined MFC/IR-UWB and piezo-resistive demonstrator. The MFC is connected to a Printed Circuit Board (PCB) with an integrated circuit comprising the TX mounted. The supply terminals are directly connected to a series of two MFC, which provide an OCV of about 1.0 V. The piezoresistive sample connected to the read-out circuit is loaded with a 654.6 g copper weight, for an overall pressure of 64 kPa. Figure 10.8 shows the measured oscillation period  $T_p$  as a function of the

supply voltage of the MFC and the absorbed current. The oscillation period  $T_p$  is measured using a  $4 \text{ GS}\cdot\text{s}^{-1}$  oscilloscope. Pulses have center frequency of about 365 MHz almost constant for the whole supply range. Results show that oscillation period can be related to the voltage across the MFC, plus a variation of about 250 ns period applying pressure. We hence demonstrate that a 10 mV supply variation can be easily detected using our read-out circuit and combined to an applied pressure information. In the experiment the consumed power of the ROC plus IR-UWB transmitter (here, prototypes, hence, not fully optimized) ranges 630 to 700  $\mu\text{W}$ , which is below the maximum power achievable by the MFC, even if needs the voltage obtained by two MFCs in series.



**Figure 10.7.** Set-up scheme for the combined MFC/IR-UWB piezo-resistive demonstrator experiment



**Figure 10.8.** A 30 minutes measurement session, with depicted MFC supply voltage  $V_{dd}$ , consumed current by the printed circuit board system and the oscillation period  $T_p$ , with both nanostructured material loaded and unloaded applied pressure 64 kPa

### 10.5. Conclusion

This Chapter has reported on a wireless monitoring system for the transmission of the voltage level across a series of MFC plus an associated pressure level acquired using a piezoresistive nanostructured material and an associated read-out circuit. The system is capable of sensing 10 mV variations across the MFC during normal operation. Our solution is conceived to provide an efficient energy source, harvesting wastewater, integrating energy management and health monitoring capabilities to sensor nodes which are not connected to the energy grid.

### 10.6. References

- [1] D. Diamond, S. Coyle, S. Scarmagnani, J. Hayes, *Chemical Reviews*, 108 (2008) 652-679.
- [2] E.F. DeLong, P. Chandler, *Nature biotechnology*, 20 (2002) 788-789.
- [3] C. Donovan, A. Dewan, D. Heo, H. Beyenal, *Environmental science & technology*, 42 (2008) 8591-8596.
- [4] K. Rabaey, W. Verstraete, *TRENDS in Biotechnology*, 23 (2005) 291-298.

- [5] D. Hidalgo, T. Tommasi, V. Cauda, S. Porro, A. Chiodoni, K. Bejtka, B. Ruggeri, *Energy*, 71 (2014) 615-623.
- [6] T. Tommasi, B. Ruggeri, I. Mazzarino, D. Hidalgo, *Proceedings of the 4th International Conference on Engineering for Waste and Biomass Valorisation*. Porto, Portugal; ISBN: 979-10-91526-00-5, (2012).
- [7] J. Wei, P. Liang, X. Huang, *Bioresource Technology*, 102 (2011) 9335-9344.
- [8] S. Das, N. Mangwani, *Journal of Scientific and Industrial Research*, 69 (2010) 727-731.
- [9] Y. Liu, F. Harnisch, K. Fricke, U. Schröder, V. Climent, J.M. Feliu, *Biosensors and Bioelectronics*, 25 (2010) 2167-2171.
- [10] C.E. Reimers, L.M. Tender, S. Fertig, W. Wang, *Environmental science & technology*, 35 (2001) 192-195.
- [11] L.M. Tender, C.E. Reimers, H.A. Stecher, D.E. Holmes, D.R. Bond, D.A. Lowy, K. Pilobello, S.J. Fertig, D.R. Lovley, *Nature biotechnology*, 20 (2002) 821-825.
- [12] C. Reimers, P. Girguis, H. Stecher, L. Tender, N. Ryckelynck, P. Whaling, *Geobiology*, 4 (2006) 123-136.
- [13] W. Eaton, J. Smith, *Smart Materials and Structures*, 6 (1997) 530.
- [14] H. Yousef, M. Boukallel, K. Althoefer, *Sensors and Actuators A: physical*, 167 (2011) 171-187.
- [15] G. Canavese, M. Lombardi, S. Stassi, C.F. Pirri, *Applied Mechanics and Materials*, 110 (2012) 1336-1344.
- [16] G. Canavese, S. Stassi, M. Stralla, C. Bignardi, C. Pirri, *Sensors and Actuators A: physical*, 186 (2012) 191-197.
- [17] A. Chiolerio, I. Roppolo, M. Sangermano, *RSC Advances*, 3 (2013) 3446-3452.
- [18] S. Stassi, G. Canavese, V. Cauda, S. Marasso, C. Pirri, *Nanoscale Research Letters*, 7 (2012) 327.
- [19] S. Stassi, V. Cauda, G. Canavese, D. Manfredi, C.F. Pirri, *European Journal of Inorganic Chemistry*, 2012 (2012) 2669-2673.
- [20] B. Ruggeri, T. Tommasi, *International Journal of Hydrogen Energy*, 37 (2012) 6491-6502.
- [21] B. Ruggeri, M. Bernardi, T. Tommasi, *International Journal of Environment and Pollution*, 49 (2012) 226-250.
- [22] X. Xie, M. Ye, L. Hu, N. Liu, J.R. McDonough, W. Chen, H. Alshareef, C.S. Criddle, Y. Cui, *Energy & Environmental Science*, 5 (2012) 5265-5270.

- [23] B.E. Logan, B. Hamelers, R. Rozendal, U. Schröder, J. Keller, S. Freguia, P. Aelterman, W. Verstraete, K. Rabaey, *Environmental science & technology*, 40 (2006) 5181-5192.
- [24] S. Stassi, G. Canavese, F. Cosiansi, R. Gazia, M. Cocuzza, *Procedia Engineering*, 47 (2012) 659-663.
- [25] D. Bloor, K. Donnelly, P. J Hands, P. Laughlin, D. Lussey, *J. Phys. D: Appl. Phys.*, 38 (2005) 2851-2860.
- [26] M. Crepaldi, D. Demarchi, *Circuits and Systems II: Express Briefs, IEEE Transactions on*, 60 (2013) 237-241.
- [27] D. Bloor, K. Donnelly, P. Hands, P. Laughlin, D. Lussey, *Journal of Physics D: Applied Physics*, 38 (2005) 2851.
- [28] P. Aelterman, K. Rabaey, H.T. Pham, N. Boon, W. Verstraete, *Environmental science & technology*, 40 (2006) 3388-3394.

# Prospective

## A hybrid solar-microbial device for sustainable hydrogen and electricity generation

### P.1. Introduction

With the drastic increase of human population, there is an ever-growing demand for energy and clean water, for the continuous economic growth and suitable habitat of the earth. For this reason, in this century one of the most daunting challenges facing science is to develop renewable energy technologies. With this purpose in mind, this work was devoted to the study of highly energy-efficient systems in order to maximize the recovery of energy from renewable energy sources such as: solar and wastewater. In this scenario, the merge of photo-electrochemical (PEC) water splitting and microbial fuel cells (MFCs), technologies still under development, represents an attractive way to design a self-sustained system for renewable energy production.

PEC water splitting offers a promising way for clean, low-cost, environmentally friendly and virtually inexhaustible fuel production from solar energy. The appealing idea is to use the light from the sun, together with appositely designed semiconducting and catalytic materials, to obtain the water dissociation into elemental hydrogen and oxygen, and eventually the production of hydrocarbon fuels if the generated hydrogen is employed to reduce CO<sub>2</sub> [1]. To overcome the thermodynamic constraints and to compensate the energy loss during the operation (e.g. due to electrical resistance of the device), an external bias of 0.2 V to 1.0 V is usually supplied to sustain the current/hydrogen generation [2]. Nevertheless, the requirement of external bias adds to the complexity and cost for hydrogen production, making it less attractive as a cost effective energy solution. However, if the external bias is supplied from a renewable and continuous energy production system, PEC water splitting can become a more challenging device for hydrogen production. For this purpose, the integration of PEC and MFC devices could represent an excellent option.

MFCs are bioelectrochemical devices where electrogenic bacteria are used to oxidize the organic matter, transfer the electrons to an electrode and generate electricity [3]. Thus, MFCs provides new opportunity for sustainable energy production from biodegradable compounds present in the wastewater, achieving simultaneous wastewater treatment [4]. The application of MFCs for wastewater treatment or bioenergy production requires the use of inexpensive electrode materials [5-7] that are electrochemically and biologically stable, and that have a

high specific surface area, electrical conductivity and appropriate mechanical strength [5, 8, 9]. In addition to bioelectricity, the electrons produced by the microorganisms can also be used to produce various chemical fuels, depending on the electron acceptors used in the catholyte [10, 11]. Considerable efforts have been made to minimize the energy loss through the optimization of MFC reactors, electrodes, as well as the type of metal catalysts on the cathode. MFCs have been investigated also as power generation systems for underwater monitoring equipments, remote sensors and biochemical oxygen demand sensors as well as hydrogen production devices [12-15]. Recently, Wang et al. [2] have demonstrated the feasibility of continuous hydrogen production based solely on solar light and biomass (wastewater) recycling, by coupling solar water splitting and microbial electrohydrogenesis in a photo-electrochemical cell-microbial fuel cell (PEC-MFC) hybrid device; however, the use of expensive electrode materials such as platinum is up-to-date the main bottleneck of this system. These microbial photoelectrochemical cells can open up many opportunities for microbial fuel cell technology because they combine respective advantages of semiconductor and microbial systems. The aim of this Chapter is to present the general concept of a hybrid device that interphase a PEC water splitting system with a series of MFC devices (denoted in following as PEC-MFC), which could generate both electricity and hydrogen gas using as external bias the potential produced by microbial fuel cells from biodegradable organic matter and solar light as the only energy sources.

## **P.2. Experimental**

### **P.2.1. PEC and MFC configuration and operation**

The configuration of the PEC-MFC device is illustrated in Figure P.1. The system is composed by a dual chamber water splitting PEC and by an assembly of three MFCs as shown in Figure 9.1.

Each MFC is composed by anode and cathode chambers, separated by a proton exchange membrane (PEM). In the MFCs, commercial carbon felt (C-FELT), polyaniline-deposited carbon felt (C-PANI) and carbon-coated Berl saddles (C-SADDLES) were used as anode electrodes. All the MFCs use commercial carbon felt in the cathode chamber. The MFCs were inoculated with the effluent of an active MFC which operated using sodium acetate as substrate and a mixed microbial population naturally present in sea water, previously enriched as is described in Section 9.2.2. A sterile and concentrate synthetic anode influent was continuously fed by a syringe pump (KF Technology, Italy) at a flow rate of  $0.42 \text{ mL}\cdot\text{h}^{-1}$

in order to provide to the individual MFCs  $1 \text{ g}\cdot\text{L}^{-1}$  sodium acetate and  $1.25 \text{ g}\cdot\text{L}^{-1}$  peptone (in anode buffer solution) per day respect to the total volume of the anolyte. The total volume of the anolyte was 500 mL which was recirculated from the anode vessel through the anode matrix at a flow rate of  $1 \text{ L}\cdot\text{h}^{-1}$  by a peristaltic pump (ISMATEC - ISM404B, Germany). The catholyte consisted of potassium ferricyanide ( $500 \text{ mL}$  at  $6.58 \text{ g}\cdot\text{L}^{-1}$ ) aqueous solution in buffer solution of inorganic salts i.e.  $\text{Na}_2\text{HPO}_4\cdot 2\text{H}_2\text{O}$  ( $8.2 \text{ g}\cdot\text{L}^{-1}$ ) and  $\text{NaH}_2\text{PO}_4\cdot\text{H}_2\text{O}$  ( $5.2 \text{ g}\cdot\text{L}^{-1}$ ), which was recirculated from the cathode vessel through the cathode matrix at a flow rate of  $1 \text{ L}\cdot\text{h}^{-1}$  by using a peristaltic pump. The oxidation/reduction of the cathode was controlled by a periodic renewal of the cathode solution when the solution was decolorized. The MFCs were operated in a continuous mode at room temperature of  $24 \pm 2 \text{ }^\circ\text{C}$  under open circuit voltage. In Chapter 9 are shown the operational experimental details of the MFCs.

In the PEC device,  $\text{ZnO@TiO}_2$  core-shell structures were used as photoanode material and prepared as a follow: first, ZnO nanowire (ZnO NWs) were grown on a commercial stainless steel grid as support by hydrothermal synthesis following the experimental procedure explained in Section 3.2.1.3 and then,  $\text{ZnO@TiO}_2$  core-shell structures were fabricated by covering the ZnO NWs with  $\text{TiO}_2$  nanoparticles by using the non-acid sol-gel synthesized explained in Section 3.2.1.4. Cathodes were fabricated by depositing a thin and dense film of Pt (thickness of about 110 nm) on a stainless steel grid support, and in following will be called "Pt/grid". Before depositing the active photoanodic and cathodic materials, the stainless steel grid supports were first accurately cleaned in ultrasonic bath for 10 min at 60 Hz using ethanol to remove pollutants from the surface and then dried in air at room temperature. A PEM-based PEC was used to study the photo-electrochemical performance of the  $\text{ZnO@TiO}_2$  core-shell structured electrode for the water splitting reaction [1]. The PEM PEC was composed by  $\text{ZnO@TiO}_2$  core-shell structures electrode used as anode, the Pt/grid electrode used as cathode and Nafion 117 used as proton conducting membrane. These three elements constitute the membrane electrode assembly (MEA) which is sandwiched between two microfluidic reaction chambers made of polydimethylsiloxane (PDMS), closed by two quartz windows placed at the front and at the back side of the device, respectively. The reaction chambers were filled and fed continuously with an electrolytic solution of NaOH ( $0.1 \text{ M}$ ,  $\text{pH} \sim 13.0$ ), using a peristaltic pump (Peripro-4H by Word Precision Instruments) at a rate of  $5 \text{ ml}\cdot\text{min}^{-1}$ : such value is able to guarantee continuous electrolyte regeneration and exit of produced gases in the reaction chambers. PEC and MFC devices were assembled and tested separately before integrating them into the hybrid device.

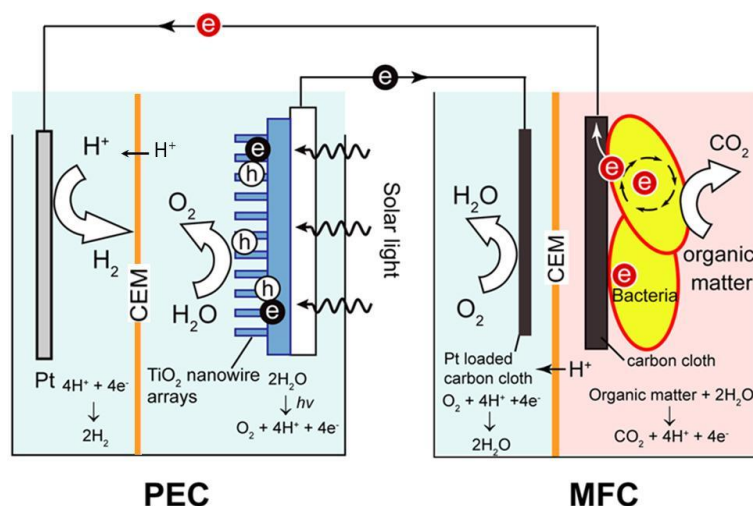


**Figure P.1.** Schematic configuration of PEC-MFC device

### P.2.2. Electrochemical and photo-electrochemical characterization

Electrochemical experiments were performed on a multi-channel VSP potentiostat/galvanostat (BioLogic). Measurements were recorded by using EC-Lab software version 10.1x for data acquisition. Electrochemical tests of the MFCs were carried out using a two electrode configuration, where the working electrode was connected to the anode and both counter and reference electrodes were connected to the cathode. Electrochemical characterizations were performed in a single MFC and in a series configuration MFCs in order to obtain the electrical contribution of all the three cells. Linear Sweep Voltammetry (LSV) curves were recorded by imposing a linear potential decrease from the Open Circuit Voltage (OCV) of the cell ( $V_0$  where  $I = 0$ ) to the Short Circuit Voltage of the cell ( $V_{sc} = 0$  where  $I = I_{max}$ ) at a scan rate of  $1 \text{ mV} \cdot \text{s}^{-1}$ . From the  $I$ - $V$  curves, the power density was calculated by the following equation:  $P = (I \cdot V) \cdot A^{-1}$ , where  $I$ ,  $V$  and  $A$  represent the recorded current, voltage output and total area of the chamber, respectively. In the PEC the electrochemical tests were performed in two-electrodes configuration, using the ZnO@TiO<sub>2</sub> core-shell structures as working electrode and the Pt/grid as counter and reference electrode. The PEC was first polarized at 2 V for 1 h to allow a full development of the concentration gradients in the cell. Then, the  $I$ - $V$  characteristic curve was measured by applying an external potential bias between 0 and 2.5 V at a rate of  $20 \text{ mV} \cdot \text{s}^{-1}$ . LSV measurements were performed under dark and under frontal simulated AM 1.5G solar light illumination ( $100 \text{ mW} \cdot \text{cm}^{-2}$  irradiation, provided by a 450 W Xe lamp with an A.M. 1.5G filter and a water filter), cutting off IR radiation, in order to avoid the heating of the device. The geometrical area of the anodic electrodes in contact with the liquid electrolyte was around  $4.38 \text{ cm}^2$ .

### P.3. Results and discussion

For the PEC device, ZnO@TiO<sub>2</sub> core-shell structures were used as photo-anode material because it is an attractive material for water oxidation, due to its favorable band gap positions, good chemical stability, easy preparation procedure and low cost [16, 17]. In addition, its one dimensional structure provides an extremely large surface area for water oxidation. Dense and vertically aligned ZnO NWs were grown on a stainless steel grid support as reported in the FESEM images in Figures P.2. ZnO NWs in Figure P.2b evidenced an average length of 2 - 3 μm with a diameter ranging between 100 and 200 nm. Figure P.2c put in evidence the good coverage of the ZnO NWs with the titania shell made of crystalline anatase nanoparticles [16, 17]. The PEC behavior of the ZnO@TiO<sub>2</sub> core-shell photo-anode was evaluated for the water photo-electrolysis reaction. The *I-V* curve from the water photo-electrolysis, in the dark and under 1 sun of illumination (AM 1.5G filter, 100 mW·cm<sup>-2</sup>) are reported in Figure P.2d. The photocurrent density (*J*) of the ZnO@TiO<sub>2</sub> core-shell photo-anode showed an important rise starting at about 1.2 V, reaching a maximum *J* value of 4.12 mA/cm<sup>2</sup> at about 2.5 V.

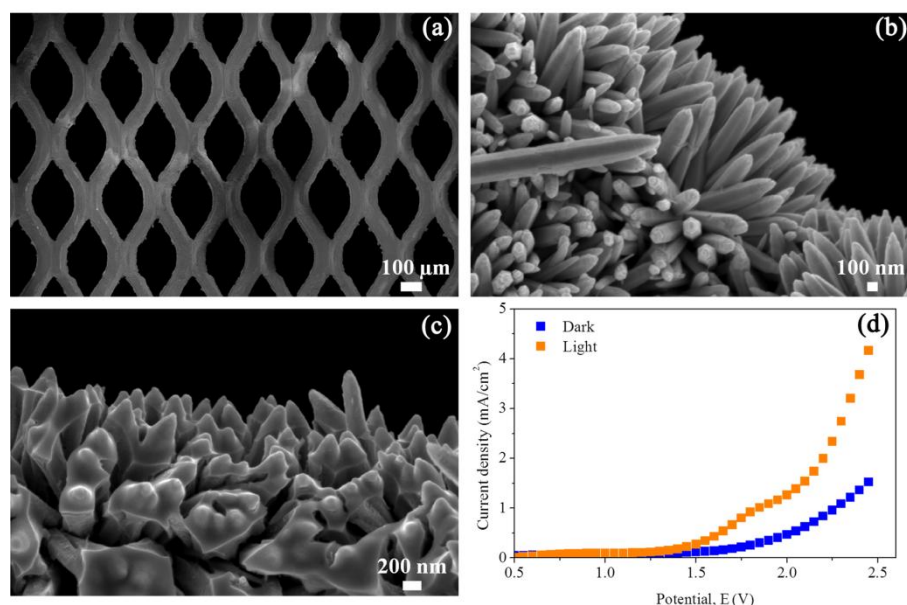


**Figure P.2.** FESEM images of (a) pristine commercial stainless steel grid support, (b) ZnO NWs structure and (c) ZnO@TiO<sub>2</sub> core-shell photo-anode and (d) *I, V* curves collected for ZnO@TiO<sub>2</sub> core-shell photo-anode with an electrolytic solution of NaOH (0.1 M), in the dark and under illumination (100 mW·cm<sup>-2</sup> irradiation, provided by a 450 W Xe lamp with an A.M. 1.5G filter and a water filter), at a scan rate of 20 mV·s<sup>-1</sup>

Before assembling the PEC-MFC hybrid system, the MFCs were maintained for more than three months under external resistance of  $1000\ \Omega$  in continuous operation as explained in Chapter 9. For this study, MFCs were characterized in term of OCV and energy generation in order to evaluate the capability of the biological systems to provide the necessary bias to the PEC. OCV of the individual MFCs was monitored during 2 h periods in order to reach quasi-steady-state conditions before starting polarization measurements. Results showed OCV values around 0.75 V for each individual cell and OCV values around 2.17 V for the three cells connected in series (see Figure P.3). Polarization and power characterization revealed that these cells operated in the ohmic region and generated a peak power of around 0.52 mW, 0.45 mW and 1 mW at a current 2.5 mA using C-FELT, C-PANI and C-SADDLES as anode materials, respectively. From these results it is possible to consider that the assembly of three MFCs connected in series might supply the necessary external bias to operate the PEC, which requires a potential  $> 1.5\ \text{V}$  in order to obtain an important rise on the current density and hence on hydrogen production.

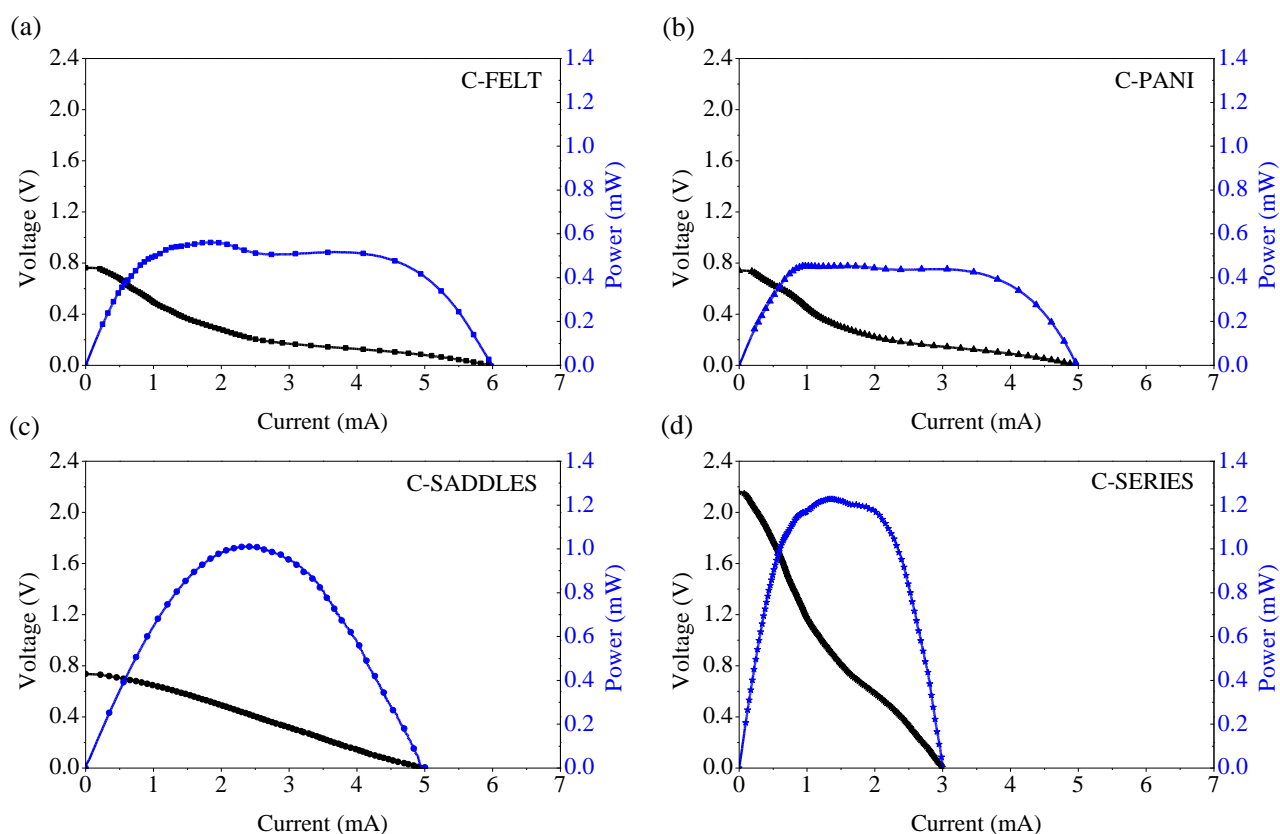


**Figure P.3.** Polarization (black line) and power (blue line) curves collected by using (a) C-FELT, (b) C-PANI, (c) C-SADDLES as anode electrode and (d) using all three MFCs in a series configuration

Figure P.4a shows the operational curves superimposed of both MFCs in series and PEC working under simulated sun-light illumination. It is possible to observe that the operation point in which both systems reach equilibrated conditions is around 1.4 V (0.77 mA). This result suggests that the integration of the systems could promote the sustainability of a self-biased PEC-MFC hybrid system.

After the PEC and MFC characterizations, in order to validate the feasibility of the PEC-MFC device concept, the hybrid device was characterized as a follow: the MFCs stack anode was connected to the PEC cathode (Pt/grid electrode), while the MFCs stack cathode was connected to the PEC ZnO@TiO<sub>2</sub> core-shell photo-anode. With this configuration, upon illumination, photo-excited electron-holes pairs are created at the ZnO@TiO<sub>2</sub> core-shell structure and subsequently separated by the electric field at the anode/electrolyte interface. The holes stay at the surface of ZnO@TiO<sub>2</sub> core-shell photo-anode and oxidize water into oxygen, electrons and H<sup>+</sup>. The electrons produced flowed through the external circuit to the MFC cathode, where they reduced the catholyte composed of potassium ferricyanide. Meanwhile, the electrogenic bacteria in the MFC anode biologically oxidize the organic matter (sodium acetate) to produce electrons, which are then transferred to the external circuit to the Pt/grid cathode of the PEC and reduce protons (H<sup>+</sup>) to hydrogen gas. Figure P.4b shows the amperometric *I-t* curve recorded for the PEC-MFC device, by applying the potential generated by MFCs operated in a series configuration to the PEC working under 1 sun of illumination. The current spike occurred when the light was turned on, and then a steady-state current was obtained after several seconds of settling. After the integration of the PEC-MFC system, a continuous decrease on the potential of the MFCs was observed from OCV around 2.17 V until to reach short-circuit current (0 V) after 30 min of operation. This fact can be explained due to PEC represent a substantial resistance for the operation of the MFCs, and thus current tended to decrease continuously during time. It can be also associated to a slower biological oxidation rate of reaction than other ones occurred in PEC, due to an increase of microorganism stress induced by the high electrons request and a faster depletion of nutrients in the anolyte [2]. After 30 min of operation, gas bubbles were not observed in the cathode chamber of the PEC.

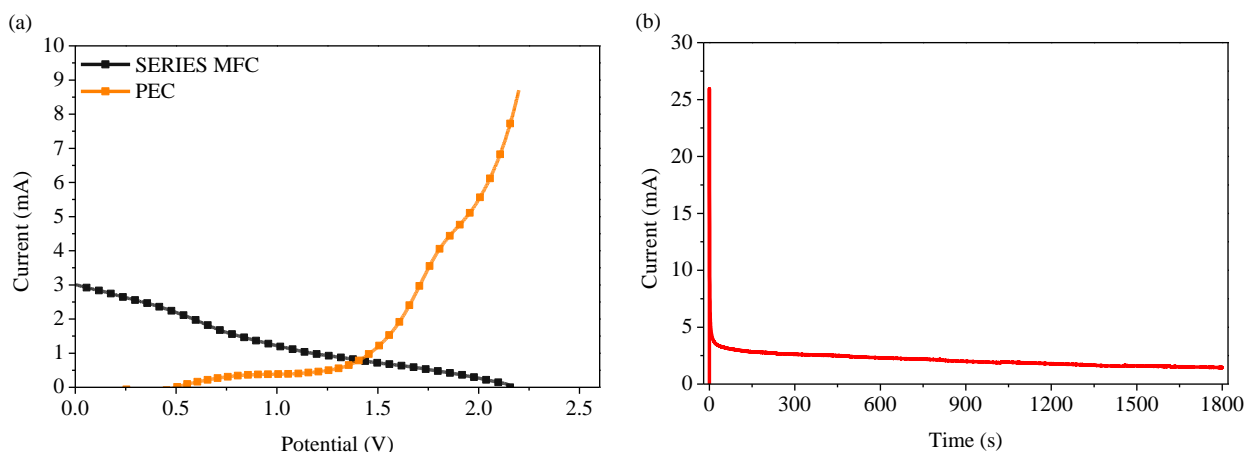


**Figure P.4.** *I,V* curves for (a) PEC under illumination at a scan rate of  $20 \text{ mV} \cdot \text{s}^{-1}$  (orange line) and series MFC (black line) at a scan rate of  $1 \text{ mV} \cdot \text{s}^{-1}$ , and (b) *I-t* curve recorded for the PEC-MFC device by applying the potential generated by MFCs operated in a series configuration and under 1 sun of illumination

#### P.4. Future works

PEC-MFC hybrid device could be a sustainable and renewable energy source with the continuous supply of sunlight and organic matter as feedings, which can not only generate electricity and hydrogen but also treat wastewater and recover contaminants at the same time (see Figure P.5). This Chapter provides new insights into the development of efficient energy solutions by integrating solar and microbial technology, which may revolutionize the conventional wastewater treatment methodologies currently applied nationwide. In order to improve PEC-MFC operation, several strategies could be taken into account: (1) employ several MFCs (more than three) in order to ensure the external bias required by the PEC, because the PEC represents a significant resistance for the system and voltage potential decreased during time until to reach steady-state conditions, (2) develop new photo-anode materials that allow a reduction of the external bias required by an improvement in the solar light absorption, and (3), improve MFC and PEC configurations in order to reduce the internal energy losses in both systems. For practical applications, the sustainability of a self-biased PEC-MFC device depends on their individual electrochemical performances. Finally, while ferricyanide solution is an excellent catholyte for MFC devices, it is not renewable in practice and its production and use may cause environmental issues. Alternatively, oxygen can be used as an electron acceptor and its application potential has been demonstrated in a variety of air cathode MFCs [18-21], which increase sustainability, reduce costs and minimize the environmental impact of MFCs.

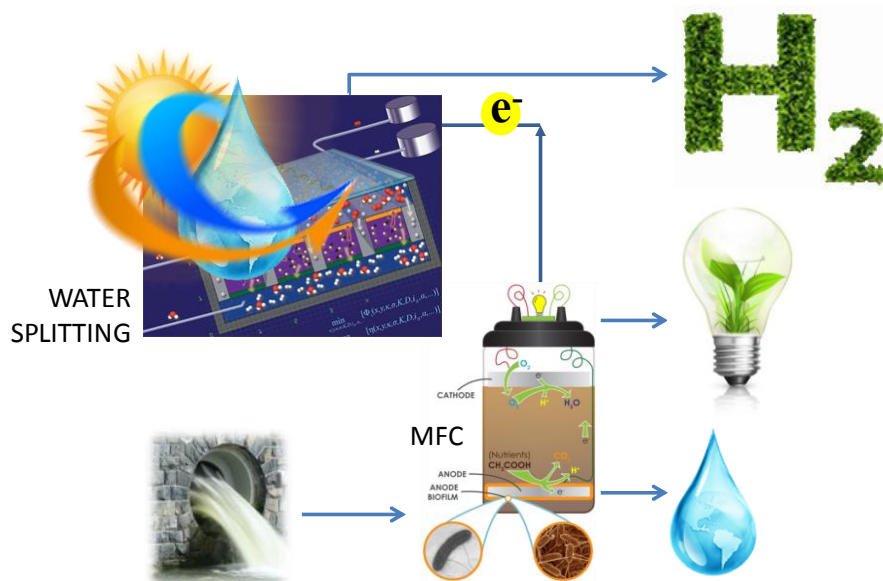


**Figure P.5.** PEC-MFC hybrid device for the sustainable and renewable production of hydrogen and electricity

### P.5. References

- [1] S. Hernández, M. Tortello, A. Sacco, M. Quaglio, T. Meyer, S. Bianco, G. Saracco, C.F. Pirri, E. Tresso, *Electrochimica Acta*, 131 (2014) 184-194.
- [2] H. Wang, F. Qian, G. Wang, Y. Jiao, Z. He, Y. Li, *Acs Nano*, 7 (2013) 8728-8735.
- [3] B.E. Logan, B. Hamelers, R. Rozendal, U. Schröder, J. Keller, S. Freguia, P. Aelterman, W. Verstraete, K. Rabaey, *Environmental science & technology*, 40 (2006) 5181-5192.
- [4] R.M. Allen, H.P. Bennetto, *Applied Biochemistry and Biotechnology*, 39 (1993) 27-40.
- [5] T. Tommasi, B. Ruggeri, I. Mazzarino, D. Hidalgo, *Proceedings of the 4th International Conference on Engineering for Waste and Biomass Valorisation*. Porto, Portugal; ISBN: 979-10-91526-00-5, (2012).
- [6] J. Wei, P. Liang, X. Huang, *Bioresource Technology*, 102 (2011) 9335-9344.
- [7] S. Das, N. Mangwani, *Journal of Scientific and Industrial Research*, 69 (2010) 727-731.
- [8] Y. Liu, F. Harnisch, K. Fricke, U. Schröder, V. Climent, J.M. Feliu, *Biosensors and Bioelectronics*, 25 (2010) 2167-2171.
- [9] D. Hidalgo, T. Tommasi, V. Cauda, S. Porro, A. Chiodoni, K. Bejtka, B. Ruggeri, *Energy*, 71 (2014) 615-623.
- [10] Y. Jiao, F. Qian, Y. Li, G. Wang, C.W. Saltikov, J.A. Gralnick, *Journal of Bacteriology*, 193 (2011) 3662-3665.
- [11] G. Wang, F. Qian, C.W. Saltikov, Y. Jiao, Y. Li, *Nano Research*, 4 (2011) 563-570.

- [12] I.S. Kim, K.-J. Chae, M.-J. Choi, W. Verstraete, *Environmental Engineering Research*, 13 (2008) 51-65.
- [13] C.E. Reimers, L.M. Tender, S. Fertig, W. Wang, *Environmental science & technology*, 35 (2001) 192-195.
- [14] L.M. Tender, C.E. Reimers, H.A. Stecher, D.E. Holmes, D.R. Bond, D.A. Lowy, K. Pilobello, S.J. Fertig, D.R. Lovley, *Nature biotechnology*, 20 (2002) 821-825.
- [15] C. Reimers, P. Girguis, H. Stecher, L. Tender, N. Ryckelynck, P. Whaling, *Geobiology*, 4 (2006) 123-136.
- [16] S. Hernández, V. Cauda, A. Chiodoni, S. Dallorto, A. Sacco, D. Hidalgo, E. Celasco, C.F. Pirri, *ACS Applied Materials & Interfaces*, 6 (2014) 12153–12167.
- [17] S. Hernández, V. Cauda, D. Hidalgo, V. Farías Rivera, D. Manfredi, A. Chiodoni, F.C. Pirri, *Journal of Alloys and Compounds*, 615 (2014) S530 – S537.
- [18] Y. Feng, X. Wang, B.E. Logan, H. Lee, *Applied Microbiology and Biotechnology*, 78 (2008) 873-880.
- [19] Z. He, Y. Huang, A.K. Manohar, F. Mansfeld, *Bioelectrochemistry*, 74 (2008) 78-82.
- [20] H. Liu, B.E. Logan, *Environmental science & technology*, 38 (2004) 4040-4046.
- [21] B. Logan, S. Cheng, V. Watson, G. Estadt, *Environmental science & technology*, 41 (2007) 3341-3346.

## Summary

The population increase, along with the rapid growth of many developing economies, indicates that the demand for energy may more than double by mid-century. The consumption of water, food, transportation and consumer products are growing and hence they require energy to the different production processes. Nowadays, the need for power is mainly satisfied by the use of conventional energy sources based on oil, coal, natural gas and nuclear power that have proven to be highly effective drivers of economic progress. Unfortunately, the increasing concentration of CO<sub>2</sub> in the atmosphere, as a result of the combustion of these carbon-based fuels, is predicted to result in unacceptable changes in the earth's climate. In addition, pollution such as sulfur dioxide emissions and oil spills also point to the need for carbon-free alternative energy sources. In contrast, many technologies based on renewable energy sources have been developed, which represent a clean energy sources that have a much lower environmental impact than conventional energy technologies. Renewable energy commercialization involves the deployment of three generations of renewable energy technologies dating back more than 100 years. First-generation technologies, which are already mature and economically competitive, include biomass, hydroelectricity, geothermal power and heat. Second-generation technologies are market-ready and are being deployed at the present time; they include solar heating, photovoltaics, wind power, solar thermal power stations, and modern forms of bioenergy. Third-generation technologies include advanced biomass gasification, hot-dry-rock geothermal power, ocean energy, artificial photosynthesis and microbial fuel cell [1-3], many of them still under development. Worldwide investments in renewable technologies amounted to more than US\$ 214 billion in 2013, with countries like China and the United States heavily investing in wind, hydro, solar and biofuels [4]. Rapid deployment of renewable energy and energy efficiency is resulting in significant energy security, climate change mitigation, and economic benefits. While many renewable energy projects are large-scale, renewable technologies are also suited to rural and remote areas and developing countries, conferring also to renewable energy the ability to lift the poorest nations to new levels of prosperity. Due to the crucial impact in humanity, the development and application potential of renewable energy is a reality.

For the development of new forms of renewable energy several efforts have been done in order to increase the performance and the efficiency of the processes. Nowadays, many researches focus their attention on the development of renewable energy from solar and

water, which represent abundant and renewable energy sources. In order to encourage the growth of new renewable energy technologies, this research work is mainly focused on the development of promising anodic materials and their potential application on emerging technologies such as artificial photosynthesis and microbial fuel cell. The investigations were carried out in two main electrochemical devices: (1) photoelectrochemical cell (PEC) for hydrogen generation through water splitting reaction and (2) microbial fuel cell (MFC) with a proton exchange membrane configuration (PEM) for direct electricity generation by microorganisms activity. The properties of a wide range of materials were analyzed in depth in order to select the most promising materials able to offer the best performance under each particular operation. As a results, according to desired properties of the investigated functional materials this research was focused on two main materials: (1)  $\text{TiO}_2$  selected as based materials for the development of anodic electrodes for the water splitting reaction due to its demonstrated application potential as photocatalysts materials such as: appropriate band gap of about 3.2 eV, high photocatalytic efficiency, good chemical, optical stability, optimal environmental and biological compatibility; and (2) carbon-based materials selected as most promising materials for the development of anodic electrodes for MFC because of its unique properties such as good conductivity, stability, biocompatibility and low cost.

Concerning the investigation on PEC for the water photoelectrolysis, different  $\text{TiO}_2$  nanostructures have been studied as anodic electrodes including: synthesis, characterization and test of  $\text{TiO}_2$ -based materials with the aim of improving the limiting factors of the photocatalytic reaction: charge recombination and separation/migration processes. As a first step, a new and low-cost synthesis procedure has been implemented for the fabrication of thick, mesoporous, transparent and crackless  $\text{TiO}_2$  films, using an acetic acid catalyzed sol gel synthesis with a high water ratio modified by the addition of a non-ionic surfactant. The high porosity, surface area, homogeneity and amount of material deposited on the substrate surface, together with the good electronic transport and stability over time, resulted in an improved photo-catalytic performance of the titania films [5]. Also, the  $\text{TiO}_2$  sol obtained by this synthesis procedure was used as interconnection layer between different nanostructured metal oxides, which has been made for instance to bond free-standing  $\text{TiO}_2$  nanotubes membranes into a transparent conductive oxide to be used in a solar energy production system (i.e. dye sensitized solar cell) [6, 7]. As a next step, the photo-catalytic properties of different  $\text{TiO}_2$  nanostructures were evaluated including:  $\text{TiO}_2$  NPs film,  $\text{TiO}_2$  NTs and  $\text{ZnO@TiO}_2$  core-shell structures. Photo-electrochemical activity measurements and electrochemical impedance spectroscopy analysis showed an improvement in charge

collection efficiency of 1D-nanostructures, related to a more efficient electron transport in the materials. The efficient application of both the TiO<sub>2</sub> NTs and the ZnO@TiO<sub>2</sub> core-shell photoanodes opens important perspectives, not only in the water splitting application field, but also for other photo-catalytic applications (e.g. photovoltaic cells, degradation of organic substances), due to their chemical stability, easiness of preparation and improved transport properties [8-10]. Different optimization strategies (*i.e.* co-catalysis, surface modifications to adsorb visible light, increase of thickness, use of concentrated solar light) were identified for each of the studied materials in order to increase their effectiveness and to achieve the efficiency values required for commercial applications. Finally, in order to improve the photo-catalytic activity of TiO<sub>2</sub> NPs, PANI/TiO<sub>2</sub> composite films have been synthesized and tested. Polyaniline (PANI) solution was synthesized by oxidative polymerization starting from aniline dimer obtaining emeraldine as the PANI conductive form. PANI/TiO<sub>2</sub> composite film was obtained by dip coating the TiO<sub>2</sub> film in the obtained PANI solution. PANI/TiO<sub>2</sub> composite film was successfully applied as anode material for the PEC water splitting reaction. The increase in the photocatalytic activity of PANI/TiO<sub>2</sub> (2-fold higher) with respect to TiO<sub>2</sub> NPs composite film should be essentially attributed to the efficient separation of electron and hole pairs, which allowed a significant improvement of the charge recombination and separation/migration processes in the TiO<sub>2</sub> NPs [11].

Different strategies were also applied in order to improve the performance of anode materials for MFCs. The investigation of commercial carbon-based materials demonstrated that these materials, normally used for other ends, are suitable electrodes for MFC and their use could reduce MFC costs and improve the energy sustainability of the process, promoting the MFC technology as possible alternative in wastewater treatment and energy generation. This demonstration allowed obtaining a wide variety of choices through which the performance of these materials can be effectively increase. In this way, to enhance power generation in MFC by using low-cost and commercial carbon-based materials several strategies can be adopted including the treatment of the surface of commercial materials to facilitate electron recovery. For this purpose, in this study nitric acid activation (C-HNO<sub>3</sub>) and PANI deposition (C-PANI) were performed in order to increase the performance of commercial carbon felt (C-FELT) as anode material in MFC. Electrochemical determinations performed in batch-mode MFC revealed a strong reduction of the activation losses contribution and an important decrease of the internal resistance of the cell using C-HNO<sub>3</sub> and C-PANI of about 2.3 and 4.4 times, respectively, with respect to C-FELT [12]. The important increase on the power and current in all of these cases were likely to be a combination of factors including: (1) enhanced

electrical conductivity, (2) increased surface area, and (3) increased affinity of the anode surfaces. Moreover, the proposed PANI deposition has multiple advantages with respect to the previous ones reported in literature [13, 14]: i) increase of PANI conductivity in the soaker solution, ii) decrease of risk hazard during polymerization by use of non-toxic starting monomer and iii) more homogeneous and faster deposition method. During this work, not only commercial carbon-based materials (untreated and treated) were evaluated, but also in order to resolve different MFC operational problems such as: biofouling, low surface area and large-scale MFC, in this work is presented the development of an innovative three-dimensional material effectively used as anode electrode. The synthesis process consisted in the deposition of a continuous and homogeneous graphite layer on the surface of commercial Berl saddles through the follow experimental procedure: impregnation, caramelization and pyrolysis of glucose used as carbon precursor. The conductive carbon-coated Berl saddles (C-SADDLES) were successfully used as anode electrode in batch-mode MFC. The results obtained show an significant improvement on power densities with respect to most of the commercial carbon-based materials tested, and are in good agreement with the results obtained using commercial carbon felt under the same MFC operation [15]. Results suggested that the carbon-coated Berl saddles offer a low-cost solution to satisfy either electrical or bioreactor requirements, increasing the reliability of the MFC processes, and seems to be a valid candidate for scaled-up systems and for continuous mode application of MFC technology. In addition, the electrochemical performance and continuous energy production of the most promising materials obtained during this work were evaluated under continuous operation MFC in a long-term evaluation test. Remarkable results were obtained for continuous MFCs systems operated with three different anode materials: C-FELT, C-PANI and C-SADDLES. From polarization curves, the maximum power generation was obtained using C-SADDLES ( $102 \text{ mW}\cdot\text{m}^{-2}$ ) with respect to C-FELT ( $93 \text{ mW}\cdot\text{m}^{-2}$ ) and C-PANI ( $65 \text{ mW}\cdot\text{m}^{-2}$ ) after three months of operation. The important reduction of the internal resistance of the MFC operated using C-SADDLES with respect to C-FELT and C-PANI could be associated to a major colonization of the electrode surface, which results in an increase on the electron transport from the microorganisms to the electrode. The highest amount of electrical energy was produced by C-PANI (1803 J) with respect to C-FELT (1664 J) and C-SADDLES (1674 J) [16, 17]. However, it is worth to note that PANI activity was reduced during time by the operating conditions inside the anode chamber such as: PANI losses, pH conditions in the anode chamber and possible degradation or deactivation of deposited PANI by microorganisms activity.

In order to demonstrate the wide application potential MFC, even if it is a technology still under development, the energy produce by MFC was effectively used to power a sensor system. This work reports the contributions of three separate fields such as: an Ultra-Wide-Band transmitter and an ad-hoc read-out circuit connected to the piezoresistive material which can be potentially operated by the power produced by MFCs. By combining the advantages from three fields in a system which enables the ultra-low-power monitoring of a microbial fuel cell voltage, the system provides an efficient energy source, harvesting wastewater, integrating energy management and health monitoring capabilities to sensor nodes which are not connected to the energy grid [18].

Finally, in this PhD thesis work is presented a general concept of the integration of both the studied devices into a hybrid one (denoted as PEC-MFC), by interfacing the water splitting PEC and the MFC devices. This concept is proposed to generate electricity and hydrogen gas using as external bias (i) the potential produced by microbial fuel cells from biodegradable organic matter and (ii) solar light, as the only energy sources. This new concept provides new insights into the development of efficient energy solutions by integrating solar and microbial technologies, which may revolutionize the conventional wastewater treatment methodologies currently applied nationwide.

To conclude, this research has resulted in new insights which are helpful for the development of anode materials and their successful application in water splitting PEC and MFC devices. Moreover, this work presents new prospective toward the development and future application of PEC and MFCs in the domain of wastewater treatment and renewable energy productions such as hydrogen and electricity. It is expected that, next to the recovery of energy from solar and wastewater, many new applications for PEC and MFCs will emerge.

## References

- [1] M.M. E. Moula, J. Maula, M. Hamdy, T. Fang, N. Jung, R. Lahdelma, *International Journal of Sustainable Built Environment*, 2 (2013) 89-98.
- [2] A.F. Collings, C. Critchley, *Artificial photosynthesis: from basic biology to industrial application*, John Wiley & Sons, 2007.
- [3] V. Shah, *Emerging environmental technologies*, Springer, 2008.
- [4] "Renewables 2014: Global Status Report" (2014).
- [5] D. Hidalgo, R. Messina, A. Sacco, D. Manfredi, S. Vankova, E. Garrone, G. Saracco, S. Hernández, *International Journal of Hydrogen Energy*, doi: 10.1016/j.ijhydene.2014.02.163 (2014).

- [6] A. Lamberti, A. Sacco, S. Bianco, D. Manfredi, F. Cappelluti, S. Hernandez, M. Quaglio, C.F. Pirri, *Physical Chemistry Chemical Physics*, 15 (2013) 2596-2602.
- [7] S. Hernández, M. Tortello, A. Sacco, M. Quaglio, T. Meyer, S. Bianco, G. Saracco, C.F. Pirri, E. Tresso, *Electrochimica Acta*, 131 (2014) 184-194.
- [8] S. Hernández, V. Cauda, A. Chiodoni, S. Dallorto, A. Sacco, D. Hidalgo, E. Celasco, C.F. Pirri, *ACS Applied Materials & Interfaces*, 6 (2014) 12153–12167.
- [9] S. Hernández, V. Cauda, D. Hidalgo, V. Farías Rivera, D. Manfredi, A. Chiodoni, F.C. Pirri, *Journal of Alloys and Compounds*, 615 (2014) S530 – S537.
- [10] D. Hidalgo, A. Sacco, A. Chiodoni, A. Lamberti, V. Cauda, E. Tresso, G. Saracco, S. Hernández, Photocatalytic and transport properties of TiO<sub>2</sub> and ZnO nanostructures for solar-driven water splitting. *Solar Energy Material and Solar Cells*. Submitted, (2014).
- [11] D. Hidalgo, S. Hernández, S. Bocchini, M. Fontana, G. Saracco, F.C. Pirri, Proceedings of the International Congress on Materials and Renewable Energy. Athens, Greece, (2013).
- [12] D. Hidalgo, T. Tommasi, S. Bocchini, A. Chiolerio, A. Chiodoni, I. Mazzarino, B. Ruggeri, Surface modification of commercial carbon felt used as anode for Microbial Fuel Cells (MFCs). *ACS Applied Materials & Interface*, (2014).
- [13] C. Li, L. Zhang, L. Ding, H. Ren, H. Cui, *Biosensors and Bioelectronics*, 26 (2011) 4169-4176.
- [14] M. Ghasemi, W.R.W. Daud, N. Mokhtarian, A. Mayahi, M. Ismail, F. Anisi, M. Sedighi, J. Alam, *International Journal of Hydrogen Energy*, 38 (2013) 9525-9532.
- [15] D. Hidalgo, T. Tommasi, V. Cauda, S. Porro, A. Chiodoni, K. Bejtka, B. Ruggeri, *Energy*, 71 (2014) 615-623.
- [16] D. Hidalgo, T. Tommasi, V. Karthikeyan, B. Ruggeri, A comparative study of the performance of commercial carbon felt and the innovative carbon-coated Berl saddles as anode electrode in MFC. Proceedings of the 2nd European regional meeting of the International Society for Microbial Electrochemistry and Technologies (ISMET). Alcalá de Henares, Spain., (2014).
- [17] D. Hidalgo, T. Tommasi, V. Karthikeyan, S. Bocchini, B. Ruggeri, Long-term evaluation of deposited polyaniline on commercial carbon felt used as anode in Microbial Fuel Cells. Proceedings of the 2nd European regional meeting of the International Society for Microbial Electrochemistry and Technologies (ISMET). Alcalá de Henares, Spain, (2014).
- [18] M. Crepaldi, A. Chiolerio, T. Tommasi, D. Hidalgo, G. Canavese, S. Stassi, D. Demarchi, F. Pirri, in: *SPIE Microtechnologies, International Society for Optics and Photonics*, 2013, pp. 876311-876311-876319.

## Publications

1. “Streamlining of commercial Berl saddles: a new material to improve the performance of microbial fuel cells”. D. Hidalgo, T. Tommasi, V. Cauda, S. Porro, A. Chiodoni, K. Bejtka, B. Ruggeri. (2014) *Energy*, 71, 615.
2. “Thick mesoporous TiO<sub>2</sub> films through a sol-gel method involving a non-ionic surfactant: characterization and enhanced performance for water photo-electrolysis”. D. Hidalgo, R. Messina, A. Sacco, D. Manfredi, S. Vankova, E. Garrone, G. Saracco, S. Hernández. (2014) *International Journal of Hydrogen Energy*.
3. “Optimization of 1D ZnO@TiO<sub>2</sub> Core–Shell Nanostructures for Enhanced Photoelectrochemical Water Splitting under Solar Light Illumination”. S. Hernández, V. Cauda, A. Chiodoni, S. Dallorto, A. Sacco, D. Hidalgo, E. Celasco, C.F. Pirri. (2014) *ACS Applied Materials & Interfaces*, 12153.
4. “Fast and low-cost synthesis of 1D ZnO/TiO<sub>2</sub> core-shell nanoarrays: characterization and enhanced photo-electrochemical performance for water splitting”. S. Hernández, V. Cauda, D. Hidalgo, V. Farías Rivera, D. Manfredi, A. Chiodoni, F.C. Pirri. (2014) *Journal of Alloys and Compounds*, 615, S530.
5. “TiO<sub>2</sub> nanotubes array as efficient transparent photoanode in Dye-sensitized Solar Cell with high electron lifetime”. A. Lamberti, A. Sacco, D. Hidalgo, S. Bianco, D. Manfredi, M. Quaglio, E. Tresso, C.F. Pirri. (2013) *Acta Physica Polonica A.*, 123, 376.
6. “A Low Complexity Wireless Microbial Fuel Cell Monitor using Piezoresistive Sensors and Impulse-Radio Ultra-Wide-Band”. M. Crepaldi, A. Chiolerio, T. Tommasi, D. Hidalgo, G. Canavese, S. Stassi, D. Demarchi, F. Pirri. (2013) *SPIE Microtechnologies, International Society for Optics and Photonics*, 876311.
7. “Comparison of photocatalytic and transport properties of TiO<sub>2</sub> and ZnO nanostructures for solar-driven water splitting”. S. Hernández, D. Hidalgo, A. Sacco, A. Chiodoni, A. Lamberti, V. Cauda, E. Tresso, G. Saracco. (2015) *Physical Chemistry Chemical Physics*. Submitted.
8. “Chemical pre-treatment of commercial carbon felt used as anode of Microbial Fuel Cells”. D.

- Hidalgo, T. Tommasi, S. Bocchini, A. Chiolerio, A. Chiodoni, I. Mazzarino, B. Ruggeri. (2015) Energy. Submitted.
9. “Enhanced performance of PANI-TiO<sub>2</sub> nanocomposite mesoporous films for sun-driven water splitting”. D. Hidalgo, S. Bocchini, M. Fontana, F. C. Pirri, G. Saracco, S. Hernández. (2015) Energy. Submitted.
  10. “New approach for low-cost microbial fuel cells for energy sustainable waste-streams treatment”. T. Tommasi, D. Hidalgo, I. Mazzarino, E. Celasco, A. Sacco, B. Ruggeri. Under preparation.
  11. “Continuous electricity generation using microorganisms from seawater in microbial fuel cells (MFCs): long-term evaluation of promising anode materials”. D. Hidalgo, T. Tommasi, V. Karthikeyan, B. Ruggeri. Under preparation.

## Participation in conference

1. “Comparative study of the performance of commercial carbon felt and the innovative carbon-coated Berl saddles as anode electrode in MFC”. D. Hidalgo, T. Tommasi, V. Karthikeyan, B. Ruggeri. 3 - 5 September 2014, Fundación General de la Universidad de Alcalá. 2<sup>nd</sup> European regional meeting of the International Society for Microbial Electrochemistry and Technologies (EU-ISMET). Alcalá de Henares, Spain. Poster Presentation.
2. “Long-term evaluation of deposited polyaniline on commercial carbon felt used as anode in Microbial Fuel Cells”. D. Hidalgo, T. Tommasi, V. Karthikeyan, S. Bocchini, B. Ruggeri. 3 - 5 September 2014, Fundación General de la Universidad de Alcalá. 2<sup>nd</sup> European regional meeting of the International Society for Microbial Electrochemistry and Technologies (EU-ISMET). Alcalá de Henares, Spain. Poster Presentation.
3. “Streamlining of commercial Berl saddles: new material to improve the performance of Microbial Fuel Cells”. D. Hidalgo, T. Tommasi, V. Cauda, S. Porro, A. Chiodoni, K. Bejtka, B. Ruggeri. 1 - 3 July 2013, University of Bolton. Materials and Renewable Energy Congress (MRE). Athens, Greece. Poster Presentation.
4. “Deposition of polyaniline in TiO<sub>2</sub> mesoporous films and its use as sensitizer for photocatalytic water splitting”. D. Hidalgo, S. Hernández, S. Bocchini, G. Saracco, F. C. Pirri. 1 - 3 July 2013, University of Bolton. Materials and Renewable Energy Congress (MRE). Athens, Greece. Oral Presentation.
5. “One Dimensional Core-Shell ZnO/TiO<sub>2</sub> Nanowires Arrays for Visible Light Driven Photoelectrochemical Water Splitting”. S. Hernández, D. Hidalgo, V. Cauda, A. Chiodoni, E. Celasco, F. C. Pirri. 1 - 3 July 2013, University of Bolton. Materials and Renewable Energy Congress (MRE). Athens, Greece. Oral Presentation.
6. “Commercial carbon-based material as anode in MFC (microbial fuel cells)”: Experimental verification. T. Tommasi, B. Ruggeri, I. Mazzarino D. Hidalgo. 12 - 15 November 2012, International Waste Working Group (IWWG). Fourth international symposium on energy from biomass and waste. Venice, Italy. ISBN 978-88-6265-006-9. Oral Presentation.